Modeling photon transport and reconstruction of optical properties for performance assessment of laser and fluorescence mammographs and analysis of clinical data

Inauguraldissertation
zur Erlangung der Doktorwürde
des Fachbereiches Physik
der Freien Universität Berlin

vorgelegt von
Ronny Ziegler
August 2008

1. Gutachter: Prof. Dr. H. Rinneberg
2. Gutachter: Prof. Dr. W. D. Brewer

Datum der Disputation: 29.10.2008

Glossary of frequently used variables

variable	unit	description
$\boldsymbol{x}$	m	spatial coordinate
$\boldsymbol{x}_\mathrm{s}$, $\boldsymbol{x}_\mathrm{d}$	m	coordinate of (physical) source and detector position
$\boldsymbol{x}'_\mathrm{s}$, $\boldsymbol{x}'_\mathrm{d}$	m	coordinate of simulated (shifted) source and detector position
$\boldsymbol{x}_{\mathrm{s}_i}$, $\boldsymbol{x}_{\mathrm{d}_i}$	m	coordinate of (physical) source and detector position of source-detector combination i
r	m	distance
$a(\boldsymbol{x})$	m^{-1}	scattering amplitude at position $\boldsymbol{x}$
b		scattering power
λ, λ_f	m	laser and fluorescence wavelength
λ_reg		regularization parameter
$\mu_\mathrm{a}(\boldsymbol{x}, \lambda)$	m^{-1}	absorption coefficient (intrinsic and dye) at position $\boldsymbol{x}$ at wavelength λ
$\mu_\mathrm{a}^0(\lambda)$	m^{-1}	absorption coefficient (intrinsic and dye) of (homogeneous) bulk at wavelength λ
$\mu_\mathrm{a}^\mathrm{sph}(\lambda)$	m^{-1}	absorption coefficient (intrinsic and dye) of lesion-simulating spherical heterogeneity used in phantom simulation or experiment at wavelength λ
$\mu_\mathrm{a}^\mathrm{chrom}(\boldsymbol{x}, \lambda)$	m^{-1}	intrinsic (chromophore) absorption coefficient at position $\boldsymbol{x}$ at wavelength λ
$\mu_{\mathrm{a},0}^\mathrm{chrom}(\lambda)$	m^{-1}	intrinsic (chromophore) absorption coefficient of (homogeneous) bulk at wavelength λ
$\mu_\mathrm{a}^\mathrm{dye}(\boldsymbol{x}, \lambda)$	m^{-1}	absorption coefficient of exogenous fluorescent dye at wavelength λ
$\overline{\mu_\mathrm{a}^\mathrm{breast}}(\lambda)$	m^{-1}	fitted average absorption coefficient of breast tissue at wavelength λ
$\mu_\mathrm{s}(\boldsymbol{x}, \lambda)$	m^{-1}	scattering coefficient at position $\boldsymbol{x}$ at wavelength λ
$\mu'_\mathrm{s}(\boldsymbol{x}, \lambda)$	m^{-1}	reduced scattering coefficient at position $\boldsymbol{x}$ at wavelength λ
$\mu'_{\mathrm{s},0}(\lambda)$	m^{-1}	reduced scattering coefficient of (homogeneous) bulk at wavelength λ
$\delta\mu_\mathrm{a}(\boldsymbol{x}, \lambda)$, $\delta\mu_\mathrm{a}^\kappa(\boldsymbol{x}, \lambda)$	m^{-1}	corrections of absorption coefficient at position $\boldsymbol{x}$ (reconstructed at nonlinear iteration step κ) at wavelength λ
$D(\boldsymbol{x}, \lambda)$	m	diffusion coefficient at position $\boldsymbol{x}$ at wavelength λ
$D^0(\lambda)$	m	diffusion coefficient of (homogeneous) bulk at wavelength λ
$D^\mathrm{sph}(\lambda)$	m	diffusion coefficient (intrinsic and dye) of lesion-simulating spherical heterogeneity used in phantom simulation or experiment at wavelength λ
$\overline{D^\mathrm{breast}}(\lambda)$	m	fitted average diffusion coefficient of breast tissue at wavelength λ

variable	unit	description
$\delta D(\boldsymbol{x},\lambda)$, $\delta D^{\kappa}(\boldsymbol{x},\lambda)$	m	corrections of diffusion coefficient at position $\boldsymbol{x}$ (reconstructed at nonlinear iteration step κ) at wavelength λ
$c_i^{\mathrm{chrom}}(\boldsymbol{x})$	M	chromophore concentration of tissue constituent i at position $\boldsymbol{x}$
η		quantum yield of fluorescent dye
τ	s	fluorescence lifetime
$\epsilon_i(\lambda)$	$\mathrm{M}^{-1}\mathrm{m}^{-1}$	molar extinction coefficient of tissue constituent i at laser wavelength
$\epsilon^{\mathrm{dye}}(\lambda)$	$\mathrm{M}^{-1}\mathrm{m}^{-1}$	molar extinction coefficient of fluorescent dye at the laser wavelength
n		refraction index
$\boldsymbol{n}$		(outward pointing) normal vector on surface $\partial\Omega$ or directional unit vector
$v = c/n$	$\mathrm{m\ s}^{-1}$	speed of light in medium
$q_0(\boldsymbol{x},\boldsymbol{x}_{\mathrm{s}},\lambda,\omega)$	$\mathrm{s\ m}^{-4}$	isotropic part of source term (in frequency domain) at position $\boldsymbol{x}$ and angular frequency ω for a source located at $\boldsymbol{x}_{\mathrm{s}}$ emitting photons at wavelength λ
$q_0^{\kappa}(\boldsymbol{x},\boldsymbol{x}_{\mathrm{s}},\lambda,\omega)$	$\mathrm{s\ m}^{-4}$	isotropic part of source term (in frequency domain) at position $\boldsymbol{x}$ and angular frequency ω (at nonlinear iteration step κ) for a source located at $\boldsymbol{x}_{\mathrm{s}}$ emitting photons at wavelength λ
$\widetilde{q_0}(\boldsymbol{x},\boldsymbol{x}_{\mathrm{s}},\lambda,t)$	m^{-4}	isotropic part of the source term in time-domain for a source located at $\boldsymbol{x}_{\mathrm{s}}$ emitting photons at wavelength λ
Ω	m^3	volume of interest
$\partial\Omega$	m^2	surface of volume Ω
κ		iteration step of nonlinear reconstruction
κ_{c}		nonlinear iteration step at convergence of absorption reconstruction
σ_{src}	m	width of 3D or 2D Gaussian blurred source
σ_{dye}	$\mathrm{m}^2\mathrm{mol}^{-1}$	molar absorption cross section of exogenous (fluorescent) dye
K		reflectivity at surface $\partial\Omega$
T_{d_i,s_i}, $T^{\mathrm{f}}_{d_i,s_i}$		ratio of instrumental factors for source-detector combination i
ξ_j		subset j of source-detector combinations corresponding to subvolume v_j
Ξ		set of source-detector combinations corresponding to complete volume of interest Ω
$\delta(\boldsymbol{x})$	m^{-3}	delta function
$\Theta(x)$		Heaviside function of scalar x
$\Phi_0^{\mathrm{inf}}(\boldsymbol{x},\boldsymbol{x}_{\mathrm{s}},\lambda,\omega)$	$\mathrm{s\ m}^{-3}$	photon density per unit angular frequency interval at position $\boldsymbol{x}$ and angular frequency ω for a source located at $\boldsymbol{x}_{\mathrm{s}}$ emitting photons at wavelength λ in an infinite homogeneous medium

variable	unit	description
$\Phi(\boldsymbol{x}, \boldsymbol{x}_\mathrm{s}, \lambda, \omega)$	s m^{-3}	photon density per unit angular frequency interval at position $\boldsymbol{x}$ and angular frequency ω for a source located at $\boldsymbol{x}_\mathrm{s}$ emitting photons at wavelength λ
$\Phi(\boldsymbol{x}, \boldsymbol{x}_\mathrm{s}, \lambda)$	m^{-3}	continuous wave photon density at position $\boldsymbol{x}$ for a source located at $\boldsymbol{x}_\mathrm{s}$ emitting photons at wavelength λ
$\Phi_0(\boldsymbol{x}, \boldsymbol{x}_\mathrm{s}, \lambda, \omega)$	s m^{-3}	photon density per unit angular frequency interval at position $\boldsymbol{x}$ and angular frequency ω for a source located at $\boldsymbol{x}_\mathrm{s}$ emitting photons at wavelength λ in a homogeneous medium (reference scan)
$\Phi_0(\boldsymbol{x}, \boldsymbol{x}_\mathrm{s}, \lambda)$	m^{-3}	continuous wave photon density at position $\boldsymbol{x}$ for a source located at $\boldsymbol{x}_\mathrm{s}$ emitting photons at wavelength λ in a homogeneous medium (reference scan)
$\widetilde{\Phi}(\boldsymbol{x}, \boldsymbol{x}_\mathrm{s}, \lambda, t)$	m^{-3}	photon density in time-domain at position $\boldsymbol{x}$ for a (pulsed) source located at $\boldsymbol{x}_\mathrm{s}$ emitting photons at wavelength λ
$\Phi_\mathrm{f}(\boldsymbol{x}, \boldsymbol{x}_\mathrm{s}, \lambda, \omega)$	s m^{-3}	fluorescence photon density per unit angular frequency interval at position $\boldsymbol{x}$ and angular frequency ω for a source located at $\boldsymbol{x}_\mathrm{s}$ emitting photons at wavelength λ
$\Phi_0^\mathrm{sim}(\boldsymbol{x}, \boldsymbol{x}_\mathrm{s}, \lambda, \omega)$	s m^{-3}	simulated photon density per unit angular frequency interval at position $\boldsymbol{x}$ and angular frequency ω for a source located at $\boldsymbol{x}_\mathrm{s}$ emitting photons at wavelength λ in a homogeneous medium (i.e. simulated photon density of reference measurement)
$\Phi_\kappa^\mathrm{sim}(\boldsymbol{x}, \boldsymbol{x}_\mathrm{s}, \lambda, \omega)$	s m^{-3}	simulated photon density per unit angular frequency interval at position $\boldsymbol{x}$ and angular frequency ω for a source located at $\boldsymbol{x}_\mathrm{s}$ emitting photons at wavelength λ in an inhomogeneous medium of optical properties reconstructed at nonlinear iteration step $\kappa - 1$ for $\kappa \geq 1$ (i.e. nonlinearly simulated photon density of inhomogeneous medium)
$G_0(\boldsymbol{x}, \boldsymbol{x}_\mathrm{s}, \lambda, \omega)$	s m^{-3}	Green's function (in frequency domain) at position $\boldsymbol{x}$ and angular frequency ω for a spatial and temporal delta-like source located at $\boldsymbol{x}_\mathrm{s}$ emitting photons at wavelength λ in a homogeneous medium
$G_\kappa(\boldsymbol{x}, \boldsymbol{x}_\mathrm{s}, \lambda, \omega)$	s m^{-3}	Green's function (in frequency domain) at position $\boldsymbol{x}$ and angular frequency ω for a spatial and temporal delta-like source located at $\boldsymbol{x}_\mathrm{s}$ emitting photons at wavelength λ in an inhomogeneous medium having optical properties reconstructed at nonlinear iteration step $\kappa - 1$ for $\kappa \geq 1$
$w(\boldsymbol{x})$	m^3	Voronoi cell volume associated with vertex $\boldsymbol{x}$
$a_i^\kappa(\boldsymbol{x}, \lambda, \omega)$	m	complex-valued sensitivity coefficient (in frequency domain) at position $\boldsymbol{x}$ and angular frequency ω of source-detector combination i for absorption coefficient reconstruction at wavelength λ using optical properties reconstructed at iteration step $\kappa - 1$ for $\kappa \geq 1$ (element of system matrix A); $a_i^{\kappa=0}(\boldsymbol{x}, \lambda, \omega)$ refers to homogeneous medium

variable	unit	description
$\hat{a}_i^{\kappa}(\boldsymbol{x}, \lambda, \omega)$	m^{-1}	complex-valued sensitivity coefficient (in frequency domain) at position $\boldsymbol{x}$ and angular frequency ω of source-detector combination i for diffusion coefficient reconstruction at wavelength λ using optical properties reconstructed at iteration step $\kappa - 1$ for $\kappa \geq 1$ (element of system matrix A); $\hat{a}_i^{\kappa=0}(\boldsymbol{x}, \lambda, \omega)$ refers to homogeneous medium
$a_i^{\mathrm{f}}(\boldsymbol{x}, \lambda, \omega)$	M^{-1}	complex-valued sensitivity coefficient (in frequency domain) at position $\boldsymbol{x}$ and angular frequency ω of source-detector combination i for dye concentration reconstruction at wavelength λ
$\boldsymbol{y}$		signal vector (reconstruction input vector)
$\boldsymbol{b}$		image update vector (reconstruction output vector)
A		system matrix (a.k.a. sensitivity matrix, stiffness matrix)
$\nu = \omega/(2\pi)$	s^{-1}	modulation frequency
ω	s^{-1}	angular (modulation) frequency
$\partial_{\boldsymbol{n}} = \boldsymbol{n} \cdot \nabla$	m^{-1}	directional derivation
$k(\lambda, \omega)$	m^{-1}	complex wave number (in frequency domain) at wavelength λ and angular frequency ω

List of acronyms

ART	Algebraic Reconstruction Technique
BI-RADS	Breast Imaging Reporting and Data System
CCD	Charge-coupled device
CG	Conjugate gradient
CT	Computed tomography
cw	Continuous wave
DBC	Dirac boundary condition
DCIS	Ductal carcinoma in situ
DOSI	Diffuse optical spectroscopic imaging
DOT	Diffuse optical tomography
DPDW	Diffuse photon density wave
FD	Frequency domain
FE	Finite element
FEM	Finite element method
HbO	Oxyhemoglobin
HbR	Deoxyhemoglobin
ICG	Indocyanine green
LCIS	Lobular carcinoma in situ
LHS	Left hand side
MC	Monte Carlo (simulations)
MF	Matching fluid (opt. properties given in Sec. A.5)
MRI	Magnetic resonance imaging
NIR	Near infrared
PDE	Partial differential equation
PTB	Physikalisch-Technische Bundesanstalt
RBC	Robin boundary condition
RHS	Right hand side
RTE	Radiative Transfer Equation
TCSPC	Time-correlated single photon counting
TPSF	Temporal point spread function
UMC Utrecht	University Medical Center Utrecht
VOI	Volume of interest

Contents

Chapter 1

Introduction

Besides its human dimension, breast cancer is of considerable socioeconomic importance. About every 8^{th} woman contracts breast cancer during her lifetime in industrialized countries (USA, Europe) and, there, breast cancer is the second leading cause of death of women [1]. Early detection of the disease is considered as the key to good prognosis and survival. Imaging modalities that are routinely used clinically to detect and diagnose breast cancer are X-ray mammography, ultra-sound (US) mammography and dynamic contrast enhanced magnetic resonance (DCE-MRI) imaging (MR mammography), with X-ray mammography used for screening. Many attempts are being currently made to improve on existing imaging modalities (e.g. X-ray mammographs to allow for digital tomosynthesis) and to develop alternative techniques that may offset some of the drawbacks of the standard modalities or that provide new information, e.g. positron emission mammography (PEM) [2, 3], electrical impedance mammography [4, 5], elastography [6], and last but not least optical mammography.

The first attempts to use visible light to detect breast tumors were made by Cutler [7] about 80 years ago, who used a classical light source (electric light bulb) to illuminate the breast and inspected the transmitted light by the naked eye. Light transmitted though the breast is exponentially attenuated with tissue thickness. Attenuation is the combined effect of absorption and scattering properties of the tissue. Whereas tissue chromophores (e.g. hemoglobin) strongly absorb light below about 650 nm, breast tissue is rather transparent in the red to near infrared (NIR) spectral range (650 nm $\leq \lambda \leq$ 950 nm, "diagnostic window") with a typical free absorption length of $l_{\text{a}} \approx 50$ cm. Therefore, all of today's optical mammographs use (laser) light sources that emit in this spectral range. In the NIR major chromophores of breast tissue are hemoglobin, oxy-hemoglobin, water and lipids. Besides absorption, NIR light is strongly scattered by tissue, the free scattering length of breast tissue is typically $l_{\text{s}} \approx 100$ μm. The microscopic scattering centers are cells, in particular cell nuclei and other cell organelles. Scattering is strongly forward peaked, aiding light transport with a free transport scattering length $l'_{\text{s}} \approx 1$ mm, after which directional correlation with the direction of the incident light is lost. The exponential attenuation constant of light k in breast tissue amounts to about $k = \sqrt{3/(l_{\text{a}} l'_{\text{s}})} \approx 0.8$ cm^{-1}. After a few millimeter, spatial coherence of the laser light is lost and radiation transport can be modeled as photon diffusion. Because of strong scattering, photons follow complicated trajectories that are considerably longer than the geometrical source-detector distance (e.g. breast thickness). The ratio of the average path length of photons to the geometrical distance ("differential path length factor") is about 10 for breast tissue.

Carcinomas beyond a few mm in diameter develop their own abnormal vasculature [8]. The higher concentration of blood in tumor tissue compared to the average blood concentration of normal breast tissue allows carcinomas to be detected by their absorption of NIR radiation. In tumor tissue total hemoglobin concentration and water concentration are each higher by about a factor 1.4 compared to normal breast tissue [9]. Although (breast) tumors are generally believed to be hypoxic on average [10], diffuse optical spectroscopic imaging (DOSI) [9] did not reveal a difference in tissue oxygen saturation

between tumors and normal breast tissue. The same conclusion was deduced from clinical studies on optical mammography [11, 12]. Furthermore, it was shown from these studies that carcinomas may exhibit both, lower as well as higher scattering, however, on average scattering is increased in carcinomas by about 20% [12, 13]. There is rather little information available on the optical properties of benign lesions. Cysts generally show considerably lower scattering than surrounding breast tissue.

Many decades after the initial attempts by Cutler, interest in optical mammography renewed, in particular since the early nineties of the last century, when adequate optoelectronic components including laser diodes and miniaturized photon detectors, compact signal processing electronics and powerful PCs became available that allowed to develop compact optical mammographs that could be operated in a clinical setting. Many different experimental instrumentations for optical mammography have been developed since then, using continuous wave (cw) laser light [14, 15], short (ps) laser pulses (time-domain instrumentation) [16, 17, 18], or amplitude-modulated laser light (frequency-domain mammographs) [19, 20, 21]. Continuous wave instruments measure light attenuation and generally cannot distinguish between scattering and absorption properties of breast tissue. Time-domain mammographs, on the other hand, record distributions of times of flight of photons caused by the different photon path lengths through tissue. By measuring the shape of the transmitted laser pulse, absorption, reducing the pulse amplitude, and scattering, affecting the width of the broadened laser pulse, can be distinguished. Frequency-domain mammographs record phase shifts and demodulation of transmitted amplitude-modulated laser radiation and hence allow to separate absorption from scattering as well, in particular when more than one modulation frequency is used. Most mammographs operate at two red to NIR wavelengths at least, instruments with up to seven wavelengths have been reported [22] in order to distinguish the contributions of the various chromophores to total absorption (tissue optical spectroscopy). Independently of the particular type of light sources used, presently all optical mammographs irradiate a small spot on the surface of the breast, one at a time, subsequently sampling many (source) positions, rather than applying the broad-beam illumination of the early instruments. At each source position, transmitted laser light is recorded simultaneously at a number of (detector) positions on the surface of the breast. While consecutive sampling of source positions increases the time required to record a mammogram, by measuring the response of the system to a (spatial) δ-like photon source at selected source positions on the breast surface, spatial resolution and contrast is improved considerably compared to the broad-beam instrumentation used initially. Many different source-detector arrangements have been realized, tomographic instruments [15, 21, 23] place sources and detectors at fixed positions over the entire surface of the breast, providing approximately complete angular sampling, whereas scanning optical mammographs [14, 16, 17, 19, 20] slightly compress the breast between two glass plates, scanning the source across one compression plate, while detectors are either placed at fixed positions or scan in tandem with the source. Such source-detector arrangements, however, allow to sample a restricted range of (projection) angles only, reducing further the limited spatial resolution of diffuse optical tomography (DOT).

At the same time when instrumental developments were pursued for optical mammography, considerable theoretical advances were made in tissue optics. Photon transport in a turbid medium such as tissue can be described by the radiative transfer equation (RTE). Because scattering dominates over absorption in the NIR, the diffusion approximation of the RTE can be used [24], except e.g. in the immediate vicinity of boundaries or close to a δ-like photon source. There exist analytical solutions to the diffusion equation for highly idealized situations (e.g. a homogeneous diffusely scattering and absorbing infinite medium with or without a spherical heterogeneity simulating a tumor) [24, 25, 26, 27], yet for more realistic numerical breast models the diffusion equation is solved numerically using finite element methods (FEM, [28, 29, 30]). Such forward calculations require the spatial distribution of the absorption and reduced scattering coefficients to be known within the volume of interest (VOI) to simulate the diffusely transmitted laser (and fluorescence) radiation. The inverse problem, i.e. reconstructing absorption and reduced scattering coefficients and the concentration of an exogenous fluorescent dye from simulated or experimental data of diffuse transmittance and reflectance taken at the surface, is ill-posed due to the large volume which influences a transmission measurement. In contrast to X-ray tomography analytical

solutions of the inverse problem are not known for diffuse optical tomography because the problem is nonlinear. Prior knowledge, e.g. on the spatial distribution of optical properties, should be included into reconstruction algorithm to reduce the degree of ill-posedness, and methods of regularization need to be applied, however, affecting the results of the reconstruction.

One may ask what advantages and disadvantages optical mammography may have over other imaging modalities to detect and diagnose breast cancer. In contrast to X-ray, MR-, and US- mammography spatial resolution of optical mammography is poor, being close to centimeters rather than millimeters, because of light scattering. However, unlike X-ray mammography, optical mammography does not use ionizing radiation and compared to DCE-MRI it is cost effective, allowing optical mammograms to be taken frequently. Most importantly, however, unlike the three other modalities optical mammography exploits the power of optical spectroscopy and, in principle, allows the metabolic state of breast tissue to be assessed non-invasively including that of benign and malignant lesions. This aim might be achieved when monitoring (neo-adjuvant) chemotherapy of known (superficial) breast tumors prior to surgery by in vivo DOSI [31]. However, up to now such hopes did not come true for optical mammography based on contrast of intrinsic chromophores. Two (retrospective) clinical studies on time-domain scanning optical mammography, both using very similar instrumentation, one employing two optical wavelengths [13], the other one up to seven wavelengths [22] yielded a true positive rate (sensitivity) of about 80%-85%, whereas the false positive rate (1-specificity) was between 40% and 50%. In other words, lesions could be detected with adequate sensitivity, but despite the considerable advances made in instrumentation and data analysis, carcinomas could not be discriminated from benign lesions. It is unlikely that this result can be improved by adding a (classical) light source that covers the entire bandwidth of the diagnostic window to improve spectroscopic resolution.

To find an explanation for this disappointing result and a way to overcome this dilemma, one may look at DOSI of breast tumors during neo-adjuvant chemotherapy [31] and to DCE-MRI [32, 33]. Without applying a contrast agent (Gd-DTPA) specificity of MR-mammography is poor, i.e. benign and malignant lesions cannot be discriminated by their properties relevant to MRI, i.e. by their proton (H_2O) density, and their relaxation rates T_1, T_2 and $T_2^\star$. Likewise, the optical properties of benign and malignant breast lesions overlap, in particular, taking the large biological variability of carcinomas into account. Discrimination of such lesions as being benign or malignant is much more likely by dynamic rather than static measurements, e.g. when the response of the lesion is monitored following administration of a suitable (fluorescent) contrast agent. Similarly, cancers can be classified as responders or non-responders to neo-adjuvant chemotherapy by monitoring changes in their optical properties using DOSI.

Neo-angiogenesis associated with tumor growth leads to tumor vasculature that is "leaky", i.e. more permeable to medium-sized molecules such as Gd-DTPA compared to healthy breast tissue or benign lesions [8]. Therefore, at the site of the carcinoma, the (unspecific) contrast agent Gd-DTPA leaves the vasculature more rapidly, resulting in early signal enhancement in (T_1-weighted) MR images of the breast, increasing specificity in this way. Likewise, after administration of a NIR fluorescent contrast agent, such as Indocyanine green (ICG) or the ICG derivative Omocyanine, these molecules are expected to extravasate more readily in tumors compared to normal breast tissue and benign breast lesions as well. By taking fluorescence mammograms besides mammograms based on the transmittance of exciting laser radiation, there is a good chance that specificity of optical mammography can sufficiently be increased. Importantly, tissue autofluorescence is low within the diagnostic window. Very recently, first fluorescence mammograms obtained from three patients with carcinomas following administration of ICG as fluorescent contrast agent were reported by an American research group and 3D reconstructions of the intrinsic optical (absorption and scattering) properties as well as the ICG concentration was carried out [34].

In this thesis, performed at the Philips Research Laboratories, Hamburg, a software suite was developed based on the finite element method to simulate propagation of NIR (laser) light and fluorescence radiation through inhomogeneous turbid media based on the diffusion equation and to carry out linear and nonlinear reconstructions of the absorption and scattering properties of the medium as well as fluorescent dye concentrations from simulated or experimental data taken in frequency domain or time-domain.

Simulations of photon densities of diffusely transmitted or remitted laser radiation and fluorescence radiation from an exogenous fluorescent contrast agent are supported by the software package for arbitrary object (breast) geometries and arrangements of sources and detectors. The software package was used to quantitatively assess the performance of various instrumental concepts for fluorescence mammographs and to analyze laser and fluorescence mammograms taken by a tomographic instrument (Philips Research) employed in a clinical study on fluorescence mammography carried out at the University Medical Center Utrecht, using Omocyanine as fluorescent dye.

This thesis is structured in the following way. After an introduction to the medical background of breast cancer and breast cancer screening (Chapter 2), the physical background of modalities used in the current workflow of mammography screening (X-ray, MRI, Ultrasound) is discussed and compared with that of optical mammography (Chapter 3). Subsequently, different instrumentations used for optical mammography are explained and the laboratory setup is outlined (Chapter 4) that was used by the Physikalisch-Technische Bundesanstalt (PTB) for phantom experiments analyzed in this thesis.

The main results of the thesis are divided into three chapters, separating topics mainly related to the forward model (Chapter 5) and image reconstruction (Chapters 6 and 7), respectively. After an introduction to the theoretical background of forward model calculations (Sec. 5.1), results of the improved time-window analysis (Sec. 5.2.1) and the performance analysis of instrumentation in optical mammography (Sec. 5.2.2) are presented.

The chapter related to image reconstruction (Chapter 6) presents, after explaining the theoretical background in Sec. 6.1.1, improvements in reconstruction algorithms and reconstruction results of phantom data, achieved in this thesis, e.g. improved data preprocessing (Sec. 6.2.1), investigation of spatial resolution (Sec. 6.2.2), and sub-volume reconstruction (Sec. 6.2.3). Furthermore, linear and nonlinear reconstructions of clinical data were carried out to determine intrinsic contrast based on absorption and fluorescent dye concentrations (Chapter 7), using algorithmic improvements introduced before.

Conclusions, summary, and outlook of the thesis are given in chapter 8, followed by an appendix containing further technical details, e.g. description of the Philips tomographic fluorescence mammograph (appendix A.1), details on numerical implementations (appendices A.2, A.3), and on phantom setups used throughout this thesis (appendices A.4, A.5, A.6). Furthermore, derivations of selected formulas are given in appendix C.

Chapter 2

Medical background

2.1 Etiopathology and treatment of breast cancer

Breast cancer mainly begins in the glands, i.e. in the lobules that provide the milk production, or in the ducts that connect lobules to the nipple. Different types of benign tumors exist that are not cancerous although having an abnormal growth. These lumps neither spread (nonmetastatic) nor are life threatening. Nonetheless, some benign breast lumps can increase the risk of getting cancer, i.e. malignant tumors. Such tumors begin with a hyperplasia, an abnormal increase in the number of cells. At this state, the tumors are regarded to be in pre-cancerous (*in situ*) state, and depending on their location, these tumors are called ductal or lobular carcinoma in situ (DCIS or LCIS, respectively), occurring 80% and 15% respectively as a pre-cancer in breasts. As *characteristicum*, DCIS and LCIS neither spread nor invasively infiltrate surrounding tissue, but micro calcifications start to exist in these tumors, making them visible on X-ray mammograms. Most cancers at *in situ* stage can be cured by surgery, hence detecting cancer at this early state is beneficial, allowing a less drastic follow-up therapy.

Within one to more than 10 years, tumors can become invasive in a next step. Invasive tumors are more dangerous and break through the duct or gland walls to invade the surrounding (fatty) tissue. These invasive cancers can be characterized being at one of the following three stages (TNM staging), i.e. being either locally confined to the breast (T-stage, USA five year survival rate 97%), spread to surrounding tissue or nearby lymph nodes (N-stage, 80%), or already metastasized and spread to distant organs (M-stage, 23%). Most of the invasive findings have their origin in the ducts or lobules (80% invasive ductal carcinoma and 10% invasive lobular carcinoma), making early diagnosis of DCIS and LCIS an important factor for successful cancer therapy.

No *sui generis* exists for breast cancer, instead it is a result of multiple genetic changes or mutations caused by several unmodifiable (e.g. age, inherited genetic mutations [35, 36], high breast density, age at first birth, early menarche, late menopause, and regular ovulation [37]) and modifiable (e.g. postmenopausal obesity, alcohol consumption, and physical inactivity [38]) risk factors.

It was shown that the use of postmenopausal hormone therapy (hormone replacement therapy, i.e. a combined estrogen and progestin therapy) with extended use increases breast cancer risk considerably [39]. This treatment of menopausal symptoms shows multiple positive and negative side effects as increased mineral bone density, decreased colorectal cancer risk, but also increased heart disease and dementia risk. Hence, treatment has to be chosen carefully and individually. While oral contraceptives may slightly increase the risk of breast cancer [40, 41], it was shown by randomized trials that breast cancer risk does not increase by use of underwire bras, antiperspirants [42] or an abortion [43].

Some of the mentioned causes for increased breast cancer risk are directly related to elevation of the exposure to ovarian hormones, because estrogen increases the chance of DNA replication errors leading to

carcinogenic mutations. Others causes are purely correlated to the socioeconomic status of the patient.

If a patient is known to have an increased risk of breast cancer, the use of a hormone chemoprevention or a prophylactic mastectomy (removal of both breasts) [44] can be adviseable. Also starting mammography screening at younger age can be a possibility for high risk patients, or taking additional tests like magnetic resonance imaging (MRI) and ultrasound (US). But a prevention of breast cancer by full mastectomy is only adviseable for a fraction of patients. For all others, early detection can be live saving. Therefore, awareness about symptoms is an important key aspect. In most cases the tumor can be detected early as a painless mass (only 10% of breast cancer patients have breast pain and no mass). Mostly, breast pain is commonly due to benign conditions and is in general not a sign for malignant breast cancer. Nonetheless, thickening, swelling, scaliness, skin irritation, ulceration, nipple symptoms as spontaneous discharge, erosion, inversion, or tenderness can be symptoms of breast cancer. Although not being useless if performed correctly, the effects of a monthly breast self examination are non conclusive and recommendations have been dropped in some countries [45]. Instead, the American Cancer Society guidelines recommend an annual clinical breast examination including mammography.

After detection of breast cancer, the treatment consits of a variety of options, depending on the type of cancer that has been found [46]. In early stages, some type of surgery is performed (lumpectomy, i.e. a local removal of the tumor) often followed by radiation therapy to prevent recurrence of the cancer. Also mastectomy, accompanied by the removal of (axillary) lymph nodes to determine the spread of the cancer, but without radiation therapy, is commonly used. As an adjuvant (i.e. after surgery) systemic treatment, chemotherapy, hormone therapy, or monoclonal antibody therapy are performed to reduce the rate of recurrence.

2.2 Screening and diagnosis

Screening aims at finding breast cancer at an early stage to allow for a cost effective and minimally invasive treatment. The gold standard for breast cancer screening is X-ray mammography, but it exposes the breast to carcinogenic ionizing radiation and causes severe pain in many patients due to the strong breast compression needed temporarily during an examination.

Qualified discussions about the justification of screening mammography to reduce mortality exist [50]. While it was shown in numerous trials performed in the USA that early detection improves treatment options and survival rates [51, 52, 53, 54], Swedish trials, on the other hand, show that mass screening for breast cancer does not increase the survival benefit, whereas it leads to increased useage of aggressive treatment [55, 56]. Nonetheless, mammography will detect about 90% of breast cancers in women without symptoms [57] and is advised for European women between an age of 50 to 69.

The typical workflow of screening is shown in Fig. 2.1 using patient numbers based on USA data. For women having normal breast cancer risk, screening mammography starts at an age of 40, with younger women not being screened due to higher breast densities. Approximately 40 million patients undergo the annual screening in the USA, with 10% having inconclusive or positive findings and undergo a call-back with subsequent US diagnosis and additional mammography. A small but increasing amount of patients (1% to 3%) is imaged by MR.

The remaining 1 million call-back-patients with suspicious, positive, or inconclusive findings undergo tissue sampling by surgery or (guided) needle biopsy for subsequent histopathology to gain confidence or to characterize the detected tumor. There is an increasing number of false-positive biopsies with nearly four times as many patients having negative, and only 200.000 patients having positive findings. This gap is especially large in the USA and the suspected reason for this is to secure clinics from litigations. Also, a significant portion of breast cancers can be found in retrospect of previously acquired X-ray mammograms, where tumors have been missed during the examinations [58].

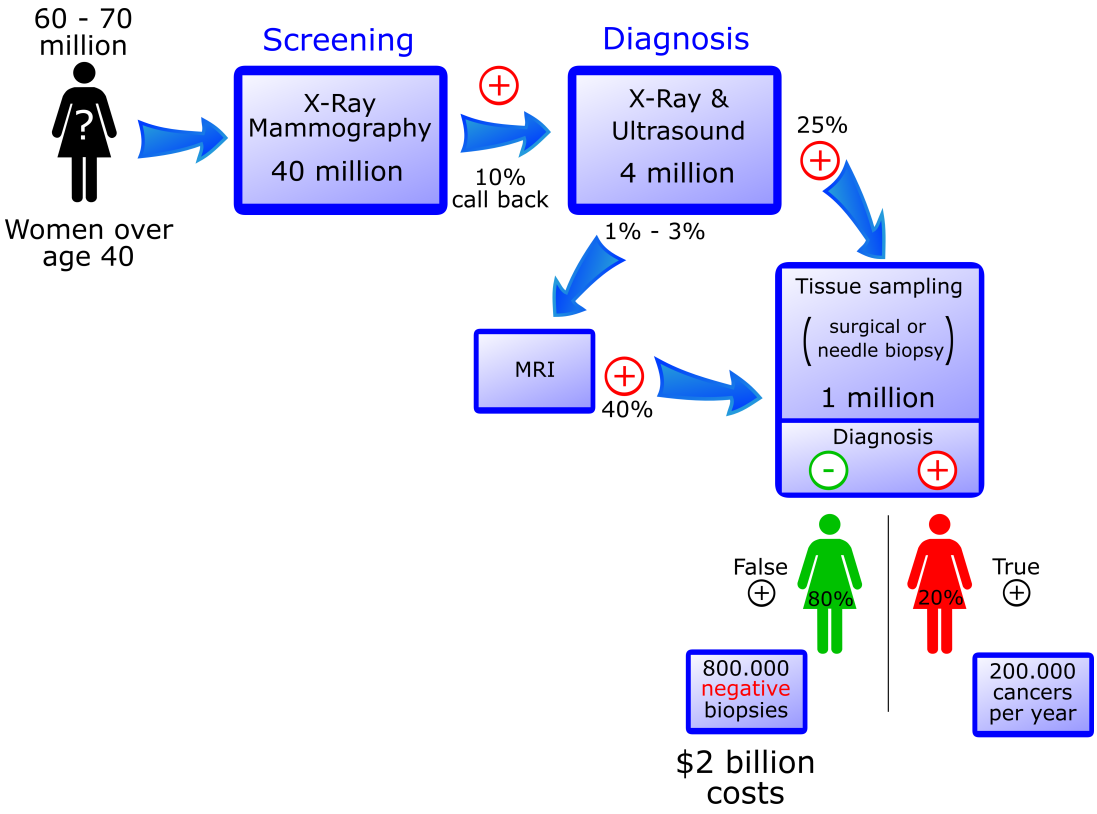

Figure 2.1: Workflow of breast cancer screening using USA data. Of 40 million women that attend the yearly screening program, 200.000 have true positive findings (malignancies) while four times as many patients who underwent biopsy had negative findings. [47, 48, 49]

Chapter 3

X-ray mammography, MRI, and ultrasound mammography

In this chapter, physical principles of X-Ray mammography, MR mammography and US mammography are briefly discussed. Differences and similarities to optical mammography are pointed out.

Several competing modalities have been adapted to mammography, e.g. acousto-optic, optoacoustic, impedance tomography, elastography, but only three modalities possess a key role in the current screening and diagnosis workflow, i.e. X-ray, magnetic resonance imaging, and ultrasound. For comparison with DOT, contrast mechanisms, image acquisition, and image reconstruction of these three modalities is explained in the following sections.

Fig. 3.1 shows the true positive rate (TPR, i.e. sensitivity) and the false positive rate (FPR, i.e. 1 − specificity) of MRI, X-ray, and US for breast cancer detection as determined in several clinical studies performed from 2000 to 2005. Although determined sensitivity and specificity are scattered quite significantly in the plot for each modality, it is evident that MRI mammography exhibits a very high sensitivity but only a slightly smaller or equal specificity compared with X-ray mammography. In contrast, the two results available for sensitivity of ultrasound seem inconclusive.

For illustration and comparison of mammograms acquired with the three modalities, data taken with each modality from a selected patient during a clinical study performed at the University Medical Clinic Utrecht in 2007 is shown for illustration in the following sections. For this puprose, data chosen was collected from a 41 year old patient bearing a cyst in the upper quadrants of her right breast (23 mm × 11 mm) and having a suspicious mass (18 mm × 11 mm) in the lower quadrants of the same breast. Although biopsy results are not available, a (benign) fibromadenoma is suspected at this location.

3.1 X-ray mammography

X-rays penetrating tissue are attenuated depending on the density and the atomic number of the material crossed, hence can be utilized to distinguish water, fat, and musculature. Furthermore, calcifications can be detected, which is exploited to find tumors in mammograms even at the *in situ* stage. Due to its rather high sensitivity and specificity and its low costs, X-ray mammography is the primary screening modality for breast cancer and reaches a high spatial resolution of approximately 50 μm, hence allowing detection of small calcifications present in DCIS or LCIS quite early, and leaving more follow-up options for therapy. Nonetheless, interpretation of mammograms, especially if taken from younger women, can

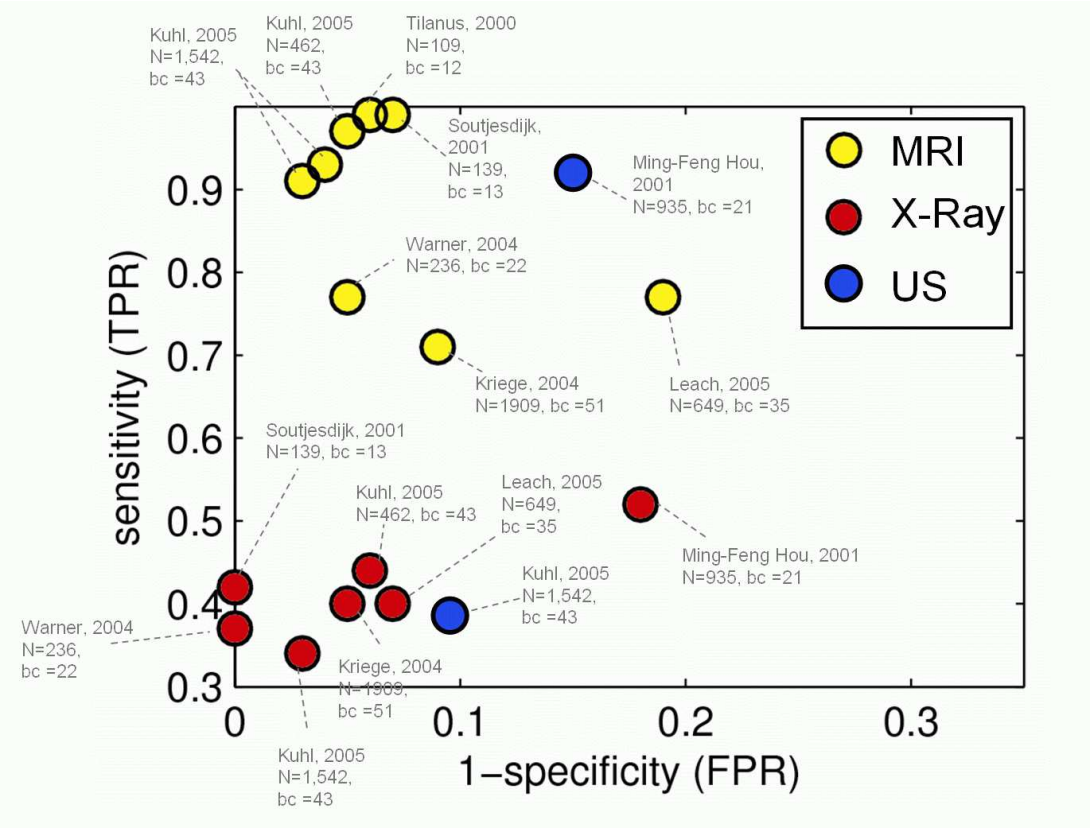

Figure 3.1: Sensitivity (true positive rate, TPR) and 1-specificity (false positive rate, FPR) of different modalities (X-ray, MR, US Mammography) from different clinical studies. N indicates the number of patients per study and bc is the number of patients with breast cancer.

be difficult due to more glands and ligaments present in the breast, obscuring abnormal findings in the images.

In contrast to NIR imaging, X-rays propagate through tissue on a straight line, with only a small number of photons undergoing scattering events (Rayleigh-scattering, Compton-effect). Furthermore, scattered photons can be filtered out in front of the detector by an anti-scatter grid. The radiation intensity I_0^{Xray} emitted from the source is attenuated while the beam is propagating on a straight line s (in 2D) through the tissue,

$$\frac{I^{\text{Xray}}(\rho,\vartheta)}{I_0^{\text{Xray}}} = \exp\left(-\int_{s(\rho,\vartheta)} \mu_{\text{Xray}}(x,y)ds\right), \tag{3.1}$$

where $\mu_{\text{Xray}}(x,y)$ is the spatial distribution of the material dependent absorption coefficients (in m^{-1}), and $I^{\text{Xray}}(\rho,\vartheta)$ is the intensity measured under projection angle ϑ and lateral offset ρ. As illustrated in Fig. 3.2, the measurement is either described by a coordinate system fixed to the object (x–y coordinates) or fixed to the source-detector combinations (ρ–ϑ coordinates).

Due to the dependence of the absorption coefficient on the X-ray tube voltage, dimensionless Hounsfield

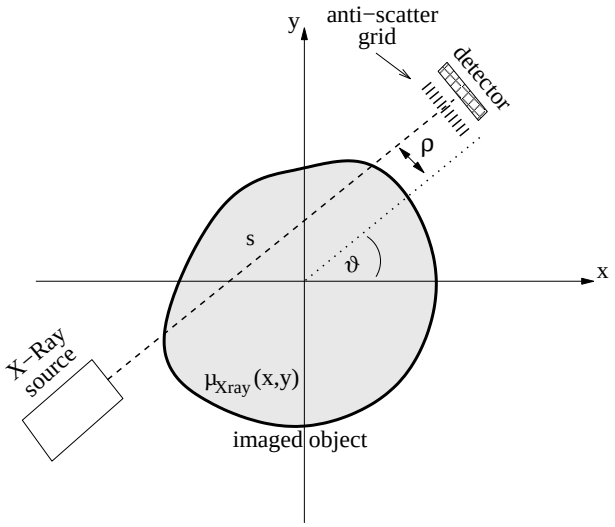

Figure 3.2: Illustration of coordinate systems in X-ray imaging. Coordinates xy are fixed to the imaged object, with its spatial distribution of absorption coefficient $\mu_{\mathrm{Xray}}(x, y)$. Orientation of the source-detector combination is described by the angle ϑ and the lateral offset ρ.

units (HU) are used, giving the variations of the absorption coefficient compared with water (in per mill),

$$HU = \frac{\mu_{\mathrm{Xray}} - \mu_{\mathrm{Xray,H_2O}}}{\mu_{\mathrm{Xray,H_2O}}} 1000, \tag{3.2}$$

resulting in a Hounsfield unit of 0 for water and -1000 for air. In several application scenarios, the image contrast can be enhanced by using contrast agent (e.g. $BaSO_4$) with increased absorption coefficient, e.g. in coronary angiography, where contrast agent is injected into one of the two major coronary arteries by a catheter to enhance visibility of vessels or measure their lumen.

The line integrals $p_{\mathrm{Xray}}(\rho, \vartheta)$ appearing in Eq. (3.1), i.e.

$$p_{\mathrm{Xray}}(\rho, \vartheta) = \ln\left(I_0^{\mathrm{Xray}} / I^{\mathrm{Xray}}(\rho, \vartheta)\right) = \int_{s(\rho,\vartheta)} \mu_{\mathrm{Xray}}(x, y) ds, \tag{3.3}$$

are the Radon-transform of $\mu_{\mathrm{Xray}}(x, y)$. The Fourier-slice theorem (in 2D) (a.k.a. central-slice theorem or projection-slice theorem) states that the 1D Fourier transform of the projections $p_{\mathrm{Xray}}(\rho, \vartheta)$ with respect to ρ of $\mu_{\mathrm{Xray}}(x, y)$ onto a line (i.e. ϑ = const.) are equal to the slice through the origin of the (2D) Fourier transform of $\mu_{\mathrm{Xray}}(x, y)$, which is parallel to the projection. Hence, the spatial distribution of the absorption coefficient $\mu_{\mathrm{Xray}}(x, y)$ can be calculated analytically from the Radon-transform $p_{\mathrm{Xray}}(\rho, \vartheta)$ via Fourier transformation, if all ρ and ϑ have been sampled. Therefore, in CT, where data acquisition is carried out with full angular sampling, an analytical reconstruction is possible (at least approximative, ignoring limitations caused by the cone-beam, spiral movement, etc). Due to the high angular sampling and the corresponding high number of projection images, CT results in a higher radiation dose compared with standard (planar) X-ray image acquisition and hence is inappropriate for breast screening. Thus, X-ray mammography is performed by a low-dose X-ray system using a planar geometry with a (up to the point of painful) strong compression to examine breasts by taking images on a silver-bromide film or by using CCD detectors (full-field digital mammography). During a standard breast screening examination in the USA, an axial and a mediolateral oblique (from breast center to upper outer quadrant) view is

taken per breast, resulting in an absorbed radiation dose of about 4 mGy. Although the exposure of the patient to radiation due to X-ray mammography induces the risk of getting cancer, 50 lives are saved due to early cancer detection per one life lost due to the ionizing radiation [59]. As CCD detectors allow for fast readout of acquired images and for digital postprocessing of the results, an axial resolution can be achieved by imaging the breast under several angles and carrying out a tomosynthesis reconstruction. During this examination, the overall dose can be kept similar to the standard screening investigation, although a larger number of low signal-to-noise projection images is taken.

As can be seen in Fig. 3.1, compared with MR mammography, X-ray mammography has a high specificity (percentage of correctly identified negatives), but a low sensitivity which ranges from 45% to about 90% depending on factors such as density of the breast. The sensitivity can be significantly lower for younger women having more glandular tissue and hence radiographically dense breasts [60], rendering screening mammography useless for such patients.

As an example of an X-ray mammogram, an image taken in mediolateral oblique view of the right breast of the selected patient is given in Fig. 3.3 (left). A lot of structures can be seen in this image, making a diagnosis problematic for an untrained observer who will have problems to find the (quite large) cyst and the suspicious mass.

3.2 MR mammography

Magnetic resonance imaging provides contrasts between different soft tissues without using ionizing radiation, but instead uses magnetization of protons in water molecules that account for approximately 2/3 of the human body.

Ground state atomic nuclei with an uneven number of protons or neutrons have an angular momentum $\hbar \boldsymbol{I}$ and a dipole moment of

$$\boldsymbol{\mu} = \gamma \hbar \boldsymbol{I}, \tag{3.4}$$

where $h = \hbar 2\pi = 6.63 \cdot 10^{-34}$ Js is Planck's constant, γ is the gyromagnetic ratio, which is characteristic for nuclei of atomic number A and proton number Z, and $\boldsymbol{I}$ is the spin of the nucleus. Quantum mechanics shows that in a magnetic field $\boldsymbol{B}_0 = (0, 0, B_z)^T$ the z component of the spin can only have discrete values, while the spin precesses around $\boldsymbol{B}_0$ with Larmor frequency

$$\omega_{\mathrm{L}} = \gamma B_z. \tag{3.5}$$

For hydrogen nuclei ($I = 1/2$, $\gamma(^1\mathrm{H}) = +2.675 \cdot 10^8$ rad/(T s), $\mu(^1\mathrm{H}) = +2.7928\ \mu_{\mathrm{N}}$, where μ_{N} is the nuclear magneton), the z component of its spin is either aligned parallel (up) or antiparallel (down) to the magnetic field, i.e. eigenvalues of $\boldsymbol{I}_z$ are given by $m = +1/2, -1/2$, respectively, each corresponding to a Zeeman energy $E_m = -\gamma \hbar B_z m$. When the hydrogen nucleus switches between these two Zeeman levels, a quantum of $\Delta E = \gamma \hbar B_z$ of magnetic dipole radiation is emitted or absorbed.

In case of investigating the human body via MRI, where the patient is positioned (partially) in a magnetic field, ensembles of hydrogen nuclei instead of a single nucleus are investigated, and occupation numbers N_{up} ($m = +1/2$) and N_{down} ($m = -1/2$) of the corresponding two energy states are given by

$$\frac{N_{\mathrm{down}}}{N_{\mathrm{up}}} = \exp\left(-\Delta E/(k_{\mathrm{B}} T)\right), \tag{3.6}$$

where $k_{\mathrm{B}} = 1.38 \cdot 10^{-23}$ Ws/K is the Boltzmann constant and T is the absolute temperature of the ensemble. Hence, in case of clinical applications ($T \approx 300$ K and B_z =1.5 T or 3 T), nuclei corresponding to the lowest energy state, i.e. spin aligned parallel to $\boldsymbol{B}_0$, outnumber the nuclei with antiparallel orientation by 10 to 20 ppm, depending on the field strength. Such ensemble of nuclei has a magnetic moment m_0, which is aligned parallel to the magnetic field $\boldsymbol{B}_0$ in equilibrium, but which can be excited towards the plane transversal to $\boldsymbol{B}_0$, when exposed to an additional field $\boldsymbol{B}_1$ (RF pulse) superimposed to $\boldsymbol{B}_0$.

Switching off $\boldsymbol{B}_1$ causes the excited magnetic moment $\boldsymbol{m} = (m_x, m_y, m_z)^{\mathrm{T}}$ to return to its equilibrium state (parallel to $\boldsymbol{B}_0$) [61],

$$\begin{aligned} \frac{dm_z}{dt} &= \gamma(\boldsymbol{m} \times \boldsymbol{B}_0)_z + (m_0 - m_z)/T_1, \\ \frac{dm_{x,y}}{dt} &= \gamma(\boldsymbol{m} \times \boldsymbol{B}_0)_{x,y} - m_{x,y}/T_2, \end{aligned} \tag{3.7}$$

a process called relaxation. The precessing magnetic moment can be detected as an AC voltage in a coil perpendicular to $\boldsymbol{B}_o$ surrounding the ensemble (free induction decay, FID). Here, T_1 is the longitudinal relaxation time caused by the exchange of energy between nuclei and the lattice, and T_2 is the transverse relaxation time due to the loss of phase coherence of the spins in the transverse plane.

In medical applications, where the field is inhomogeneous due to the presence of the patient, the Larmor frequencies ω_{L} of the nuclei slightly vary with location inside the inhomogeneous magnetic field, reducing the coherence of the ensemble, hence causing a reduced transverse relaxation time $T_2^\star$ with

$$\frac{1}{T_2^\star} = \frac{1}{T_2} + \gamma \Delta B(\boldsymbol{x}), \tag{3.8}$$

where $\Delta B(\boldsymbol{x}) = B(\boldsymbol{x}) - B_z$ is the variation in the magnetic field, and $\boldsymbol{x}$ is a spatial coordinate. Nonetheless, this destructive interference of the transverse magnetizations is reversible if a selected (180°) RF-pulse is applied at a time $T_{\mathrm{E}}/2$ after the first RF-pulse. In doing so, the magnetizations of regions with varying Larmor frequency result in a coherent transversal magnetization at time T_{E} after the first RF-pulse, causing increased signal in the RF coil (spin echo) [62]. The amplitude of the refocussed magnetization is down by the factor $\exp(-T_{\mathrm{E}}/T_2)$. The additional contribution $\gamma \Delta B(\boldsymbol{x})$ to the effective relaxation rate $1/T_2^\star$ are not of stochastic origin and hence compensated provided movements can be excluded.

The signal measured in the RF coil is caused by all spins inside the imaged volume. Nonetheless, spatial resolution can be achieved by applying three gradient fields. Therefore, an additional magnetic gradient field $\boldsymbol{G}_z = (0, 0, \partial B_z/\partial z)^T$ is superimposed to $\boldsymbol{B}_0$ during the RF-pulse, causing a spatial dependence of the Larmor frequency $\omega_{\mathrm{L}}(z) = \gamma\,(B_z + z \partial B_z/\partial z)$. Hence, by choosing the corresponding angular frequency of the RF-pulse, only nuclei inside a selected slice perpendicular to $\boldsymbol{G}_z$ are excited (slice selection) and contribute to the measurement signal. The thickness of the slice depends on the RF bandwidth. Subsequently, a phase gradient $\boldsymbol{G}_y = (0, \partial B_z/\partial y, 0)^T$ is applied for a time τ_{phase} and a read out gradient $\boldsymbol{G}_x = (\partial B_z/\partial x, 0, 0)^T$ is used. Presence of a gradient field introduces a phase shift of the previously coherent magnetizations in the selected xy slice. By introducing spatial frequencies

$$k_y = \gamma \int_{\tau_{\mathrm{phase}}} \boldsymbol{G}_y(t')dt', \tag{3.9}$$

and using varying gradient fields $\boldsymbol{G}_y$, the measurement signal $s(k_x, k_y)$ at selected values $k_y = -k_{y,\max}/2$, ..., $+k_{y,\max}/2$ is sampled. In contrast, the read out gradient $\boldsymbol{G}_x$ samples various k_x by using (consecutive) read out times t

$$k_x(t) = \gamma \int_t \boldsymbol{G}_x(t')dt'. \tag{3.10}$$

It can be shown that the (complex) measurement signal $s(k_x, k_y)$ of the RF coil is given by the Fourier transform of the transversal magnetization ($M_\perp(x, y) = dm_\perp(x, y)/dV$) of the selected slice with respect to the spatial frequencies k_x, k_y, i.e. the measurement signal is given in k-space by

$$s(k_x, k_y) = \int_{\mathrm{slice}} dxdy M_\perp(x, y) \exp\left(-i(k_x x + k_y y)\right). \tag{3.11}$$

Therefore, an analytical reconstruction of the magnetization distribution is possible in MR imaging by performing Fourier transformation. If the k-space is sampled in Cartesian coordinates, real-time imaging

can be achieved (in 2D) by Fast Fourier Transformation. Although data acquisition in three dimensional k-space and subsequent analytical reconstruction is possible, often slice selection is used, where adjacent 2D slices are reconstructed and are merged into a 3D image, to reduce acquisition time. Each image represents a selected time-point during relaxation. By using sequences of magnetic field gradients and RF-pulses, images with varying contrasts depending on T_1, T_2, $T_2^\star$, and magnetization can be achieved.

In general, MRI is an expensive modality (approximately 600 US Dollar per examination) and hence is not used for breast cancer screening except for high risk patients or patients with difficult to read mammograms [63]. Furthermore, MR mammography is sometimes used for (neo-adjuvant) breast cancer therapy monitoring [64].

Due to the structural information provided by MRI, tumors are visible on images due to increased vascularization. However, also benign lesions have more blood vessels, thus differential diagnosis is improved by using a contrast agent, e.g. by intravenously injecting gadolinium-DTPA, which is paramagnetic and reduces the relaxation times of neighboring hydrogen nuclei. The (unspecific) contrast agent accumulates in the tumor due to enhanced extravasation, similar to unspecific fluorescent dyes used in optical imaging (see Sec. 5.1.3). Furthermore, dynamic contrast-enhanced MRI (DCE-MRI) investigates wash-in and wash-out dynamics of the contrast agent, allowing determination of physiological parameters as perfusion and permeability of vessels in addition to morphological information. Comparable, physiological information can be gained in optical imaging from spectral measurements and by investigating the temporal characteristics of the fluorescent dye. DCE-MRI of breast cancer has a high sensitivity (94%) but a specificity which is slightly below X-ray mammography.

The mammogram given in Fig. 3.3 (right) shows a coronal gadolinium-enhanced MRI slice[1] through the right breast and intersects the cyst and the suspicious mass. The cyst can be seen as a darker area at the rim of the otherwise bright glandular tissue. The suspicious mass is clearly brightened, although being expected to be a (benign) fibroadenoma and not a malignant tumor.

3.3 Ultrasound mammography

Ultrasound imaging uses focused sound waves to create areas of compression and rarefaction in tissue by piezo-ceramic elements that are coupled to the surface of the tissue. Vibrations of the elements are caused by electric current and, depending on the medical application, create coherent sound waves of frequencies between 2 to 20 MHz. While sound waves of high frequencies achieve a better spatial resolution for imaging applications, they suffer from a lower depth of penetration, for the absorption coefficient approximately increases linearly with the sound frequency used. The piezo-ceramic elements can also measure echo amplitudes to reconstruct anatomy of organs and tissue by using detection location and amplitude delay of reflected sound waves.

In an idealized model, the propagation of sound waves in a homogeneous medium is described by the wave equation

$$\triangle p^{\mathrm{US}}(\boldsymbol{x}) - \rho_{\mathrm{US}}\kappa_{\mathrm{US}}\frac{\partial^2 p^{\mathrm{US}}(\boldsymbol{x})}{\partial^2 t} = 0, \tag{3.12}$$

where $\triangle$ is the Laplace operator, ρ_{US} is the density of the medium at equilibrium, κ is its compressibility, and $p^{\mathrm{US}}(\boldsymbol{x})$ is the acoustic pressure. The speed of the sound in the medium is given by

$$v_{\mathrm{US}} = \frac{1}{\sqrt{\rho_{\mathrm{US}}\kappa_{\mathrm{US}}}} = \lambda_{\mathrm{US}}\nu_{\mathrm{US}}, \tag{3.13}$$

where λ_{US} is the wavelength and ν_{US} is the frequency of the Ultrasound, respectively. The propagation speed v_{US} is approximately 1500 m/s in tissue, while the acoustic impedance is defined by $Z_{\mathrm{US}} = \rho_{\mathrm{US}}v_{\mathrm{US}}$.

[1] The scan protocol included an axial high-resolution T_1-weighted fast gradient echo (HR-T1FFE) fat suppressed series (TE/TR 1.7/4.5 ms, inversion delay SPAIR 130 ms, flip angle 10°; FOV 340×340 mm^2, acquired voxel size $0.66 \times 0.66 \times 1.6$ mm^3, reconstructed voxel size $0.66 \times 0.66 \times 0.8$ mm^3) [65].

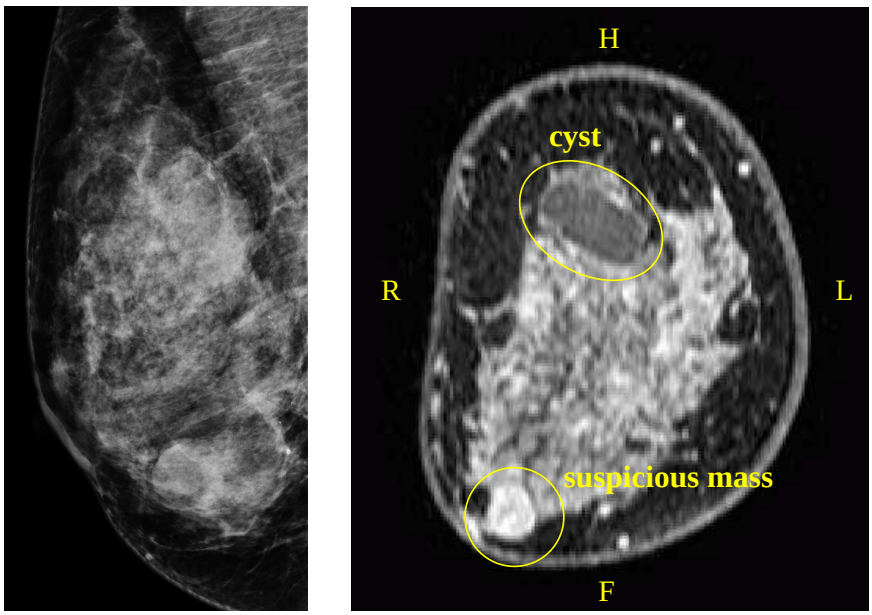

Figure 3.3: (left) Mediolateral oblique X-ray image of right breast of a patient bearing a cyst and a suspected fibroadenoma (suspicious mass). (right) Coronal Gd-enhanced MR slice intersecting the cyst in the upper quadrants of the breast and the suspicious mass in the lower quadrants. (H: head, F: foot, R: right, L: left)

The propagation of sound in tissue is influenced by absorption, coherent reflection, refraction, scattering, and diffraction. A planar sound wave of sound pressure p_0^{US} at the transducer face propagating a distance r through a homogeneous medium, is damped due to the attenuation coefficient μ_{US} by [66]

$$p^{\mathrm{US}}(r) = p_0^{\mathrm{US}} \exp(-\mu_{\mathrm{US}} r/2). \tag{3.14}$$

Scattering of sound waves due to acoustic impedance irregularities can be approximated by the Rayleigh-scattering, which models the medium as consisting of (hard) spheres having a radius R_{sph} smaller than the wavelength λ_{US} of the sound wave, i.e.

$$2\pi R_{\mathrm{sph}}/\lambda_{\mathrm{US}} \ll 1. \tag{3.15}$$

Note that in NIR imaging Eq. (3.15) is rendered invalid due to the shorter optical wavelengths used. Therefore, Mie-theory has to be used (see Sec. 5.1.3) to model the scattering of light, which includes the Rayleigh scattering as approximation for small particle radii, but is also valid for large partice radii.

An US transducer is build up of an array of piezo-ceramic elements, and the focusing of the sound wave can be achieved purely by diffraction, even without the need of additional acoustic lenses. The lateral range, where the wave of increased pressure inside the tissue propagates, is approximately limited by the width of active transducer elements (d_{US}) of the array and hence allows a spatial focus of the sound wave, see Fig. 3.4 left. In axial direction, the scan field can be separated into a near filed (of length $d_{\mathrm{US}}^2/4\lambda_{\mathrm{US}}$ for the given example) and a far field. By switching through subsequent groups of adjacent piezo-ceramic elements, lateral resolution can be achieved.

Further beamshaping is possible by activating (adjacent) elements of the transducer array with a phase shift, e.g. to achieve a propagation of the wave front under an angle α, when the adjacent elements of

the transducer are excited with a (constant) temporal delay, as illustrated in Fig. 3.4 right. Such phased arrays can perform a sector scan, hence increasing the area imaged without moving the transducer. Furthermore, conventional US uses multiple transmit foci, i.e. the focus of the sound wave emitted is varied in axial direction by utilizing a phase delay between elements of the transducer array. Similarly, phase delays can be used during detection of reflected sound waves to achieve dynamic focussing, i.e. the time delay of a reflected sound wave propagating from the location of reflection towards the various elements of the detection array is exploited. In doing so, the axial and lateral position of the detection focus can be varied, determining the origin of the reflected sound waves caused by variations in acoustic impedance and the amplitude of the wave, i.e. a sonogram is created in this way, where image contrast corresponds to the spatial distribution of acoustic impedance variations.

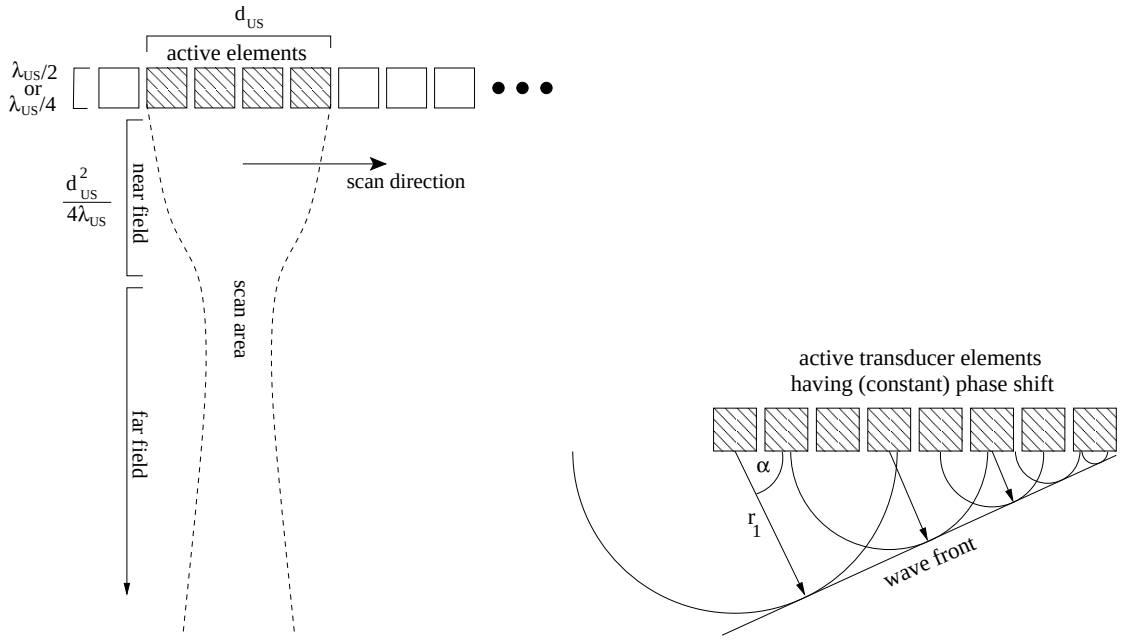

Figure 3.4: (left) Linear transducer array used for scanning. A subset of adjacent transducer elements of width d_{US} creates sound waves propagating in a confined area (scan area). (right) Phased array used for sector scans. Active transducer elements have a phase shift causing the wave front to propagate under angle α.

Breast abnormalities found in X-ray mammography or in a clinical breast examination are diagnosed by US. Although US has a good axial resolution, image contrast can be low and suffers from noise. Furthermore, US is quite operator dependent and therefore not used as a screening tool. Nontheless, US is the preferred modality to differentiate whether a detected abnormality is a breast lump filled with fluid (a cyst) or whether it is a solid mass, because the modality is sensitive to acoustic impedance variations of tissue. For this purpose, a handheld probe (transducer) is gently pressed onto the breast over the region of interest. An US examination can be performed fast and cheaply compared with X-ray and MRI mammography, and does not present potential harm to the patient, i.e. no ionizing radiation is used. Sensitivity and specificity of ultrasound are given as 90% and 78%, respectively, in [60] but more recent results (as given in Fig. 3.1) are inconclusive.

For illustration, Fig. 3.5 presents two sonograms of the diseased breast of the same patient as shown in Fig. 3.3, recorded by an US probe. The sonograms are taken with the probe located at the position of

the suspected fibroadenoma (left) and at the position of the cyst (right), with the abnormalities showing up as areas of reduced acoustic impedance (dark areas). Orientation of the transducer on the right breast is illustrated by the schematic sketch of the breast quadrants at the right bottom of each image, where the dot is associated with one side of the transducer and corresponds to the dot in the upper left part of each panel.

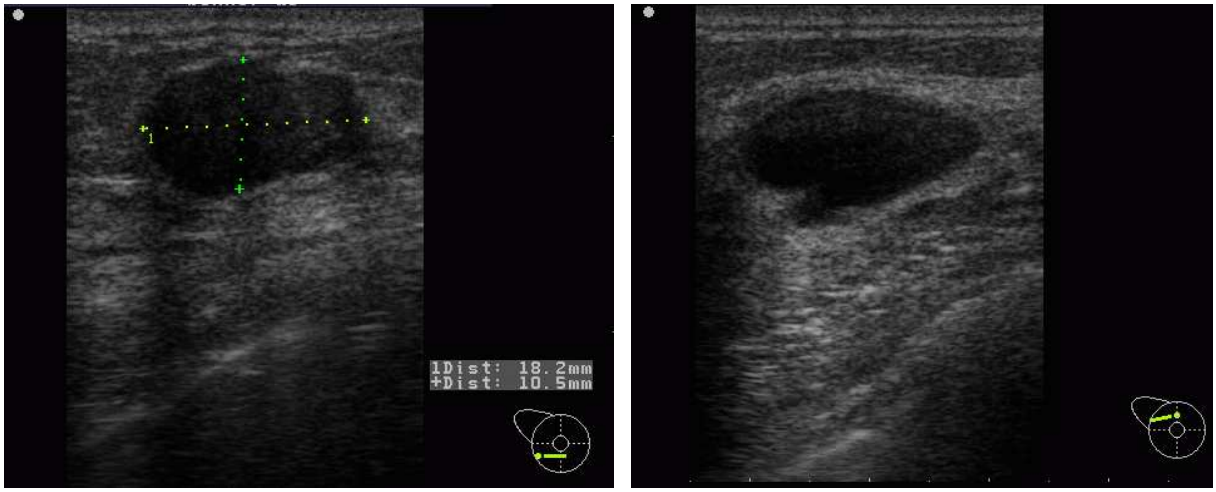

Figure 3.5: US sonograms of the ipsilateral breast of the same patient as given in Fig. 3.3, taken at the location of the suspicious mass (left panel) and at the location of the cyst (right panel). Orientation of the transducer is illustrated using a sketched coronal breast view presented at the right bottom of each panel.

Chapter 4

Instrumentation and data acquisition for laser and fluorescence mammography

A brief overview on optical mammography is given, and instrumental concepts for laser and fluorescence mammographs are discussed. In this thesis, cw tomographic data recorded by the Philips fluorescence mammograph (see appendix A.1) and time-domain transmittance and reflectance data recorded with a laboratory setup will be reconstructed. The laboratory setup mimicking the scanning PTB fluorescence mammograph with parallel plate geometry is briefly described and examples of measured and simulated TPSFs are given.

4.1 Optical Mammography

First research of diffuse optical imaging began around 1929 [7] and was started again around 1977, as the relative good transparency of biological materials at near-infrared (NIR) wavelengths was used to monitor tissue [67]. But at that time, light sources did not provide enough intensity in the NIR spectral range for probing larger volumes without damaging the tissue. Since then, new possibilities have evolved from improvements in monochromatic light sources (lasers), but penetration depths reached are still limited to several cm thickness, hence mammography is an ideal application for diffuse optical imaging.

Several applications of diffuse optical imaging are investigated by research groups, like bedside monitoring for hemorrhage detection [68, 69], measurement of blood oxygenation [70, 20, 71], functional imaging of brain activities [72], Alzheimer diagnosis [73], early diagnosis of rheumatic disease in joints [74], prostate cancer detection [75], and monitoring of breast cancer during neo-adjuvant chemotherapy [76].

In DOT, spatial information is gained by probing the tissue from several positions using NIR light sources coupled into the tissue by fibers and detecting radiation of diffusely scattered light transmitted through or diffusely reflected from the tissue. The detected light is sensitive to absorption and scattering hence physiological and structural information of the investigated tissue can be reconstructed.

Human tissue has the lowest absorbance at NIR wavelengths, yet light undergoes a high number of scattering events while propagating through the tissue. Due to this scattering, tissue probing is influenced by the optical properties of an extended volume between source and detector, and not only along a straight line as in X-ray imaging. Subsequently, a low spatial resolution is inherent in DOT. Therefore, DOT is sometimes combined with other modalities to improve spatial resolution (DOT and US [77, 78], DOT

and MRI [79, 80, 81, 82], DOT and computer tomography [83]) but making it less cost effective.

Patient studies using DOT for breast cancer detection [13, 11] revealed that intrinsic properties of tissue alone are not sufficient to differentiate malignant and benign tumors [84, 85], even when multiple wavelengths in the NIR spectral range are used, to gain information about tissue chromophore concentrations [12]. Nontheless, it is expected that by using contrast agents [86] that either increase absorption contrast [87, 88] or emit fluorescence light [89] increase specificity, and hence provide differential diagnosis, i.e. allow to differentiate between malignant and benign tumors.

Fluorescent dyes used for this application have their absorption and emission spectrum in the NIR range, so that fluorophores inside the tissue can be excited by NIR laser light emitted from fibers located at the breast surface, and emitted fluorescence photons can travel towards a detector at the tissue surface.

Depending on the yet unknown performance of fluorescence enhanced DOT, the modality could be used for several application scenarios like screening of young women, of women with high hereditary risk, women with radiographically dense breasts, for reduction of biopsies with benign outcome, or even as screening standard. Although spatial resolution in DOT is low due to the blurring from the scattering of light in tissue, and early diagnosis, e.g. of LCIS and DCIS, is the key for effective therapy (80% of detected lesions are already smaller than 20 mm in diameter in common screening [90]), increased specificity by a fluorescent dye is expected to improve the value of DOT in clinical applications regarding differential diagnosis. But such classification of fluorescence enhanced DOT can not be given without further clinical trials (phase III studies). Therefore, no investigation of differential diagnosis achieved by fluorescence enhanced DOT can be given in this thesis.

4.2 Detection concepts

The existing DOT systems can be grouped into three categories regarding the different source and detection techniques used.

i) The cheapest and most compact setup uses continuous wave (cw) laser sources and measures the light intensity emitted from the tissue via a number of individual photodiode detectors [15] or via a CCD camera. Furthermore, such approach benefits from the availability of high power laser diodes and high sensitive detectors, but it lacks a reliable separation of scattering and absorption properties of tissue which is a severe drawback in image reconstruction.

ii) Separation of optical properties can be achieved by frequency domain measurements, where amplitude-modulated laser sources at a single [91] or at multiple frequencies [92] are used and the amplitude demodulation and the phase shift caused by the tissue are measured.

iii) A third and most expensive setup uses pulsed laser sources (from fs to ps range) and measures times of flight of single photons (time-correlated single photon counting, TCSPC) [93, 22, 94], thus covering a large bandwidth of modulation frequencies. Due to high equipment costs, these systems often use a small number of sources and detectors, although compensate this drawback by scanning across the investigated object.

Furthermore, hybrid systems exist that use cw and amplitude modulated sources and corresponding detector techniques simultaneously [20, 34] to combine their advantages, i.e. to determinate optical properties by frequency domain measurements and to gain spatial resolution by numerous cw measurements. Additionally, laser sources at multiple wavelengths in the NIR spectral range can be used [12] to determine the concentrations of the tissue constituents via a spectral model [95] with an optimal set of wavelengths [96, 97].

Apart from the different source and detector technologies used in setups, competing detection and source arrangement geometries exist for DOT of the female breast. In handheld probes [98], source and detector fibers are integrated into a plate that is pressed against the patient's breast, providing only

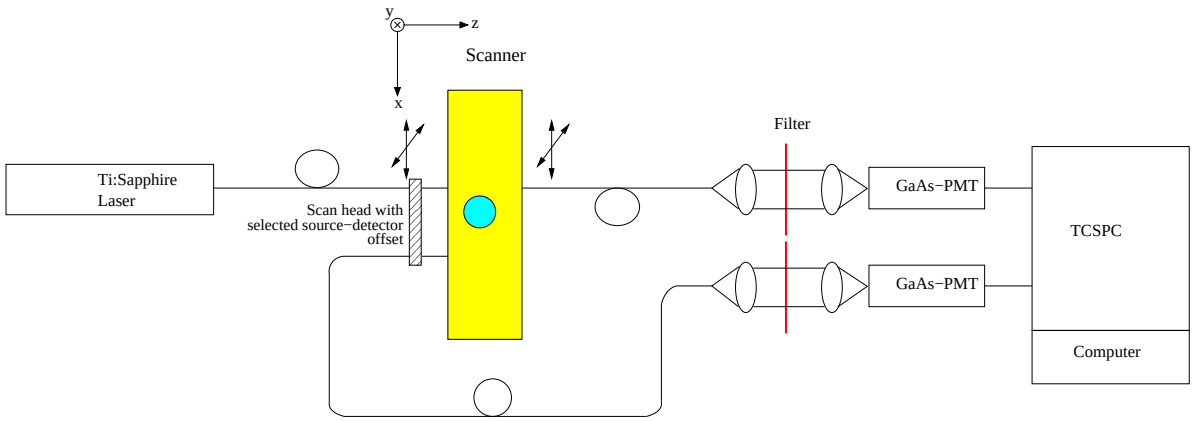

Figure 4.1: PTB laboratory setup for time-resolved measurements in slab geometry (top view with coordinate system). TCSPC = time-correlated single photon counting.

poor angular sampling resulting in low spatial resolution. Such setups are mainly used for diffuse optical spectroscopic imaging (DOSI). Some (stationary) systems arrange sources and detectors interleaved on a single ring [99] with the pendulous breast positioned at its center. Others use multiple rings or distribute sources and detectors on the surface of a cup [15, 21, 100], respectively, leaving the breast uncompressed for high patient comfort. Although providing slightly less patient comfort, arrangements using parallel plates [13, 20, 22] with gentle compression of the breast benefit from a lower breast thickness leading to higher signal strength. Therefore, such systems have better detection sensitivity, as will be shown in this thesis. Furthermore, the planar geometry lends itself for using of CCD cameras for detection, and projection images allow to detect lesions without the need for image reconstruction.

Several mammographs use liquids having similar optical properties as tissue to fill the gap between breast surface and fibers and to achieve better coupling of sources and detectors to the tissue [15, 23] compared with direct contact in air.

Commercialization of DOT using different system approaches has been investigated by companies like IDSI (Imaging Diagnostic Systems Inc., Plantation, Florida, USA), ART (Advanced Research Technologies Inc., Montreal, Canada), Zeiss, Siemens, and Philips (Philips Medical Systems, Best, The Netherlands). Currently, commercially available DOT systems for the European and Canadian market are available from ART only.

4.3 Laboratory setup for time-domain measurements

In this section, measurements are described that were taken at the PTB and were used for data analysis and reconstruction of optical properties in this thesis. Therefore, the instrumentation is briefly described.

Fig. 4.1 shows a schematic view of the laboratory setup used to perform time-resolved measurements in slab geometry that have been analyzed throughout this thesis. Measurements were taken on slab-like, absorbing, diffusely scattering, and fluorescent phantoms containing absorbing, scattering, and fluorescent inhomogeneities, using sub ps laser pulses and time correlated single photon counting. The source of excitation photons was scanned across the entrance face of the phantom (cuvette), and at each source position, data were collected in transmission and reflection at various detector positions. These measurements simulate *in vivo* data that will be obtained employing a scanning, time-domain fluorescence mammograph, where the breast is gently compressed between two parallel glass plates, and source and detector optical fibers scan synchronously at various source-detector offsets, allowing to record laser and

fluorescence mammograms.

For the phantom studies, a Ti:Sapphire laser provided short (100 fs) pulses at $\lambda = 730$ nm incident on the entrance face of the cuvette ($z = 0$) by a multicore fiber with 2 mm diameter consisting of 100 μm multimode fibers (numerical aperture NA=0.22). Because of the open design of the laboratory setup, ambient light contributed to the background of the detected laser and fluorescence signals. In order to minimize the influence of ambient light, a rather high laser power (100 mW) incident on the entrance window of the phantom was chosen. Transmitted and diffusely reflected light is collected by fiber bundles (4 mm diameter, NA=0.54) and subsequently attenuated correspondingly by sets of filters in front of the photocatode of a (cooled) photomultiplier tube (R7400U-02, Hamamatsu Photonics GmbH, Herrsching, Germany), to achieve photon count rates of about 1 MHz, representing optimum values with respect to scan time. The photomultiplier tube (PMT) signal is amplified and fed into a time-correlated single-photon counting electronics (SPC-134, Becker & Hickl GmbH, Germany).

Because taking different filter sets, each set of raw data corresponding to a particular source-detector offset had to be corrected for filter transmittance before entering reconstruction. Data preprocessing is described in more detail in Sec. 6.2.1.

Homogeneous phantoms were created by filling a cuvette ($25 \times 25 \times 6$ cm^3) with absorbing and scattering fluid, simulating compressed breast tissue. Additionally, fluorescent dye was added to simulate background fluorescence. Reflection measurements are prone to artefacts that originate from reflections of the incident laser radiation on the front glass face of the cuvette and from light guiding effects within the glass plane. Such light has not or only partially sampled the diffusely scattering medium inside the cuvette and its intensity may be several orders of magnitude larger than that of the diffusely backscattered light [101]. To avoid such problems, the entrance face of the cuvette was made from regularly perforated, blackened sheet metal (1.5 mm thick) backed by a thin transparent plastic foil. The 2.5 mm pitch of the perforated sheet metal is commensurate to the step size of the scan across the entrance face.

4.4 Temporal point spread functions

In tissue, due to numerous scattering events, photons travel from a source towards a detector along various trajectories of different path lengths. Therefore, after injection of a short laser pulse into the scattering medium, distributions of times of flight of transmitted laser photons or distributions of times of arrival of fluorescence photons are observed, corresponding to temporal point spread functions (TPSF) [102], which are characteristic for each medium and its optical properties.

For illustration, Fig. 4.2a shows four different TPSFs measured in (on-axis) transmission through a diffusely scattering homogeneous cuboid phantom, 6 cm thick, with and without one of three different spheres (2 cm diameter) centered in beam direction. One sphere ("pure absorber") has an absorption contrast of 2:1 with respect to the surrounding medium, a second one ("pure scatterer") a scattering contrast of 0.5:1, and the third one increased absorption (2:1) and lower scattering (0.5:1) contrast. However, the spheres where made from rubber finger stalls and filled with corresponding liquid. The walls of the finger stalls contributed to some extent to scattering and absorption.

Photons were counted up to several ns in time bins of approximately 160 ps. All of the presented TPSFs have their maximum of photon counts at 2.5 ns to 3 ns, which shows that due to the many scattering events these photons have path lengths more then ten times the distance between source and detector position. As can be seen by comparing the four different TPSFs, a variation in optical properties modifies amplitude and phase. A sphere having an increased absorption coefficient decreases the amplitude of the associated TPSF (blue line) compared with the TPSF of the homogeneous medium (magenta line), whereas the pulse slope is unchanged corresponding to the same response. The photons are absorbed to a higher degree, but the pathlength of unabsorbed photons reaching the detector stays unchanged, therefore resulting in the same phase of the TPSF. When only the diffusion coefficient of the sphere is increased (red line), photons in general reach the detector faster (undergoing fewer scattering

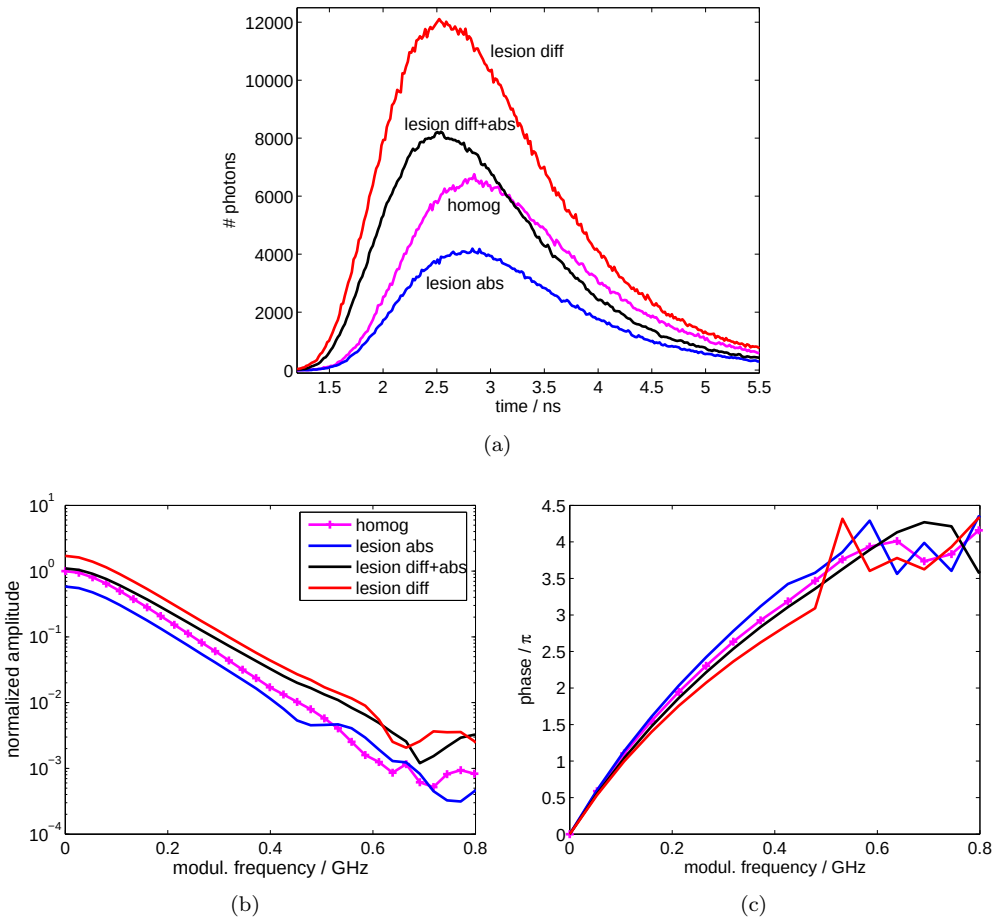

Figure 4.2: TPSFs measured in (on-axis) transmission through a 6 cm cuvette filled with scattering liquid and one of three different (2 cm diameter) spheres centered in beam direction. The three spheres have different contrasts in the absorption and diffusion coefficient (2:1). Measurement data is given in photon counts in time-domain (a), and as Fourier amplitude (b) and phase (c) in frequency domain.

events and hence having shorter path lengths), resulting in a phase shift, i.e. an earlier peak value of the TPSF. Additionally, the amplitude increases since the sphere is more transparent compared to the surrounding medium. When diffusion and absorption are increased simultaneously (black line), the TPSF exhibits a similar peak time as for the pure scatterer, but simultaneously the amplitude is reduced by the increased absorption coefficient.

Hence, raw data are sometimes analyzed to detect effects of scattering and absorption coefficient variations by investigating the total number of photons at selected time points or intervals. This so-called time-window analysis is used as standard technique to generate projection mammograms displaying predominantly absorption and scattering properties of breast tissue. Although sufficient for lesion detection (as will be shown in Sec. 5.2.1), a more elaborate method for separating the absorption and scattering properties is derived and compared with the standard time-window analysis by using simulated data and a realistic noise model. Furthermore, the new method provides absolute optical properties from a simple analysis of raw data without fitting experimental to simulated TPSFs.

For numerical stability, analysis of TPSFs will mainly be carried out in frequency domain in the following of this thesis. Therefore, the same TPSFs as given in Fig. 4.2a are plotted in frequency domain after a discrete Fourier transformation. The Fourier (modulation) amplitude (Fig. 4.2b) and the phase shift (see Fig. 4.2c) of the same four different TPSFs are given for modulation frequencies $\nu = \omega/2\pi$ from 0 to 700 MHz. Discrete Fourier transformation results in a limited set of data points in this frequency band. Although data taken at higher frequencies provide a larger phase shift, data suffer from low signal-to-noise ratios. Noise can be reduced by counting more photons, yet at longer acquisition times.

As can be seen from Fig. 4.2, changes in the absorption and diffusion coefficients lead to changes in the Fourier amplitude over the entire frequency band including $\nu = 0$. On the other hand, all phase shifts start at zero for $\nu = 0$ and therefore cw experiments can not discriminate between changes in absorption and scattering. Furthermore, Fourier amplitude and phase shifts are very smooth at low frequencies. Therefore, measurements performed at multiple frequencies do not significantly increase the information content.

Chapter 5

Forward modeling

DOT images the optical properties of a biological tissue by measuring NIR laser light transmitted through or backscattered from the tissue. For this purpose, the light is radiated into the tissue from a multitude of positions, and the photon density emitted from the surface of the tissue is measured with detectors surrounding the region of interest. Based on these measurements, images can be reconstructed, which represent the spatial distribution of absorption and scattering properties of the examined tissue by investigating the variations in amplitude and (optionally) phase. Determination of the optical properties inside the tissue from measurements at the tissue surface is an inverse problem for which no closed form solution (as e.g. the inverse Radon transformation for computed tomography reconstruction) exists. A general approach to solve the inversion problem in such a situation is to use an iterative algorithm composed of two main steps:

i) Simulating diffuse transmitted of reflected photon densities for given values of the tissue optical properties.

ii) Modification of the assumed tissue optical properties based on the difference of simulated and measured data, i.e. the image update.

The first step is also called the forward model. Here, accuracy and efficiency are most important. The forward model is largely determined by the underlying physics of the data acquisition process. The forward model must be able to predict measurements to within the experimental error. Any systematic model errors will likely lead to reconstruction artefacts.

The second step, i.e. the image update, determines the convergence properties of the iterative algorithm, its speed and robustness against measurement noise. This step is constrained to a much lesser degree than the forward model, and it is this step where most reconstruction algorithms differ. Hence, an accurate prediction of the light propagation is an essential prerequisite for the reconstruction.

Ignoring polarization and interference, the propagation of light can be described by the radiative transfer equation (RTE), an integro-differential equation that has been introduced by Chandrasekhar in 1960 [103]. This model takes anisotropic scattering into account, can be used for scattering and absorbing media, and is valid even in void regions. This model is unnecessary complex when applied to human tissue. In this case, the reduced scattering coefficient μ_s' is larger than the absorption coefficient by several orders of magnitude. After a few reduced scattering lengths $l_s' = 1/\mu_s'$, the correlation between the actual and the previous (incident) light direction is lost and an isotropic situation prevails at locations that are apart from light sources and boundaries by several reduced free scattering lengths at least. Therefore, in these cases, the RTE can be approximated by an isotropic diffusion equation to describe photon transport in biological tissue in the NIR spectral range with the reduced scattering coefficient $\mu_s' = (1-g)\mu_s$ entering

the diffusion equation rather than the scattering coefficients μ_s itself. The factor g is called anisotropy factor and represents the average of $\cos\theta$, with θ being the scattering angular distribution.

It has been shown by comparing (numerical) solutions of the diffusion equation with results of Monte Carlo (MC) simulations that this approximation is valid for human tissue in most parts of a large volume, but deviations occur near source positions or at boundaries [104, 105]. Nonetheless, the diffusion approximation is used in most cases for the simulation of NIR light propagation in breast tissue due to its speed gain and its robustness in numerical calculations.

For volumes including void or non-scattering regions, e.g. the simulation of reflectance measurements of the brain with its non-scattering cerebrospinal fluid below the skull, often a more elaborate model is applied including the RTE for regions where the diffusion equation is invalid [106, 107].

For fluorescence enhanced DOT a fluorescent dye is added to the medium, therefore an additional diffusion equation is needed describing the propagation of fluorescence light. The diffusion equation at the laser wavelength models the absorption and scattering of the transmitted laser photons by the tissue, which contains additional absorption by the fluorescent dye. When laser photons are absorbed by the fluorescent dye which is distributed throughout the tissue, dye molecules are excited. From all of these excited molecules, a certain percentage given by the fluorescence quantum yield emits fluorescence light in a spectrum which is characteristic for each dye. The propagation of these fluorescence photons is modeled analogously to the transmitted laser photons, although using a modified source term, which couples both differential equations.

In this chapter we introduce the diffusion equation in time- and frequency domain (see Sec. 5.1.1) and explain how absorption and scattering coefficients of breast tissue can be calculated using a spectral model (Sec. 5.1.3). We present analytical solutions of the diffusion equation at laser and fluorescence wavelength for a homogeneous medium and explain how solutions for slab geometry can be constructed from those solutions (see Sec. 5.1.4). Since analytical solutions are known only for simple geometries and simple distributions of optical properties, we explain how the diffusion equation can be solved numerically using Galerkin's method, which transforms a differential equation into an integral equation. By discretizing the volume of interest (VOI) on a finite element (FE) grid, the resulting system of linear equations can be solved by standard methods (e.g. conjugate gradient). We show that the FE method is more flexible than analytical solutions and can be applied to steady-state (Sec. 5.1.5), to time-domain (Sec. 5.1.6), and to frequency domain solutions and allows to carry out numerical simulations being less limited in geometry and in distributions of optical properties, although needing longer calculation times.

Furthermore, forward model calculations are used to characterize and investigate effects of system noise, as a key factor in limiting the performance of DOT. A design study is carried out by using a realistic noise model derived from measurements and applied to simulated data, to analyze existing (cw) detection setups and to determine their limiting factors (Sec. 5.2.2). Such performance studies, investigating two different geometries (breast slightly compressed between two parallel plates and an uncompressed breast in a cup) and different noise settings, give insight into the limiting factors of detection sensitivity. To this end, dye concentration contrast, breast compression, absolute, and relative noise contributions is varied in the numerical phantoms and their influence on detection limits are investigated.

5.1 Theoretical background

5.1.1 The diffusion equation for laser and fluorescence light

Transport of laser and fluorescence radiation in biological tissue is modeled as diffusion of photons. The corresponding diffusion equations are derived from the radiative transfer equation and limitations are briefly discussed. Further details can be found in appendix C.3.

The time-dependent distribution of light in a scattering and absorbing medium can be described by the radiative transfer equation [103, 108], which is a conservation equation on the volume $\Omega \ni \boldsymbol{x}$ with

boundary $\partial\Omega$,

$$\left(\frac{1}{v}\frac{\partial}{\partial t} + \partial_{\boldsymbol{n}} + \mu_{\mathrm{a}}(\boldsymbol{x},\lambda) + \mu_{\mathrm{s}}(\boldsymbol{x},\lambda)\right)\widetilde{I}\left(\boldsymbol{x},\boldsymbol{x}_{\mathrm{s}},\lambda,\boldsymbol{n},t\right) = \mu_{\mathrm{s}}(\boldsymbol{x},\lambda)\int_{4\pi}\theta_{\mathrm{p}}(\boldsymbol{n},\boldsymbol{n}')\widetilde{I}\left(\boldsymbol{x},\boldsymbol{x}_{\mathrm{s}},\lambda,\boldsymbol{n}',t\right)d\boldsymbol{n}' + \widetilde{S}\left(\boldsymbol{x},\boldsymbol{x}_{\mathrm{s}},\lambda,\boldsymbol{n},t\right), \tag{5.1}$$

with $v = c/n$ the speed of light in the medium of refraction index n, $\widetilde{I}\left(\boldsymbol{x},\boldsymbol{x}_{\mathrm{s}},\lambda,\boldsymbol{n},t\right)$ the radiance at position $\boldsymbol{x}$ in the direction $\boldsymbol{n}$ at wavelength λ, the scattering coefficient $\mu_{\mathrm{s}}(\boldsymbol{x},\lambda) = 1/l_{\mathrm{s}}(\boldsymbol{x},\lambda)$ with l_{s} being the free scattering length, the (normalized) phase function $\theta_{\mathrm{p}}(\boldsymbol{n},\boldsymbol{n}')$ representing the angular scattering distribution, the spatial and angular distribution of the source $\widetilde{S}\left(\boldsymbol{x},\boldsymbol{x}_{\mathrm{s}},\lambda,\boldsymbol{n},t\right)$ for a time-dependent source located at $\boldsymbol{x}_{\mathrm{s}}$, and the absorption coefficient $\mu_{\mathrm{a}}(\boldsymbol{x},\lambda)$. The directional derivative is abbreviated by $\partial_{\boldsymbol{n}} := \boldsymbol{n}\cdot\nabla$. In our case, the radiance $\widetilde{I}\left(\boldsymbol{x},\boldsymbol{x}_{\mathrm{s}},\lambda,\boldsymbol{n},t\right)$ corresponds to the photon flux density in the direction $\boldsymbol{n}$ per unit solid angle ($1/(\mathrm{s\ m^2\ sr})$).

The anisotropy factor g is defined as [109]

$$g = \int_{4\pi}(\boldsymbol{n}\cdot\boldsymbol{n}')\ \theta_{\mathrm{p}}(\boldsymbol{n},\boldsymbol{n}')d\boldsymbol{n}', \tag{5.2}$$

and the reduced scattering coefficient as

$$\mu_{\mathrm{s}}'(\boldsymbol{x},\lambda) = \mu_{\mathrm{s}}(\boldsymbol{x},\lambda)(1-g), \tag{5.3}$$

which takes the anisotropy of multiple scattering events into account as an averaging factor.

For the phase function, often the Henyey-Greenstein function is used [110], expressed in terms of the anisotropy factor g and the scattering angle θ ($\cos\theta = \boldsymbol{n}\cdot\boldsymbol{n}'$),

$$\theta_{\mathrm{HG}}(\boldsymbol{n},\boldsymbol{n}') = \frac{1}{4\pi}\frac{1-g^2}{\left(1+g^2-2g\boldsymbol{n}\cdot\boldsymbol{n}'\right)^{3/2}}. \tag{5.4}$$

The RTE can be used for radiation transport in media with anisotropic scattering and for radiation transport in void regions or regions with no or low scattering as well, thus modeling more scenarios than needed for light propagation in human breast tissue at NIR wavelengths. Despite anisotropic scattering in breast tissue ($g \approx 0.8-0.99$ [111]) the radiance $\widetilde{I}\left(\boldsymbol{x},\boldsymbol{x}_{\mathrm{s}},\lambda,\boldsymbol{n},t\right)$ and the spatial and angular distribution of the source $\widetilde{S}\left(\boldsymbol{x},\boldsymbol{x}_{\mathrm{s}},\lambda,\boldsymbol{n},t\right)$ are nearly isotropic except at positions $\boldsymbol{x}$ that are within several reduced scattering lengths l_{s}' from source positions $\boldsymbol{x}_{\mathrm{s}}$ and from the tissue boundaries. Therefore, for the remaining volume, one carries out a multipole expansion of the radiance and the spatial and angular distribution of the source up to first order (P1 approximation) [30], yielding

$$\widetilde{S}\left(\boldsymbol{x},\boldsymbol{x}_{\mathrm{s}},\lambda,\boldsymbol{n},t\right) = \frac{1}{4\pi}\left(\widetilde{S}_0\left(\boldsymbol{x},\boldsymbol{x}_{\mathrm{s}},\lambda,t\right) + 3\widetilde{\boldsymbol{S}}_1\left(\boldsymbol{x},\boldsymbol{x}_{\mathrm{s}},\lambda,t\right)\cdot\boldsymbol{n}\right), \tag{5.5}$$

where $\widetilde{S}_0\left(\boldsymbol{x},\boldsymbol{x}_{\mathrm{s}},\lambda,t\right) = v\widetilde{q}_0\left(\boldsymbol{x},\boldsymbol{x}_{\mathrm{s}},\lambda,t\right)$ is the isotropic part and $\widetilde{\boldsymbol{S}}_1\left(\boldsymbol{x},\boldsymbol{x}_{\mathrm{s}},\lambda,t\right)$ is the dipolar part. Likewise,

$$\widetilde{I}\left(\boldsymbol{x},\boldsymbol{x}_{\mathrm{s}},\lambda,\boldsymbol{n},t\right) = \frac{1}{4\pi}\left(v\widetilde{\Phi}\left(\boldsymbol{x},\boldsymbol{x}_{\mathrm{s}},\lambda,t\right) + 3\widetilde{\boldsymbol{J}}\left(\boldsymbol{x},\boldsymbol{x}_{\mathrm{s}},\lambda,t\right)\cdot\boldsymbol{n}\right), \tag{5.6}$$

where $v\widetilde{\Phi}\left(\boldsymbol{x},\boldsymbol{x}_{\mathrm{s}},\lambda,t\right)$ is the isotropic part with $\widetilde{\Phi}\left(\boldsymbol{x},\boldsymbol{x}_{\mathrm{s}},\lambda,t\right)$ being the photon density and $\widetilde{\boldsymbol{J}}\left(\boldsymbol{x},\boldsymbol{x}_{\mathrm{s}},\lambda,t\right)$ is the (net) photon current density ($1/(\mathrm{s\ m^2})$)

$$\widetilde{\boldsymbol{J}}\left(\boldsymbol{x},\boldsymbol{x}_{\mathrm{s}},\lambda,t\right) = \int_{4\pi}\boldsymbol{n}'\widetilde{I}\left(\boldsymbol{x},\boldsymbol{x}_{\mathrm{s}},\lambda,\boldsymbol{n}',t\right)d\boldsymbol{n}'. \tag{5.7}$$

Analogously, the photon density can be expressed as

$$\widetilde{\Phi}(\boldsymbol{x}, \boldsymbol{x}_\mathrm{s}, \lambda, t) \quad = \quad \frac{1}{v} \int_{4\pi} \widetilde{I}(\boldsymbol{x}, \boldsymbol{x}_\mathrm{s}, \lambda, \boldsymbol{n}', t) d\boldsymbol{n}' \,. \tag{5.8}$$

Using Eq. (5.1) and the expressions (5.5), (5.6), (5.7), (5.8) results in the diffusion equation

$$\left\{ \nabla \cdot D(\boldsymbol{x}, \lambda) \nabla - \mu_\mathrm{a}(\boldsymbol{x}, \lambda) - \frac{1}{v} \frac{\partial}{\partial t} \right\} \widetilde{\Phi}(\boldsymbol{x}, \boldsymbol{x}_\mathrm{s}, \lambda, t) = -\widetilde{q_0}(\boldsymbol{x}, \boldsymbol{x}_\mathrm{s}, \lambda, t), \tag{5.9}$$

which models the transport of light in a highly scattering medium as a diffusive process characterized by the diffusion coefficient $D(\boldsymbol{x}, \lambda) = 1/3\mu_\mathrm{s}'(\boldsymbol{x}, \lambda)$. A derivation of the diffusion equation from the RTE and a discussion of the approximations made is given in appendix C.3.

The (net) photon current density $\widetilde{\boldsymbol{J}}(\boldsymbol{x}, \boldsymbol{x}_\mathrm{s}, \lambda, t)$ satisfies a Fick-law,

$$\widetilde{\boldsymbol{J}}(\boldsymbol{x}, \boldsymbol{x}_\mathrm{s}, \lambda, t) = -vD(\boldsymbol{x}, \lambda) \nabla \widetilde{\Phi}(\boldsymbol{x}, \boldsymbol{x}_\mathrm{s}, \lambda, t). \tag{5.10}$$

Besides simulations in time-domain, we carry out calculations in frequency domain using the diffusion equation to model the propagation of excitation (laser) light pulses through the turbid medium [30]:

$$\nabla \cdot D(\boldsymbol{x}, \lambda) \nabla \Phi(\boldsymbol{x}, \boldsymbol{x}_\mathrm{s}, \lambda, \omega) - \mu_\mathrm{a}(\boldsymbol{x}, \lambda) \Phi(\boldsymbol{x}, \boldsymbol{x}_\mathrm{s}, \lambda, \omega) - \frac{i\omega}{v} \Phi(\boldsymbol{x}, \boldsymbol{x}_\mathrm{s}, \lambda, \omega) = -q_0(\boldsymbol{x}, \boldsymbol{x}_\mathrm{s}, \lambda, \omega), \tag{5.11}$$

where $\Phi(\boldsymbol{x}, \boldsymbol{x}_\mathrm{s}, \lambda, \omega)$ is the (laser) photon density per unit interval of angular frequency ω inside the medium, and $q_0(\boldsymbol{x}, \boldsymbol{x}_\mathrm{s}, \lambda, \omega)$ is the source term given in $\mathrm{s/m^4}$. The time-dependent photon density $\widetilde{\Phi}(\boldsymbol{x}, \boldsymbol{x}_\mathrm{s}, \lambda, t)$ is obtained by Fourier transformation from the photon density in frequency domain,

$$\widetilde{\Phi}(\boldsymbol{x}, \boldsymbol{x}_\mathrm{s}, \lambda, t) = \frac{1}{2\pi} \int_{-\infty}^{+\infty} \Phi(\boldsymbol{x}, \boldsymbol{x}_\mathrm{s}, \lambda, \omega) e^{+i\omega t} d\omega. \tag{5.12}$$

When using an exogenous fluorescent dye at a concentration $c(\boldsymbol{x})$ in the scattering medium, the absorption coefficient $\mu_\mathrm{a}(\boldsymbol{x}, \lambda)$ is given by the contribution of tissue chromophores and of the dye, $\mu_\mathrm{a}(\boldsymbol{x}, \lambda) = \mu_\mathrm{a}^\mathrm{chrom}(\boldsymbol{x}, \lambda) + \mu_\mathrm{a}^\mathrm{dye}(\boldsymbol{x}, \lambda)$. The propagation of the fluorescence light inside the tissue can be described by an analogous diffusion equation, where the source term $q^\mathrm{f}(\boldsymbol{x}, \boldsymbol{x}_\mathrm{s}, \lambda, \omega)$ is proportional to the laser photon density, the absorption coefficient of the dye, and the fluorescence quantum yield η:

$$\nabla \cdot D(\boldsymbol{x}, \lambda_\mathrm{f}) \nabla \Phi_\mathrm{f}(\boldsymbol{x}, \boldsymbol{x}_\mathrm{s}, \lambda, \omega) - \mu_\mathrm{a}(\boldsymbol{x}, \lambda_\mathrm{f}) \Phi_\mathrm{f}(\boldsymbol{x}, \boldsymbol{x}_\mathrm{s}, \lambda, \omega) - \frac{i\omega}{v} \Phi_\mathrm{f}(\boldsymbol{x}, \boldsymbol{x}_\mathrm{s}, \lambda, \omega) = -\frac{\eta \mu_\mathrm{a}^\mathrm{dye}(\boldsymbol{x}, \lambda)}{1 + i\omega\tau} \Phi(\boldsymbol{x}, \boldsymbol{x}_\mathrm{s}, \lambda, \omega), \tag{5.13}$$

with

$$q^\mathrm{f}(\boldsymbol{x}, \boldsymbol{x}_\mathrm{s}, \lambda, \omega) = \frac{\eta \mu_\mathrm{a}^\mathrm{dye}(\boldsymbol{x}, \lambda)}{1 + i\omega\tau} \Phi(\boldsymbol{x}, \boldsymbol{x}_\mathrm{s}, \lambda, \omega). \tag{5.14}$$

The density of fluorescence photons per unit interval of angular frequency ω is designated as $\Phi_\mathrm{f}(\boldsymbol{x}, \boldsymbol{x}_\mathrm{s}, \lambda, \omega)$. The absorption and diffusion coefficient at the fluorescence wavelength are represented by $\mu_\mathrm{a}(\boldsymbol{x}, \lambda_\mathrm{f})$ and $D(\boldsymbol{x}, \lambda_\mathrm{f})$, respectively. In the following we assume the diffusion coefficients at the excitation and fluorescence wavelengths to be equal, i.e. $D(\boldsymbol{x}, \lambda_\mathrm{f}) = D(\boldsymbol{x}, \lambda) = 1/3\mu_\mathrm{s}'(\boldsymbol{x}, \lambda)$, this assumption being a good one because of the rather small Stoke's shifts of the NIR dyes used (typically 20 nm). In Eq. (5.13) we have assumed the fluorophore lifetime τ and quantum yield η to be independent of position $\boldsymbol{x}$. Strictly speaking, an equation such as (5.13) should be solved for the entire emission spectrum $\eta(\lambda_\mathrm{f})$. However, since the fluorescence is not measured spectrally resolved in the experiments analyzed in this thesis, an equation such as (5.13) is solved for an averaged fluorescence wavelength λ_f. Furthermore, we neglect any re-emission of fluorescence by the dye itself.

In Eq. (5.13) the term $1/(1+i\omega\tau)$ results in a phase shift of the density of fluorescence photons due to the exponential fluorescence decay. Equation (5.13) neglects any tissue autofluorescence, i.e. fluorescence from chromophores, since tissue autofluorescence is low in the diagnostic window.

For continuous wave sources, one can derive the corresponding equations from (5.11) and (5.13) by setting $\omega = 0$.[1]

In order to simulate measured distributions of times of flight of laser photons (i.e. temporal point spread functions (TPSFs)) and distributions of times of arrival of fluorescence photons, the two diffusion equations (5.11) and (5.13) were solved on an FE grid sequentially, using the `deal.II` finite element library [113] for several modulation frequencies, followed by Fourier transformation. We used a modified Robin boundary condition [114, 115]

$$[\Phi(\boldsymbol{x}, \boldsymbol{x}_\mathrm{s}, \lambda, \omega) + 2A(\lambda)\boldsymbol{n} \cdot D(\boldsymbol{x}, \lambda)\nabla\Phi(\boldsymbol{x}, \boldsymbol{x}_\mathrm{s}, \lambda, \omega)]_{\partial\Omega(\zeta)} = 0, \tag{5.15}$$

where ζ is a point on the surface $\partial\Omega$ having reflectivity $K(\lambda)$, $\boldsymbol{n}$ the outward pointing surface normal at ζ, and

$$A(\lambda) = \frac{1 + K(\lambda)}{1 - K(\lambda)}. \tag{5.16}$$

The boundary condition is applied to both diffusion equations. Details on the chosen RBC are presented in appendix A.2.

The diffusion approximation holds true for isotropic light sources, but the light is coupled into the cup by a fiber with a certain numerical aperture (i.e. in a non-isotropic way). As usual, we modeled this situation by shifting the light source position in beam direction by one transport scattering length and assume an isotropic source at the shifted position [28].

5.1.2 Light sources S_0 and source terms q_0 for pulsed and cw irradiation

In this thesis, two illumination scenarios will be considered, i.e. injection of a short, δ-like laser pulse at position $\boldsymbol{x}_\mathrm{s}$ containing a total of N_phot photons, and injection of cw laser radiation at position $\boldsymbol{x}_\mathrm{s}$, corresponding to the rate R_phot of injected photons per second. In this section, we model the spatial dependence of the source term as $\delta(\boldsymbol{x} - \boldsymbol{x}_\mathrm{s})$, other spatial source term models that are more suited for numerical simulations are discussed in a later section (Sec. 5.1.7). Furthermore, throughout this thesis we set $N_\mathrm{phot} = 1$ and $R_\mathrm{phot} = 1/\mathrm{s}$. For irradiation with a short laser pulse we set $\widetilde{S}_0(\boldsymbol{x}, \boldsymbol{x}_\mathrm{s}, \lambda, t) = N_\mathrm{phot}\delta(t)\delta(\boldsymbol{x} - \boldsymbol{x}_\mathrm{s})$, yielding

$$S_0(\boldsymbol{x}, \boldsymbol{x}_\mathrm{s}, \lambda, \omega) = N_\mathrm{phot}\delta(\boldsymbol{x} - \boldsymbol{x}_\mathrm{s}) \tag{5.17}$$

and

$$q_0(\boldsymbol{x}, \boldsymbol{x}_\mathrm{s}, \lambda, \omega) = \frac{N_\mathrm{phot}}{v}\delta(\boldsymbol{x} - \boldsymbol{x}_\mathrm{s}). \tag{5.18}$$

For cw irradiation we model the source as $\widetilde{S}_0(\boldsymbol{x}, \boldsymbol{x}_\mathrm{s}, \lambda, t) = R_\mathrm{phot}\delta(\boldsymbol{x} - \boldsymbol{x}_\mathrm{s})$, and therefore

$$S_0(\boldsymbol{x}, \boldsymbol{x}_\mathrm{s}, \lambda, \omega) = R_\mathrm{phot}\delta(\boldsymbol{x} - \boldsymbol{x}_\mathrm{s})2\pi\delta(\omega). \tag{5.19}$$

When solving the frequency domain diffusion equation for $\omega = 0$, using as source term $q_0(\boldsymbol{x}, \boldsymbol{x}_\mathrm{s}, \lambda, \omega) = R_\mathrm{phot}\delta(\boldsymbol{x} - \boldsymbol{x}_\mathrm{s})/v$ the resulting Fourier amplitude $\Phi(\boldsymbol{x}, \boldsymbol{x}_\mathrm{s}, \lambda, \omega = 0)$ of the photon density is used to calculate the time-independent photon density $\Phi(\boldsymbol{x}, \boldsymbol{x}_\mathrm{s}, \lambda)$, i.e.

$$\Phi(\boldsymbol{x}, \boldsymbol{x}_\mathrm{s}, \lambda) \equiv R_\mathrm{phot}\int_{-\infty}^{+\infty}\Phi(\boldsymbol{x}, \boldsymbol{x}_\mathrm{s}, \lambda, \omega)\delta(\omega)\exp(+i\omega t)d\omega = R_\mathrm{phot}\Phi(\boldsymbol{x}, \boldsymbol{x}_\mathrm{s}, \lambda, \omega = 0). \tag{5.20}$$

[1] There is some disagreement in the literature about the definition of the diffusion coefficient. It can be shown that for the steady-state case the diffusion coefficient depends on the absorption coefficient as well [112] and is usually approximated in the NIR by $D(\boldsymbol{x}, \lambda) = 1/3(\mu_\mathrm{s}'(\boldsymbol{x}, \lambda) + \mu_\mathrm{a}(\boldsymbol{x}, \lambda))$, giving only a small deviation in numerical calculations due to $\mu_\mathrm{a}(\boldsymbol{x}, \lambda) \ll \mu_\mathrm{s}'(\boldsymbol{x}, \lambda)$ throughout the tissue volume.

5.1.3 Tissue spectral model, NIR dyes and their accumulation in tumors

The absorption coefficient of breast tissue and its spectral dependence are expressed by the concentration and absorption spectra of major tissue constituents. The spectral dependence of the reduced scattering coefficient is based on Mie theory. Absorption and emission spectra of exogenous fluorescent dyes (contrast agents) are shown and the processes leading to accumulation of such dyes in tumors are briefly discussed.

Only a few chromophores dominate the absorption coefficient of tissue in the NIR wavelength band. Main contributions stem from blood (deoxyhemoglobin (HbR) and oxyhemoglobin (HbO)), water (H_2O), and fat. Their absorption spectra (absorption coefficients) are shown in Fig. 5.1 throughout the NIR band. As can be seen from this figure, the chromophores are less absorbing in the NIR region, i.e. the total absorption coefficient is rather low. Therefore, this wavelength band is ideal for probing large tissue volumes by the attenuation of transmitted NIR radiation. For shorter wavelengths ($\lambda < 650$ nm), tissue absorption increases due to the presence of HbR and HbO, whereas water and fat begin to dominate absorption at long wavelengths ($\lambda > 950$ nm).

We model the absorption properties of a female breast within the wavelength range 690 nm $\leq \lambda \leq$ 850 nm taking the absorption of HbR ($i = 1$), HbO ($i = 2$), and H_2O ($i = 3$) into account, but neglecting the contribution of fat [116]. The intrinsic absorption coefficient can be calculated from the molar extinction coefficients of these constituents [15, 20]

$$\mu_{\mathrm{a}}^{\mathrm{chrom}}(\boldsymbol{x}, \lambda) = \sum_{i=1}^{3} \varepsilon_i(\lambda) c_i^{\mathrm{chrom}}(\boldsymbol{x}) \ln 10, \tag{5.21}$$

and are chosen for water as listed in [117], for HbR and HbO as given in [118]. Likewise, the absorption coefficient of the dye can be expressed as

$$\mu_{\mathrm{a}}^{\mathrm{dye}}(\boldsymbol{x}, \lambda) = \epsilon^{\mathrm{dye}}(\lambda) c(\boldsymbol{x}) \ln 10. \tag{5.22}$$

For the scattering coefficient, a simplified Mie scattering model is used [119, 120],

$$\mu_{\mathrm{s}}'(\boldsymbol{x}, \lambda) = a(\boldsymbol{x}) \left(\frac{\lambda}{\lambda_0} \right)^{-b}, \tag{5.23}$$

with scattering amplitude $a(\boldsymbol{x})$, and scattering power b representing model parameters. The slope of the scattering coefficient, given by the scattering power b, is related to the average particle size and steepens for smaller particles, while the scattering amplitude a is related to the number density of particles times their cross-section [119, 120]. The reference wavelength λ_0 in Eq. (5.23) can be chosen arbitrarily and is set to 1000 nm in the following.

When multiple laser wavelengths are used to measure tissue optical properties, the absorption coefficient for each selected wavelength can be determined separately. Alternatively, the concentration of the constituents can be calculated using the spectral model as a constraint. To determine chromophore concentrations, the number of wavelengths measured has to be at least equal to the number of free parameters of the model. Therefore, in the NIR spectral range, at least six different wavelengths are needed to determine the concentration of the main chromophores ($i = 1, 2, 3$), the fluorophore concentration $c(\boldsymbol{x})$, the scattering amplitude $a(\boldsymbol{x})$, and the scattering power b. A detailed description is given in Sec. 6.2.5 how to determine these parameters from multi-spectral cw measurements. It was shown in [96] that an optimal set of wavelengths exists to determine these model parameters most accurately, if the number of wavelengths is predetermined. This conclusion was extended in [97] additionally taking measurement errors of the absorption spectra into account.

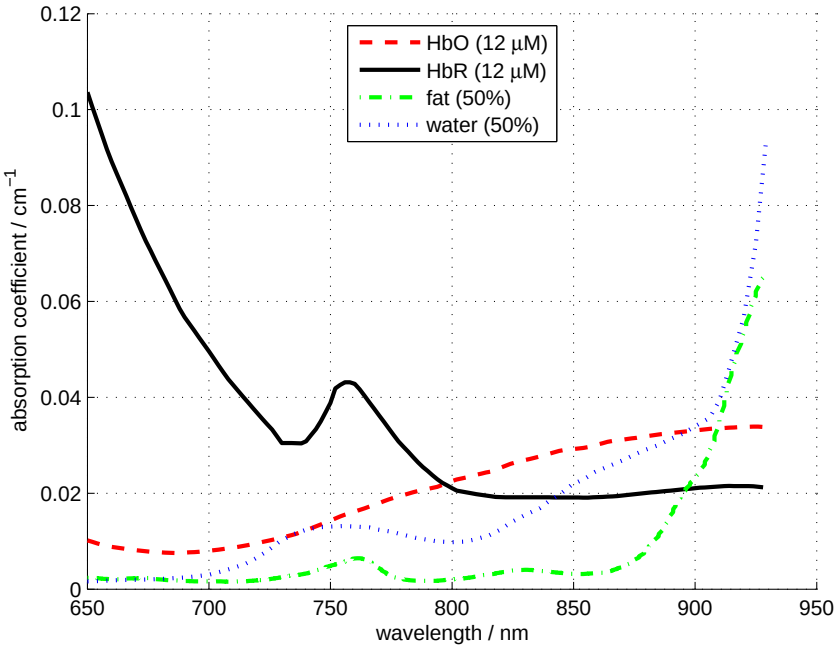

Figure 5.1: Absorption spectra of tissue chromophores oxyhemoglobin (dashed red line), deoxyhemoglobin (solid black line), fat (dashed-dotted green line), and water (dotted blue line) within the NIR band. Breast tissue is least absorbing (transmissive window) throughout the NIR band. Hemoglobin and deoxyhemoglobin predominantly absorb light at lower wavelengths ($\lambda < 650$ nm), water and fat at higher wavelengths ($\lambda > 950$ nm).

By deriving concentrations of chromophores instead of absorption and scattering coefficients at various wavelengths, metabolic information about tissue and tumors is obtained. This information is exploited by diffuse optical spectroscopic imaging (DOSI) of breast tumors for therapy monitoring [121, 9].

Several fluorescent NIR dyes exist to increase contrast between normal tissue and tumors and have been investigated and used during phantom and (phase I) patient measurements [87, 88, 34] (SF64 a.k.a. Omocyanine [122], NIR 96010 a.k.a. SIDAG [123], and Indocyanine Green (ICG) [124, 125]).

Fig. 5.2 shows the absorption and emission spectrum of Omocyanine together with its chemical structure, while the absorption spectra of these three dyes are compared in Fig. 5.3. In addition, the emission spectrum Omocyanine is also shown. Each spectrum can shift slightly depending on the medium the dye is dissolved in (e.g. water, phosphate buffered saline (PBS), serum) due to the various degrees of aggregation. The spectral shifts of the absorption and emission spectra of these dyes in serum are caused by binding of the dyes to proteins, e.g. albumin.

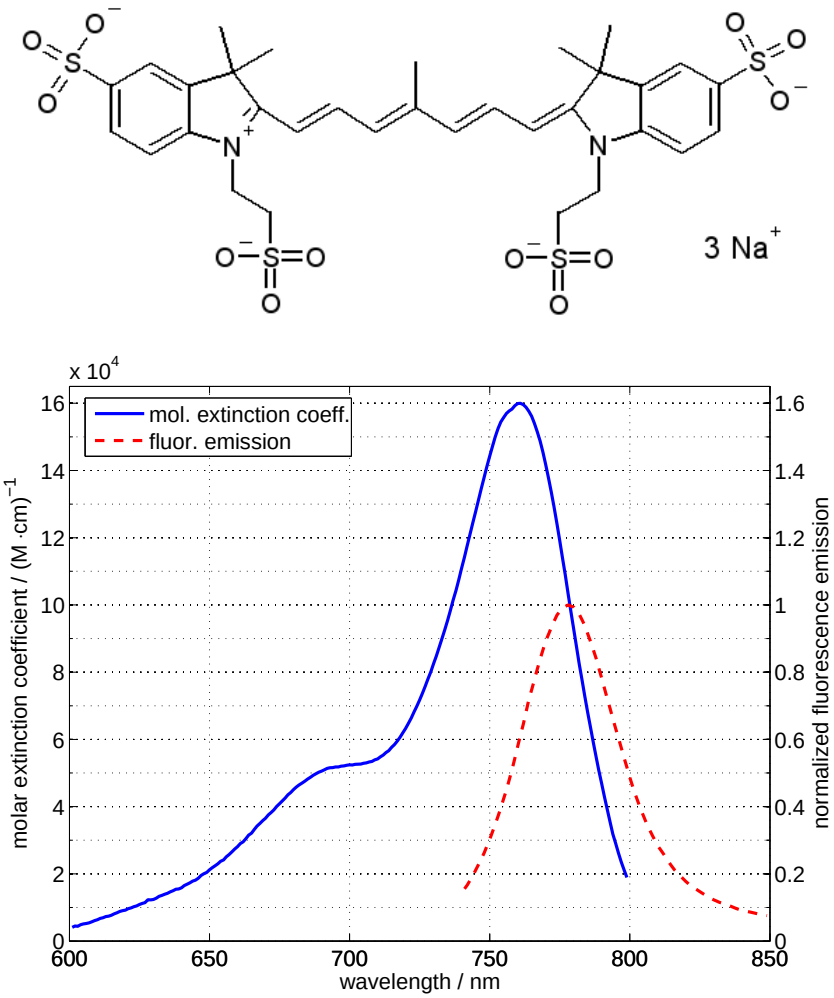

Figure 5.2: Chemical structure of Omocyanine and its absorption and emission spectrum [122].

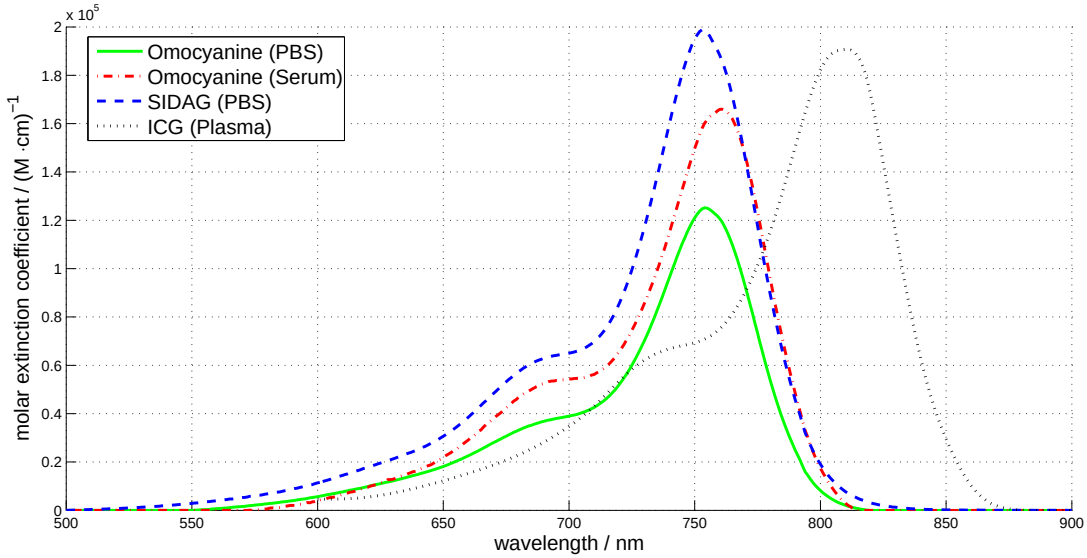

Figure 5.3: Absorption spectra of NIR dyes used: Omocyanine, SIDAG, and ICG in the NIR wavelength band.

Hitherto, these fluorescent dyes used in patients are unspecific, i.e. they accumulate at the tumor position mainly due to extravasation caused by the increased permeability (leakiness of vessel membranes) of the tumor vasculature. In contrast, specific dyes target certain proteins (e.g. fibronectin) that are expressed at the cells surface e.g. during neo-angiogenesis. But such dyes are still at a research stage and not yet available for patient measurements and will need several years before an approval for clinical applications can be obtained.

The unspecific dyes mentioned above are generally administered by intravenous injection. Depending on the molecular size of a particular dye and its binding to other molecules or proteins contained in the blood plasma, each dye or dye-protein complex has a characteristic wash-in and wash-out behavior. Therefore, optimal concentration contrast between tumor and normal tissue might be achieved after minutes to hours before dyes are mainly excreted via urine or feces. Fluorescence measurements should be carried out at a time after injection of the dye at which dye contrast is optimal and dye concentration is sufficiently high to provide strong fluorescence signals. A phase I clinical study was carried out at the University Medical Center Utrecht to determine optimal time after injection of Omocyanine and the required dose of the dye. Compared to the Omocyanine fluorescence intensities generally recorded, autofluorescence contributions are low in the NIR spectral range and can be neglected.

5.1.4 Analytical solutions of the diffusion equation

The analytical solution of the frequency domain diffusion equation for a homogeneous infinite slab is derived. Analytical solutions for other simple geometries are found in appendix C.1.

For some simple geometries, analytical solutions of the diffusion equation are known in frequency domain and time-domain. Solutions for the infinite homogeneous medium, homogeneous half space, and homogeneous infinite slab were reported in the literature [24]. For the (partially) homogeneous infinite medium with a nonfluorescent of fluorescent spherical heterogeneity analytical exact solutions exist [25, 26], whereas for an infinite half space and an infinite slab containing a spherical heterogeneity ap-

proximate analytical solutions have been reported [27, 126]. In the following, we will state the analytical solutions for homogeneous infinite medium and homogeneous slab geometry. Although solutions for a homogeneous slab with an additional fluorescent sphere have been used to validate the numerical simulations, the solution of the diffusion equations have been presented in [27] and can be found in the appendix C.1.

The frequency domain solution of Eq. (5.11) for the homogeneous infinite medium ($D(\boldsymbol{x},\lambda) = D^0(\lambda)$, $\mu_\mathrm{a}(\boldsymbol{x},\lambda) = \mu_\mathrm{a}^0(\lambda)$) with a delta-like source term $q_0(\boldsymbol{x},\boldsymbol{x}_\mathrm{s},\lambda,\omega) = (1/v)\delta(\boldsymbol{x}-\boldsymbol{x}_\mathrm{s})$ at source position $\boldsymbol{x}_\mathrm{s}$ is given by

$$\Phi_0^\mathrm{inf}(\boldsymbol{x},\boldsymbol{x}_\mathrm{s},\lambda,\omega) = \frac{1}{4\pi v D^0(\lambda)} \frac{\exp\left(-ik(\lambda,\omega)|\boldsymbol{x}-\boldsymbol{x}_\mathrm{s}|\right)}{|\boldsymbol{x}-\boldsymbol{x}_\mathrm{s}|}, \tag{5.24}$$

with

$$k^2(\lambda,\omega) = \frac{-\mu_\mathrm{a}^0(\lambda) - i\omega/v}{D^0(\lambda)}. \tag{5.25}$$

A derivation of the real and imaginary parts of $k(\lambda,\omega)$ is presented in appendix C.2.3. For the source term chosen, the photon density corresponds to the Green's function of the infinite homogeneous medium,

$$\Phi_0^\mathrm{inf}(\boldsymbol{x},\boldsymbol{x}_\mathrm{s},\lambda,\omega) = G_0^\mathrm{inf}(\boldsymbol{x},\boldsymbol{x}_\mathrm{s},\lambda,\omega). \tag{5.26}$$

Solutions for a finite medium (Ω) that solve the Robin boundary condition (Eq. (5.15)), i.e. have a non-vanishing flux and a given photon density at the medium surface $\delta\Omega$ are approximated by solutions fullfilling the Dirichlet boundary condition, i.e. $\Phi(\boldsymbol{x},\boldsymbol{x}_\mathrm{s},\lambda,\omega)|_{\boldsymbol{x}\in\delta\Omega'} = 0$, at an extrapolated surface $\delta\Omega'$ that has been shifted outwards of the investigated volume Ω. This approach allows to approximate the Robin boundary condition by using virtual sources and results in a simple analytical solution. For a boundary having reflectivity $K(\lambda)$ this shift is given by

$$r_\mathrm{RBC}(\lambda) = 2D^0(\lambda)\frac{1+K(\lambda)}{1-K(\lambda)}. \tag{5.27}$$

The solution for semi-infinite slab geometry can be written as an infinite sum [76],

$$\Phi_0^\mathrm{slab}(\boldsymbol{x},\boldsymbol{x}_\mathrm{s},\lambda,\omega) = \sum_{j=-\infty}^{\infty} \left(\Phi_j^+(\boldsymbol{x},\boldsymbol{x}_\mathrm{s},\lambda,\omega) - \Phi_j^-(\boldsymbol{x},\boldsymbol{x}_\mathrm{s},\lambda,\omega)\right), \tag{5.28}$$

using infinite medium solutions analogous to Eq. (5.24),

$$\Phi_j^\pm(\boldsymbol{x},\boldsymbol{x}_\mathrm{s},\lambda,\omega) = \frac{1}{4\pi v D^0(\lambda)} \frac{\exp\left(-ik(\lambda,\omega)|\boldsymbol{x}-\boldsymbol{r}_j^\pm(\lambda)|\right)}{|\boldsymbol{x}-\boldsymbol{r}_j^\pm(\lambda)|}, \tag{5.29}$$

where $\boldsymbol{r}_j^\pm(\lambda)$ is the position of the jth positive or negative (virtual) source that is chosen to comply with the Dirichlet boundary condition at $\delta\Omega'$. The displacements of the positive and negative virtual sources are shown in Fig. 5.4 and can be calculated from the slab thickness d, and the (reflectivity dependent) extrapolated boundary shift r_RBC. We chose the slab surface to lie in the xy plane without loss of generality, and used the same reflectivity $K(\lambda)$ at both interfaces. Here,

$$\begin{aligned} \boldsymbol{r}_j^+(\lambda) &= \quad \boldsymbol{x}_\mathrm{s}' + j\boldsymbol{r}_\mathrm{shift}(\lambda), \\ \boldsymbol{r}_j^-(\lambda) &= \boldsymbol{x}^-(\lambda) + j\boldsymbol{r}_\mathrm{shift}(\lambda), \end{aligned} \tag{5.30}$$

where $\boldsymbol{x}_\mathrm{s}'$ is the shifted source position, and the distance between two positive respectively two negative sources is given by

$$\boldsymbol{r}_\mathrm{shift}(\lambda) = \left(0, 0, 2d + 4r_\mathrm{RBC}(\lambda)\right)^\mathrm{T}, \tag{5.31}$$

and

$$\boldsymbol{x}^{-}(\lambda) = \boldsymbol{x}'_{\mathrm{s}} + (2r_{\mathrm{RBC}}(\lambda) + 2/\mu'_{\mathrm{s}}(\lambda))\boldsymbol{e}_{\mathrm{z}}, \tag{5.32}$$

with $\boldsymbol{e}_{\mathrm{z}}$ being the unit vector in z direction, and $|\boldsymbol{x}_{\mathrm{s}} - \boldsymbol{x}'_{\mathrm{s}}| = 3D^0(\lambda)$ the shift of the source into the slab volume (as depicted in Fig. 5.4), provided the laser source is emitting light via a fiber source oriented perpendicularly to the interface.

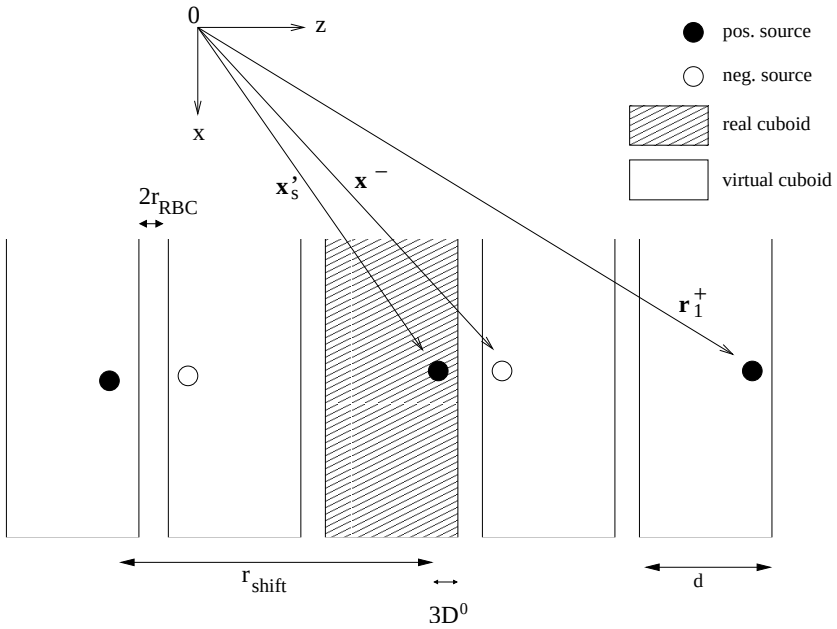

Figure 5.4: Arrangement (in xz plane) of real source at $\boldsymbol{x}_{\mathrm{s}}$ and virtual (positive and negative) mirror sources used for the diffusion equation solution in slab geometry. The origin of the right-handed coordinate system is indicated by 0.

5.1.5 Solving the steady-state diffusion equation numerically via Galerkin's method

The method to discretize the continuous wave and frequency domain diffusion equations on a finite element grid is described, which forms the basis of the FEM calculations used throughout this thesis. The differential equations are converted to integral equations, which can be written in matrix form.

Analytical solutions are limited to simple geometries and a homogeneous medium with or without a spherical heterogeneity. An analytical solution is not known, when sources and detectors are positioned on a more complex (e.g. ring or cup) geometry. As will be shown later, the same holds true for reconstructions, where the diffusion equation has to be solved for arbitrary heterogeneous distributions of optical properties. Therefore, a numerical solution of the diffusion equation is needed for several applications. In this section we show, how the diffusion equation can be discretized and solved on a finite element grid. For this purpose, we use Galerkin's method [127], which transforms the differential equation into an integral equation, allowing a discretization of the integrals and hence a formulation as a system of linear equations.

To solve the cw diffusion equation (i.e. Eq. (5.11) for $\omega = 0$) on an FEM grid, we use the expansion

$$\Phi^{\mathrm{FEM}}(\boldsymbol{x}, \boldsymbol{x}_{\mathrm{s}}, \lambda) = \sum_{i=1}^{N} \phi_i(\boldsymbol{x}_{\mathrm{s}}, \lambda)\varphi_i(\boldsymbol{x})\,, \tag{5.33}$$

where $\varphi_i(\boldsymbol{x})$ is a piecewise linear function (after transformation to the unit cell) that is centered at the ith vertex of the grid and linearly decreases from one to zero to all neighboring vertices. N is the total number of vertices, and ϕ_i is the corresponding expansion coefficient. All expansion coefficients ϕ_1 to ϕ_N define the nodal solution vector $\boldsymbol{\Phi}_{\mathrm{nodal}}(\boldsymbol{x}_{\mathrm{s}}, \lambda) = [\phi_1(\boldsymbol{x}_{\mathrm{s}}, \lambda), ..., \phi_N(\boldsymbol{x}_{\mathrm{s}}, \lambda)]^T$.

For simplicity, the spectral dependence of the shape functions $\varphi_i(\boldsymbol{x})$ is neglected throughout this section. Likewise, we use the abbreviations $\Phi^{\mathrm{FEM}} := \Phi^{\mathrm{FEM}}(\boldsymbol{x}, \boldsymbol{x}_{\mathrm{s}}, \lambda)$, $\varphi_j := \varphi_j(\boldsymbol{x})$, $q_0 := q_0(\boldsymbol{x}, \boldsymbol{x}_{\mathrm{s}}, \lambda)$, $D := D(\boldsymbol{x}, \lambda)$, $\mu_{\mathrm{a}} := \mu_{\mathrm{a}}(\boldsymbol{x}, \lambda)$, and $A(\lambda) := A$ to shorten notation. Fig. 5.5 illustrates the shape function on a simple 2D quadratic FEM grid. Although illustration is limited to a 2D FE grid, computations have conclusively been calculated on 3D grids.

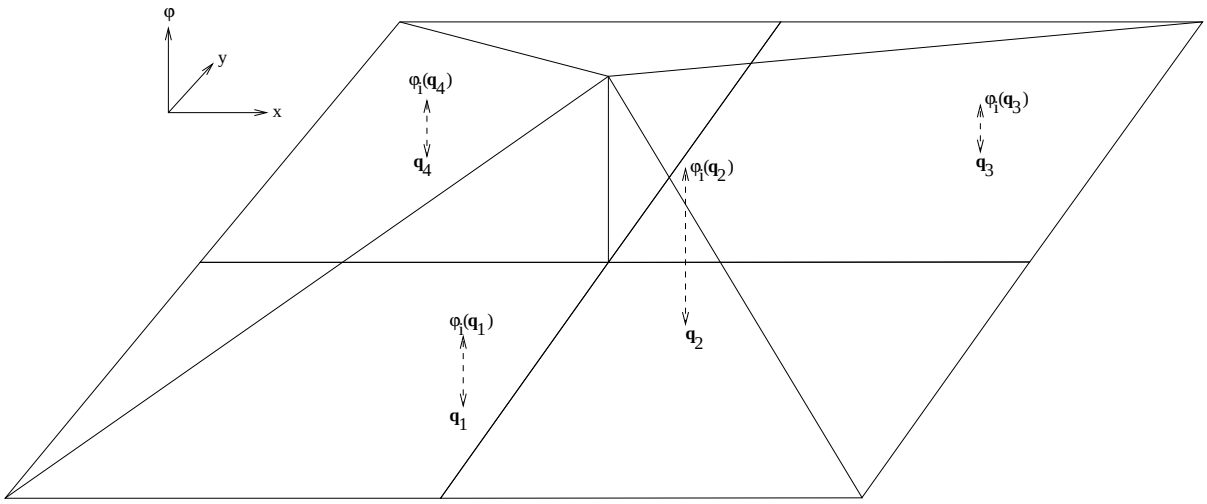

Figure 5.5: Extraction of a 2D quadratic FEM grid with shape function $\varphi_i(\boldsymbol{x})$ and quadrature points $\boldsymbol{q}_1, ..., \boldsymbol{q}_4$.

Inserting $\Phi^{\mathrm{FEM}}(\boldsymbol{x}, \boldsymbol{x}_{\mathrm{s}}, \lambda)$ into the diffusion equation (5.11 with $\omega = 0$), multiplying with φ_j, and integrating, one obtains

$$\int_{\Omega} d\Omega\varphi_j \left(\nabla \cdot D\nabla\Phi^{\mathrm{FEM}} - \mu_{\mathrm{a}}\Phi^{\mathrm{FEM}}\right) = -\int_{\Omega} d\Omega\varphi_j q_0\,. \tag{5.34}$$

Integration by parts (see Eq. (C.63) using $v = \varphi$ and $\mathbf{a} = D\nabla\Phi^{\mathrm{FEM}}$) results in

$$-\int_{\Omega} d\Omega D\nabla\varphi_j \cdot \nabla\Phi^{\mathrm{FEM}} + \int_{\partial\Omega} d\omega D\varphi_j \partial_n\Phi^{\mathrm{FEM}} - \int_{\Omega} d\Omega\varphi_j\mu_{\mathrm{a}}\Phi^{\mathrm{FEM}} = -\int_{\Omega} d\Omega\varphi_j q_0\,, \tag{5.35}$$

which can be simplified using the boundary condition (5.15) to obtain the following integral formulation of the diffusion equation (5.11),

$$\int_{\Omega} d\Omega \left(D\nabla\varphi_j \cdot \nabla\Phi^{\mathrm{FEM}} + \varphi_j\mu_{\mathrm{a}}\Phi^{\mathrm{FEM}}\right) = \int_{\Omega} d\Omega\varphi_j q_0 - \int_{\partial\Omega} d\omega \frac{\varphi_j\Phi^{\mathrm{FEM}}}{2A}\,, \tag{5.36}$$

for all $\varphi_j(\boldsymbol{x})$ with $j \in \{1, ..., N\}$.

This system of equations can be written as a matrix equation

$$[K(\lambda) + C(\lambda) + B(\lambda)]\, \boldsymbol{\Phi}_{\text{nodal}}(\boldsymbol{x}_\text{s}, \lambda) = Q(\boldsymbol{x}_\text{s}, \lambda)\,, \tag{5.37}$$

with the matrix and vector components:

$$K_{ij}(\lambda) = \int_\Omega d\Omega D(\boldsymbol{x}, \lambda) \nabla\varphi_i(\boldsymbol{x}) \cdot \nabla\varphi_j(\boldsymbol{x}) \tag{5.38}$$

$$C_{ij}(\lambda) = \int_\Omega d\Omega \mu_\text{a}(\boldsymbol{x}, \lambda) \varphi_i(\boldsymbol{x}) \varphi_j(\boldsymbol{x}), \tag{5.39}$$

$$B_{ij}(\lambda) = \int_{\partial\Omega} d\omega \frac{\varphi_i(\boldsymbol{x})\varphi_j(\boldsymbol{x})}{2A(\lambda)}, \tag{5.40}$$

$$Q_j(\boldsymbol{x}_\text{s}, \lambda) = \int_\Omega d\Omega \varphi_j(\boldsymbol{x}) q_0(\boldsymbol{x}, \boldsymbol{x}_\text{s}, \lambda), \tag{5.41}$$

where all matrices K, C, and B are sparse. As depicted in Fig. 5.5, the integrals of the matrix-components Eq. (5.38) to Eq. (5.41) are approximated by sums over n_q quadrature points $\boldsymbol{q}_n$ having quadrature weight $w(\boldsymbol{q}_n)$ (i.e. pixel or voxel size), e.g.

$$K_{ij}(\lambda) = \sum_{n=1}^{n_\text{q}} w(\boldsymbol{q}_n) D\left(\boldsymbol{q}_n, \lambda\right) \nabla\varphi_i\left(\boldsymbol{q}_n\right) \cdot \nabla\varphi_j\left(\boldsymbol{q}_n\right)\,. \tag{5.42}$$

To calculate the nodal solution vector $\boldsymbol{\Phi}_\text{nodal}$, we solve the symmetric and positive definite matrix $K + C + B$ given in equation (5.37) by using a conjugate gradient (CG) iterative solver with a symmetric successive overrelaxation method (SSOR) as preconditioner to speed up the convergence [128]. Details on the implementation using the `deal.II` library are given in the appendix A.3. Subsequently, the FEM solution $\Phi^\text{FEM}(\boldsymbol{x})$ is obtained by inserting the coefficients ϕ_i into equation (5.33).

The fluorescence diffusion equation (Eq. (5.13) with $\omega = 0$) is solved in essentially the same way

$$[K(\lambda_\text{f}) + C(\lambda_\text{f}) + B(\lambda_\text{f})]\, \boldsymbol{\Phi}^\text{f}_\text{nodal}(\boldsymbol{x}_\text{s}, \lambda) = Q^\text{f}(\boldsymbol{x}_\text{s}, \lambda)\,, \tag{5.43}$$

yielding the nodal solution vector of fluorescence photons $\boldsymbol{\Phi}^\text{f}_\text{nodal}(\boldsymbol{x}_\text{s}, \lambda) = \left[\phi^\text{f}_1(\boldsymbol{x}_\text{s}, \lambda), ..., \phi^\text{f}_N(\boldsymbol{x}_\text{s}, \lambda)\right]^T$. The expression for the matrices K, C, and B are the same as for the laser photons (Eq. (5.38) to Eq. (5.40)) except for the source term, which is given by

$$Q^\text{f}_j(\boldsymbol{x}_\text{s}, \lambda) = \int_\Omega d\Omega \varphi_j(\boldsymbol{x}) \eta \mu_a^\text{dye}(\boldsymbol{x}, \lambda) \Phi^\text{FEM}(\boldsymbol{x}, \boldsymbol{x}_\text{s}, \lambda). \tag{5.44}$$

It should be noted that the same FEM grid and hence the same shape functions are used to solve the laser and fluorescence diffusion equations.

The FEM solution $\Phi^\text{FEM}_\text{f}(\boldsymbol{x}, \boldsymbol{x}_\text{s}, \lambda)$ for fluorescence photons of wavelength λ_f after excitation of the fluorescent dye at wavelength λ is obtained as

$$\Phi^\text{FEM}_\text{f}(\boldsymbol{x}, \boldsymbol{x}_\text{s}, \lambda) = \sum_{i=1}^{N} \phi^\text{f}_i(\boldsymbol{x}_\text{s}, \lambda) \varphi_i(\boldsymbol{x}). \tag{5.45}$$

The coefficients ϕ^f_i are calculated analogously to ϕ_i using CG as iterative solver and SSOR as preconditioner.

The frequency domain solutions $\Phi^\text{FEM}(\boldsymbol{x}, \boldsymbol{x}_\text{s}, \lambda, \omega \neq 0)$ can be derived by substituting the absorption coefficient $\mu_\text{a}(\boldsymbol{x}, \lambda)$ with $\mu_\text{a}(\boldsymbol{x}, \lambda) + i\omega/v$. Likewise, to obtain $\Phi^\text{FEM}_\text{f}(\boldsymbol{x}, \boldsymbol{x}_\text{s}, \lambda, \omega \neq 0)$ the analogous substitution at the fluorescence wavelength has to be made. These substitutions result in complex matrices $C(\lambda)$ and $C(\lambda_\text{f})$, requiring a different iterative solver. Therefore, a biconjugate gradient (BI-CGSTAB) iterative solver with a Jacobi preconditioner is used.

5.1.6 Numerical solutions in time-domain using time steps

The following paragraph describes how the time-domain diffusion equation is discretized on a finite element grid for numerical integration. A matrix equation analogous to the cw case has to be solved for each time step, making this method too time consuming and prone to numerical instabilities. Instead, to obtain time-domain solutions of the diffusion equation, frequency domain solutions are calculated at a finite number of angular frequencies followed by Fourier transformation.

The derivation of the integral formulation of the diffusion equation in time-domain is similar to the cw case discussed in the previous section. One expands the time-dependent FEM solution in terms of time-independent shape function

$$\widetilde{\Phi}^{\mathrm{FEM}}(\boldsymbol{x}, \boldsymbol{x}_{\mathrm{s}}, \lambda, t) = \sum_{i=1}^{N} \widetilde{\phi}_i(\boldsymbol{x}_{\mathrm{s}}, \lambda, t)\varphi_i(\boldsymbol{x}), \tag{5.46}$$

where the expansion coefficients $\widetilde{\phi}_i(\boldsymbol{x}_{\mathrm{s}}, \lambda, t)$ are time-dependent.

Multiplying the time-dependent diffusion equation (5.9) with the shape function $\varphi_j(\boldsymbol{x})$ and integrating, one obtains

$$\int_\Omega d\Omega\varphi_j(\boldsymbol{x}) \left\{ \nabla \cdot D(\boldsymbol{x}, \lambda)\nabla - \mu_{\mathrm{a}}(\boldsymbol{x}, \lambda) - \frac{1}{v}\frac{\partial}{\partial t} \right\} \widetilde{\Phi}^{\mathrm{FEM}}(\boldsymbol{x}, \boldsymbol{x}_{\mathrm{s}}, \lambda, t) = -\int_\Omega d\Omega\varphi_j(\boldsymbol{x})\widetilde{q_0}(\boldsymbol{x}, \boldsymbol{x}_{\mathrm{s}}, \lambda, t). \tag{5.47}$$

Again, to simplify notation we abbreviate $\widetilde{\Phi} := \widetilde{\Phi}(\boldsymbol{x}, \boldsymbol{x}_{\mathrm{s}}, \lambda, t)$, $\widetilde{q_0} = \widetilde{q_0}(\boldsymbol{x}, \boldsymbol{x}_{\mathrm{s}}, \lambda, t)$, $D := D(\boldsymbol{x}, \lambda)$, $\mu_{\mathrm{a}} := \mu_{\mathrm{a}}(\boldsymbol{x}, \lambda)$ and $\varphi_j := \varphi_j(\boldsymbol{x})$ throughout this section. In this way, one obtains

$$\int_\Omega d\Omega \left(D\nabla\varphi_j \cdot \nabla\widetilde{\Phi}^{\mathrm{FEM}} + \mu_{\mathrm{a}}\varphi_j\widetilde{\Phi}^{\mathrm{FEM}} + \varphi_j\frac{\partial}{v\partial t}\widetilde{\Phi}^{\mathrm{FEM}} \right) = -\int_{\partial\Omega} d\omega \frac{\varphi_j\widetilde{\Phi}^{\mathrm{FEM}}}{2A} + \int_\Omega d\Omega\varphi_j\widetilde{q_0}. \tag{5.48}$$

The latter equation is written as matrix equation

$$[K(\lambda) + C(\lambda) + B(\lambda)]\, \widetilde{\boldsymbol{\Phi}}_{\mathrm{nodal}}(\boldsymbol{x}_{\mathrm{s}}, \lambda, t) + M\frac{1}{v}\frac{\partial\widetilde{\boldsymbol{\Phi}}_{\mathrm{nodal}}(\boldsymbol{x}_{\mathrm{s}}, \lambda, t)}{\partial t} = \widetilde{Q}(\boldsymbol{x}_{\mathrm{s}}, \lambda, t), \tag{5.49}$$

where $K_{ij}(\lambda)$, $C_{ij}(\lambda)$, $B_{ij}(\lambda)$ are given by Eq. (5.38), (5.39), (5.40), and

$$M_{ij} = \int_\Omega d\Omega\varphi_i(\boldsymbol{x})\varphi_j(\boldsymbol{x}), \tag{5.50}$$

$$\widetilde{Q_j}(\boldsymbol{x}_{\mathrm{s}}, \lambda, t) = \int_\Omega d\Omega\varphi_j(\boldsymbol{x})\widetilde{q_0}(\boldsymbol{x}, \boldsymbol{x}_{\mathrm{s}}, \lambda, t). \tag{5.51}$$

The time-dependent nodal solution vector of equation (5.49),

$$\widetilde{\boldsymbol{\Phi}}_{\mathrm{nodal}}(\boldsymbol{x}_{\mathrm{s}}, \lambda, t) = \left[\widetilde{\phi}_1(\boldsymbol{x}_{\mathrm{s}}, \lambda, t), \widetilde{\phi}_2(\boldsymbol{x}_{\mathrm{s}}, \lambda, t), ..., \widetilde{\phi}_N(\boldsymbol{x}_{\mathrm{s}}, \lambda, t)\right]^T, \tag{5.52}$$

is obtained by using iterative time increments Δt, hence the name time-slice method. The nodal solution for $t = \Delta t$ is obtained according to [129, 28] by

$$F_+(\lambda)\widetilde{\boldsymbol{\Phi}}_{\mathrm{nodal}}(\boldsymbol{x}_{\mathrm{s}}, \lambda, t = \Delta t) = \widetilde{Q}(\boldsymbol{x}_{\mathrm{s}}, \lambda, t = 0), \tag{5.53}$$

where

$$F_\pm(\lambda) = \frac{1}{2}K(\lambda) + \frac{1}{2}C(\lambda) + \frac{1}{2}B(\lambda) \pm \frac{1}{v\Delta t}M. \tag{5.54}$$

For subsequent iteration steps $k \geq 1$ the nodal solution vectors are calculated by a recursion formula, i.e.

$$F_+(\lambda)\widetilde{\mathbf{\Phi}}_{\text{nodal}}(\boldsymbol{x}_\text{s}, \lambda, t = (k+1)\Delta t) = F_-(\lambda)\widetilde{\mathbf{\Phi}}_{\text{nodal}}(\boldsymbol{x}_\text{s}, \lambda, t = k\Delta t), \tag{5.55}$$

which, for a homogeneous medium and a regular grid, is stable provided Δt is sufficiently small [130], i.e.

$$\Delta t \leq \frac{h_{\text{grid}}^2}{4Dv}\,, \tag{5.56}$$

where h_{grid} is the vertex distance of the (2D) grid.

Compared to the cw matrix equation given in (5.37), an additional matrix $2M/(v\Delta t)$ appears in Eq. (5.55) on the LHS as result of Eq. (5.54). The matrices C and M (Eq. (5.39) and (5.50)) have the same dependence on the shape function. Therefore, every incremental step simulating the propagation of diffuse light during the time Δt is equal to a solution of the cw equation with an increased absorption coefficient $\mu'_\text{a}(\boldsymbol{x}, \lambda) = \mu_\text{a}(\boldsymbol{x}, \lambda) + 1/(v\Delta t)$ and a modified source term $F_-(\lambda)\widetilde{\mathbf{\Phi}}_{\text{nodal}}(\boldsymbol{x}_\text{s}, \lambda, t = k\Delta t)$ of the previous iteration step.

We compared a TPSF simulated by the time-slice method with the distribution of times of flight of laser photons measured in transmission through a glass cuvette filled with scattering solution ($\mu_\text{a}^0 = (0.0043 \pm 0.002)$ mm^{-1}, $D^0 = (0.37 \pm 0.13)$ mm) and a spherical absorbing lesion ($\mu_\text{a}^\text{sph} = (0.0087 \pm 0.005)$ mm^{-1}, $D^\text{sph} = (0.36 \pm 0.13)$ mm, $r^\text{sph} = 15$ mm) at its center.

The source term was modeled according to equation (5.53) as a spatial delta peak located at the (shifted) source position, i.e. $\widetilde{q}_0(\boldsymbol{x}, \boldsymbol{x}_\text{s}, \lambda, t) = \delta(\boldsymbol{x} - \boldsymbol{x}'_\text{s})/(v\Delta t)$ at $t = 0$, and $\widetilde{q}_0(\boldsymbol{x}, \boldsymbol{x}_\text{s}, \lambda, t) = 0$ for all following time steps $\Delta t = 50$ ps. Equation (5.55) was solved iteratively up to $t = 8$ ns. The resulting TPSF was convolved with the instrumental response function and is shown in Fig. 5.6 (full line). The simulated curve has two free parameters, the time origin t_0 and the total number of photons. For comparison, simulated data is scaled to have the same integral photon count as the measurement data (plusses). The simulated TPSF is in good agreement with the measurement and photon counts show a maximum approximately 3 ns after the laser pulse.

In water the light needs approximately 270 ps for the distance between source and detector (6 cm), but due to the many scattering events in the turbid medium the path length for photons detected at peak time (3 ns) is longer by a factor of approximately 10.

Refinement problems

The stability constraint (5.56) imposes a limitation for the forward model calculations. With a decrease of the minimum vertex distance h_{grid} the number of simulation steps needed increases quadratically. Due to local refinement of the FEM grid at sources and detectors the smallest h_{grid} defines the maximal acceptable time step even on an elsewhere coarse grid, as will be shown in the following.

To illustrate the stability problems that occur when the condition (5.56) is violated, we numerically calculated the photon density on a locally refined 2D grid via the time-slice method. In Fig. 5.7a we show the generated grid, which is formed as a rectangle and is locally refined at the source and detector positions ($\boldsymbol{x}'_\text{s} \approx (0, 19)$ mm, $\boldsymbol{x}_\text{d} = (0, -20)$ mm). Each FE grid vertex is indicated by a dot. An additional (artificial) refinement was performed around the center of the rectangle.

Figure 5.7b shows a min/max gray scale image of the photon density at $t = 3$ ns that has been calculated for 60 time steps of $\Delta t = 50$ ps, violating Eq. (5.56) by six orders of magnitude at refined positions. In Fig. 5.7c, a line plot of the same photon density is given for $x = 0$. The photon density shows unphysical oscillating and even negative values around the source position rather than the smooth variation expected because of the wide spectrum of modulation frequencies contained in the delta function $\delta(t)\delta(\boldsymbol{x} - \boldsymbol{x}'_\text{s})$, whereas the solution behaves numerically stable at the detector position. Furthermore, numerical instabilities are observed at positions, where additional local refinement of the grid was performed, i.e. at the center of the rectangle.

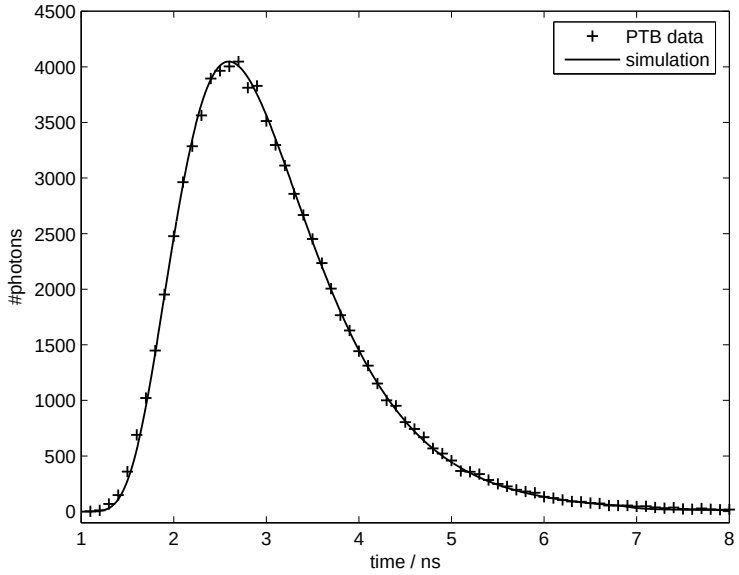

Figure 5.6: Laser photon TPSF simulated by time-slices method (black line) compared with measurement data (plusses) for an absorbing lesion in a 6 cm thick cuvette filled with scattering solution. The simulated TPSF has been scaled to the same total photon counts as recorded in the measurement and shifted in time.

To circumvent these numerical instabilities, one must choose smaller time steps Δt, but at the expense of longer calculation times. Therefore, the time slice method was not pursued any further in this thesis. Instead, the diffusion equation is solved in frequency domain for typically five angular frequency components up to $\omega_{\max} = 2\pi \cdot 500$ MHz and, subsequently, the solutions are Fourier transformed to time-domain (see appendix A.3.3).

5.1.7 Source term modeling

Different approximations to a spatial delta function used as source term are discussed that avoid numerical instabilities. The source terms are adapted to narrow laser pulses that are coupled into the medium by means of narrow optical fibers.

For analytical solutions we often model the source term by a (temporal and) spatial delta distribution located at the source position. This approximation is sufficient, if a short pulsed (100 fs to ps) laser source is used, and the source-detector distance is large compared with the reduced scattering length, l'_s.

The situation is more difficult for numerical FEM calculations of the diffusion equation and extra care has to be taken in modeling source terms. An isotropic source modelled in the diffusion equation does not correspond to experimental situations, where light from a certain direction impinges on the surface $\partial\Omega$, e.g. by using a laser beam or optical fibers.

Using a spatial delta distribution as source term has obvious drawbacks, if calculated on a grid. It is not always feasible to have a grid vertex exactly at the source position (e.g. if optical properties change between nonlinear iterations and therefore the shift of the source by $1/\mu'_s$ slightly changes due to updated reduced scattering coefficients). The sharp decrease of laser light photon density around the source position can result in numerical instabilities, sometimes causing unphysical negative photon densities. This problem can be alleviated but not solved by refining the grid around the source position.

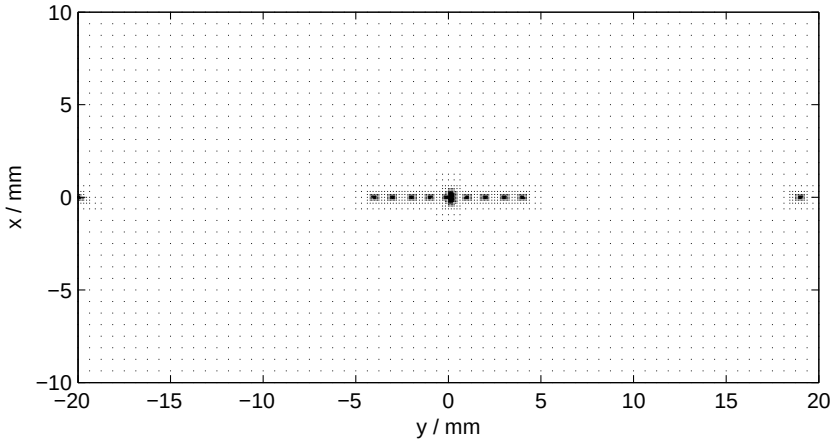

(a)

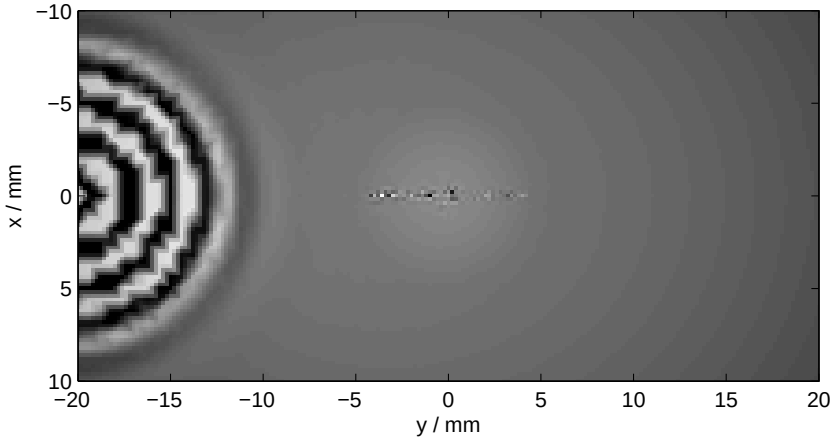

(b)

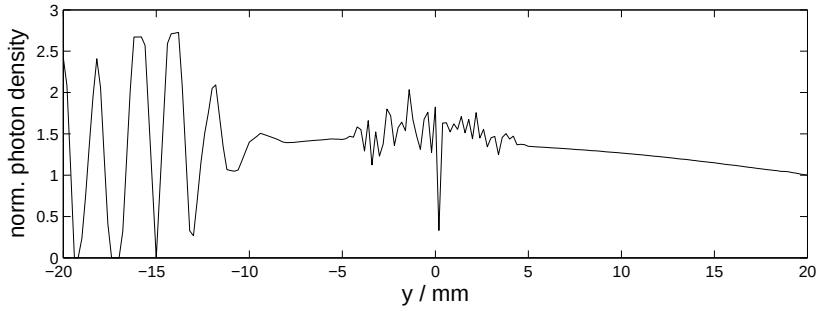

(c)

Figure 5.7: Numerical instabilities of time-slices method introduced by refinement of FE grid: (a) The two dimensional grid with refinements at source position $\boldsymbol{x}'_{\mathrm{s}} \approx (0, 19)$ mm, at detector position $\boldsymbol{x}_{\mathrm{d}} = (0, -20)$ mm, and refinements around the center position. FE grid vertices are indicated by dots. (b) Gray scale plot of simulated photon density via time-step method on corresponding grid at $t = 3$ ns. (c) Line plot of corresponding simulated photon density for $x = 0$, and normalized to the photon density at the detector position.

Furthermore, a delta distribution as a source term does not describe the physical situation that we have in a laboratory experiment, where the laser is coupled into the tissue by a fiber having a numerical aperture. This situation can be described more realistically by a Gaussian blurred source having a certain width of several mm.

In diffusion approximation, the (anisotropic) laser beam source that is coupled into the tissue at the surface is often modeled as an isotropic source shifted into the tissue by one reduced scattering length, yielding the maximum of the photon density located at this shifted source position and not at the tissue surface itself. For the simulation of photon densities at detector positions any inaccuracies associated with the shifted source are attenuated and can be neglected. In contrast, when reconstructing absorption and scattering properties, photon densities need to be calculated at the source position or within positions smaller than one free scattering length and the approximation of a shifted photon source causes severe artifacts in the reconstructed optical properties. As will be shown in more detail in Chapter 6, the gradient of the photon density is used when reconstructing scattering properties. Because of the shift of the simulated source position into the tissue volume, we get an unphysical photon density gradient value between source position and tissue surface, causing edge artifacts in reconstructions. The situation can be alleviated by modified source terms, i.e. by a source term that exponentially decays in beam direction and has its maximum at the tissue surface.

In the following, the implementation of different source terms that have been used throughout this thesis are described in detail. For a source located at $\boldsymbol{x}_\mathrm{s}$, i.e. at the true (physical) position at the point ζ on the boundary $\partial\Omega$, the source term as given in Eq. (5.11) is modeled by

$$q_0(\boldsymbol{x}, \boldsymbol{x}_\mathrm{s}, \lambda, \omega) = \frac{S_0(\boldsymbol{x}, \boldsymbol{x}_\mathrm{s}, \lambda, \omega)}{v \| S_0(\boldsymbol{x}, \boldsymbol{x}_\mathrm{s}, \lambda, \omega) \|_1} \tag{5.57}$$

where $\| \cdot \|_1$ is the L_1-norm (volume integral over $\boldsymbol{x}$).

Point source

The simplest form of an isotropic source is a point source located at $\boldsymbol{x}_\mathrm{s}$. If the source is not located exactly on a vertex of the chosen grid, the closest vertex is used as source position instead. The source is modeled using

$$S_0(\boldsymbol{x}, \boldsymbol{x}_\mathrm{s}, \lambda, \omega) = \begin{cases} 1/w(\boldsymbol{x}_\mathrm{s}) \text{ for } \boldsymbol{x} = \boldsymbol{x}_\mathrm{s} \\ 0 \text{ else} \end{cases} \quad \text{for all } \lambda \text{ and } \omega. \tag{5.58}$$

Here, $w(\boldsymbol{x}_\mathrm{s})$ is the Voronoi cell volume [131] associated with the vertex at position $\boldsymbol{x}_\mathrm{s}$.

Fiber source

When light from an optical fiber impinges perpendicularly on the surface, the source is modeled as shifted point source with a displacement in the fiber direction $-\boldsymbol{n}$ by one reduced scattering length, i.e. $1/\mu_\mathrm{s}'(\boldsymbol{x}_\mathrm{s}, \lambda)$. Thus, the shifted source position $\boldsymbol{x}_\mathrm{s}'(\lambda)$ is calculated by

$$\boldsymbol{x}_\mathrm{s}'(\lambda) = \boldsymbol{x}_\mathrm{s} + \frac{1}{\mu_\mathrm{s}'(\boldsymbol{x}_\mathrm{s}, \lambda)}(-\boldsymbol{n})\,. \tag{5.59}$$

Therefore, the resulting source term is constructed using

$$S_0(\boldsymbol{x}, \boldsymbol{x}_\mathrm{s}, \lambda, \omega) = \begin{cases} 1/w(\boldsymbol{x}_\mathrm{s}', \lambda) \text{ for } \boldsymbol{x} = \boldsymbol{x}_\mathrm{s}'(\lambda) \\ 0 \text{ else} \end{cases} \quad \text{for all } \omega. \tag{5.60}$$

Since the shift of the source depends on wavelength, the chosen FE grid with a refinement at source position depends implicitly on the wavelength.

Gaussian blurred source

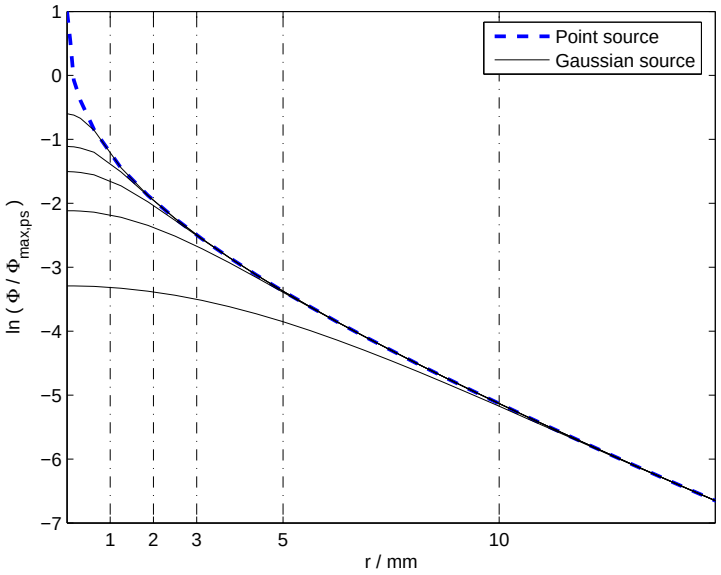

Figure 5.8: Plot of the radial dependence ($r = |\boldsymbol{x} - \boldsymbol{x}_\mathrm{s}|$) of simulated photon densities within a homogeneous infinite medium using Gaussian blurred sources of various widths (FWHM = 1 mm, 2 mm, 3 mm, 5 mm, and 10 mm) compared with a point source. All photon densities are normalized to the maximum of the simulated photon density $\Phi_{\mathrm{max,ps}}$ corresponding to a point source. Logarithms of normalized photon densities are plotted.

Using a point source in FEM calculations means trying to simulate a spatial delta distribution numerically on a coarse grid. Moreover, it is known analytically that the photon density close to the source position $\boldsymbol{x}_\mathrm{s}$ is proportional to $\exp(-k\,|\boldsymbol{x} - \boldsymbol{x}_\mathrm{s}|) \,/\, |\boldsymbol{x} - \boldsymbol{x}_\mathrm{s}|$, i.e. the solution for a point source is singular at the source position. It is not surprising that this attempt will fail numerically.

To ease these problems, Gaussian blurred sources can be used. The slope of such sources is less steep at or close to the center position and therefore such sources are less critical in numerical simulations. Gaussian blurred sources are defined by

$$S_0(\boldsymbol{x}, \boldsymbol{x}_\mathrm{s}, \lambda, \omega) = \frac{1}{(2\pi\sigma_\mathrm{src}^2)^{3/2}} \exp \frac{-(\boldsymbol{x} - \boldsymbol{x}_\mathrm{s})^2}{2\sigma_\mathrm{src}^2} \quad \text{for all } \lambda \text{ and } \omega, \tag{5.61}$$

where σ_src is the source width. Such a source term is nonvanishing throughout the entire volume, hence it contributes to each vertex of the grid.

In Fig. 5.8 we show a comparison of photon densities deduced from a point source and Gaussian blurred sources of varying source width (FWHM $= 2\sqrt{2\ln(2)}\sigma_\mathrm{src} = 1$ mm, 2 mm, 3 mm, 5 mm, and 10 mm). The photon densities are normalized to the maximum of the photon density corresponding to a point source, and their dependence on source-detector distance $r = |\boldsymbol{x} - \boldsymbol{x}_\mathrm{s}|$ is illustrated in a semi-logarithmic plot. As can be seen by comparing photon densities from point and Gaussian blurred sources, deviations can be found mainly at distances smaller then the given source width, and values of photon densities coincide at larger distances.

Obviously, it is also possible to use shifted Gaussian sources, shifted along $-\boldsymbol{n}$ by an amount $1/\mu_\mathrm{s}'(\boldsymbol{x}_\mathrm{s}, \lambda)$. The displacement of the source is calculated as was shown for fiber sources by Eq. (5.59) and $\boldsymbol{x}_\mathrm{s}$ is replaced

by $\boldsymbol{x}'_{\mathrm{s}}$ on the RHS of Eq. (5.61).

Exponentially attenuated sources

We used an additional source term to simulate light injected into the medium by an optical fiber with a certain numerical aperture and oriented perpendicularly to the surface. The exponentially attenuated source is given by

$$\begin{aligned} S_0(\boldsymbol{x}, \boldsymbol{x}_{\mathrm{s}}, \lambda, \omega) = \frac{\mu'_{\mathrm{s}}(\boldsymbol{x}_{\mathrm{s}}, \lambda) + \mu'_{\mathrm{a}}(\boldsymbol{x}_{\mathrm{s}}, \lambda)}{2\pi\sigma^2_{\mathrm{src}}} \exp\left(-\left[\mu'_{\mathrm{s}}(\boldsymbol{x}_{\mathrm{s}}, \lambda) + \mu_{\mathrm{a}}(\boldsymbol{x}_{\mathrm{s}}, \lambda)\right]\left|\boldsymbol{x}_{\parallel}\right|\right) \\ \cdot \exp(-\boldsymbol{x}^2_{\perp}/2\sigma^2_{\mathrm{src}}) \qquad \text{for all } \lambda \text{ and } \omega, \end{aligned} \tag{5.62}$$

where $\boldsymbol{x}_{\parallel} = [\boldsymbol{n} \cdot (\boldsymbol{x} - \boldsymbol{x}_{\mathrm{s}})] \cdot \boldsymbol{n}$, $\boldsymbol{x}_{\perp} = -[\boldsymbol{n} \cdot (\boldsymbol{x} - \boldsymbol{x}_{\mathrm{s}})] \cdot \boldsymbol{n} + \boldsymbol{x} - \boldsymbol{x}_{\mathrm{s}}$, $\boldsymbol{n}$ is the outward pointing surface normal at source position $\boldsymbol{x}_{\mathrm{s}}$, and σ_{src} is the width of the source perpendicular to the fiber axis. In this thesis, exponentially attenuated sources have been positioned on the surface $\partial\Omega$ only.

Fig. 5.9 compares simulated photon densities corresponding to an exponentially attenuated source ($\sigma_{\mathrm{src}} = 2$ mm) and a (shifted) fiber source. All photon densities were normalized to the maximum photon density obtained with the fiber source. The panels on the LHS plot the logarithms of the normalized photon densities versus the distance $|\boldsymbol{x}_{\parallel}|$ along the beam direction, whereas panels on the RHS illustrate normalized photon densities perpendicular to this direction at axial slices of $x_{\parallel} = -\boldsymbol{n} \cdot (\boldsymbol{x} - \boldsymbol{x}_{\mathrm{s}})$.

Panels on the top correspond to zero reflectivity ($K = 0$), while the bottom panels were calculated assuming a reflectivity of $K = 1$. As can be seen by comparing the top and bottom panels, the higher reflectivity leads to higher photon density at the surface. Furthermore, at large distances along the beam direction, the exponentially attenuated source leads to a slightly higher photon density compared to the shifted fiber source.

5.2 Results using forward simulations

5.2.1 Data analysis of time-domain measurements

A model independent raw data analysis (time-window analysis) to derive mammograms from measured distribution of times of flight is motivated by numerical simulations, and methods of improvement are suggested.

Data collected via TCSPC allows to separate scattering from absorption. In such measurements, variations in the absorption coefficient modify the total number of photons collected, i.e. the amplitude of the TPSF is in- or decreased, while variations in the diffusion coefficient change the number of scattering events for each photon traveling from the source to the detector, hence changing the path length of the trajectories for all transmitted photons, introducing a temporal shift and a narrowing or broadening of the TPSF. Therefore, effects caused by variations in absorption can be seen best by analyzing late photons that have traveled along the longest trajectories through the investigated object. On the other hand, the initial rise of the TPSF, or more generally the initial part of the TPSF is most sensitive towards changes in the reduced scattering coefficient.

For simplicity, the following discussion is limited to a slab of 6 cm thickness and an on-axis arrangement of source ($z = 0$) and detector ($z = 6$ cm). By limiting all calculations to one wavelength, the notation of the simulated photon densities can be simplified to

$$\widetilde{\Phi}(x, y, t) := \widetilde{\Phi}(\boldsymbol{x}_{\mathrm{d}}, \boldsymbol{x}_{\mathrm{s}}, \lambda, t). \tag{5.63}$$

with $\boldsymbol{x}_{\mathrm{s}} = (x, y, 0)$ and $\boldsymbol{x}_{\mathrm{d}} = (x, y, 6\text{ cm})$, and for the homogeneous bulk to

$$\widetilde{\Phi}_{\mathrm{bulk}}(t) := \widetilde{\Phi}_{\mathrm{bulk}}(\boldsymbol{x}_{\mathrm{d}}, \boldsymbol{x}_{\mathrm{s}}, \lambda, t). \tag{5.64}$$

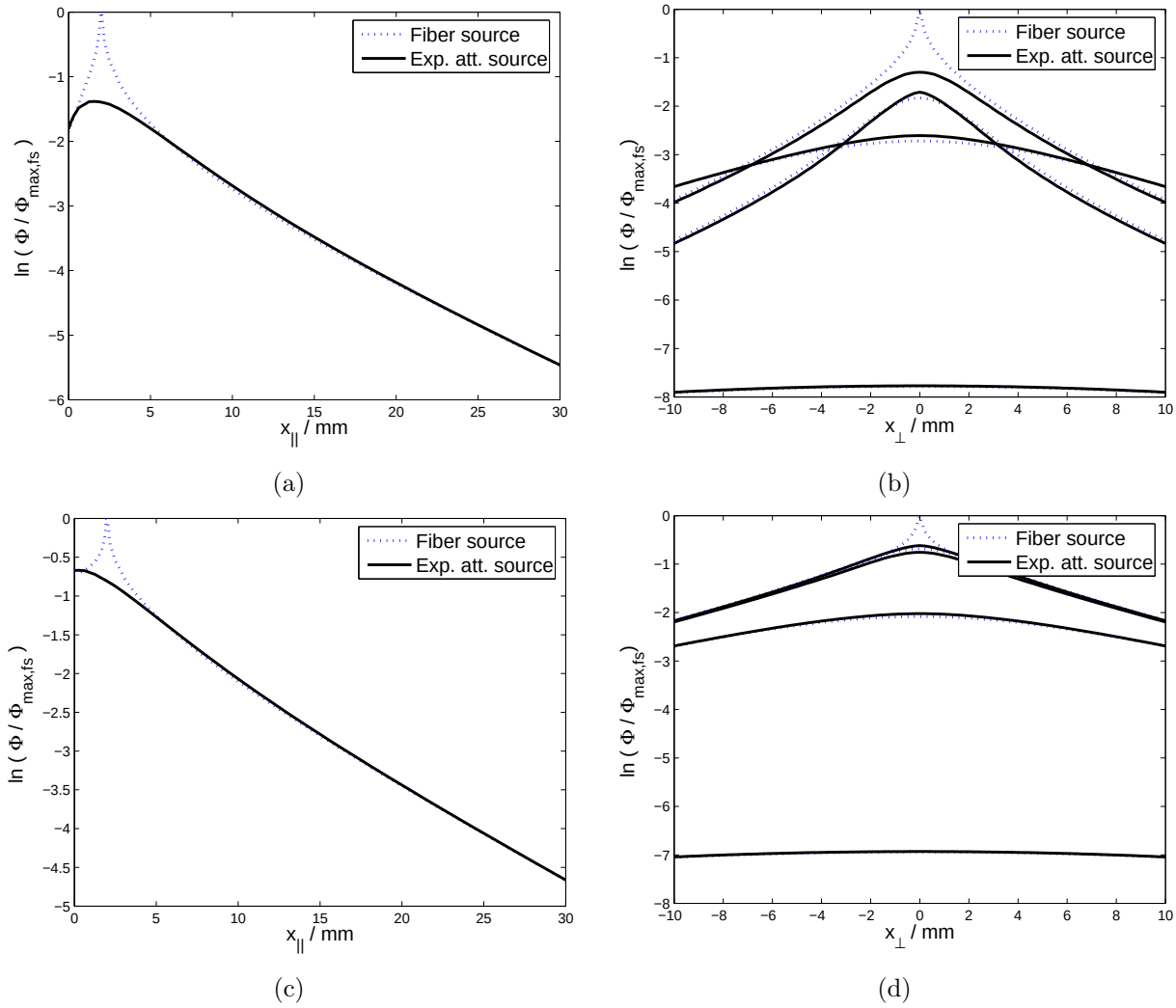

Figure 5.9: Photon densities normalized to the maximum of the fiber source along beam direction (a, c) and perpendicular to beam direction (b, d) corresponding to an exponentially attenuated source (black line) and fiber source (dotted blue line), respectively. The volume boundary is located at $x_{\parallel} = 0$ in each case. The top panels correspond to a reflectivity of $K = 0$, the bottom panels to $K = 1$. The black lines in the top and bottom panel on the right hand side correspond to photon densities at $x_{\parallel} = 2$ mm, 0 mm, 10 mm and 50 mm and $x_{\parallel} = 0$ mm, 2 mm, 10 mm and 50 mm, respectively (from top to bottom at $x_{\perp} = 0$).

From TPSFs measured in slab geometry, projection mammograms are generally generated by time-window analysis. To this end, $\widetilde{\Phi}_{\mathrm{bulk}}(t)$ measured in the homogeneous part of the breast or phantom is divided into ten contiguous time windows, each containing 10% of the total number of photons detected, i.e.

$$\frac{\int_{t_{i-1}}^{t_i} \widetilde{\Phi}_{\mathrm{bulk}}(t)dt}{\int_0^{\infty} \widetilde{\Phi}_{\mathrm{bulk}}(t)dt} = 0.1, \tag{5.65}$$

where $i = 1, ..., 10$. Fig. 5.10 illustrates the time-slicing of a simulated TPSF $\widetilde{\Phi}_{\mathrm{bulk}}(t)$ (solid line) calculated for a 6 cm thick homogeneous slab with $K = 0.5$, $n = 1.3$, $\mu_{\mathrm{a}}^0 = 0.0045$ mm^{-1}, $D^0 = 0.34$ mm. Time windows are colored alternately in green and yellow.

The same time windows are used to analyze TPSFs $\widetilde{\Phi}(x, y, t)$ measured at any point x, y of the scanned area. Projection mammograms associated with a selected time-window N_i ($t_{i-1} \leq t < t_i$) are generated by calculating normalized photon counts in this time-window N_i, i.e.

$$\frac{N_i(x, y)}{N_{i,\mathrm{bulk}}} = \frac{\int_{t_{i-1}}^{t_i} \widetilde{\Phi}(x, y, t)dt}{\int_{t_{i-1}}^{t_i} \widetilde{\Phi}_{\mathrm{bulk}}(t)dt}. \tag{5.66}$$

Mammograms showing photon counts in the first time window, i.e. associated with early arriving photons, show predominantly effects of scattering, while mammograms at later time windows, e.g. N_8, are sensitive to changes in absorption since late arriving photons travel along long trajectories.

Such projection images turned out to be helpful in detecting areas having reduced scattering (e.g. cysts) or increased absorption (e.g. tumors) coefficients in optical mammograms without the need for image reconstruction. Furthermore, this method of data analysis does not depend on a physical model and hence turned out to be very robust. Also, projection images calculated in this way can be used in tomosynthesis reconstructions, yielding 3D spatial information of changes of absorption and reduced scattering coefficients, yet not providing absolute values of optical properties.

Additionally, two simulations were carried out, each with one spherical heterogeneity ($r_{\mathrm{sph}} = 0.25$ cm) located at $(x_{\mathrm{l}}, y_{\mathrm{l}}, z_{\mathrm{l}}) = (0, 0, 3)$ cm, one sphere (pure absorber) having an absorption coefficient larger by 10% ($\mu_{\mathrm{a}}^{\mathrm{sph}} = 0.00495$ mm^{-1}) and the other one (pure scatterer) with a reduced scattering coefficient larger by 10% ($D^{\mathrm{sph}} = 0.32$ mm), resulting in simulated TPSFs $\widetilde{\Phi}_{\mathrm{a}}(0, 0, t)$ and $\widetilde{\Phi}_{\mathrm{s}}(0, 0, t)$, respectively. This notation indicates that the center of the spherical heterogeneity falls on the line of sight connecting source and detector. The difference of TPSFs caused by the increase of absorption or reduced scattering coefficients of the spherical heterogeneity is given by

$$\begin{aligned} \Delta\widetilde{\Phi}_{\mathrm{s}}(0, 0, t) &= \widetilde{\Phi}_{\mathrm{bulk}}(t) - \widetilde{\Phi}_{\mathrm{s}}(0, 0, t), \\ \Delta\widetilde{\Phi}_{\mathrm{a}}(0, 0, t) &= \widetilde{\Phi}_{\mathrm{bulk}}(t) - \widetilde{\Phi}_{\mathrm{a}}(0, 0, t). \end{aligned} \tag{5.67}$$

To identify effects on the TPSF caused by changes of the scattering or absorption coefficients, the dimensionless motivation function $f_{\mathrm{mot}}(t) = \Delta\widetilde{\Phi}_{\mathrm{s}}(0, 0, t)/m_{\mathrm{s}} - \Delta\widetilde{\Phi}_{\mathrm{a}}(0, 0, t)/m_{\mathrm{a}}$ is introduced, with the normalization factors

$$\begin{aligned} m_{\mathrm{s}} &= \max\left(\left|\widetilde{\Phi}_{\mathrm{bulk}}(t) - \widetilde{\Phi}_{\mathrm{s}}(0, 0, t)\right|\right), \\ m_{\mathrm{a}} &= \max\left(\left|\widetilde{\Phi}_{\mathrm{bulk}}(t) - \widetilde{\Phi}_{\mathrm{a}}(0, 0, t)\right|\right), \end{aligned} \tag{5.68}$$

thus treating the influence of absorption and scattering on an equal footing. The absolute value $|f_{\mathrm{mot}}|$ is shown in Fig. 5.10 as dashed line. As can be seen, the motivation function has two extrema, the first one at early times resulting from the changes in the reduced scattering coefficient, while the second one at a later time is caused by changes in the absorption coefficient. The zero crossing of f_{mot} is located at $t' \approx 1.9$ ns. This time depending on the optical properties, e.g. of the homogeneous slab.

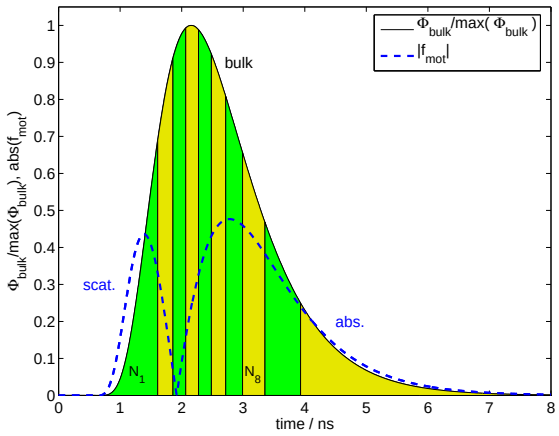

Figure 5.10: Standard time-slicing method applied to the (normalized) TPSF (full line) of the homogeneous background medium and its associated motivation curve (blue dashed line) showing the areas of predominant influences of variations of the reduced scattering coefficient and absorption coefficient. Time windows are alternately colored in green and yellow.

To compare the motivation function with the times associated with the time intervals N_1 and N_8, the center of mass for the two parts of the motivation function is calculated separately, i.e.

$$t_{\mathrm{cm}}^{\mathrm{scat}} = \frac{\int_0^{t'} t f_{\mathrm{mot}}(t)dt}{\int_0^{t'} f_{\mathrm{mot}}(t)dt} = 1.4 \text{ ns}, \tag{5.69}$$

and

$$t_{\mathrm{cm}}^{\mathrm{abs}} = \frac{\int_{t'}^{\infty} t f_{\mathrm{mot}}(t)dt}{\int_{t'}^{\infty} f_{\mathrm{mot}}(t)dt} = 3.4 \text{ ns}, \tag{5.70}$$

giving similar results as the standard time-window analysis. This shows that the usage of N_1 for detection of changes of the scattering coefficient and of N_8 for the detection of changes of the absorption coefficient is a reasonable approximation.

Decoupling of time windows

In the following paragraph, a more elaborate approach is introduced to separate the effects of scattering and absorption in a given projection mammogram. For this purpose, we assume that a change in the perturbed TPSF $\widetilde{\Phi}(x, y, t)$ compared with the TPSF of the bulk, i.e.

$$\Delta\widetilde{\Phi}(x, y, t) = \widetilde{\Phi}_{\mathrm{bulk}}(t) - \widetilde{\Phi}(x, y, t) \tag{5.71}$$

can be expressed as a linear superposition of TPSFs caused by the absorption and by the reduced scattering coefficient,

$$\Delta\widetilde{\Phi}(x, y, t) = c_{\mathrm{s}}(x, y)\Delta\widetilde{\Phi}_{\mathrm{s}}(0, 0, t) + c_{\mathrm{a}}(x, y)\Delta\widetilde{\Phi}_{\mathrm{a}}(0, 0, t). \tag{5.72}$$

The definition of the L_1 pseudo norm

$$\langle f|g\rangle = \frac{1}{t_{\mathrm{e}} - t_{\mathrm{s}}} \int_{t_{\mathrm{s}}}^{t_{\mathrm{e}}} f(t)g(t)dt, \tag{5.73}$$

where t_s and t_e are the start and end time of the TPSF, respectively, allows to write

$$\begin{aligned} N_\mathrm{s} &= \langle \Delta\Phi_\mathrm{s} | \Delta\Phi_\mathrm{s} \rangle \,, \\ N_\mathrm{a} &= \langle \Delta\Phi_\mathrm{a} | \Delta\Phi_\mathrm{a} \rangle \,. \end{aligned} \tag{5.74}$$

To solve for c_s and c_a, the relations

$$\begin{aligned} \langle \Delta\Phi_\mathrm{s} | \Delta\Phi \rangle &= N_\mathrm{s} c_\mathrm{s} + c_\mathrm{a} \langle \Delta\Phi_\mathrm{s} | \Delta\Phi_\mathrm{a} \rangle \,, \\ \langle \Delta\Phi_\mathrm{a} | \Delta\Phi \rangle &= N_\mathrm{a} c_\mathrm{a} + c_\mathrm{s} \langle \Delta\Phi_\mathrm{s} | \Delta\Phi_\mathrm{a} \rangle \end{aligned} \tag{5.75}$$

are used, and after some further algebra one obtains

$$c_\mathrm{a} = \frac{\langle \Delta\Phi_\mathrm{a} | \Delta\Phi \rangle - N_\mathrm{s}^{-1} \langle \Delta\Phi_\mathrm{s} | \Delta\Phi \rangle \langle \Delta\Phi_\mathrm{s} | \Delta\Phi_\mathrm{a} \rangle}{N_\mathrm{a} - N_\mathrm{s}^{-1} \langle \Delta\Phi_\mathrm{s} | \Delta\Phi_\mathrm{a} \rangle^2}, \tag{5.76}$$

$$c_\mathrm{s} = \frac{\langle \Delta\Phi_\mathrm{s} | \Delta\Phi \rangle - N_\mathrm{a}^{-1} \langle \Delta\Phi_\mathrm{a} | \Delta\Phi \rangle \langle \Delta\Phi_\mathrm{a} | \Delta\Phi_\mathrm{s} \rangle}{N_\mathrm{s} - N_\mathrm{a}^{-1} \langle \Delta\Phi_\mathrm{a} | \Delta\Phi_\mathrm{s} \rangle^2}. \tag{5.77}$$

To decouple the effects caused by variations in absorption and scattering, assumptions about the functions $\Delta\widetilde{\Phi}_\mathrm{s}(0,0,t)$ and $\Delta\widetilde{\Phi}_\mathrm{a}(0,0,t)$ have to be made. These functions can be calculated exactly, when the size, shape, and position of the heterogeneity embedded in the homogeneous medium are known. Generally, this information generally is not available prior to reconstructions. As an initial guess, the functions $\Delta\widetilde{\Phi}_\mathrm{s}(0,0,t)$ and $\Delta\widetilde{\Phi}_\mathrm{a}(0,0,t)$ that will be used in the following for decoupling are calculated from a homogeneous medium having shifted optical properties. To estimate the error that is introduced by this approach, the functions $\Delta\widetilde{\Phi}_\mathrm{s}(0,0,t)$ and $\Delta\widetilde{\Phi}_\mathrm{a}(0,0,t)$ are computed additionally for a single centered sphere, i.e. using the exact perturbation of the phantom. Therefore, the functions $\Delta\widetilde{\Phi}_\mathrm{s}(0,0,t)$ and $\Delta\widetilde{\Phi}_\mathrm{a}(0,0,t)$ are calculated numerically for two setups,

i) for a homogeneous medium with shifted optical properties, i.e. with absorption and scattering coefficient increased by 10% (1%), and

ii) for the homogeneous medium ($\mu_\mathrm{a}^0 = 0.0045$ mm^{-1}, $D^0 = 0.34$ mm^{-1}) with a centered spherical lesion (radius $r_\mathrm{sph} = 2.5$ mm) and absorption and scattering coefficients increased by 10% (1%).

Results for $\Delta\widetilde{\Phi}_\mathrm{s}(0,0,t)$ and $\Delta\widetilde{\Phi}_\mathrm{a}(0,0,t)$ normalized to their maxima are shown in Fig. 5.11 for a 1% increase (full lines) and a 10% increase (full lines with plusses) of the absorption and scattering coefficient of the spherical heterogeneity. As can be seen, results obtained from 1% or 10% increases in the absorption coefficient and reduced scattering coefficient coincide within line thickness, indicating that the linear ansatz is still valid at the small changes considered. For larger spheres, when the linear approach no longer holds true, the normalized functions $\Delta\widetilde{\Phi}_\mathrm{a}(0,0,t)/\max(\Delta\widetilde{\Phi}_\mathrm{a}(0,0,t))$ and $\Delta\widetilde{\Phi}_\mathrm{s}(0,0,t)/\max(\Delta\widetilde{\Phi}_\mathrm{s}(0,0,t))$ for 1% and 10% will no longer coincide. Furthermore, as can be seen from Fig. 5.11, the results for the homogeneous medium shifted by 1% or 10% in its reduced scattering coefficient or its absorption coefficient no longer agree with the normalized results obtained for a sphere of radius $r_\mathrm{sph} = 2.5$ mm. This is to be expected since the shifted homogeneous medium corresponds to a large sphere with $r_\mathrm{sph} \to \infty$.

For comparison of the standard time window approach and the decoupling method derived in this section, TPSFs corresponding to on-axis scans of 425 source positions $x = -6$ cm, ..., $+6$ cm, $y = -4$ cm, ..., $+4$ cm, $z = 0$ with a step size of $\Delta x = \Delta y = 5$ mm were simulated. For this purpose, data was calculated using an FE cuboid of volume $\Omega = 16 \times 12 \times 6$ cm^3 (6 cm thickness), with two spheres of radius $r_\mathrm{sph} = 7.5$ mm positioned at $x_\mathrm{l} = \pm 2.5$ cm , $y_\mathrm{l} = 0$, and $z_\mathrm{l} = 2.2$ cm. The optical properties of the background medium of the slab were set to $\mu_\mathrm{a}^0 = 0.0045$ mm^{-1} and $D^0 = 0.37$ mm, while the two lesions had a 2:1 contrast of absorption and scattering coefficient, respectively. To suppress numerical

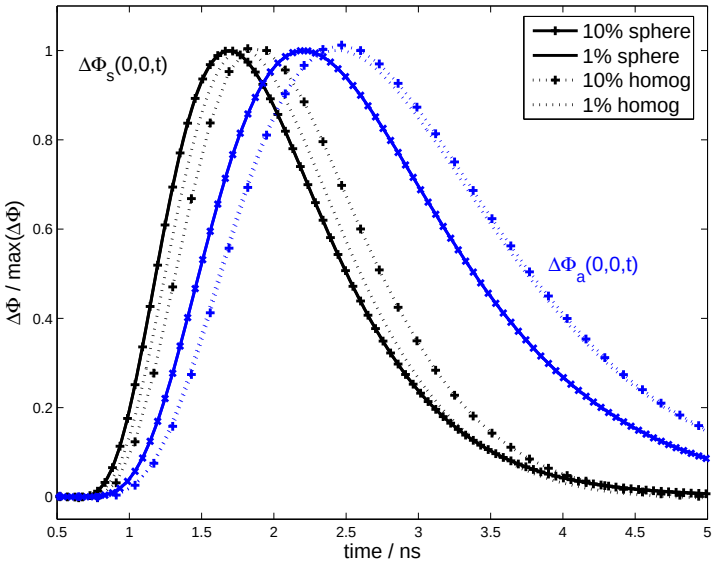

Figure 5.11: Functions $\Delta\widetilde{\Phi}_{\mathrm{s}}(0,0,t)$ and $\Delta\widetilde{\Phi}_{\mathrm{a}}(0,0,t)$ simulated for a homogeneous phantom containing a spherical heterogeneity ($r_{\mathrm{sph}} = 2.5$ mm) centered on the line of sight between source and detector with 10% (full lines with plusses) and 1% (full lines) increase in absorption coefficient (blue) and reduced scattering coefficient (black), and for homogeneous media (dotted lines) having the same increase in the optical properties. Solid lines and solid lines with plusses are indistinguishable within the line thickness.

errors, the homogeneous background scan was simulated for all 425 source positions using the same FE grid, but with the two lesions removed in the numerical phantom.

Data was simulated in frequency domain using 8 equidistant angular frequencies from $\omega_1 = 0$ to $\omega_8 = 2\pi \cdot 1.2$ GHz. Poisson noise, 1% Gaussian noise, and a noise floor estimated from experiments were added to the simulated data in time-domain. Results are compared in Fig. 5.12, presenting the calculated absorption and reduced scattering coefficients (left and right panel of top row, respectively) in mm^{-1} by the new decoupling method and by using and the standard time-window method (bottom row), investigating the difference of photon counts of the N_1 (right) and N_8 (left) time bins corresponding to the simulation of the bulk and with additional sphere, respectively. Decoupling was achieved by the functions $\Delta\widetilde{\Phi}_{\mathrm{a}}(0,0,t)$ and $\Delta\widetilde{\Phi}_{\mathrm{s}}(0,0,t)$ computed for a homogeneous medium with a 1% increase in absorption and reduced scattering coefficient, respectively.

As can be seen in Fig. 5.12, the results of both methods look quite similar. Although the proposed decoupling method shows a reduced cross-talk between absorption and scattering, it has a lower signal-to-noise ratio in the image corresponding to the reduced scattering coefficient (Fig. 5.12 top right). Although the time-windows analysis is not based on a physical model, the use of photon counts N_1 and N_8 in the first and eights time windows is sufficient to discriminate changes in scattering from absorption. As improvement, the proposed decoupling allows calculating projection images of optical properties in absolute values. As drawback, these optical properties suffer from an error introduced by calculating $\Delta\widetilde{\Phi}_{\mathrm{a}}(0,0,t)$ and $\Delta\widetilde{\Phi}_{\mathrm{s}}(0,0,t)$, i.e. by assuming a homogeneous shift of optical properties throughout the volume. Such an approach suffers from lower absorption and scattering contrast of heterogeneities because of partial volume effects.

We conclude this section on data analysis of time-domain measurements by pointing out the close relation of the decoupling method with first order time-dependent perturbation theory, considering the

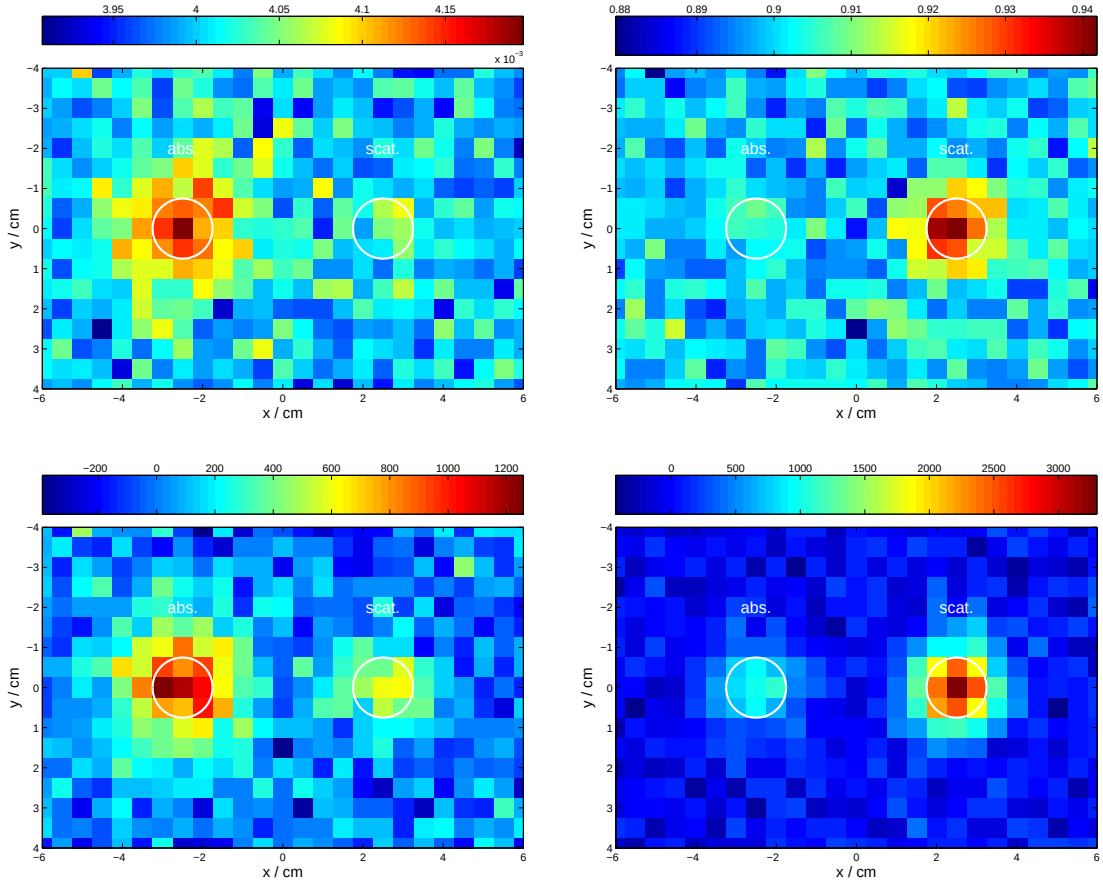

Figure 5.12: Projection images (top row) calculated by using the decoupling method, yielding reconstructed absorption coefficients (top row left) and reduced scattering coefficients (top row right) given in mm^{-1}. The bottom row shows projection images obtained by the standard time-window analysis illustrating photon counts in the eights (N_8) window (bottom row left) and in the first (N_1) window (bottom row right).

same situation, i.e. a homogeneous slab with background optical properties μ_a^0, D^0, on-axis arrangement of source and detector and a spherical heterogeneity of radius r_{sph} centered on the line of sight halfway between source and detector with absorption and diffusion coefficients $\mu_a^{sph} = \mu_a^0 + \delta\mu_a$ and $D^{sph} = D^0 + \delta D$. Similar to Eq. (5.71) and (5.72) the transmitted photon density following injection of a temporal and spatial delta-like laser pulse is written as

$$\widetilde{\Phi}(x, y, t) = \widetilde{\Phi}_{bulk}(t) + \delta\widetilde{\Phi}(x, y, t), \tag{5.78}$$

with

$$\delta\widetilde{\Phi}(x, y, t) = \delta\mu_a f_a(x, y, t) + \delta D f_D(x, y, t) \tag{5.79}$$

where $f_a(x, y, t)$ and $f_D(x, y, t)$ are called (first order) shape functions. Generally, these shape functions depend on the size and shape of the homogeneous background medium, on its optical properties and on the size, shape and location of the heterogeneity, being itself homogeneous, but do not depend on the changes $\delta\mu_a$ and δD of the heterogeneity [132]. One may analyze temporal point spread functions recorded through the compressed breast at zero source detector offset (on-axis geometry) by a scanning mammograph using first order perturbation theory [133]. In this case a virtual spherical heterogeneity is assumed on the line of sight between source and detector that moves together with the source and detector fiber and the temporal point spread function measured at each scan position is analyzed for changes $\delta\mu_a$ and δD, generating optical mammograms that reflect absorption and scattering properties.

5.2.2 Performance analysis of instrumentation in optical mammography

A statistical test is presented using simulated photon migration data and a noise model derived from the Philips tomographic fluorescence mammograph to predict its detection limits. This method allows to assess the spatial distribution of the detection sensitivity of arbitrary geometries and noise without requiring phantom measurements and reconstructions. The minimal detectable lesion size at selected lesion positions is determined and the predicted results compared with phantom measurements carried out with the Philips mammograph. In addition, we apply our method to predict the smallest size of detectable lesions at various positions in cup and slab geometry and model how detection sensitivity depends for the latter geometry on breast compression and lesion fluorescence contrast. Our investigation shows that lesion detection is limited by absolute noise in cup geometry and by relative noise in slab geometry.

The spatial resolution of the DOT images is quite low, since the photons are scattered many times, before they leave the tissue. Furthermore, the reconstruction problem is under-determined, because the number of measurements is usually lower than the number of reconstructed image elements.

Due to these two problems, DOT image reconstruction is a challenging task. To reconstruct a meaningful image, the use of regularization schemes and/or the consideration of a-priori information is necessary. Some methods to regularize the reconstruction and to use a-priori information are described in the literature [30]. The content of the resulting images is highly dependent on the choice of the reconstruction algorithm. Due to this fact, the question is nontrivial, whether a heterogeneity of a certain size and a certain contrast in its optical properties can be detected with an optical tomograph.

A method to predict, what lesions can be detected with a particular optical imaging system, is desirable for the system design as well as for comparison of different systems of e.g. different source-detector arrangements. In the contrast detail analysis [134, 135], one defines objects with different optical contrast, simulates or measures data for these objects and then judges, whether the object is visible or not in the reconstructed image. This method is widely used, but also very time-consuming. Another disadvantage is that its results do not depend on imaging hardware alone, but additionally on the image reconstruction method used. It is then difficult to determine if the reconstruction algorithm or the imaging system is limiting the performance.

A comparison of imaging systems and detector configurations based on a singular value decomposition of the system matrix containing all source-detector combinations has been proposed before [136, 137]. Although that approach can predict which system geometry has a better detection sensitivity, it can neither predict detection limits quantitatively, nor calculate spatial dependence of detection limits.

In the following, an alternative method is presented, which analyzes the raw data to decide, whether an object causes a statistically significant signal above the background level. The method is based on simulations and on a noise model of the photon densities measured by the imaging system. This approach has the advantage that only the system hardware is characterized, thus making it possible to simulate the effects of hardware changes, e.g. changes in geometry, in the number of detectors and sources, and their arrangement, and of noise reduction on the detection sensitivity. The results can be easily used to identify the main limiting components and serve as guidelines for system improvements.

A disadvantage of this approach is that there is no guarantee that the object can indeed be recognized in a reconstructed image, since contrast depends also on the image reconstruction algorithm used. It follows that our method gives an answer to the question, which lesions can definitely not be detected using the selected hardware, but no answer, which lesion can be recognized using the system and a selected reconstruction algorithm.

In the following, we investigate the sensitivity of fluorescence measurements performed in cup geometry by using raw data analysis. The predictions of this analysis are compared with sensitivity limits gained from a contrast detail analysis using phantoms consisting of lesion-simulating inhomogeneities immersed in a cup-shaped detection chamber filled with scattering liquid.

In this section we explain the method of raw data analysis followed by the derivation of the noise model. Data on laser and fluorescence transmission are simulated applying the diffusion approximation for selected geometries.

The section describes the phantom measurements that were performed to validate the raw data analysis, and explains, how to scale simulated data to measurement data for quantitative comparison.

Furthermore, we compare the contrast detail analysis and raw data analysis for a series of phantom experiments performed in cup geometry. This comparison shows that the predictions of the raw data analysis are accurate for the selected measurement system.

Chi-square test

The minimal lesion size that can be detected in scans of transmitted laser radiation (absorption scan) or fluorescence radiation (fluorescence scan) is estimated by analyzing simulated data for a phantom modeling a breast carrying a lesion. A large number of simulations was carried out, where the position, diameter, and optical contrast of the lesion were varied. The following sections describe in detail the raw data analysis method, the breast phantoms and the numerical simulations.

For the determination of sensitivity limits, we analyze simulated data with the chi-square test [138]. This allows to predict and compare detection limits for different imaging systems and detector configurations. The test method (Sec. 5.2.2) is based on a description of the system geometry and on a noise model that allows to predict, how measurements are affected by noise.

First, we explain the idea of the test method for the case of fluorescence detection. Subsequently we discuss the case of absorption measurements. To determine, whether a lesion is detectable under a certain condition, two data sets for the fluorescence reconstruction are simulated: one data set S^{f} with the lesion, and one data set R^{f} without the lesion. Each data set is the ratio of two simulations and consists of m values S_j^{f} and R_j^{f}, respectively ($j = 1, ..., m$):

$$S_j^{\mathrm{f}} = \frac{\Phi_{\mathrm{f,L},j}}{\Phi_{\mathrm{L},j}} \tag{5.80}$$

and

$$R_j^{\mathrm{f}} = \frac{\Phi_{\mathrm{f,B},j}}{\Phi_{\mathrm{B},j}}. \tag{5.81}$$

Here, m is the total number of source-detector combinations in set M, Φ_{L} is the density of transmitted laser photons per unit interval of frequency for the breast with the lesion-simulating heterogeneity, and Φ_{B} is the corresponding density for the breast without any lesion. This definition of data sets as ratio of two measurements corresponds to the normalized Born-approximation [139, 140] used in reconstruction algorithms. The subscript f indicates the detection at the fluorescence wavelength. Background absorption, absorption coefficient of the fluorescent dye and scattering properties of the homogeneous background medium enter into the photon densities $\Phi_{\mathrm{B,j}}$ and $\Phi_{\mathrm{f,B,j}}$ in Eq. (5.81), whereas the background absorption, the absorption coefficient of the dye and the scattering properties of the heterogeneity are additionally contained in the photon densities $\Phi_{\mathrm{L,j}}$ and $\Phi_{\mathrm{f,L,j}}$ in Eq. (5.80).

These simulations reflect ideal measurements without noise. Now N noise realizations $\widehat{S}_j^{i(\mathrm{f})}$ of the simulation with the lesion are generated using a noise model,

$$\widehat{S}_j^{i(\mathrm{f})} = S_j^{\mathrm{f}} + X_j^i\left(\sigma\left(S_j^{\mathrm{f}}\right)\right). \tag{5.82}$$

Here, $\sigma(S_j^{\mathrm{f}})$ represents the standard deviation for data point S_j^{f} at the fluorescence wavelength. $X(\sigma)$ is a random variable of Gaussian distribution with zero mean and standard deviation σ. The values for $\sigma(S_j^{\mathrm{f}})$ are calculated by error propagation (see below) from the errors of the transmitted photon densities $\Phi_{\mathrm{f,L},j}$ and $\Phi_{\mathrm{L},j}$, which are known from experiment. We now apply a test, whether there is a statistically significant difference between R_j^{f} and $\widehat{S}_j^{i(\mathrm{f})}$ (null hypothesis). For this purpose, we calculate the chi-square values χ_i^2 for the difference between $\widehat{S}_j^{i(\mathrm{f})}$ and R_j^{f}:

$$\chi_i^2 = \sum_{j\in M'}\left(\frac{\widehat{S}_j^{i(\mathrm{f})} - R_j^{\mathrm{f}}}{\sigma(R_j^{\mathrm{f}})}\right)^2. \tag{5.83}$$

Since the location of the lesion is known, it is also known, which data points are influenced by its presence. Therefore, we restrict the summation in Eq. (5.83) to that subset of source-detector combinations j that contain information about the lesion. The subset was defined in the following way:

$$M' = \left\{ j \in M \middle| \frac{\left|S_j^{\mathrm{f}} - R_j^{\mathrm{f}}\right|}{\max S^{\mathrm{f}}} > 0.001 \right\}, \tag{5.84}$$

i.e., taking all m' data points into account, where the presence of the lesion leads to a change in the simulated data by more than 0.1% of the maximum value.

The distribution of χ_i^2 is known for the case that $\widehat{S}_j^{i(\mathrm{f})}$ is a noisy realization of R_j^{f}. Or, in other words, the probability p_i that $\widehat{S}_j^{i(\mathrm{f})}$ is measured without the lesion being present can be calculated from the χ_i^2 distribution of m' degrees of freedom [141]. We calculate the probability $1-p$ for a χ_i^2 value to lie between a lower (x_{l}) and an upper (x_{u}) threshold to be

$$1 - p = P\left(\frac{x_{\mathrm{u}}}{2}, \frac{m'}{2}\right) - P\left(\frac{x_{\mathrm{l}}}{2}, \frac{m'}{2}\right) \tag{5.85}$$

with

$$P\left(\frac{x}{2}, \frac{m'}{2}\right) = \frac{1}{\Gamma(m'/2)}\int_0^{x/2} t^{\frac{m'}{2}-1}\exp(-t)dt, \tag{5.86}$$

given by the incomplete gamma function and the degree of freedom m'. The upper and lower boundary x_{u} and x_{l} are chosen such that the probability $(1-p)$ is distributed equally below and above the median value of χ_i^2.

One can say that the lesion is detectable in the data set $\widehat{S}_j^{i(\mathrm{f})}$ if p_i is below some threshold p_T. We introduce δ_i to count the number of data sets with detectable lesions:

$$\delta_i = \begin{cases} 1 & : \text{ if } p_i < p_\mathrm{T} \\ 0 & : \text{ otherwise} \end{cases} . \tag{5.87}$$

The choice of p_T has some influence on the results of the analysis, but the influence is rather small. In the following, we use $p_\mathrm{T} = 1\%$, unless stated otherwise.

We define the significance ratio r_sgn as the fraction of the data sets $\widehat{S}_j^{i(\mathrm{f})}$ that differed statisticly from R_j^f:

$$r_\mathrm{sgn} = \frac{1}{N} \sum_{i=1}^{N} \delta_i. \tag{5.88}$$

We count a lesion as detectable, if it was detected in at least 80% of these noise realizations, i.e. $r_\mathrm{sgn} \geq 0.8$.

The discussion given above applies to fluorescence measurements, but it can be transferred to measurements of transmitted laser photons as well. In this case we take the density of transmitted laser photons $\Phi_\mathrm{F,j}$ through the homogeneous background medium as a reference, but without absorption by the fluorescent dye. The definition of the noise-free data sets S^x and R^x corresponds to the Rytov-approximation [142]:

$$S_j^\mathrm{x} = -\ln\left(\frac{\Phi_{\mathrm{L},j}}{\Phi_{\mathrm{F},j}}\right) \tag{5.89}$$

and

$$R_j^\mathrm{x} = -\ln\left(\frac{\Phi_{\mathrm{B},j}}{\Phi_{\mathrm{F},j}}\right). \tag{5.90}$$

Similar to equation (5.82), the data sets $\widehat{S}_j^{i(\mathrm{x})}$ with noise added are generated by

$$\widehat{S}_j^{i(\mathrm{x})} = S_j^\mathrm{x} + X_j^i\left(\sigma\left(S_j^\mathrm{x}\right)\right). \tag{5.91}$$

and the χ_i^2 values as

$$\chi_i^2 = \sum_{j \in M'} \left(\frac{\widehat{S}_j^{i(\mathrm{x})} - R_j^\mathrm{x}}{\sigma(R_j^\mathrm{x})}\right)^2. \tag{5.92}$$

with M' given by

$$M' = \left\{ j \in M \,\middle|\, \left|S_j^\mathrm{x} - R_j^\mathrm{x}\right| > 0.001 \right\}. \tag{5.93}$$

CW noise model

We define the noise for each of the transmitted photon densities Φ_B, $\Phi_\mathrm{f,B}$, Φ_L, $\Phi_\mathrm{f,L}$, and Φ_F as

$$\sigma_{X,j}^{(\mathrm{f,x})} = \sqrt{\left(n_\mathrm{r}\Phi_{X,j}\right)^2 + \left(n_\mathrm{a}\right)^2}, \tag{5.94}$$

with $X = \mathrm{B}, \mathrm{L}, \text{or } \mathrm{F}$, and $\Phi_{X,j}$ the simulated photon density at the fluorescence or laser wavelength, respectively. n_r and n_a are free parameters of the noise model and called relative and absolute noise of the measurement system, respectively. The simulated transmitted photon densities need to be scaled properly to experimental data, before Eq. (5.94) is evaluated with n_a given in fA. Furthermore, to prevent numerical problems introduced by low signal strengths, we additionally use the constraints for scaled photon densities $\Phi_{\mathrm{f,B},j} > 3n_\mathrm{a}$ and $\Phi_{\mathrm{F},j} > 6n_\mathrm{a}$. Here, n_a is the expected noise floor of the detection setup.

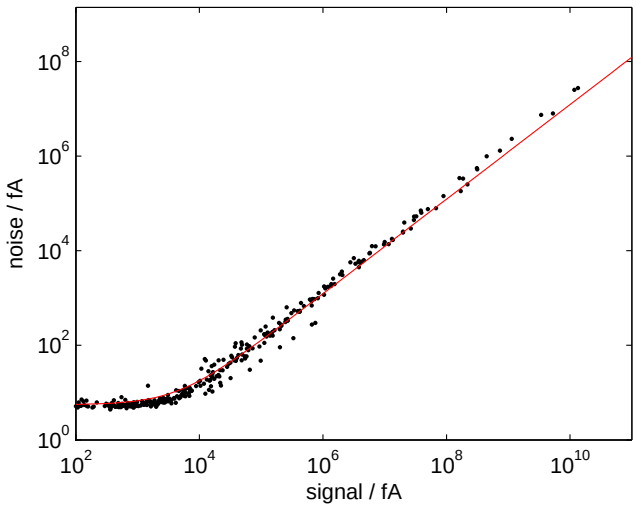

Figure 5.13: Dependence of noise on signal strength determined by a calibration experiment. The measurement noise (dots) and the fitted noise model (solid line) are given on a logarithmic scale.

Our noise model describes well the experimentally observed dependency of noise on signal strength as is shown in Fig. 5.13. We present the measurement noise of a reference scan and its dependence on the signal strength as dots, whereas the noise model of Eq. (5.94) fitted to the measurement data is given as a solid line. It can be seen that the noise floor ($n_\mathrm{a} = 5.5$ fA) is dominant for low signal strengths, whereas a simple linear relation between noise and signal strength holds true for signals in excess of about $5 \cdot 10^4$ fA. Our model slightly underestimates noise at large signal strengths. The parameters of the noise model are of course highly dependent on the system hardware (type and output power of lasers, detector type, quantum efficiency of the detectors, etc.). The procedure to scale simulated to measured data is described in the following paragraph.

The noise of the data sets R_j^x, S_j^x can be calculated by error propagation from the noise of the transmitted photon densities at the laser wavelength

$$\sigma\left(R_j^\mathrm{x}\right) = \sqrt{\left(\frac{\sigma_{\mathrm{B},j}^\mathrm{x}}{\Phi_{\mathrm{B},j}}\right)^2 + \left(\frac{\sigma_{\mathrm{F},j}^\mathrm{x}}{\Phi_{\mathrm{F},j}}\right)^2}, \tag{5.95}$$

$$\sigma\left(S_j^\mathrm{x}\right) = \sqrt{\left(\frac{\sigma_{\mathrm{L},j}^\mathrm{x}}{\Phi_{\mathrm{L},j}}\right)^2 + \left(\frac{\sigma_{\mathrm{F},j}^\mathrm{x}}{\Phi_{\mathrm{F},j}}\right)^2}, \tag{5.96}$$

and likewise for the fluorescence data sets R_j^f, S_j^f as

$$\sigma\left(R_j^\mathrm{f}\right) = \sqrt{\left(\frac{\sigma_{\mathrm{B},j}^\mathrm{f}}{\Phi_{\mathrm{B},j}}\right)^2 + \left(\sigma_{\mathrm{B},j}^\mathrm{x}\frac{\Phi_{\mathrm{f,B},j}}{\Phi_{\mathrm{B},j}^2}\right)^2}, \tag{5.97}$$

$$\sigma\left(S_j^\mathrm{f}\right) = \sqrt{\left(\frac{\sigma_{\mathrm{L},j}^\mathrm{f}}{\Phi_{\mathrm{L},j}}\right)^2 + \left(\sigma_{\mathrm{L},j}^\mathrm{x}\frac{\Phi_{\mathrm{L},j}}{\Phi_{\mathrm{f,L},j}^2}\right)^2}, \tag{5.98}$$

using Eq. (5.80), (5.81), and (5.94).

Forward simulations of data

We use the steady state (cw) diffusion approximation to model the propagation of laser and fluorescence light through the turbid medium [30]. The density per unit frequency interval $\Phi(\boldsymbol{x})$ of laser photons is obtained by solving the cw diffusion equation, i.e. Eq. (5.11) for $\omega = 0$, where $q_0(\boldsymbol{x}, \boldsymbol{x}_\mathrm{s}, \lambda, \omega = 0) = \delta(\boldsymbol{x} - \boldsymbol{x}'_\mathrm{s})/v$ is the source term given by a delta distribution with its peak value at the (shifted) source position $\boldsymbol{x}'_\mathrm{s}$ (see Sec. 5.1.7) and v the speed of light in the medium, and $D(\boldsymbol{x}, \lambda)$ and $\mu_\mathrm{a}^\mathrm{chrom}(\boldsymbol{x}, \lambda)$ represent the spatial distribution of the diffusion and absorption coefficients, respectively. For the numerical breast model ($\Phi(\boldsymbol{x}, \boldsymbol{x}_\mathrm{s}, \lambda) = \Phi_\mathrm{L}(\boldsymbol{x}, \boldsymbol{x}_\mathrm{s}, \lambda)$), the absorption coefficient $\mu_\mathrm{a}(\boldsymbol{x}, \lambda) = \mu_\mathrm{a}^\mathrm{dye}(\boldsymbol{x}, \lambda) + \mu_\mathrm{a}^\mathrm{chrom}(\boldsymbol{x}, \lambda)$ consists of the chromophore contribution $\mu_\mathrm{a}^\mathrm{chrom}(\boldsymbol{x}, \lambda)$ and of the contribution of the fluorescent dye. In this case the parameters $D(\boldsymbol{x}, \lambda)$, $\mu_\mathrm{a}(\boldsymbol{x}, \lambda)$, $\mu_\mathrm{a}^\mathrm{dye}(\boldsymbol{x}, \lambda)$, $c(\boldsymbol{x})$ are related to two homogeneous regions, i.e. to the background medium and to the heterogeneity. The density $\Phi(\boldsymbol{x}, \boldsymbol{x}_\mathrm{s}, \lambda) = \Phi_\mathrm{B}(\boldsymbol{x}, \boldsymbol{x}_\mathrm{s}, \lambda)$ of laser photons is obtained from Eq. (5.11) taking the homogeneous background medium into account only. For the reference experiment ($\Phi(\boldsymbol{x}, \boldsymbol{x}_\mathrm{s}, \lambda) = \Phi_\mathrm{F}(\boldsymbol{x}, \boldsymbol{x}_\mathrm{s}, \lambda)$), Eq. (5.11) is solved for the same background medium, but without fluorescent dye added ($\mu_\mathrm{a}^\mathrm{dye}(\boldsymbol{x}, \lambda) = 0$).

The density of fluorescence photons per unit frequency interval ($\Phi_\mathrm{f}(\boldsymbol{x}, \boldsymbol{x}_\mathrm{s}, \lambda)$) is obtained from equation (5.13), Furthermore, a single fluorescence wavelength λ_f rather than a fluorescence spectrum is considered, and the fluorescence quantum yield η is taken to be constant, i.e. to be independent of position $\boldsymbol{x}$. We neglect any re-emission of fluorescence by the dye and in the following set $D(\boldsymbol{x}, \lambda) = D(\boldsymbol{x}, \lambda_\mathrm{f})$ for simplicity, this assumption being justified because of the rather small Stoke's shift observed of the NIR dye used. For the breast simulating situation, $\Phi_{\mathrm{f,L}}(\boldsymbol{x}, \boldsymbol{x}_\mathrm{s}, \lambda)$ is obtained from Eq. (5.13) for $\omega = 0$ with the density of laser photons $\Phi_\mathrm{L}(\boldsymbol{x}, \boldsymbol{x}_\mathrm{s}, \lambda)$ entering on the RHS, while the density of fluorescence photons $\Phi_{\mathrm{f,B}}(\boldsymbol{x}, \boldsymbol{x}_\mathrm{s}, \lambda)$ describing the background situation is calculated using $\Phi_\mathrm{B}(\boldsymbol{x}, \boldsymbol{x}_\mathrm{s}, \lambda)$.

In order to simulate distributions of laser and fluorescence photons using the source and detector locations of the cup-geometry, the coupled diffusion equations (5.11) and (5.13) were solved on a Finite Element (FE) grid for $\omega = 0$, using the `deal.II` finite-element library [113] and a proprietary simulation software. We used a Robin boundary condition given in Eq. (5.15).

The diffusion approximation holds true for isotropic light sources, but the light is coupled into the cup by a fiber with a certain numerical aperture (i.e. in a non-isotropic way). As usual, we modeled this situation by shifting the light source position in beam direction by one transport scattering length and assume an isotropic source at the shifted position [28].

Fluorescence phantom study

To validate the results on lesion detection sensitivity derived from raw data analysis, a series of phantom experiments was carried out by Alfons Schipper, Rik Habers, and Michiel van Beek to determine the detection sensitivity for fluorescent lesions via a contrast detail analysis. The chosen phantoms simulated the ideal case, when a breast fills the cup entirely, so that no additional scattering fluid is required to fill the gap between breast and cup surface. A scattering liquid ($\mu_\mathrm{a}^\mathrm{chrom} = 0.0033\ \mathrm{mm}^{-1}$ and $\mu'_\mathrm{s} = 1.3\ \mathrm{mm}^{-1}$ at the laser wavelength $\lambda = 690$ nm) was used as background medium with the fluorescent dye (Omocyanine [123]) concentration of 10 nM.

The lesion-simulating heterogeneity consisted of a single fluorescent object submerged into the fluorescent scattering fluid. This object was filled with the same scattering fluid, but with different concentrations of the dye. The position and size of the object and the contrast between background and lesion was varied. Fig. 5.14 shows the coordinates of the 2 lesion positions that were examined.

The heterogeneity was made of two hollow delrin cones mounted on top of each other. Three sizes are available with 10, 15, and 20 mm diameter, corresponding to volumes of 0.26, 0.88, and 2.1 ml, respectively (see Fig. 5.15).

Table 5.1 gives an overview of all measurements that were performed. Here, c_lesion is the dye concentration inside the cones.

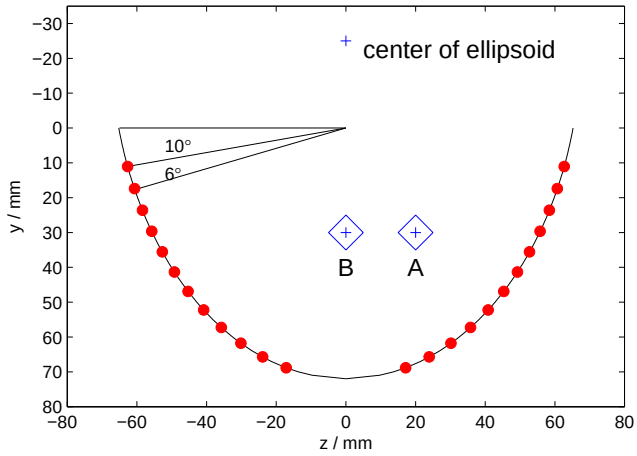

Figure 5.14: Cup axial cross section and lesion positions. The black line outlines the cup shape. The dots are the positions of the fiber rings. The rhombuses show the lesion positions A ($y = 30$ mm, $z = 20$ mm) and B ($y = 30$ mm, $z = 0$ mm).

Figure 5.15: Photograph of the phantom lesions. The lesions consist of two hollow cones made of delrin. The center diameters are 20, 15, and 10 mm.

Table 5.1: List of all experiments of the fluorescence phantom study. The background concentration of the fluorescent dye was 10 nM in all cases.

number	position	size / mm	c_{lesion} / nM
1	A	20	100
2	A	20	50
3	A	20	30
4	A	20	20
5	A	15	50
6	A	10	50
7	B	20	100
8	B	20	50
9	B	20	30
10	B	20	20

Scaling of simulated data to measurement data

The noise model used in this study has two free parameters: the relative noise n_{r}, and the absolute noise n_{a}. In contrast to the relative noise, the absolute noise is given in some physical units, either as noise equivalent power, photo current, or else. Simulated data need to be expressed in the same physical units as used to measure absolute noise in order to evaluate Eq. (5.94).

Fig. 5.16 shows the transmitted light intensities recorded by the measurement system during a typical reference scan (black plusses). The light intensities are given in fA and displayed on a logarithmic scale. The dots are the results of a simulation scaled to fit the measured data best. The scaling factor was determined independently for several reference scans using various wavelengths and optical properties.

Comparison of experiment and theory

In this section, we compare the results of the raw data analysis with the results of the fluorescence phantom measurements. To this end, we simulated data for lesion positions A and B and all lesion sizes (small, medium, and large) and all concentration contrasts (1:2, 1:3, 1:5, and 1:10) using spherical inhomogeneities with the same volume as the delrin double cones (see Fig. 5.15). The optical properties of the background medium were the same as in the reference experiments, and a 10 nM background concentration of the dye was used ($\mu_{\text{a}}^{\text{dye}} = 0.002$ cm^{-1}).

The top image in Figure 5.17 shows the results of the raw data analysis for position A. The gray level scale shows the significance ratio r_{sgn} (see Eq. (5.88)), where white represents detectable lesions and black undetectable lesions.

We use symbols to illustrate the results of the phantom measurements, where "+" stands for a visible lesion, and "0" denotes a lesion that could not be detected on dye concentration images reconstructed from measured data. According to the raw data analysis, the detection of the smallest lesion is borderline, i.e. at the detection limit of the instrument. From measured data, the concentration of the fluorescent dye was reconstructed with axial slices containing position A as shown in Fig. 5.18.

The arrangement of panels of Fig. 5.18 corresponds to the arrangement of symbols shown in Fig. 5.17 (top). All images shown in Fig. 5.18 were scaled separately in such a way that 99% of all voxels fall into the gray level scale. This is essentially a min/max scaling, but ignores extreme outliers which can

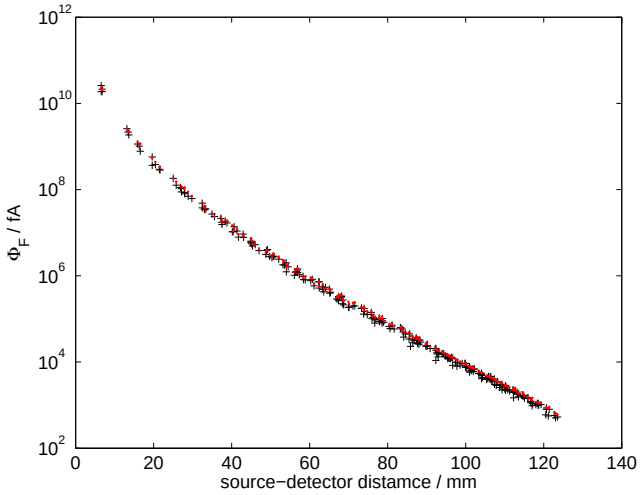

Figure 5.16: Scaling of simulated to measured data (transmitted laser intensities Φ_F). The plus symbols are data from a reference scan, the dots are the scaled results of a simulation. The scaling factor was determined by minimizing the difference of the logarithms of measured and simulated data using a least-squares fit. The accuracy for the scaling factor is estimated to be 10%.

sometimes occur at source or detector positions.

In the images presenting the medium or the large heterogeneity, the lesion is clearly visible, but in the case of the smallest lesion, the lesion signal approaches the non-uniformity of the background as predicted by the raw-data analysis.

Fig. 5.17 (bottom) shows the significance ratio r_{sgn} and the reconstruction results of the phantom measurements at position B. As can be seen from the raw data analysis, the detection of the largest lesion with lowest concentration contrast is borderline. Accordingly on the images representing reconstructed dye concentration from phantom measurements (not shown), this lesion is still visible, but its contrast approaches that of image artifacts. Generally, the visibility of lesions in images of dye concentrations reconstructed from phantom measurements agrees with the predictions of the raw data analysis. It follows that for this simple setting (a single lesion in an otherwise homogeneous background) the results of contrast detail analysis and raw data analysis are not far apart. This conclusion might no longer hold true, when the lesion is to be detected on a background that shows some structures in itself. Also, the lesion signal must be larger than background variations in order to be detected. In this case, the spatial resolution that can be achieved in the reconstruction is important, because increasing spatial resolution leads to an increased peak height of the lesion in the reconstructed dye concentration. We expect that the gap between predictions of the raw data analysis and the actual lesion visibility in reconstructed images will be larger for objects located within a varying background.

Conclusions

We presented a statistical method using simulated data and a realistic noise model to calculate the performance of a diffuse fluorescence optical tomography system. Our approach allows to numerically study the detection limits of a heterogeneity on a given background without the need for phantom experiments and the need for reconstructions. By our method, one calculates the ultimate detection limit given by the geometry, the background optical properties, lesion optical contrast, and the noise of the measurement system. In case, a lesion of particular size, location and dye concentration contrast

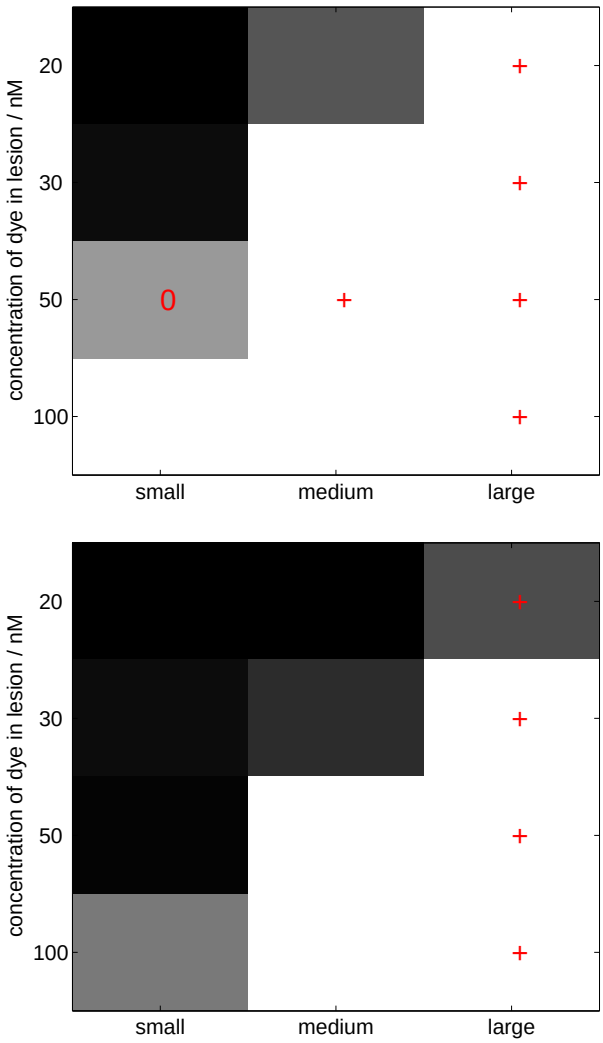

Figure 5.17: Results on detection sensitivity from raw data analysis for lesion position A (top) and B (bottom) for different lesion sizes and dye contrast. The gray level indicates the significance ratio r_{sgn} (see Eq. (5.88)), where black stands for undetectable lesions, and white represents a detectable lesion. Symbols mark those settings that were measured in phantom experiments. Detected lesions in the reconstructed images are marked with a "+" and with "0" otherwise.

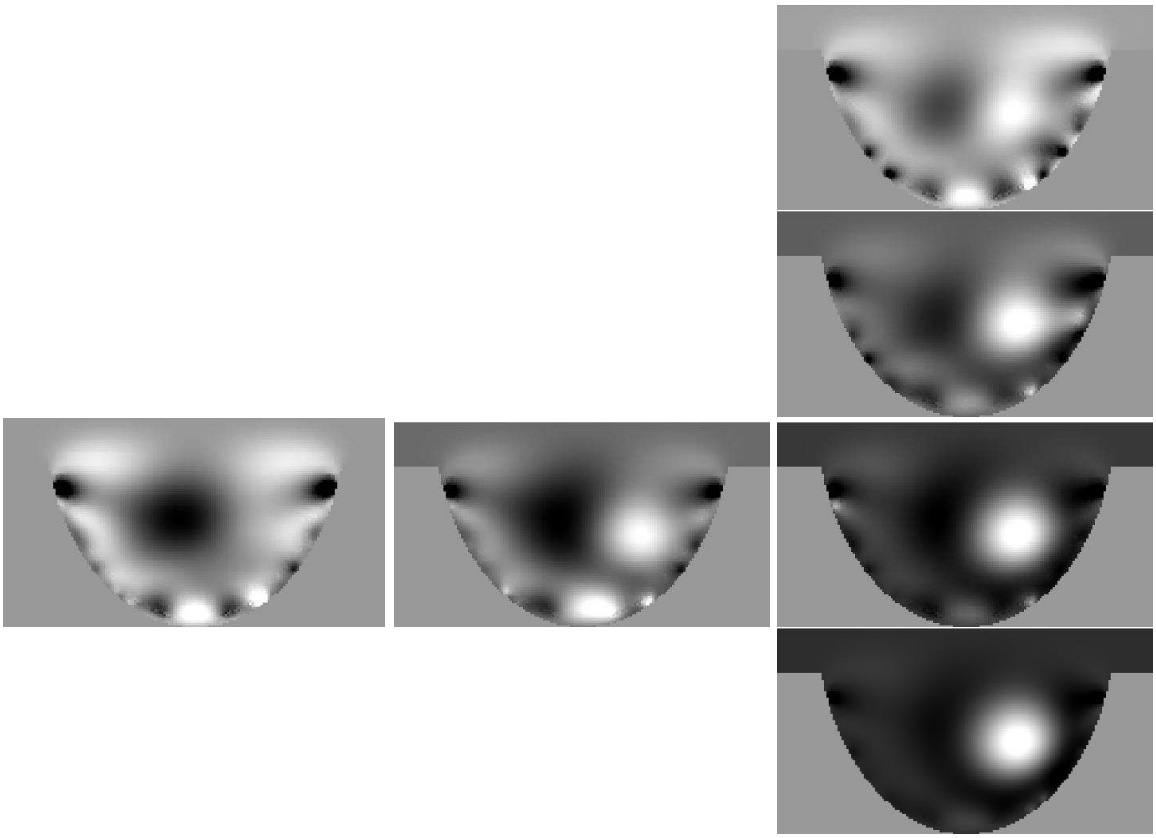

Figure 5.18: Slices of the reconstructed dye concentration through volumes containing the lesion at position A. All images are scaled separately in such a way that 99% of all voxels fall into the gray level scale (essentially min/max scaling). The arrangement of the panels corresponds to the detectability matrix shown in Fig. 5.17 (top).

falls below the ultimate detection limit it will definitely not be detected in reconstructed images, yet for lesions above this limit, detection is not guaranteed by our analysis. Our method can be used to predict the influence of changes of the system hardware on the detectability of lesions. Hardware changes could be for example different numbers of sources and detectors used, different noise properties, or a different imaging geometry.

The sensitivity of detection was predicted for a cup geometry using simulated fluorescence data with a 2:1 to 10:1 dye contrast and lesions of various sizes at different positions within the detection volume. The predicted sensitivities were compared with phantom measurements of the same system setup (same geometry and noise) and, generally, predicted and observed lesion detectabilities agreed well.

Analysis of slab and cup geometry for breast imaging

Besides handheld probes primarily used for diffuse optical spectroscopic imaging (DOSI) at the site of a known breast tumor to deduce tumor metabolic information [9], two general types of source-detector arrangements exist for diffuse optical imaging, either using parallel plates with slight compression of the breast, or tomographic systems with sources and detectors distributed on a ring or on the surface of a cup without compression of the breast tissue.

Cup geometry offers higher patient comfort because the breast is not compressed. Spatial resolution is isotropic due to the tomographic data acquisition. Slab geometry allows only limited angular sampling resulting in anisotropic spatial (depth) resolution along the compression direction [143]. This drawback can be overcome in part by performing both transmittance and reflectance measurements [144]. However, due to the reduced thickness of the compressed breast signal strengths in transmission are higher and, generally, a smaller dynamic range is required for detection using a slab system.

Here, we analyze the detection sensitivity of both geometries. Our method is based on a statistical test on simulated data using a realistic noise model derived from the system's hardware as explained in the previous paragraph. Using the same noise model for the cup and the slab geometry, we investigate lesion detection sensitivity for three different patient types, a small dense breast with high attenuation of NIR light, a medium size breast with small attenuation and a large breast with average attenuation. Using the statistical chi-square test on simulated data, we analyze the impact of the measurement geometry and of several other factors on the sensitivity for lesion detection in slab geometry.

First, we perform simulations that predict the smallest lesion size that can be detected at selected positions from densities of transmitted laser photons (absorption scan) and fluorescence photons (fluorescence scan) for cup and slab geometry. These results give insight into which factors limit detection sensitivity for both systems. Further, we investigate how lesion detectability in slab geometry depends on relative and absolute noise. From this analysis the upper noise limits are derived for the detection of a 5 mm diameter lesion assuming a fluorescent dye contrast of 5:1.

Since the amount of breast compression is a free parameter, it is important to understand how lesion contrast and hence detectability depends on slab thickness. By investigating the detection limit for a lesion at the center of the compressed breast and by varying slab thickness, we simulated how compression influences detection sensitivity for several noise settings.

Fluorescence detection of a lesion depends strongly on fluorescent dye contrast, i.e. on the ratio of the concentration of the fluorescent dye in the lesion and the surrounding tissue (background). This important factor is unknown, and hence we investigated how a slab geometry mammograph performs at various assumed dye contrasts.

In the appendix further details are given on assumed lesion positions (appendix A.4.1), on source-detector arrangements (scan heads) and on scan geometry (appendix A.4.2), on phantom geometry, and on the finite element grids used for the forward model calculations (appendix A.4.3).

Forward simulations and chi-square analysis

The minimal detectable lesion size is estimated by analyzing simulated data for a numerical phantom modeling a (homogeneous) breast containing a single (spherical) heterogeneity simulating a lesion. A large number of simulations was carried out varying the position, diameter, and dye contrast of the lesion. In addition, three different model breasts with different optical densities were investigated, corresponding to a small (high attenuation), medium size (small attenuation), and large breast (average attenuation), respectively. From the noise model, which was deduced from measurements using a cup tomograph, we added noise to simulated data and determined the detectability of a lesion by the χ^2 test (null hypothesis). Further details of this method are explained in [145]. For each case detection sensitivity was deduced from simulated data and the results of both geometries were compared.

Numerical phantoms for slab and cup geometry

We used three numerical phantoms each with the same optical properties adapted to the slab and the cup geometry. A crucial parameter for the comparison is the assumed reduction of the breast thickness achieved by compression (compression factor) in a slab measurement. We assumed a compression factor of approximately two which is a conservative estimate.

Data from a clinical trial conducted during the European research project "OPTIMAMM"[13] resulted in thicknesses of gently compressed breasts ranging between 4 and 9 cm, with an average thickness of about 6 cm.

The cup measurement system supports three different sizes (80B, 80D, and 80F) to achieve a good fit of the cup measurement chamber to the size of a patient's breast. The geometry of each of these three cups was explained in more detail in [145]. During a clinical trial with the cup measurement system at the University Medical Center Utrecht 80D and 80F cups were used in most cases. Thus, most likely, the generally achieved compression is underestimated when we associate the 80B cup with a 6 cm slab as is done in the following. Furthermore, we compare the 80D cup with the 7 cm slab, and the 80F cup with the 9 cm slab.

Phantom optical properties

For the cup geometry the numerical breast phantom is chosen to fit each of the three cup sizes perfectly, so that no additional scattering fluid is needed to match the breast to the size of the cup. The upper rim of the cup is assumed to touch the breast wall. In slab geometry, the three numerical phantoms simulate breasts gently compressed between two plates of $d = 6$ cm, 7 cm, and 9 cm separation, with the breast being immersed in scattering fluid to fill the remaining volume. The compression plates are assumed to extend to the breast wall.

To realistically simulate the absorption and scattering spectra of a breast, the absorption coefficient of the numerical phantom is given by the molar extinction coefficients ε_i of five ($i = 1, ..., 5$) constituents and their concentrations $c_i(\boldsymbol{r})$: Water (H_2O, $i = 1$), deoxyhemoglobin (HbR, $i = 2$), oxyhemoglobin (HbO, $i = 3$), the fluorescent dye (Omocyanine [122], $i = 4$), and fat ($i = 5$).

The chromophore absorption can be calculated from the molar extinction coefficients of these constituents [15, 20] as given in Eq. (5.21), and the absorption coefficient of the dye by Eq. (5.22), setting $\epsilon^{\mathrm{dye}} = \epsilon_4$. The extinction coefficients were chosen for water as listed in [117], for HbR and HbO as reported in [118], and for Omocyanine as given in [122]. The contribution of fat [116] can be ignored at the excitation ($\lambda = 730$ nm) and fluorescence ($\lambda_{\mathrm{f}} = 780$ nm) wavelength used in this study. For the scattering coefficient, a simplified Mie scattering model as given in Eq. (5.23) is used. Its reference wavelength λ_0 can be chosen arbitrarily and is set to 1000 nm in the following. The absorption coefficient of the homogeneous part of our numerical breast models, i.e. outside the lesion simulating heterogeneity, is denoted as $\mu_{a,0}^{\mathrm{chrom}}$, with the dye absorption $\mu_{a,0}^{\mathrm{dye}}$ not being included. Setting $\mu_{\mathrm{t}} = \mu_{\mathrm{a},0}^{\mathrm{chrom}} + \mu_{\mathrm{s}}'$ three

Table 5.2: Constituents and corresponding concentrations for three numerical breast phantoms. The breast tissue has an attenuation coefficient of $k = \sqrt{3\mu_{\mathrm{a},0}^{\mathrm{chrom}}\mu_{\mathrm{t}}}$ at the laser wavelength (730 nm), without the absorption contribution $\mu_{\mathrm{a},0}^{\mathrm{dye}}$ of the fluorescent dye included.

Slab	$d = 6$ cm	$d = 7$ cm	$d = 9$ cm
Cup	80B	80D	80F
H_2O	60 %	47 %	47 %
HbR	$8 \cdot 10^{-6}$ M	$5 \cdot 10^{-6}$ M	$3 \cdot 10^{-6}$ M
HbO	$17 \cdot 10^{-6}$ M	$12 \cdot 10^{-6}$ M	$8 \cdot 10^{-6}$ M
dye	$2 \cdot 10^{-8}$ M	$2 \cdot 10^{-8}$ M	$2 \cdot 10^{-8}$ M
$\mu_{\mathrm{a},0}^{\mathrm{chrom}}$	0.0048 mm^{-1}	0.0033 mm^{-1}	0.0024 mm^{-1}
$\mu_{\mathrm{a},0}^{\mathrm{dye}}$	0.0004 mm^{-1}	0.0004 mm^{-1}	0.0004 mm^{-1}
a	1.62 mm^{-1}	0.95 mm^{-1}	1.59 mm^{-1}
b	0.68	0.68	0.67
μ_{s}'	2.01 mm^{-1}	1.18 mm^{-1}	1.96 mm^{-1}
k	170 m^{-1}	108 m^{-1}	120 m^{-1}

different values for the light attenuation $k = \sqrt{3\mu_{\mathrm{a},0}^{\mathrm{chrom}}\mu_{\mathrm{t}}}$ were selected for the phantom ranging from extremely dense ($k = 170$ m^{-1}) small breasts to medium dense ($k = 120$ m^{-1}) large breasts. The optical properties of the phantoms were defined by first selecting realistic values for blood and water content in tissue, subsequently the scattering amplitude and scattering power were fine-tuned to match the desired k-value. In each case, the fluorescent dye concentration amounted to 20 nM in the homogeneous part outside the lesion simulating heterogeneity.

Inside the numerical breast the single spherical heterogeneity is embedded assuming various diameters ($d = 5$ mm, 7.5 mm, 10 mm, 12.5 mm, and 15 mm). For each lesion, we chose a reduced water fraction but increased HbR and HbO concentrations, compared to surrounding breast tissue, i.e. 0.8 times the breast's concentration of H_2O, and twice the breast's concentration of HbR and HbO [13, 12]. The scattering amplitude of the lesion is increased by 20%, while the scattering power is decreased by 20% [13]. However, more recent spectroscopic measurements on 58 malignant breast tumors [9] indicate that on average HbR, HbO concentrations, and water percentage are increased by a factor of about 1.4.

The dye concentration contrast of the lesion was chosen to be 5 : 1. Table 5.2.2 lists HbR, HbO, Omocyanine concentrations, and H_2O percentage for the background tissue, Table 5.3 for the lesions of our numerical phantoms. The tissue optical properties of the three different breast types chosen fall within a realistic range as reported in [146]. In each case fluorescence quantum efficiency η was set to 0.1.

To calculate the detection limits of the two systems at various lesion positions $(x_{\mathrm{l}}, y_{\mathrm{l}}, z_{\mathrm{l}})$ inside the slab and cup, five lesions of various diameters were assumed at selected positions inside the breast. For the cup phantom, the lesions were confined in the yz plane of the cup changing their positions at a step size of 10 mm. For the slab phantom a detailed explanation of the selected lesion positions is given in appendix A.4.1.

The scattering liquid without any fluorescent dye added and used to fill the remaining space of the slab outside the breast has optical properties of $\mu_{\mathrm{a}} = 0.0033$ mm^{-1} and $\mu_{\mathrm{s}}' = 1.3$ mm^{-1}. Due to the

Table 5.3: Optical properties of simulated spherical lesions for the three phantoms of Table 5.2.2. Compared with breast tissue, the lesions have a reduced amount of H_2O, and doubled concentrations of HbR and HbO.

Slab	$d = 6$ cm	$d = 7$ cm	$d = 9$ cm
Cup	80B	80D	80F
H_2O	48 %	37.6 %	37.6 %
HbR	$16 \cdot 10^{-6}$ M	$10 \cdot 10^{-6}$ M	$6 \cdot 10^{-6}$ M
HbO	$34 \cdot 10^{-6}$ M	$24 \cdot 10^{-6}$ M	$16 \cdot 10^{-6}$ M
dye	10^{-7} M	10^{-7} M	10^{-7} M
a	1.94 mm^{-1}	1.14 mm^{-1}	1.91 mm^{-1}
b	0.57	0.57	0.56

compression of the breast by the slab mammograph, the sources couple light directly into the tissue at most positions, scattering fluid near a source position is only present at the tip of the breast.

Detector setup and scan head geometry

In order to investigate the effect of geometry on detection sensitivity, the same sources (lasers) and photodetectors (diodes) were used in each case. The relative and absolute noise of the detectors is discussed in detail in [145].

In the slab setup considered, two sources scan in tandem (on-axis arrangement) across an area of (8×9) cm^2 on both sides of the compression unit at increments of 2.5 mm, and each scan head carries a detector plate besides the source. Scanning covers an area of (18×13) cm^2 (from $x = -9$ cm to $x = 9$ cm, and from $y = 0$ cm to $y = 13$ cm) due to the ± 5 cm maximal offset in x and $+4$ cm maximal offset in y direction between sources and detectors. Due to the number of source positions that are sampled by each scan head, the slab and cup systems have a comparable number of total source-detector combinations. A detailed description of the detector positions can be found in appendix A.4.2.

Smallest detectable lesion size for slab and cup geometry

In Figure 5.19 (top) the baseline signal strengths associated with different source-detector combinations of the slab geometry are plotted versus the corresponding source-detector distances. Noise-free simulated data are integrated into this figure for the three homogeneous breast phantoms with $d = 6$ cm (circles), 7 cm (squares), and 9 cm (triangles) with the lesion simulating heterogeneity removed and with the scattering liquid added to fill the remaining slab volume. The laser light had an intensity incident on the surface of the phantom of about 5 W/cm^2 at a dwell-time of 100 ms, which was below but close to the regulatory limit[2]. All simulated data have been converted to absolute units (fA) as explained in [145].

In Fig. 5.19 absorption data are represented by open symbols, whereas filled symbols correspond to fluorescence data. Absorption signal strengths for a particular source-detector combination j corresponds to the density of transmitted laser photons $\Phi_{\mathrm{B},j}$ through the homogeneous breast model, being proportional to the current at the particular photodiode detector. Likewise, fluorescence signal strength corresponds to the density of transmitted fluorescence photons $\Phi_{\mathrm{f,B},j}$ through the homogeneous breast phantom. The dotted horizontal line represents the absolute noise floor $n_{\mathrm{a}} = 5.4$ fA.

[2]European Standard EN 60825-1 Safety of laser products Part 1, *Equipment classification, requirements and user's guide*, March 1994.

For absorption scans, all simulated data are above the absolute noise level by several orders of magnitude, but for fluorescence scans some off-axis data at large source-detector distances are below the absolute noise level. Due to the high attenuation coefficient of $k = 170\ \mathrm{m}^{-1}$ of the $d = 6$ cm slab phantom, some data corresponding to low signal strengths reach the absolute noise level even at smaller source-detector distances. In Fig. 5.19 (right), the three symbols (circle, square, and triangle) correspond to the 80B, 80D, and 80F cup, respectively. Fig. 5.19 shows the large dynamic range of absorption and fluorescence signals of the cup geometry compared with the slab geometry.

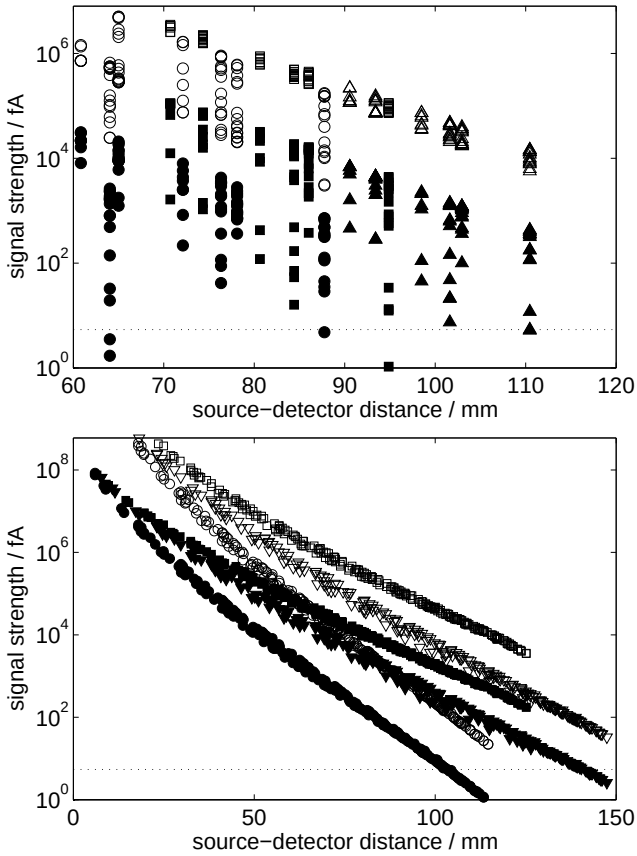

Figure 5.19: Noise-free signal strength for slab (left) and cup (right) geometry calculated from three homogeneous numerical breast phantoms, $d = 6$ cm/80B cup (circles), 7 cm/80D cup (squares), and 9 cm/80F cup (triangles) with (top) and without (bottom) additional scattering fluid. Open symbols represent simulated absorption data, filled symbols correspond to simulated fluorescence data. The horizontal dotted line indicates the absolute noise level.

The parameters of the noise model are chosen according to the photodiode detectors with large dynamic range used in the existing cup system. Accordingly, the absolute noise was set to $n_\mathrm{a} = 5.4$ fA. This value was deduced from a reference scan with the existing cup mammograph using the scattering fluid only and 100 ms integration time.

Lesion detection limits corresponding to absorption and fluorescence measurements were obtained from the raw data analysis. Forward model calculations for all 6 phantoms (three slab thicknesses and three cup sizes) were performed using the background and lesion optical properties given in Table 5.2.2

and 5.3, respectively. Subsequently, noise was added to the simulated data, using $N = 100$ realizations of noise throughout this study.

The results on detection sensitivity are shown in Fig. 5.20 for the slab for an assumed relative noise level of $n_r = 1\%$. Detection limits are given for $d = 6$ cm (left), 7 cm (middle), and 9 cm (right) thicknesses of absorption (top) and fluorescence (bottom) scans. The gray scale level of each square represents the minimal detectable lesion diameter at this position. A black square indicates that none of the lesions considered can be detected. The solid line shows the outer contour of the simulated breast and the black dots are the source positions of the two scan heads in the $x = 0$ slice. The detection limit is quite homogeneous along the z-direction throughout the entire breast phantom. However, the detection limit (lesion diameter) increases at the breast tip (e.g. $d = 6$ cm, absorption) due to the presence of the additional scattering fluid, and near the chest wall (e.g $d = 9$ cm, fluorescence) due to the scan head geometry and the undersampling of this breast area. A lesion of 7.5 mm diameter is detectable at the center of the breast in all six cases. At $d = 6$ cm even a lesion of 5 mm diameter is detectable at the center position in an absorption scan. The slab system allows to detect lesions that are located closer to the breast wall by 1 cm than the closest source position sampled.

Results on detection sensitivity for the cup geometry at a relative noise level of $n_r = 1\%$ and an absolute noise of $n_a = 5.4$ fA are presented in Fig. 5.21 with the same arrangement of panels with respect to breast type, absorption, and fluorescence data as in Fig. 5.20 and using the same gray level scale. Due to the larger distances between sources and detectors, the noise floor affects detection sensitivity more strongly, especially for low intensity fluorescence measurements. Therefore, only large lesions can be detected in the case of a dense breast or a large breast.

Dependence of detection limits on noise

In this section we investigate how relative and absolute noise contributions influence detection limits in slab geometry. For this purpose, we compare simulations with different noise settings, varying both the absolute and relative noise.

Sensitivity calculations were performed at four different settings of relative noise ($n_r = 1\%, 0.5\%, 0.1\%$, and 0%) and two settings of absolute noise ($n_a = 5.4$ fA, 0.54 fA). This approach allows us to determine the maximal detector noise that can be tolerated to reach a given detection limit at the center of the slab. A relative noise of 0.1% can be achieved in practice, when laser and fluorescence photons are detected simultaneously avoiding sequential scans at both wavelengths.

In Fig. 5.22 we show how relative noise affects the detection of a 5 mm diameter lesion keeping the absolute noise fixed at $n_a = 5.4$ fA. Each square shows the maximal relative noise level that still allows to detect of the lesion at this position. A black square indicates that even without any relative noise ($n_r = 0$) the lesion can not be seen because of the absolute noise floor. The results are given for absorption (top row) and fluorescence (bottom row) scans for the phantoms $d = 6$ cm, $d = 7$ cm, and $d = 9$ cm (left, middle, and right column).

The different gray scale levels of the squares show that a relative noise level between 0 and 1% is needed to detect the 5 mm diameter lesion. A relative noise of 0.5% would be sufficient to detect this lesion in most of the breast volume for the three given absorption scans.

At a relative noise of 0.1% the 5 mm diameter lesion can be detected within the entire bulk in absorption and fluorescence scans. Apart from the fluorescence scan of the $d = 9$ cm phantom this lesion can be detected even 1 cm closer to the chest wall than the closest source position sampled.

It seems unnecessary to reach relative noise levels below 0.1%. Such improvement would only allow to additionally detect a lesion close to the chest wall of the $d = 9$ cm case. Everywhere else, a relative noise level of 0.1% seems adequate for a detection of 5 mm diameter lesions.

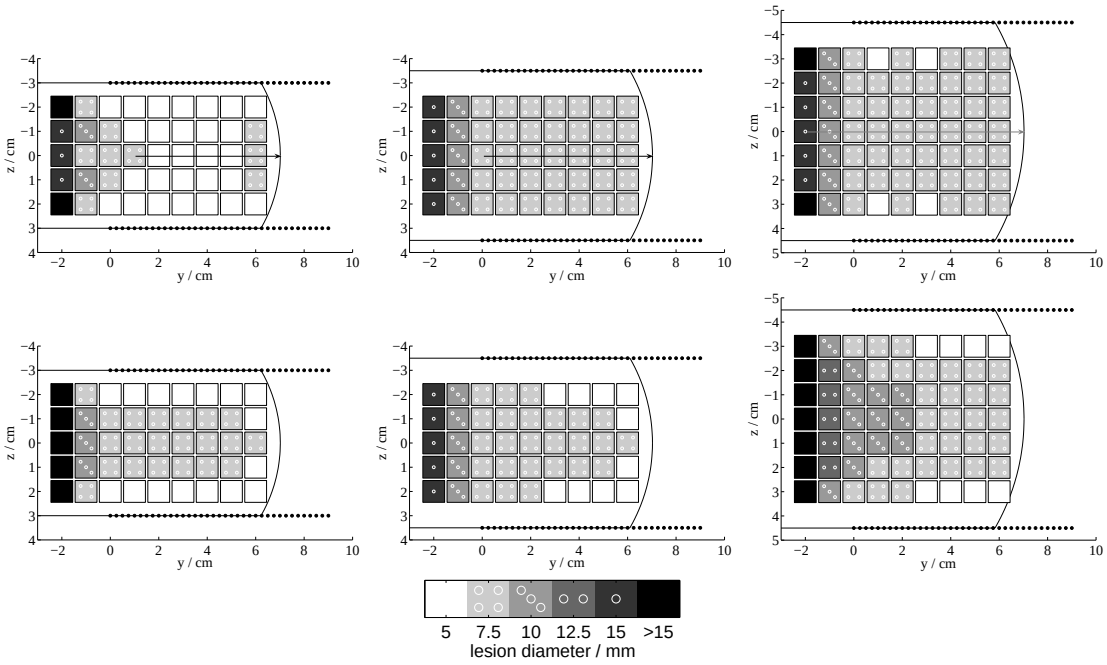

Figure 5.20: Detection limits (diameter of spherical lesion) deduced from the χ^2 test and an assumed 80% lesion detectability limit [145] of absorption (top) and fluorescence (bottom) scans for $n_\mathrm{r} = 1\%$ relative noise, and $n_\mathrm{a} = 5.4$ fA absolute noise. Results are given for $d = 6$ cm, $d = 7$ cm, and $d = 9$ cm slab thickness (left, middle, and right column) with background and lesion optical properties listed in Tables 5.2.2 and 5.3, respectively. The gray scale value of each square represents the minimal lesion diameter that can be detected at the given lesion position. Black means that none of the considered lesions could be detected. The black dots indicate the source positions in the $x = 0$ slice on both compression plates. The radius vector of the spherical calotte simulating the breast tip is included for easy comparison with Fig. A.4 illustrating the geometry of the breast phantoms.

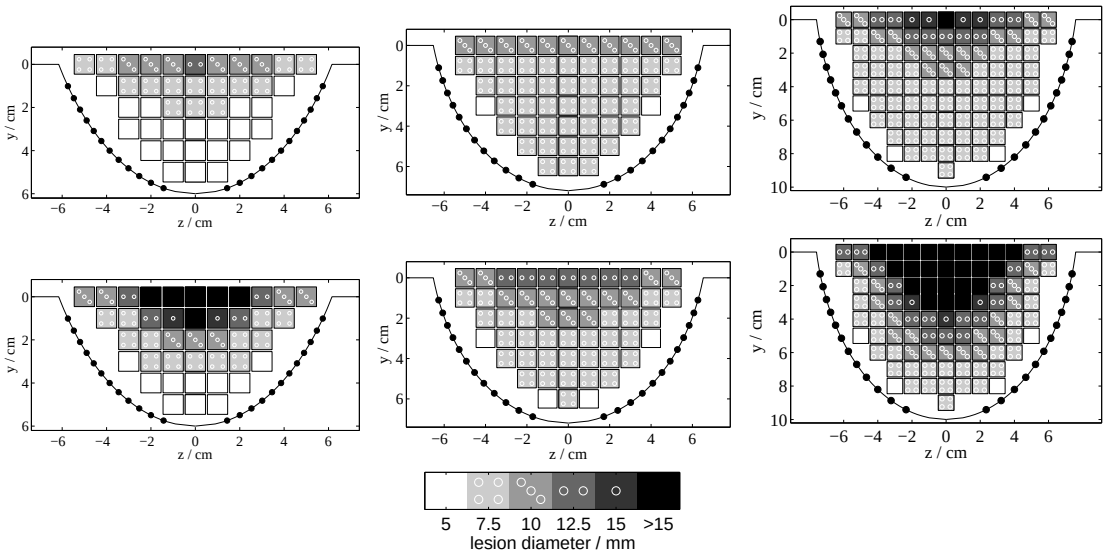

Figure 5.21: Detection limits of the cup system for absorption (top) and fluorescence (bottom) scans deduced from the χ^2 test and a 80% detectability of the lesions for $n_\mathrm{r} = 1\%$ relative noise and $n_\mathrm{a} = 5.4$ fA absolute noise. Results are given for the 80B, 80D, and 80F cup (left, middle, and right column). The gray scale value of each square represents the minimum lesion diameter that can be detected at the given lesion position. Black means that none of the considered lesions could be detected. The black dots indicate the source positions on the cup surface in the $x = 0$ slice.

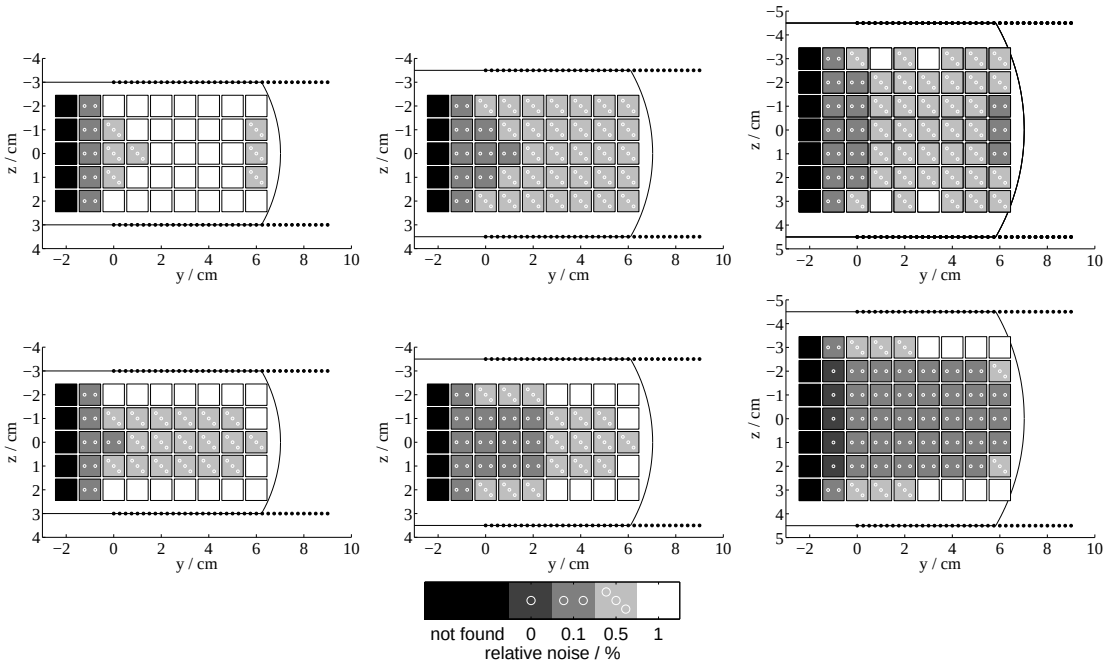

Figure 5.22: Relative noise limits for the detection of a 5 mm diameter lesion in absorption (top) and fluorescence (bottom) scans deduced from the χ^2 test for a 80% detectability of the lesion ($x = 0$ slices). Black indicates that the lesion can not be detected due to the absolute noise floor of $n_\mathrm{a} = 5.4$ fA.

Dependence on compression for slab geometry

To investigate the effect of compression on lesion detection sensitivity, we simulated a compressed breast with reduced breast thicknesses using the optical properties of the 80B case (see Tab. 5.2.2 and 5.3), i.e. assuming an attenuation $k = 170$ m^{-1}.

The slab thickness was varied from $d = 9$ cm to $d = 3$ cm in increments of 0.5 cm. The entire geometry including source and detector positions, lesion position and diameters, and the FE grid were kept the same for all thicknesses, i.e. the geometry was not scaled down to the reduced slab thickness; instead, both rim areas overlapping the scanning surface were clipped, to produce the desired thickness.

It was assumed that the optical properties were identical for all thicknesses, which is a rather crude approximation since breast compression will influence blood flow, at least at high pressures.

The sources scanned the same area as described previously for the $d = 6$ cm case. To reduce computational efforts, lesions of various diameters were assumed at one position only ($x_\mathrm{l} = z_\mathrm{l} = 0$, $y_\mathrm{l} = 3$ cm), i.e. close to the center of the slab. Simulations were carried out for diameters of 3 mm, 3.5 mm, 4 mm, 4.5 mm, 5 mm, 7.5 mm, 10 mm, 12.5 mm, and 15 mm. For diameters below 10 mm, the FE grid was additionally refined at the lesion position when simulating absorption and fluorescence scans for a homogeneous breast, a breast with the lesion in place, and the reference scan.

For an optically dense breast with $k = 170$ m^{-1} it is expected that compression will dramatically improve detection sensitivity, because the average length of the photon trajectories through the tissue dominates sensitivity. This can be seen by plotting the lesion signal over lesion size and slab thickness. The effect of compression on lesion signal and hence lesion detectability was simulated and results are illustrated in Fig. 5.23 and Fig. 5.24.

Fig. 5.23 shows the largest signal change due to the presence of the lesion at the position assumed above, i.e. the relative lesion fluorescence signal

$$L^\mathrm{f} = \max_j \left(\frac{S_j^\mathrm{f} - R_j^\mathrm{f}}{R_j^\mathrm{f}} \right), \tag{5.99}$$

for the simulated parameter space (breast thickness from 3 cm to 9 cm in increments of 0.5 cm, lesion diameter from 3 mm to 1.5 cm). Here, $S_j^\mathrm{f} = \Phi_{\mathrm{f,L},j}/\Phi_{\mathrm{L},j}$ is the ratio of densities of transmitted fluorescence photons, and transmitted laser photons with the lesion in place and $R_j^\mathrm{f} = \Phi_{\mathrm{f,B},j}/\Phi_{\mathrm{B},j}$ the corresponding ratio with the heterogeneity removed. The subscript j denotes a particular source-detector combination. A motivation and detailed discussion of these parameters can be found in [145].

As can be seen in Fig. 5.23, the relative lesion fluorescence signal decreases from more than 20% to below 0.5% by varying breast thickness and lesion diameter within the limits given above.

For a lesion diameter of 5 mm the relative lesion fluorescence signal is below 5% ($k = 170$ m^{-1}) at all thicknesses ($d \geq 3$ cm) and even below 0.5% at breast thicknesses exceeding 7 cm. Therefore, it can be anticipated that the total noise on the data must be below 0.5% when a 5 mm diameter lesion is to be detected. Support for this simple scaling approach to give correct estimates for noise requirements is provided by the following results of detailed simulations.

In Fig. 5.24 we present detection limits for various selected relative and absolute noise parameters for a lesion at the center position. The two images correspond to different absolute noise floors of $n_\mathrm{a} = 5.4$ fA (top) and $n_\mathrm{a} = 0.54$ fA (bottom). For each of the two scenarios we calculated detection limits (lesion diameters) for different relative noise values ($n_\mathrm{r} = 1\%$, 0.5%, 0.1%, and 0%) and plotted the lesion detection limits for each of these four relative noise settings as a function of breast thickness. The gray scale coding indicates the relative noise level required for detection of the lesion of a particular diameter. A region associated with a certain gray level indicates how detection sensitivity changes with breast thickness at the center position. The region in pale gray means that a lesion can not be detected at all, due to the presence of the noise floor.

The detection limit suffers strongly from the absolute noise, for a slab thickness of 7 cm or larger. For such compressed breast thicknesses only large lesions with diameters of 1 cm or larger can be detected at the center position.

For a slab thickness of $d = 9$ cm signal attenuation becomes so strong that fluorescence detection of a lesion is hardly possible. At this thickness, lesions can only be detected with diameters of 1.4 cm at least. However, it should be kept in mind that the strong attenuation coefficient of $k = 170$ m^{-1} is generally associated with small breasts, whereas large breasts, yielding a thickness of 9 cm after gentle compression exhibit lower attenuation. Rather, the purpose of this section is to demonstrate the strong dependence of detection sensitivity on breast thickness.

Fig. 5.24 (bottom) shows the simulation results assuming an absolute noise floor one order of magnitude lower, i.e. $n_a = 0.54$ fA. Such a reduction of the noise floor can be achieved by using e.g. photomultipliers instead of photodiodes, and the associated gain in detection sensitivity can be seen by comparing Fig. 5.24 top and bottom. For the lower absolute noise floor the region indicating undetectable lesions has shrunk considerably. Fig. 5.24 bottom also shows that little can be gained in detection sensitivity by reducing the relative noise below the 0.1% level.

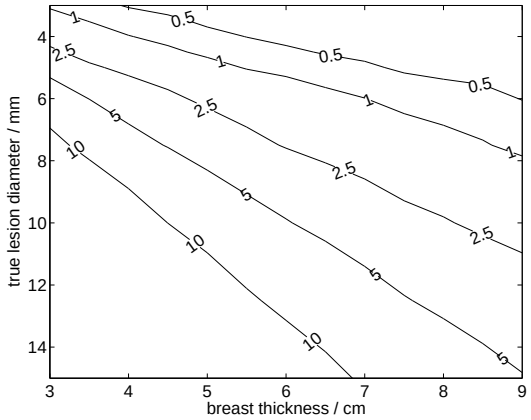

Figure 5.23: Relative lesion fluorescence signal L^f (in %) depending on true lesion diameter and breast thickness ($k = 170$ m^{-1}).

Detection sensitivity and dye contrast for slab geometry

One important parameter for fluorescence enhanced optical mammography is the fluorescent dye contrast. While specific tumor targeting dyes are expected to achieve highest concentration contrast, such dyes are presently not available for clinical use. Rather, unspecific fluorescent dyes exploiting the enhanced vascular permeability of tumors are likely to become available first. Concentration contrast between tumor and surrounding tissue are expected to be in the range of 2:1 to 5:1 for such dyes. In this section we investigate to what extent lesion detection sensitivity improves with concentration contrast. For this purpose we calculated lesion detection sensitivity for an optically dense breast ($k = 170$ m^{-1}, $d = 6$ cm) assuming various lesion diameters (3 mm, 3.5 mm, 4 mm, 4.5 mm, 5 mm, 7.5 mm, 10 mm, 12.5 mm, and 15 mm) and dye contrasts of 1.5:1 to 5:1 at increments of 0.5 with the lesion located at the position $x_l = z_l = 0$, $y_l = 3$ cm and assume a fluorescence quantum efficiency of the dye of $\eta = 0.1$. Again, the FE grid was refined at the lesion position for lesion diameters below 10 mm when performing simulations of absorption and fluorescence scans with and without the lesion being present and for the reference scan.

In Fig. 5.25 (top) we plot the relative lesion fluorescence signal L^f as defined in Eq. (5.99) versus the

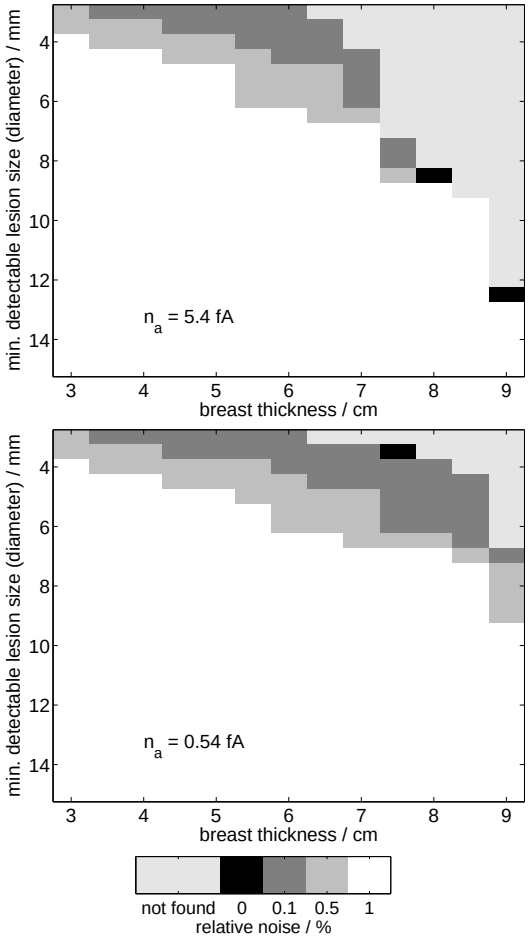

Figure 5.24: Lesion detection limits (lesion diameter) versus thickness of compressed breast for various relative and absolute (n_a) noise levels. A white area indicates a lesion of corresponding diameter can be detected at the 1% relative noise level in a compressed breast with associated breast thickness ($k = 170\ \mathrm{m}^{-1}$). The different gray scale areas indicate that the lesion can be detected at the corresponding or lower relative noise. The pale gray area shows that no lesion can be detected due to the presence of the absolute noise floor.

true lesion diameter and the breast thickness. L^{f} varies between 10% and slightly below 0.1% in the entire sampled parameter space. For the concentration contrast of 2:1, a lesion of 5 mm diameter positioned at the center produces a signal being at most 0.1% larger than the background. It follows that the noise on the signal must be below this threshold if the lesion is to be detected.

The plot in Fig. 5.25 (bottom) shows the detection sensitivity (lesion diameter) assuming an absolute noise floor $n_{\mathrm{a}} = 5.4$ fA. The diagram shows the detectability for four settings of relative noise ($n_{\mathrm{r}} = 1\%$, $n_{\mathrm{r}} = 0.5\%$, $n_{\mathrm{r}} = 0.1\%$, and $n_{\mathrm{r}} = 0\%$) encoded by the gray scale values. A pale gray colored region indicates that no lesions can be detected, not even in the absence of relative noise because of presence of the absolute noise floor.

The graph shows how strongly the detection sensitivity limit depends on concentration contrast. A contrast of at least 2.5:1 is required to detect a 5 mm diameter lesion at the center position ($d = 6$ cm). Surprisingly, higher concentration contrasts will only moderately improve lesion detection limits, provided relative noise can be kept at the 0.1% level.

Conclusions

We numerically investigated the detection of a single scattering, absorbing and fluorescent (spherical) heterogeneity simulating a breast bearing a tumor after administration of a fluorescent dye as unspecific contrast agent. The lesion is embedded in an otherwise homogeneous background medium of similar scattering and absorption properties, but lower concentration of the fluorescent dye. Three different numerical breast phantoms corresponding to a small strongly attenuating breast, a medium size (small attenuation), and a large (average attenuation) breast were used in our study, simulating densities of transmitted laser and fluorescence photons for two different source-detector geometries, i.e. a cup-based tomographic mammograph (cup-geometry) and a scanning mammograph, where the breast is gently compressed between two parallel plates (slab geometry).

Lesion detection sensitivity, expressed by the diameter of the smallest spherical heterogeneity that can be detected in absorption and fluorescence scans, was derived from simulated data with noise added taken from a realistic noise model, applying a chi-square test (null hypothesis). Lesion detection sensitivity was determined for the three different breast models and for both (cup, slab) geometries, systematically varying the position of the lesion within the breast volume. For the slab geometry, lesion detection sensitivity was additionally explored changing relative as well as absolute noise contributions. Because of the smaller thickness of the compressed breast, lesion detection sensitivity of the slab geometry depends on relative noise contributions, the noise floor plays a minor role only due to the higher transmitted laser and fluorescence intensities. In contrast, because of the larger source-detector separations sampled by the tomographic mammograph and hence lower transmitted intensities, lesion detection sensitivity is limited in this case by the absolute noise.

Lesion detection sensitivity is fairly homogeneous throughout the slab volume. Except for large thicknesses of the compressed breast, the detection sensitivity drops slightly towards the mammilla due to the presence of the scattering liquid used to fill the remaining slab volume not covered by the breast. We systematically investigated how detection of a lesion at the center of the breast improves with increased compression. A 5 mm diameter lesion is the required detection limit for an optical mammograph to be competitive with existing modalities. At a relative noise level of 0.1% a 5 mm diameter lesion can be detected in almost the entire volume of the compressed breast at the absorption contrast (2:1) and fluorescent dye concentration contrast (5:1) assumed for the three different breast models. In slab geometry lesions can be detected being closer to the breast wall by up to 1 cm compared to the closest source or detector position.

A dye concentration contrast below 2.5:1 does not allow to detect a 5 mm diameter lesion at the center of a small dense ($k = 170$ m^{-1}) compressed breast ($d = 6$ cm) in fluorescence scans. Concentration contrasts above this level are needed to detect a lesion of this size. The increase in lesion detection sensitivity is rather limited at higher concentration contrasts, provided the relative noise can be maintained at the

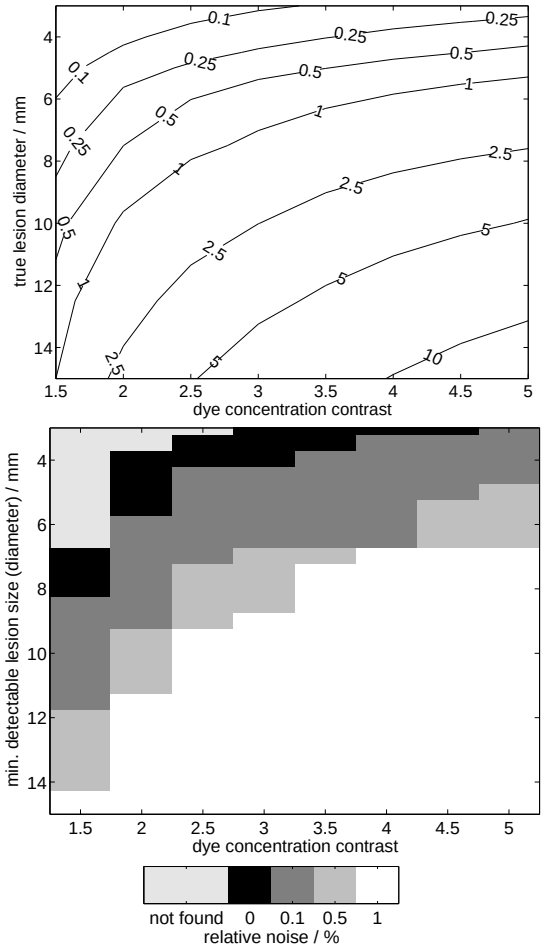

Figure 5.25: Relative lesion fluorescence signal L^{f} (in %) depending on fluorescent dye concentration contrast and true lesion diameter (top). Detection limits (lesion diameter) versus fluorescent dye concentration contrast (bottom) for various relative noise levels at fixed absolute noise floor ($n_{\mathrm{a}} = 5.4$ fA). A white region indicates that lesions with corresponding diameters and concentration contrast can be detected at a relative noise of $n_{\mathrm{r}} = 1\%$ or better. The same holds true for regions with other grayscale values indicating the corresponding relative noise level. The region in pale gray shows, that no lesion can be detected due to the presence of the absolute noise floor.

0.1% level.

All lesion detection sensitivities reported in this section refer to a homogeneous background on which the absorbing and fluorescent lesion is to be detected. In case this background has some structure in itself, relative and absolute noise may no longer represent the dominant limitations rather than the spatial variations of the background signals.

Chapter 6

Reconstruction algorithms and methods

Due to the many scattering events of NIR light in (breast) tissue, reconstruction for diffuse optical tomography is a challenging task. As NIR light does not travel from the source to the detector directly (like in X-ray imaging), we are not only sensitive to the optical properties on the line of sight between source and detector, but instead probe an extended volume. Detection sensitivity of DOT is not constant throughout the investigated tissue, but instead is higher close to source and detector positions, increasing the complexity of reconstructions even further and the probability of artefacts in the reconstruction images at these positions.

Several reconstruction methods have been adapted to diffuse optical tomography like tomosynthesis, which has the advantage of being a fast and robust reconstruction method but is limited to planar geometries. Additionally, (CT-like) Radon transformation based reconstructions have been carried out, neglecting the scattering of light inside the tissue sampled [147, 148], but results from patient data seem to be inconclusive. As a promising new method, shape function reconstruction for optical mammography is still under development [149, 150, 151] but until now has not been used with clinical data. Furthermore, computationally intensive RTE based reconstructions [152] and hybrid reconstructions combining both, the RTE and the diffusion equation [106, 107], were applied to clinical data mainly to volumes containing void or non-scattering regions (e.g. optical imaging of the brain), i.e. volumes, where the diffusion approximation is not longer valid everywhere.

Considerable progress has been made over the last years adding anatomic prior knowledge (spatial priors) from other modalities (e.g. MRI) to the DOT reconstruction [81, 82]. Although being promising, such reconstructions will not be discussed here, for a multimodal approach was not aim of this thesis. Instead, we perform reconstructions based on forward model calculations of the diffusion approximation carried out on an FE grid, as was proposed in [28, 153, 29, 115]. Reconstructions of absorption and scattering coefficients are carried out iteratively (nonlinearly) in two alternating steps:

i) Data for all source-detector combinations is simulated for assumed spatial distributions of absorption and diffusion coefficients using the diffusion equation. At the first iteration step, data is simulated assuming homogeneous optical properties, i.e. due to the lack of prior information we assume optical properties corresponding to the scattering liquid used in the reference scan for the breast tissue as start value. In subsequent iterations, the estimate of the optical properties is based on the last reconstruction result.

ii) By using a perturbative approach (Rytov approximation [142]) deviations between simulated and measured data are used to update the optical properties that have been assumed in the forward

model simulations. These improved optical properties are the reconstructed images of absorption and scattering coefficients.

Forward model simulations and reconstruction steps are iterated until convergence of the reconstructed optical properties is reached.

Simultaneous reconstruction of absorption and reduced scattering coefficients can be achieved from time-resolved or frequency domain measurements only, but not from cw measurements taken at a single wavelength. Nonetheless, such separation of $\mu_a(\boldsymbol{x}, \lambda)$ and $\mu_s'(\boldsymbol{x}, \lambda)$ is crucial for a quantitative determination of optical properties. Therefore, prior to reconstructions based on cw measurements, averaged optical properties of breast tissue are calculated from multi-wavelength cw measurements performed with the Philips tomographic fluorescence mammograph using a spectral model. The feasibility of such spectral fit of optical properties in the presence of a scattering fluid is shown by numerical phantoms and by determining optical properties of breast tissue of patients that attended a clinical study. Subsequently, the fitted averaged optical properties of a patient's breasts were used to initialize the nonlinear reconstructions of clinical data, showing improvements in reconstructed images over the results obtained assuming general optical properties of breast tissue.

For fluorescence reconstruction, i.e. the reconstruction of the concentration of an exogenous fluorescent dye serving as contrast agent, the (linear) Born approximation is used, which is equivalent to the Rytov approximation in first order. Hence, fluorescence reconstructions are carried out analogously but non-iteratively. For simplification of numerical calculations, the fluorescence emission was modeled at a single wavelength throughout this thesis, not taking the emission spectrum of a fluorescent dye into account. Furthermore, although reabsorption of fluorescent photons by the fluorophore are taken into account, the emission of fluorescence being proportional to η^2 is neglected.

6.1 Theoretical background

6.1.1 Linear reconstruction based on Rytov and normalized Born approximation

We motivate the Rytov (laser radiation) and normalized Born (fluorescence radiation) approximations for solving the frequency domain diffusion equation with spatially varying optical properties. The sensitivity factors that weight the influence of local changes in the absorption and diffusion coefficient and of the concentration of a fluorescent dye on transmitted photon densities are introduced and absorption sensitivity factors for a homogeneous medium are illustrated. The derivation of the Rytov and normalized Born approximations from the diffusion equation is given in appendix C.2.1.

The reconstruction of absorption and scattering coefficients is based on the Rytov approximation. This approximation describes how ratio of the photon density transmitted through the breast partially filling the measurement chamber (cup) to the photon density recorded when the cup is filled with the reference (scattering) liquid is related to changes (differences) $\delta\mu_a$ in the absorption coefficient and to changes δD in the diffusion coefficient with respect to the reference values. More explicitly, denoting the laser photon density transmitted through the breast and through the reference liquid as $\Phi(\boldsymbol{x}_{d_i}, \boldsymbol{x}_{s_i}, \lambda, \omega)$

and $\Phi_0(\boldsymbol{x}_{d_i}, \boldsymbol{x}_{s_i}, \lambda, \omega)$, respectively, the Rytov approximation reads [142]

$$\begin{aligned}\ln\left(\frac{\Phi(\boldsymbol{x}_{d_i}, \boldsymbol{x}_{s_i}, \lambda, \omega)}{\Phi_0(\boldsymbol{x}_{d_i}, \boldsymbol{x}_{s_i}, \lambda, \omega)}\right) = &- v \int_\Omega \delta\mu_\mathrm{a}(\boldsymbol{x}, \lambda) \underbrace{\frac{G_0(\boldsymbol{x}_{d_i}, \boldsymbol{x}, \lambda, \omega) G_0(\boldsymbol{x}, \boldsymbol{x}_{s_i}, \lambda, \omega)}{G_0(\boldsymbol{x}_{d_i}, \boldsymbol{x}_{s_i}, \omega)}}_{a_i'(\boldsymbol{x}, \lambda, \omega)} d\Omega \\ &- v \int_\Omega \delta D(\boldsymbol{x}, \lambda) \underbrace{\frac{\nabla G_0(\boldsymbol{x}_{d_i}, \boldsymbol{x}, \lambda, \omega) \cdot \nabla G_0(\boldsymbol{x}, \boldsymbol{x}_{s_i}, \lambda, \omega)}{G_0(\boldsymbol{x}_{d_i}, \boldsymbol{x}_{s_i}, \lambda, \omega)}}_{\widehat{a}_i'(\boldsymbol{x}, \lambda, \omega)} d\Omega,\end{aligned} \tag{6.1}$$

where i denotes the particular source-detector combination. In first order (linear approximation) the propagation of light through the turbid medium is described by using homogeneous Green's functions $G_0(\boldsymbol{x}, \boldsymbol{x}', \omega, \lambda)$, which are the pulse response functions[1] (fundamental solutions) of the diffusion equation (5.11), i.e. these functions describe the propagation of light though a medium having a homogeneous absorption and diffusion coefficient for a δ-like source located at $\boldsymbol{x}'$. Therefore, the first integral kernel $a_i'(\boldsymbol{x}, \lambda, \omega)$ in Eq. (6.1) can be interpreted as corresponding to the probability that light travels from the source position $\boldsymbol{x}_{s_i}$ to position $\boldsymbol{x}$, where it is attenuated by the perturbation of the absorption coefficient $\delta\mu_\mathrm{a}(\boldsymbol{x}, \lambda)$, before it reaches the detector at position $\boldsymbol{x}_{d_i}$. In other words, the integration kernel $a_i'(\boldsymbol{x}, \lambda, \omega)$ weights the effect that a change $\delta\mu_\mathrm{a}(\boldsymbol{x}, \lambda)$ in the absorption coefficient at position $\boldsymbol{x}$ has on the (normalized) difference $(\Phi(\boldsymbol{x}_{d_i}, \boldsymbol{x}_{s_i}, \lambda, \omega) - \Phi_0(\boldsymbol{x}_{d_i}, \boldsymbol{x}_{s_i}, \lambda, \omega))/\Phi_0(\boldsymbol{x}_{d_i}, \boldsymbol{x}_{s_i}, \lambda, \omega) \approx \ln\{\Phi(\boldsymbol{x}_{d_i}, \boldsymbol{x}_{s_i}, \lambda, \omega)/\Phi_0(\boldsymbol{x}_{d_i}, \boldsymbol{x}_{s_i}, \lambda, \omega)\}$. An analogous interpretation can be given for the second integration kernel $\widehat{a}_i'(\boldsymbol{x}, \lambda, \omega)$, weighting the effect of changes $\delta D(\boldsymbol{x}, \lambda)$ in the diffusion coefficient at position $\boldsymbol{x}$ on this normalized difference. Since diffusion is driven by gradients, the second kernel $\widehat{a}_i'(\boldsymbol{x}, \lambda, \omega)$ involves gradients of the (homogeneous) Green's functions.

Strictly speaking, the light traveling from source at $\boldsymbol{x}_{s_i}$ to the detector at $\boldsymbol{x}_{d_i}$ samples the entire volume Ω as can be seen from the volume integrals of Eq. (6.1). However, the norm of the weighting factors (sensitivity factors) $a_i'(\boldsymbol{x}, \lambda, \omega)$ and $\widehat{a}_i'(\boldsymbol{x}, \lambda, \omega)$ are larger than a chosen cut-off value within a restricted volume only, defining a "sensitivity volume" essentially sampled by the photons. For illustration, Fig. 6.1 shows the kernel $a'(x, y = 0, z, \omega = 0)$ for a homogeneous slab (top row) for zero source-detector offset (left) $\boldsymbol{x}_\mathrm{s} = (0, 0, 0)$, $\boldsymbol{x}_\mathrm{d} = (0, 0, 6\ \mathrm{cm})$ and for a source-detector offset of 5 cm $\boldsymbol{x}_\mathrm{d} = (5\ \mathrm{cm}, 0, 6\ \mathrm{cm})$. The weighting factors $a'(x, y = 0, z, \omega = 0)$ are normalized to the value at the corresponding center position, i.e. on the center line from the source to the detector at the particular depth z. The two panels in the bottom row show the kernels $a'(x, y = 0, z, \omega = 0)$ in the presence of a spherical pure absorber (absorption contrast 5:1) that have been calculated using exact Green's functions rather than those of the homogeneous medium. As can be seen from Fig. 6.1, the shape of the sensitivity volume depends (banana shapes [154]) on the location of the source $\boldsymbol{x}_\mathrm{s}$ and the detector $\boldsymbol{x}_\mathrm{d}$, and the sensitivity factors are strongly affected by the presence of the absorber.

To reconstruct optical properties, $\delta\mu_\mathrm{a}(\boldsymbol{x}, \lambda)$ and $\delta D(\boldsymbol{x}, \lambda)$ have to be calculated by inversion of the integral equation Eq. (6.1). For this purpose, the integral equations for all source-detector combinations i are discretized on a grid and the resulting system of linear equations is written as a matrix equation, whereby optical properties at each grid vertex can be in principle calculated by a matrix inversion. To prevent numerical errors [155], care has to be taken in the selection of the FE grid. Throughout this thesis, the same grids were used for the forward model simulations and reconstructions.

Due to the dimension of the matrix describing the linear system of equations, an analytical inversion is not feasible, thus calculations can only be performed by an iterative method, e.g. using conjugate gradient [153, 156] (CG) or the algebraic reconstruction technique (ART) for inversion. While matrix inversions by CG in general need fewer iteration steps for convergence, this method has a higher memory demand and needs longer times for calculations at each iteration step. It was shown in research related to this thesis that the residuum of simulated and measured data converges more slowly when using an ART

[1] Green's functions obey the symmetry relation $G_0(\boldsymbol{x}, \boldsymbol{x}', \omega, \lambda) = G_0(\boldsymbol{x}', \boldsymbol{x}, \omega, \lambda)$.

inversion method compared with a CG inversion, but the properties reconstructed by ART can converge faster in certain scenarios [157].

The number of unknowns during reconstructions, i.e. the optical properties associated with each vertex of the reconstructed volume, is larger than the number of simulated or experimental data collected at the surface and the presence of noise results in an ill-posed and ill-conditioned problem. Furthermore, ill-posedness is caused by a strong overlap of the sensitivity volumes of neighboring source and detector positions. In addition, reconstruction of DOT suffers from nonuniqueness [158], for different distributions of optical properties inside the volume can result in the same transmitted photon densities at the positions sampled on the surface. Therefore, a Tikhonov regularization [159] has to be used during reconstructions, however, affecting the results. Above all, the reconstruction is based on a first order perturbation approach, being limited to small deviations in optical properties. This may be true for phantoms e.g. with homogeneous optical properties apart from a small heterogeneity with slightly changed absorption and diffusion coefficients. In contrast, breast tissue is rather heterogeneous and may have optical properties significantly different from the scattering liquid used in the reference experiment violating the prerequisite of perturbation theory. In this case, a homogeneous breast model with an estimated shape and fitted (average) tissue optical properties derived from multi-wavelength *in vivo* data is a better starting point and can bypass this limitation [160].

In order to apply the diffusion approximation, generally the (point) source is shifted into the tissue by by one reduced scattering length. Therefore, the maximum of the corresponding Green's function is located inside the tissue and not at its surface, as expected in the experimental situation. Consequently, the component of the gradient of the Green's function in beam direction changes sign at the (shifted) source location. Although still producing artifacts during the reconstruction, this problem can be meliorated partially by using Gaussian blurred or exponentially attenuated sources for the numerical calculation of Green's functions.

In the presence of a fluorescent dye of concentration $c(\boldsymbol{x})$, the ratio of the transmitted density of fluorescence photons $\Phi_\mathrm{f}(\boldsymbol{x}_{d_i}, \boldsymbol{x}_{s_i}, \lambda, \omega)$ at the detector position $\boldsymbol{x}_{d_i}$ to that of transmitted laser photons $\Phi(\boldsymbol{x}_{d_i}, \boldsymbol{x}_{s_i}, \lambda, \omega)$ is related to the dye concentration by the normalized Born approximation [139, 140],

$$\frac{\Phi_\mathrm{f}(\boldsymbol{x}_{d_i}, \boldsymbol{x}_{s_i}, \lambda, \omega)}{\Phi(\boldsymbol{x}_{d_i}, \boldsymbol{x}_{s_i}, \lambda, \omega)} = \frac{v\eta\epsilon^\mathrm{dye}(\lambda)\ln 10}{1 + i\omega\tau} \int_\Omega c(\boldsymbol{x}) \underbrace{\frac{G_0(\boldsymbol{x}_{d_i}, \boldsymbol{x}, \lambda_\mathrm{f}, \omega) G_0(\boldsymbol{x}, \boldsymbol{x}_{s_i}, \lambda, \omega)}{G_0(\boldsymbol{x}_{d_i}, \boldsymbol{x}_{s_i}, \lambda, \omega)}}_{a_i^{\mathrm{f}\prime}(\boldsymbol{x}, \lambda, \omega)} d\Omega, \tag{6.2}$$

where $\boldsymbol{x}_{s_i}$ is the position of the source of (laser) photons (see Sec. C.2.1).

6.1.2 Iterative nonlinear reconstruction of absorption and reduced scattering coefficients

An iterative scheme based on the linear Rytov and normalized Born approximations is described to nonlinearly reconstruct absorption and reduced scattering coefficients. The change of the nonlinearly computed sensitivity factors due to the presence of a pure absorber over the first order result is shown. Linear and nonlinear reconstructions of the absorption and reduced scattering coefficients from simulated noise-free data of a 2D phantom with two heterogeneities are illustrated and compared.

Modeling the propagation of light in Eq. (6.1) by homogeneous Green's functions is an approximation. Although breast tissue is inhomogeneous, we do not know the corresponding Green's functions prior to reconstructions. Therefore, reconstructions begin using a homogeneous model. Nonetheless, the perturbations in the medium can influence the propagation of light significantly as is illustrated in Fig. 6.1 (bottom panels), where the sensitivity profiles are plotted for the same homogeneous medium but with with an additional sphere (pure absorber, contrast 5:1) of 1 cm radius located at $x = 1$ cm, $z = 3$ cm. As

can be seen, such heterogeneity disturbs the sensitivity profiles, making the use of homogeneous Green's functions in Eq. (6.1) questionable, especially when large variations of optical properties are present.

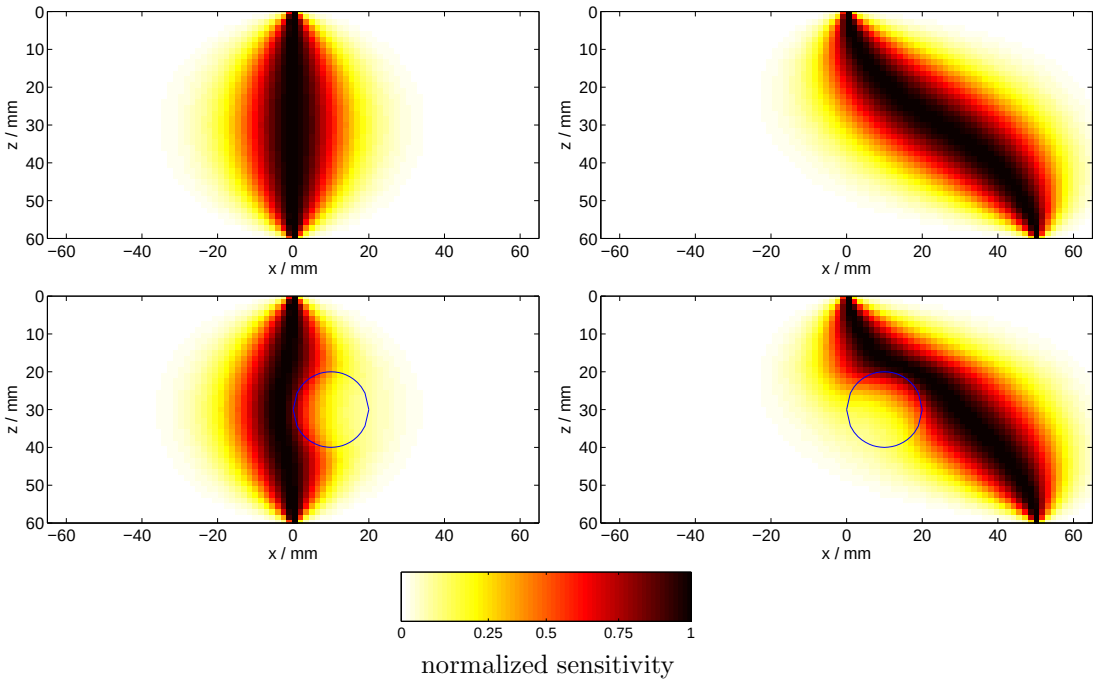

Figure 6.1: Illustration of normalized sensitivity profiles (banana shapes) in homogeneous (top row) and inhomogeneous medium (bottom row) for on-axis (left) and off-axis (right) geometry. The spherical heterogeneity (1 cm radius, located at $x = 1$ cm, $z = 3$ cm) has an increased absorption coefficient (contrast 5:1) and is indicated by the blue circle. The sensitivity profiles correspond to $\omega = 0$.

Taking inhomogeneous optical properties into account during reconstructions improves the predicted optical properties and the spatial resolution. This effect is illustrated in Fig. 6.2, where absorption and reduced scattering coefficients (left and right column, respectively) of a numerical 2D phantom representing a coronal slice through a breast in cup geometry (top row) is reconstructed from (noise-free) frequency domain data using homogeneous Green's functions (middle row) and using inhomogeneous Greens functions calculated iteratively (bottom row). The simulated breast phantom bears two inhomogeneities, a pure absorber (contrast 2:1) and one with increased absorption coefficient (contrast 2:1) and higher reduced scattering coefficient (contrast 1.36:1). The numerical breast does not fill the cup shape completely and scattering fluid, having a similar attenuation coefficient as the breast but a higher reduced scattering coefficient, fills the gap between cup (gray region) and breast tissue. The reconstructions using homogeneous Green's functions are more blurred compared with the results of the nonlinear reconstructions, which show more distinct features of constant optical properties.

Even though nonlinear reconstructions use inhomogeneous Green's functions, the method can fail to converge, if large perturbations in optical properties compared with the reference scene are present. Each iteration step is based on first order perturbation theory, and in case the first iteration fails since changes in the optical properties are too large compared to the reference, subsequent iterations might not correct the unrealistic optical properties obtained in the first step, and the entire reconstruction procedure may fail. Hence, initializing reconstructions with a realistic image, i.e. an estimated breast shape with averaged optical properties derived from *in vivo* data, improves convergence and is necessary

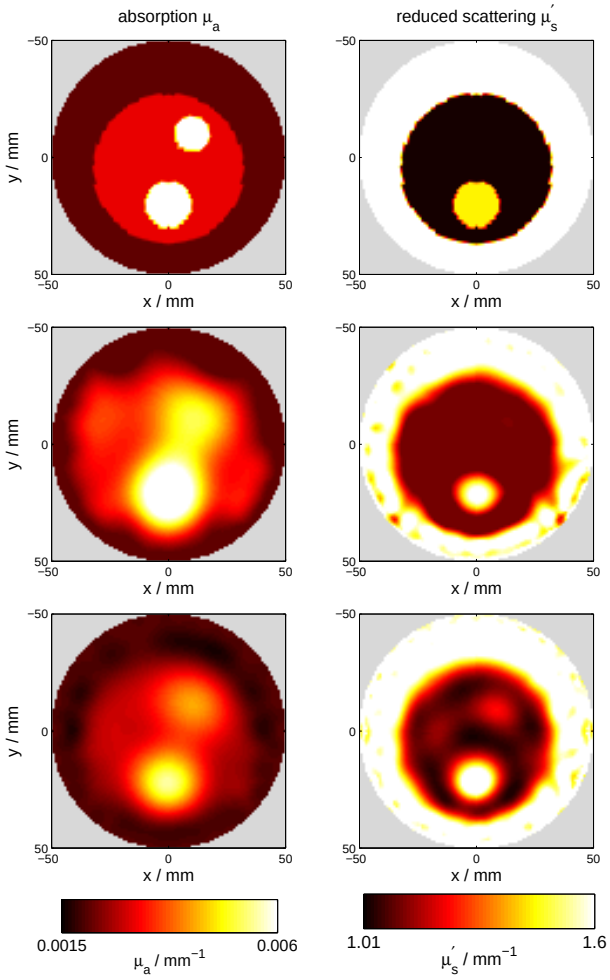

Figure 6.2: Comparison of 2D linear and nonlinear reconstructions using simulated (noise-free) frequency domain data acquired in ring geometry: (top row) phantom optical properties, (middle row) reconstructed image after linear iteration step, i.e. using homogeneous Green's functions, and (bottom row) reconstructed image after seven steps of nonlinear iterations. The same scale applies to all three images of a column.

for the nonlinear method, especially when reconstructing patient data (Sec. 6.2.4).

Iterative reconstruction methods are widely used in literature [161]. These reconstructions are initialized using homogeneous Green's functions that are updated at each iteration step, taking the reconstructed optical properties of the last iteration step into account for the following step, resulting in more accurate optical properties. Such CG based nonlinear algorithms have already been used in reconstructions of absorption and scattering coefficients of patient data collected in frequency domain [21] but are limited to smaller numbers of source-detector combinations and grid vertices due to the higher memory requirement compared with an ART approach [157]. A similar implementation of the nonlinear reconstruction, as presented in this thesis, has been proposed in [162], but was abandoned because of concerns about the computational times required. Implementing parallelization of forward model calculations and developing the sub-volume reconstruction method (Sec. 6.2.3) leads to a sufficient increase in computation speed.

6.1.3 Discretization of Rytov and Born approximations and algorithms for numerical reconstructions

The Rytov and normalized Born approximations are discretized to yield a matrix equation that is solved numerically by FEM for the absorption and reduced scattering coefficients and for fluorescent dye concentrations (image vectors). Rather than inverting the system matrix, regularization and ART reconstruction with noise-weighted relaxation and normalization of image vectors is applied.

In the following, algorithms are introduced that are used throughout this thesis for nonlinear reconstruction of absorption and scattering coefficients and for reconstruction of fluorescent dye concentrations. Furthermore, the matrix equations corresponding to the discretization on an FE grid are derived and the implementation of regularization used during ART based reconstructions is explained.

Using the Rytov-approximation for each iteration step κ of a nonlinear reconstruction algorithm, the change of the absorption coefficient $\delta\mu_{\mathrm{a}}^{\kappa}(\boldsymbol{x},\lambda)$ and diffusion coefficient $\delta D^{\kappa}(\boldsymbol{x},\lambda)$ between object measurement, with the heterogeneity in place, and reference measurement with (homogeneous) background optical properties ($D(\boldsymbol{x},\lambda) = D^0(\lambda)$, $\mu_{\mathrm{a}}(\boldsymbol{x},\lambda) = \mu_{\mathrm{a}}^0(\lambda) = \mu_{\mathrm{a},0}^{\mathrm{chrom}}(\lambda) + \mu_{\mathrm{a},0}^{\mathrm{dye}}(\lambda)$, where $\mu_{\mathrm{a},0}^{\mathrm{dye}}(\lambda) = \epsilon^{\mathrm{dye}}(\lambda) c_0 \ln 10$) can be written as (see Sec. C.2.2)

$$\begin{aligned}\ln\left(\frac{\Phi(\boldsymbol{x}_{d_i},\boldsymbol{x}_{s_i},\lambda,\omega)}{\Phi_0(\boldsymbol{x}_{d_i},\boldsymbol{x}_{s_i},\lambda,\omega)}\frac{\Phi_0^{\mathrm{sim}}(\boldsymbol{x}_{d_i},\boldsymbol{x}_{s_i},\lambda,\omega)}{\Phi_\kappa^{\mathrm{sim}}(\boldsymbol{x}_{d_i},\boldsymbol{x}_{s_i},\lambda,\omega)}\right) = &- v\int_\Omega \delta\mu_{\mathrm{a}}^{\kappa}(\boldsymbol{x},\lambda)\frac{G_\kappa(\boldsymbol{x}_{d_i},\boldsymbol{x},\lambda,\omega)G_\kappa(\boldsymbol{x},\boldsymbol{x}_{s_i},\lambda,\omega)}{G_\kappa(\boldsymbol{x}_{d_i},\boldsymbol{x}_{s_i},\omega)}d\Omega \\ &- v\int_\Omega \delta D^{\kappa}(\boldsymbol{x},\lambda)\frac{\nabla G_\kappa(\boldsymbol{x}_{d_i},\boldsymbol{x},\lambda,\omega)\cdot\nabla G_\kappa(\boldsymbol{x},\boldsymbol{x}_{s_i},\lambda,\omega)}{G_\kappa(\boldsymbol{x}_{d_i},\boldsymbol{x}_{s_i},\lambda,\omega)}d\Omega.\end{aligned} \tag{6.3}$$

Here, $G_\kappa(\boldsymbol{x},\boldsymbol{x}_{s_i},\lambda,\omega)$ is the Green's function of iteration $\kappa = 0,1,2,...$ at point $\boldsymbol{x}$ for a point source of laser photons at $\boldsymbol{x}_{s_i}$. The iteration $\kappa = 0$ corresponds to the homogeneous case. The Green's function $G_\kappa(\boldsymbol{x},\boldsymbol{x}_{s_i},\lambda,\omega)$ is obtained by solving Eq. (5.11) for the background medium with absorption and diffusion coefficient

$$\begin{aligned}\mu_{\mathrm{a}}^{\kappa}(\boldsymbol{x},\lambda) &= \mu_{\mathrm{a}}^0(\lambda) + \sum_{0\le i<\kappa}\delta\mu_{\mathrm{a}}^{i}(\boldsymbol{x},\lambda) \\ D^{\kappa}(\boldsymbol{x},\lambda) &= D^0(\lambda) + \sum_{0\le i<\kappa}\delta D^{i}(\boldsymbol{x},\lambda).\end{aligned} \tag{6.4}$$

Here, $\mu_{\mathrm{a}}^0(\lambda)$ and $D^0(\lambda)$ are the optical properties of the homogeneous medium at the reference scan (see above) and the source is modeled by a shifted Gaussian blurred or an exponentially attenuated source term (see Sec. 5.1.7).

The simulated data $\Phi_\kappa^{\mathrm{sim}}(\boldsymbol{x}_{d_i}, \boldsymbol{x}_{s_i}, \lambda, \omega)$ is the solution of Eq. (5.11) with the distribution $\mu_{\mathrm{a}}^\kappa(\boldsymbol{x}, \lambda)$ and $D^\kappa(\boldsymbol{x}, \lambda) = 1/3\mu'_{\mathrm{s},\kappa}(\boldsymbol{x}, \lambda)$ of the absorption and diffusion coefficient and the (unshifted) source of source-detector combination i located at $\boldsymbol{x}_{s_i}$, and, in our case, is given by the Green's function, i.e. $\Phi_\kappa^{\mathrm{sim}}(\boldsymbol{x}_{d_i}, \boldsymbol{x}_{s_i}, \lambda, \omega) = G_\kappa(\boldsymbol{x}_{d_i}, \boldsymbol{x}_{s_i}, \lambda, \omega)$.

Sampling transmitted laser radiation and fluorescence radiation for a total of k source-detector combinations i ($i = 1, ..., k$), the integral equations (6.3) are discretized for p frequency components ω_q ($q = 1, ..., p$) on an FE grid of N vertices. This yields a system of linear equations $\boldsymbol{y} = A\boldsymbol{b}$, with image update vector $\boldsymbol{b} = (\delta\mu_{\mathrm{a}}^\kappa(\boldsymbol{x}_1, \lambda), ..., \delta\mu_{\mathrm{a}}^\kappa(\boldsymbol{x}_N, \lambda), \delta D^\kappa(\boldsymbol{x}_1, \lambda), ..., \delta D^\kappa(\boldsymbol{x}_N, \lambda))^T$ and the $2 \cdot k \cdot p$ component signal vector $\boldsymbol{y}$,

$$\boldsymbol{y} = \begin{pmatrix} \Re\ \ln\left(\frac{\Phi(\boldsymbol{x}_{d_1},\boldsymbol{x}_{s_1},\lambda,\omega_1)}{\Phi_0(\boldsymbol{x}_{d_1},\boldsymbol{x}_{s_1},\lambda,\omega_1)}\frac{\Phi_0^{\mathrm{sim}}(\boldsymbol{x}_{d_1},\boldsymbol{x}_{s_1},\lambda,\omega_1)}{\Phi_\kappa^{\mathrm{sim}}(\boldsymbol{x}_{d_1},\boldsymbol{x}_{s_1},\lambda,\omega_1)}\right) \\ \Im\ \ln\left(\frac{\Phi(\boldsymbol{x}_{d_1},\boldsymbol{x}_{s_1},\lambda,\omega_1)}{\Phi_0(\boldsymbol{x}_{d_1},\boldsymbol{x}_{s_1},\lambda,\omega_1)}\frac{\Phi_0^{\mathrm{sim}}(\boldsymbol{x}_{d_1},\boldsymbol{x}_{s_1},\lambda,\omega_1)}{\Phi_\kappa^{\mathrm{sim}}(\boldsymbol{x}_{d_1},\boldsymbol{x}_{s_1},\lambda,\omega_1)}\right) \\ \vdots \\ \Re\ \ln\left(\frac{\Phi(\boldsymbol{x}_{d_k},\boldsymbol{x}_{s_k},\lambda,\omega_1)}{\Phi_0(\boldsymbol{x}_{d_k},\boldsymbol{x}_{s_k},\lambda,\omega_1)}\frac{\Phi_0^{\mathrm{sim}}(\boldsymbol{x}_{d_k},\boldsymbol{x}_{s_k},\lambda,\omega_1)}{\Phi_\kappa^{\mathrm{sim}}(\boldsymbol{x}_{d_k},\boldsymbol{x}_{s_k},\lambda,\omega_1)}\right) \\ \Im\ \ln\left(\frac{\Phi(\boldsymbol{x}_{d_k},\boldsymbol{x}_{s_k},\lambda,\omega_1)}{\Phi_0(\boldsymbol{x}_{d_k},\boldsymbol{x}_{s_k},\lambda,\omega_1)}\frac{\Phi_0^{\mathrm{sim}}(\boldsymbol{x}_{d_k},\boldsymbol{x}_{s_k},\lambda,\omega_1)}{\Phi_\kappa^{\mathrm{sim}}(\boldsymbol{x}_{d_k},\boldsymbol{x}_{s_k},\lambda,\omega_1)}\right) \\ \vdots \\ \Re\ \ln\left(\frac{\Phi(\boldsymbol{x}_{d_k},\boldsymbol{x}_{s_k},\lambda,\omega_p)}{\Phi_0(\boldsymbol{x}_{d_k},\boldsymbol{x}_{s_k},\lambda,\omega_p)}\frac{\Phi_0^{\mathrm{sim}}(\boldsymbol{x}_{d_k},\boldsymbol{x}_{s_k},\lambda,\omega_p)}{\Phi_\kappa^{\mathrm{sim}}(\boldsymbol{x}_{d_k},\boldsymbol{x}_{s_k},\lambda,\omega_p)}\right) \\ \Im\ \ln\left(\frac{\Phi(\boldsymbol{x}_{d_k},\boldsymbol{x}_{s_k},\lambda,\omega_p)}{\Phi_0(\boldsymbol{x}_{d_k},\boldsymbol{x}_{s_k},\lambda,\omega_p)}\frac{\Phi_0^{\mathrm{sim}}(\boldsymbol{x}_{d_k},\boldsymbol{x}_{s_k},\lambda,\omega_p)}{\Phi_\kappa^{\mathrm{sim}}(\boldsymbol{x}_{d_k},\boldsymbol{x}_{s_k},\lambda,\omega_p)}\right) \end{pmatrix}. \tag{6.5}$$

The $(2kp) \times 2N$ system matrix A is given by

$$A = \begin{pmatrix} \Re\ a_1^\kappa(\boldsymbol{x}_1,\lambda,\omega_1) & ... & \Re\ a_1^\kappa(\boldsymbol{x}_N,\lambda,\omega_1) & \Re\ \widehat{a}_1^\kappa(\boldsymbol{x}_1,\lambda,\omega_1) & ... & \Re\ \widehat{a}_1^\kappa(\boldsymbol{x}_N,\lambda,\omega_1) \\ \Im\ a_1^\kappa(\boldsymbol{x}_1,\lambda,\omega_1) & ... & \Im\ a_1^\kappa(\boldsymbol{x}_N,\lambda,\omega_1) & \Im\ \widehat{a}_1^\kappa(\boldsymbol{x}_1,\lambda,\omega_1) & ... & \Im\ \widehat{a}_1^\kappa(\boldsymbol{x}_N,\lambda,\omega_1) \\ \vdots & & \vdots & \vdots & & \vdots \\ \Re\ a_k^\kappa(\boldsymbol{x}_1,\lambda,\omega_1) & ... & \Re\ a_k^\kappa(\boldsymbol{x}_N,\lambda,\omega_1) & \Re\ \widehat{a}_k^\kappa(\boldsymbol{x}_1,\lambda,\omega_1) & ... & \Re\ \widehat{a}_k^\kappa(\boldsymbol{x}_N,\lambda,\omega_1) \\ \Im\ a_k^\kappa(\boldsymbol{x}_1,\lambda,\omega_1) & ... & \Im\ a_k^\kappa(\boldsymbol{x}_N,\lambda,\omega_1) & \Im\ \widehat{a}_k^\kappa(\boldsymbol{x}_1,\lambda,\omega_1) & ... & \Im\ \widehat{a}_k^\kappa(\boldsymbol{x}_N,\lambda,\omega_1) \\ \vdots & & \vdots & \vdots & & \vdots \\ \Re\ a_k^\kappa(\boldsymbol{x}_1,\lambda,\omega_p) & ... & \Re\ a_k^\kappa(\boldsymbol{x}_N,\lambda,\omega_p) & \Re\ \widehat{a}_k^\kappa(\boldsymbol{x}_1,\lambda,\omega_p) & ... & \Re\ \widehat{a}_k^\kappa(\boldsymbol{x}_N,\lambda,\omega_p) \\ \Im\ a_k^\kappa(\boldsymbol{x}_1,\lambda,\omega_p) & ... & \Im\ a_k^\kappa(\boldsymbol{x}_N,\lambda,\omega_p) & \Im\ \widehat{a}_k^\kappa(\boldsymbol{x}_1,\lambda,\omega_p) & ... & \Im\ \widehat{a}_k^\kappa(\boldsymbol{x}_N,\lambda,\omega_p) \end{pmatrix}, \tag{6.6}$$

where the complex-valued sensitivity coefficients are given by

$$a_i^\kappa(\boldsymbol{x}, \lambda, \omega) = -v\frac{G_\kappa(\boldsymbol{x}_{d_i}, \boldsymbol{x}, \lambda, \omega)G_\kappa(\boldsymbol{x}, \boldsymbol{x}_{s_i}, \lambda, \omega)}{G_\kappa(\boldsymbol{x}_{d_i}, \boldsymbol{x}_{s_i}, \lambda, \omega)}w(\boldsymbol{x}) \tag{6.7}$$

for absorption and

$$\widehat{a}_i^\kappa(\boldsymbol{x}, \lambda, \omega) = -v\frac{\nabla G_\kappa(\boldsymbol{x}_{d_i}, \boldsymbol{x}, \lambda, \omega) \cdot \nabla G_\kappa(\boldsymbol{x}, \boldsymbol{x}_{s_i}, \lambda, \omega)}{G_\kappa(\boldsymbol{x}_{d_i}, \boldsymbol{x}_{s_i}, \lambda, \omega)}w(\boldsymbol{x}) \tag{6.8}$$

for scattering. Here, $w(\boldsymbol{x})$ denotes the Voronoi cell volume [131] associated with the vertex $\boldsymbol{x}$.

When the convergence criterion of the nonlinear reconstruction is reached at iteration step κ_{c}, the fluorescence reconstruction uses the Born-approximation [139, 140]

$$\frac{\Phi_{\mathrm{f}}(\boldsymbol{x}_{d_i}, \boldsymbol{x}_{s_i}, \lambda, \omega)}{\Phi(\boldsymbol{x}_{d_i}, \boldsymbol{x}_{s_i}, \lambda, \omega)} = \frac{v\eta\epsilon^{\mathrm{dye}}(\lambda)\ln 10}{1 + i\omega\tau}\int_\Omega c(\boldsymbol{x})\frac{G_{\kappa_{\mathrm{c}}}(\boldsymbol{x}_{d_i}, \boldsymbol{x}, \lambda_{\mathrm{f}}, \omega)G_{\kappa_{\mathrm{c}}}(\boldsymbol{x}, \boldsymbol{x}_{s_i}, \lambda, \omega)}{G_{\kappa_{\mathrm{c}}}(\boldsymbol{x}_{d_i}, \boldsymbol{x}_{s_i}, \lambda, \omega)}d\Omega, \tag{6.9}$$

with the fluorescence photon density $\Phi_{\mathrm{f}}(\boldsymbol{x}_{d_i}, \boldsymbol{x}_{s_i}, \lambda, \omega)$ per unit interval of angular frequency ω at the detector position $\boldsymbol{x}_{d_i}$ and for a point source of laser photons at $\boldsymbol{x}_{s_i}$, and the Green's functions at the fluorescence wavelength $G_{\kappa_c}(\boldsymbol{x}_{d_i}, \boldsymbol{x}, \lambda_{\mathrm{f}}, \omega)$ for a point source at $\boldsymbol{x}$ emitting at the fluorescence wavelength. In Eq. (6.9) we have assumed the quantum efficiency η and the fluorescence lifetime τ to be independent of location $\boldsymbol{x}$. The Green's function $G_{\kappa_c}(\boldsymbol{x}, \boldsymbol{x}_{s_i}, \lambda_{\mathrm{f}}, \omega)$ is obtained by solving Eq. (5.13) for the inhomogeneous medium with the optical properties reconstructed from Eq. (6.4) at iteration step κ_c, replacing the expression on the RHS of Eq. (5.13) by $-q_0^{\kappa_c}(\boldsymbol{x}, \boldsymbol{x}_{\mathrm{s}}, \lambda, \omega)$, see Sec. 5.1.7. Throughout our reconstructions from phantom data we used the approximation $G_{\kappa_c}(\boldsymbol{x}_{d_i}, \boldsymbol{x}, \lambda_{\mathrm{f}}, \omega) = G_{\kappa_c}(\boldsymbol{x}_{d_i}, \boldsymbol{x}, \lambda, \omega)$, hence ignoring the change in optical properties between excitation and fluorescence wavelength. For the phantom experiments analyzed in this thesis, this assumption is well justified since optical properties only slightly change with wavelengths in the spectral range considered and the Stoke's shift is comparable to the width of the fluorescence band.

We note in passing that under the assumptions made ($\mu_{\mathrm{a}}^{\mathrm{f}}(\boldsymbol{x}, \lambda) = \mu_{\mathrm{a}}(\boldsymbol{x}, \lambda), D^{\mathrm{f}}(\boldsymbol{x}, \lambda) = D(\boldsymbol{x}, \lambda)$, and hence $G_{\kappa_c}(\boldsymbol{x}_{d_i}, \boldsymbol{x}, \lambda_{\mathrm{f}}, \omega) = G_{\kappa_c}(\boldsymbol{x}_{d_i}, \boldsymbol{x}, \lambda, \omega)$) Eq. (6.9) has a simple physical meaning: setting $\mu_{\mathrm{a}}^{\mathrm{dye}}(\boldsymbol{x}, \lambda) = \epsilon^{\mathrm{dye}}(\lambda) c(\boldsymbol{x}) \ln 10$, the integral

$$v \int_{\Omega} \mu_{\mathrm{a}}^{\mathrm{dye}}(\boldsymbol{x}, \lambda) \frac{G_{\kappa_c}(\boldsymbol{x}_{d_i}, \boldsymbol{x}, \lambda, \omega) G_{\kappa_c}(\boldsymbol{x}, \boldsymbol{x}_{s_i}, \lambda, \omega)}{G_{\kappa_c}(\boldsymbol{x}_{d_i}, \boldsymbol{x}_{s_i}, \lambda, \omega)} d\Omega \tag{6.10}$$

corresponds to the relative increase $\Delta\Phi(\boldsymbol{x}_{d_i}, \boldsymbol{x}_{\boldsymbol{s_i}}, \lambda, \omega)/\Phi_0(\boldsymbol{x}_{d_i}, \boldsymbol{x}_{\boldsymbol{s_i}}, \lambda, \omega)$ in laser transmission when absorption of laser photons by the dye is neglected. It follows

$$\frac{\Phi_{\mathrm{f}}(\boldsymbol{x}_{d_i}, \boldsymbol{x}_{\boldsymbol{s_i}}, \lambda, \omega)}{\Phi(\boldsymbol{x}_{d_i}, \boldsymbol{x}_{\boldsymbol{s_i}}, \lambda, \omega)} = \frac{\eta(\lambda)}{1 + i\omega\tau} \frac{\Delta\Phi(\boldsymbol{x}_{d_i}, \boldsymbol{x}_{\boldsymbol{s_i}}, \lambda, \omega)}{\Phi_0(\boldsymbol{x}_{d_i}, \boldsymbol{x}_{\boldsymbol{s_i}}, \lambda, \omega)}. \tag{6.11}$$

For fluorescence reconstruction, the system matrix simplifies to

$$A = \begin{pmatrix} \Re\, a_1^{\mathrm{f}}(\boldsymbol{x}_1, \lambda, \omega_1) & \dots & \Re\, a_1^{\mathrm{f}}(\boldsymbol{x}_N, \lambda, \omega_1) \\ \Im\, a_1^{\mathrm{f}}(\boldsymbol{x}_1, \lambda, \omega_1) & \dots & \Im\, a_1^{\mathrm{f}}(\boldsymbol{x}_N, \lambda, \omega_1) \\ \vdots & & \vdots \\ \Re\, a_k^{\mathrm{f}}(\boldsymbol{x}_1, \lambda, \omega_1) & \dots & \Re\, a_k^{\mathrm{f}}(\boldsymbol{x}_N, \lambda, \omega_1) \\ \Im\, a_k^{\mathrm{f}}(\boldsymbol{x}_1, \lambda, \omega_1) & \dots & \Im\, a_k^{\mathrm{f}}(\boldsymbol{x}_N, \lambda, \omega_1) \\ \vdots & & \vdots \\ \Re\, a_k^{\mathrm{f}}(\boldsymbol{x}_1, \lambda, \omega_p) & \dots & \Re\, a_k^{\mathrm{f}}(\boldsymbol{x}_N, \lambda, \omega_p) \\ \Im\, a_k^{\mathrm{f}}(\boldsymbol{x}_1, \lambda, \omega_p) & \dots & \Im\, a_k^{\mathrm{f}}(\boldsymbol{x}_N, \lambda, \omega_p) \end{pmatrix}, \tag{6.12}$$

with the dye concentration sensitivity coefficients given by the general expression

$$a_i^{\mathrm{f}}(\boldsymbol{x}, \lambda, \omega) = \frac{v\eta\epsilon^{\mathrm{dye}}(\lambda) \ln 10}{1 + i\omega\tau} \frac{G_{\kappa_c}(\boldsymbol{x}_{d_i}, \boldsymbol{x}, \lambda_{\mathrm{f}}, \omega) G_{\kappa_c}(\boldsymbol{x}, \boldsymbol{x}_{s_i}, \lambda, \omega)}{G_{\kappa_c}(\boldsymbol{x}_{d_i}, \boldsymbol{x}_{s_i}, \lambda, \omega)} w(\boldsymbol{x}), \tag{6.13}$$

and the image vector $\boldsymbol{b} = (c(\boldsymbol{x}_1), ..., c(\boldsymbol{x}_N))^T$. Using the linear Born approximation, the signal vector of

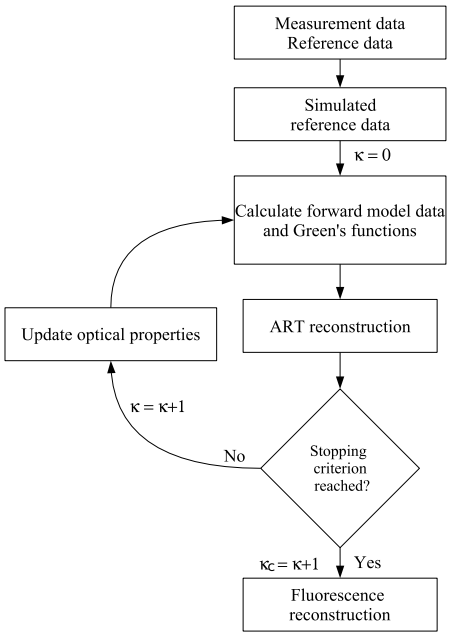

Figure 6.3: Scheme of the nonlinear reconstruction of the spatial distribution of optical properties and fluorescent dye concentration, initialized with a homogeneous distribution at iteration $\kappa = 0$.

the fluorescence reconstruction is given by

$$\boldsymbol{y} = \begin{pmatrix} \Re \frac{\Phi_{\mathrm{f}}(\boldsymbol{x}_{d_1},\boldsymbol{x}_{s_1},\lambda,\omega_1)}{\Phi(\boldsymbol{x}_{d_1},\boldsymbol{x}_{s_1},\lambda,\omega_1)} \\ \Im \frac{\Phi_{\mathrm{f}}(\boldsymbol{x}_{d_1},\boldsymbol{x}_{s_1},\lambda,\omega_1)}{\Phi(\boldsymbol{x}_{d_1},\boldsymbol{x}_{s_1},\lambda,\omega_1)} \\ \vdots \\ \Re \frac{\Phi_{\mathrm{f}}(\boldsymbol{x}_{d_k},\boldsymbol{x}_{s_k},\lambda,\omega_1)}{\Phi(\boldsymbol{x}_{d_k},\boldsymbol{x}_{s_k},\lambda,\omega_1)} \\ \Im \frac{\Phi_{\mathrm{f}}(\boldsymbol{x}_{d_k},\boldsymbol{x}_{s_k},\lambda,\omega_1)}{\Phi(\boldsymbol{x}_{d_k},\boldsymbol{x}_{s_k},\lambda,\omega_1)} \\ \vdots \\ \Re \frac{\Phi_{\mathrm{f}}(\boldsymbol{x}_{d_k},\boldsymbol{x}_{s_k},\lambda,\omega_p)}{\Phi(\boldsymbol{x}_{d_k},\boldsymbol{x}_{s_k},\lambda,\omega_p)} \\ \Im \frac{\Phi_{\mathrm{f}}(\boldsymbol{x}_{d_k},\boldsymbol{x}_{s_k},\lambda,\omega_p)}{\Phi(\boldsymbol{x}_{d_k},\boldsymbol{x}_{s_k},\lambda,\omega_p)} \end{pmatrix}. \tag{6.14}$$

ART reconstruction with noise weighted relaxation and normalized image vector

Calculation of the image vector is carried out by using the algebraic reconstruction technique, which iteratively uses single rows of the system matrix. To solve the ill-posed and ill-conditioned system of linear equations, a regularization has to be applied, and details on its chosen implementation are explained.

Reconstructions are performed using the algebraic reconstruction technique (ART), which has the advantage that only single rows of the system matrix describing the sensitivity of light inside the volume for all source-detector combinations is needed at each step (for that reason it is also known as "row action method"). The algorithm tries to minimize the difference between the measured data and the

simulated data (if the regularization term is ignored). ART is known to need more iterations than CG before convergence is reached, but minimizing the difference between measurement and forward model data does not imply that the image converges to the true scenario. Furthermore, the first (linear) ART iteration step can converge faster to the correct image for certain scenarios, although having a larger residuum in data [157]. Another benefit of ART is its flexibility, where each update step can simply be adapted to the physical problem, e.g. it was shown in work related to this thesis that ART can be adapted to spectral reconstructions [157], to reconstructions achieving separation of absorption and scattering [163], and to reconstructions incorporating different noise (see Sec. 6.1.3).

As mentioned before, the algebraic reconstruction technique acts only on single rows of [164]

$$A = (A_{ij})_{i\in I, j\in J}, \tag{6.15}$$

with $I = \{1, \ldots, 2kp\}$ and $J = \{1, ..., 2N\}$ for absorption and diffusion reconstruction and $J = \{1, ..., N\}$ for fluorescence reconstruction, to solve for

$$\boldsymbol{b} = (b_j)_{j\in J}. \tag{6.16}$$

The difference between measurement data and forward model data $\Delta y_{i_l} = y_{i_l} - \sum_j A_{i_l j} b_j^l$ is reduced at every ART iteration step l. At each of these iterations, a random row i_l of the signal vector $\boldsymbol{y}$ is chosen with associated source-detector combination i and angular frequency component ω_q. Subsequently, all image elements $j \in J$ are updated by

$$b_j^{l+1} = b_j^l + r_{\mathrm{rlx}}(i, \omega_q) \frac{A_{i_l j} \Delta y_{i_l}}{\sum_m A_{i_l m}^2}, \tag{6.17}$$

where $m = 1, ..., 2N$ for absorption and diffusion reconstructions, $m = 1, ..., N$ for fluorescence reconstructions, and r_{rlx} being a weighting factor. The ART algorithm uses each source-detector combination, each frequency component and real and imaginary part of the measurement data once, hence resulting in $2kp$ total iterations. For this, the iteration process is initialized at $l = 0$ with $\boldsymbol{b} = 0$.

To handle the variations in measurement noise that are associated with transmission and reflection measurements, with different source-detector combinations (source-detector offsets), and frequency components ω_q, a noise weighted back projection is introduced [165]. Each ART back projection [164]

$$x_j^{k+1} = x_j + r_{\mathrm{rlx}}(i, \omega_q) \frac{A_{ij} \Delta y_i}{\sum_l A_{il}^2} \tag{6.18}$$

is scaled with a noise-dependent relaxation factor

$$r_{\mathrm{rlx}}(i, \omega_q) = \frac{\sigma_0^{\mathrm{err}}}{\sigma_i^{\mathrm{err}}(\omega_q)}, \tag{6.19}$$

where $\sigma_i^{\mathrm{err}}(\omega_q)$ is the noise of angular frequency component ω_q at the source-detector combination i. Since the reconstruction inputs are the real and imaginary parts of

$$\ln\left(\frac{\Phi(\boldsymbol{x}_{d_i}, \boldsymbol{x}_{s_i}, \lambda, \omega_q)\Phi_0^{\mathrm{sim}}(\boldsymbol{x}_{d_i}, \boldsymbol{x}_{s_i}, \lambda, \omega_q)}{\Phi_0(\boldsymbol{x}_{d_i}, \boldsymbol{x}_{s_i}, \lambda, \omega_q)\Phi^{\mathrm{sim}}(\boldsymbol{x}_{d_i}, \boldsymbol{x}_{s_i}, \lambda, \omega_q)}\right) \tag{6.20}$$

and

$$\frac{\Phi_{\mathrm{f}}(\boldsymbol{x}_{d_i}, \boldsymbol{x}_{s_i}, \lambda, \omega_q)}{\Phi(\boldsymbol{x}_{d_i}, \boldsymbol{x}_{s_i}, \lambda, \omega_q)}, \tag{6.21}$$

we estimate the corresponding noise $\sigma_i^{\mathrm{err}}(\omega_q)$ by analyzing data from a homogeneous region of the object scan and put it in relation to the lowest signal noise σ_0^{err} at $\omega = 0$.

Rather than solving $\boldsymbol{y} = A\boldsymbol{b}$ we searched for the minimum of

$$\boldsymbol{y} = \underset{\boldsymbol{y}'}{\operatorname{argmin}}\{\|A'\boldsymbol{b}' - \boldsymbol{y}'\|^2 + \|L(\lambda_{\mathrm{reg}})\boldsymbol{b}'\|^2\} \tag{6.22}$$

to achieve regularization by the parameter λ_{reg}. The new matrix $A' = (A'_{ij})_{i\in I, j\in J}$ and the new vector $\boldsymbol{b}' = (b'_j)_{j\in J}$ are calculated by

$$A'_{ij} = A_{ij}\gamma_j, \tag{6.23}$$

and

$$b'_j = b_j/\gamma_j, \tag{6.24}$$

with $\gamma_j = \Delta\mu_{\mathrm{a}}^{\star} + \mu_{\mathrm{a}}^0$ for $j \leq N$ and $\gamma_j = \Delta D^{\star} + D^0$ for $j > N$ for absorption and diffusion reconstruction and $\gamma_j = 1$ for fluorescence reconstruction. The normalization of the vector $\boldsymbol{b}$ makes the image vector $\boldsymbol{b}'$ dimensionless and effectuates that updates of the image during each ART back projection are distributed equally for the absorption and the scattering image. Since the norm of $\boldsymbol{b}'$ for $j \leq N$ and $j > N$ are of comparable size, the regularization term λ_{reg} has comparable effects on the absorption and scattering images.

The values $\Delta\mu_{\mathrm{a}}^{\star}$ and $\Delta D^{\star}$ are the estimated (*a priori* known) absorption and scattering coefficient deviations of the heterogeneity compared with the homogeneous medium and accelerate the convergence of the nonlinear reconstruction algorithm.

The regularization matrix $L(\lambda_{\mathrm{reg}})$ has been chosen as a diagonal matrix throughout this thesis with

$$\mathrm{diag}(L) = \Big(\underbrace{\sqrt{\lambda_{\mathrm{reg}}(\mu_{\mathrm{a}})}, ..., \sqrt{\lambda_{\mathrm{reg}}(\mu_{\mathrm{a}})}}_{N \text{ times}}, \underbrace{\sqrt{\lambda_{\mathrm{reg}}(D)}, ..., \sqrt{\lambda_{\mathrm{reg}}(D)}}_{N \text{ times}}\Big), \tag{6.25}$$

defining a different regularization parameter for the absorption and diffusion coefficients, i.e. $\lambda_{\mathrm{reg}}(\mu_{\mathrm{a}})$ and $\lambda_{\mathrm{reg}}(D)$ respectively. In case of spatial priors being used during the reconstruction (e.g. segmenting the volume into regions of similar optical properties by analyzing MR images acquired from the patient's breast), the regularization matrix L is not diagonal but off-diagonal elements connect coxels which belong to the same region [166]. However, such spatial priors gained from multimodal approaches were not aim of this thesis.

Values of the Green's functions and its gradients are calculated on the FE grid numerically and stored in a table. The rows of A are calculated on-the-fly from the Green's function table by the reconstruction algorithm. A schematic view of the nonlinear reconstruction algorithm is given in Fig. 6.3. The complete algorithm can be summarized in the following pseudocode:

Algorithm 1: nonlinear reconstruction

Step 1: Collection of measurement data for the object scan, $\widetilde{\Phi}(\boldsymbol{x}_{d_i}, \boldsymbol{x}_{s_i}, \lambda, t)$, i.e. with the heterogeneity in place, and for the reference scan (homogeneous medium), $\widetilde{\Phi}_0(\boldsymbol{x}_{d_i}, \boldsymbol{x}_{s_i}, \lambda, t)$ of all source-detector combinations i. Fourier-transformation, and additional preprocessing of measurement data, if needed (see Sec. 6.2.1).

Step 2: Simulation of the reference scan data, $\Phi_0^{\mathrm{sim}}(\boldsymbol{x}_{d_i}, \boldsymbol{x}_{s_i}, \lambda, \omega_q)$, for all source-detector combinations i and all angular frequency components ω_q ($q = 1, ..., p$) used in the reconstruction, by solving Eq. (5.11) for a homogeneous medium with the absorption coefficient $\mu_{\mathrm{a}}^0(\lambda)$ and the diffusion coefficient $D^0(\lambda)$ of the reference scan.

Step 3: Calculation of the Green's functions $G_\kappa(\boldsymbol{x}_{d_i}, \boldsymbol{x}, \lambda, \omega_q)$, respectively $G_\kappa(\boldsymbol{x}, \boldsymbol{x}_{s_i}, \lambda, \omega_q)$ for all detector positions $\boldsymbol{x}_{d_i}$, all source positions $\boldsymbol{x}_{s_i}$, and all angular frequency components ω_q. Simulated data $\Phi_\kappa^{\mathrm{sim}}(\boldsymbol{x}_{d_i}, \boldsymbol{x}_{s_i}, \lambda, \omega_q)$ are calculated by the forward model with the reconstructed spatial distributions $\mu_{\mathrm{a}}^\kappa(\boldsymbol{x}, \lambda)$ and $D^\kappa(\boldsymbol{x}, \lambda)$ for each source-detector combination i

and angular frequency ω_q. This calculation can be omitted for $\kappa = 0$, because in this case the result is equal to $\Phi_0^{\text{sim}}(\boldsymbol{x}_{d_i}, \boldsymbol{x}_{s_i}, \lambda, \omega_q)$ corresponding to the reference scan.

Step 4: The results obtained in the previous steps ($G_\kappa(\boldsymbol{x}, \boldsymbol{x}_{s_i}, \lambda, \omega_q)$, $G_\kappa(\boldsymbol{x}_{d_i}, \boldsymbol{x}, \lambda, \omega_q)$, $\Phi_0^{\text{sim}}(\boldsymbol{x}_{d_i}, \boldsymbol{x}_{s_i}, \lambda, \omega_q)$, and $\Phi_\kappa^{\text{sim}}(\boldsymbol{x}_{d_i}, \boldsymbol{x}_{s_i}, \lambda, \omega_q)$), and the experimental data ($\Phi_0(\boldsymbol{x}_{d_i}, \boldsymbol{x}_{s_i}, \lambda, \omega_q)$, and $\Phi(\boldsymbol{x}_{d_i}, \boldsymbol{x}_{s_i}, \lambda, \omega_q)$) are used to solve Eq. (6.3) via ART to reconstruct the difference of optical properties $\delta\mu_{\text{a}}^{\kappa}(\boldsymbol{x}, \lambda)$ and $\delta D^{\kappa}(\boldsymbol{x}, \lambda)$ (see Eq. (6.5) to (6.8)).

Step 5: When a given stopping criterion is reached (e.g. the norm of the reconstructed image update vector $\boldsymbol{b}$ is lower than a given limit), fluorescence reconstruction is started in step 7, and $\kappa_{\text{c}} = \kappa + 1$. If the stopping criterion has not been reached, the spatial distribution of optical properties inside the reconstructed volume is updated according to Eq. (6.4). The iteration number is increased and calculations are continued at step 3.

Step 6: Using the reconstructed absorption, $\mu_{\text{a}}^{\kappa_{\text{c}}}(\boldsymbol{x}, \lambda)$, and diffusion coefficient $D^{\kappa_{\text{c}}}(\boldsymbol{x}, \lambda)$, the Green's functions $G_{\kappa_{\text{c}}}(\boldsymbol{x}_{d_i}, \boldsymbol{x}, \lambda_{\text{f}}, \omega_q)$ and $G_{\kappa_{\text{c}}}(\boldsymbol{x}, \boldsymbol{x}_{s_i}, \lambda, \omega_q)$ are calculated for each source and detector position. The fluorescent dye concentration is reconstructed according to Eq. (6.9) via ART (see Eq. (6.12), (6.13), and (6.14)).

6.2 Results

6.2.1 Data preprocessing

Before experimental data can be used for reconstructions, instrumental factors have to be taken into account. This section describes how such factors can be obtained from a raw data analysis. Furthermore, we explain how to subtract the homogeneous background fluorescence signal from raw data to improve dye concentration reconstructions.

Before experimental data can be used for image reconstructions, several steps of data preprocessing are needed. A large amount of data is collected by time-domain measurements. Using the complete data set of all collected TPSFs is not practical during the reconstruction process, because the resulting linear system of equations is too large and can not be solved on todays hardware. To reduce the amount of data, one can either use temporal filters [167] or carry out the reconstruction in frequency domain, as will be performed in the following. For this purpose, time-domain data have to be Fourier transformed and frequency components with sufficiently high signal-to-noise ratios have to be selected.

Furthermore, as was mentioned in Sec. 4.3, measurements in slab geometry were carried out sequentially using different filter combinations for the reference scan and object scan as well as for different source-detector offsets. As was shown in [168] an optode calibration can be performed by the reconstruction itself, but needs an additional free parameter that has to be chosen by hand. In contrast, throughout this thesis, a calibration is performed on raw data thus avoiding a free parameter. To this end, an area in the transmittance or reflectance image of the object scan taken at a particular source-detector offset $\Delta\boldsymbol{x}_{d_i,s_i} = \boldsymbol{x}_{d_i} - \boldsymbol{x}_{s_i}$ is selected that is presumably not affected (NA) by the presence of the heterogeneity and the data recorded are averaged over this area. Likewise, an area of the reference scan taken at the same source-detector offset is selected, and the corresponding data are averaged. The scaling factor T_{d_i,s_i} is given by

$$T_{d_i,s_i} = \frac{\left(\Phi^{\text{meas}}(\boldsymbol{x}_{d_i}, \boldsymbol{x}_{s_i}, \lambda, \omega_q)\right)_{\text{ave,NA}}}{\left(\Phi_0^{\text{meas}}(\boldsymbol{x}_{d_i}, \boldsymbol{x}_{s_i}, \lambda, \omega_q)\right)_{\text{ave}}}, \tag{6.26}$$

and takes e.g. filter transmittance or detector efficiency into account. It follows that the corrected data

$$\frac{\left(\Phi(\boldsymbol{x}_{d_i}, \boldsymbol{x}_{s_i}, \lambda, \omega_q)\right)}{\left(\Phi_0(\boldsymbol{x}_{d_i}, \boldsymbol{x}_{s_i}, \lambda, \omega_q)\right)} = \frac{1}{T_{d_i,s_i}} \frac{\Phi^{\text{meas}}(\boldsymbol{x}_{d_i}, \boldsymbol{x}_{s_i}, \lambda, \omega)}{\Phi_0^{\text{meas}}(\boldsymbol{x}_{d_i}, \boldsymbol{x}_{s_i}, \lambda, \omega)} \tag{6.27}$$

enter Eq. (6.3) and (6.5).

For the fluorescence contrast reconstruction, instrumental factors are be taken into account by a similar approach. Before reconstruction of the measured fluorescence data was started, four preprocessing steps were applied to the raw fluorescence data:

i) At each angular frequency ω_q and source-detector combination i selected, the data measured at the fluorescence wavelength was normalized by the corresponding measured data at the laser wavelength yielding $\Phi_{\mathrm{f}}^{\mathrm{meas}}(\boldsymbol{x}_{d_i}, \boldsymbol{x}_{s_i}, \lambda, \omega_q)/\Phi^{\mathrm{meas}}(\boldsymbol{x}_{d_i}, \boldsymbol{x}_{s_i}, \lambda, \omega_q)$, eliminating the corresponding Fourier component of the instrumental response function.

ii) For the angular frequencies and source-detector combinations selected, simulated data were generated in frequency domain at the laser ($\Phi_0^{\mathrm{sim}}(\boldsymbol{x}_{d_i}, \boldsymbol{x}_{s_i}, \lambda, \omega_q)$) and fluorescence ($\Phi_{\mathrm{f0}}^{\mathrm{sim}}(\boldsymbol{x}_{d_i}, \boldsymbol{x}_{s_i}, \lambda, \omega_q)$) wavelengths by solving Eq. (5.11) and (5.13) in 3D for a homogeneous slab.

iii) To correct fluorescence scan data for experimental factors, we set

$$\left(\frac{\Phi_{\mathrm{f}}^{\mathrm{meas}}(\boldsymbol{x}_{d_i}, \boldsymbol{x}_{s_i}, \lambda, \omega_q)}{\Phi^{\mathrm{meas}}(\boldsymbol{x}_{d_i}, \boldsymbol{x}_{s_i}, \lambda, \omega_q)}\right)_{\mathrm{ave,NA}} = T_{d_i,s_i}^{\mathrm{f}} \frac{\Phi_{\mathrm{f0}}^{\mathrm{sim}}(\boldsymbol{x}_{d_i}, \boldsymbol{x}_{s_i}, \lambda, \omega_q)}{\Phi_0^{\mathrm{sim}}(\boldsymbol{x}_{d_i}, \boldsymbol{x}_{s_i}, \lambda, \omega_q)}, \tag{6.28}$$

where T_{d_i,s_i}^{f} is a scaling factor taking experimental factors into account, in particular transmittance of long pass and band pass filters used and detector efficiencies at the laser and fluorescence wavelength. Again, the average on the LHS is taken over a subset of measured data (area) that is unaffected by the presence of the heterogeneity and $\Phi_{\mathrm{f0}}^{\mathrm{sim}}(\boldsymbol{x}_{d_i}, \boldsymbol{x}_{s_i}, \lambda, \omega_q)$, $\Phi_0^{\mathrm{sim}}(\boldsymbol{x}_{d_i}, \boldsymbol{x}_{s_i}, \lambda, \omega_q)$ refer to simulated data of the homogeneous medium without the heterogeneity being present. The corrected data

$$\frac{\Phi_{\mathrm{f}}(\boldsymbol{x}_{d_i}, \boldsymbol{x}_{s_i}, \lambda, \omega_q)}{\Phi(\boldsymbol{x}_{d_i}, \boldsymbol{x}_{s_i}, \lambda, \omega_q)} = \frac{1}{T_{d_i,s_i}^{\mathrm{f}}} \frac{\Phi_{\mathrm{f}}^{\mathrm{meas}}(\boldsymbol{x}_{d_i}, \boldsymbol{x}_{s_i}, \lambda, \omega_q)}{\Phi^{\mathrm{meas}}(\boldsymbol{x}_{d_i}, \boldsymbol{x}_{s_i}, \lambda, \omega_q)} \tag{6.29}$$

enter into Eq. (6.9) and Eq. (6.14).

iv) In order to improve image quality [169], the mean homogeneous background value

$$\frac{\Phi_{\mathrm{f0}}^{\mathrm{sim}}(\boldsymbol{x}_{d_i}, \boldsymbol{x}_{s_i}, \lambda, \omega_q)}{\Phi_0^{\mathrm{sim}}(\boldsymbol{x}_{d_i}, \boldsymbol{x}_{s_i}, \lambda, \omega_q)} \tag{6.30}$$

is subtracted from the corrected data, yielding

$$\begin{aligned}
&\frac{\Phi_{\mathrm{f}}(\boldsymbol{x}_{d_i}, \boldsymbol{x}_{s_i}, \lambda, \omega_q)}{\Phi(\boldsymbol{x}_{d_i}, \boldsymbol{x}_{s_i}, \lambda, \omega_q)} - \frac{\Phi_{\mathrm{f0}}^{\mathrm{sim}}(\boldsymbol{x}_{d_i}, \boldsymbol{x}_{s_i}, \lambda, \omega_q)}{\Phi_0^{\mathrm{sim}}(\boldsymbol{x}_{d_i}, \boldsymbol{x}_{s_i}, \lambda, \omega_q)} \\
&= \frac{1}{T_{d_i,s_i}^{\mathrm{f}}} \left(\frac{\Phi_{\mathrm{f}}^{\mathrm{meas}}(\boldsymbol{x}_{d_i}, \boldsymbol{x}_{s_i}, \lambda, \omega_q)}{\Phi^{\mathrm{meas}}(\boldsymbol{x}_{d_i}, \boldsymbol{x}_{s_i}, \lambda, \omega_q)} - \left(\frac{\Phi_{\mathrm{f}}^{\mathrm{meas}}(\boldsymbol{x}_{d_i}, \boldsymbol{x}_{s_i}, \lambda, \omega_q)}{\Phi^{\mathrm{meas}}(\boldsymbol{x}_{d_i}, \boldsymbol{x}_{s_i}, \lambda, \omega_q)} \right)_{\mathrm{avg,NA}} \right) \\
&= \frac{v\eta\epsilon(\lambda)^{\mathrm{dye}} \ln 10}{1 + i\omega_q\tau} \int \delta c(\boldsymbol{x}) \frac{G_{\kappa_{\mathrm{c}}}(\boldsymbol{x}_{d_i}, \boldsymbol{x}, \lambda_{\mathrm{f}}, \omega_q) G_{\kappa_{\mathrm{c}}}(\boldsymbol{x}, \boldsymbol{x}_{s_i}, \lambda, \omega_q)}{G_{\kappa_{\mathrm{c}}}(\boldsymbol{x}_{d_i}, \boldsymbol{x}_{s_i}, \lambda, \omega_q)} d\Omega,
\end{aligned} \tag{6.31}$$

where $\delta c(\boldsymbol{x}) = c(\boldsymbol{x}) - c_0$ is the difference between the dye concentration and the background concentration value. To present absolute values $c(\boldsymbol{x})$ rather than only differences $\delta c(\boldsymbol{x})$ between the object and the reference fluid, the optical properties of the background scattering liquid, in particular the homogeneous background dye concentration c_0, were considered to be *a priori* knowledge. These optical properties can be deduced by an analysis of the reference scan data.

Reconstruction of $\delta c(\boldsymbol{x})$ using Eq. (6.31) is carried out analogously as described for the reconstruction of $c(\boldsymbol{x})$ using Eq. (6.9).

6.2.2 Localization and spatial resolution

The axial definition achieved by various detection schemes based on the parallel-plate geometry was investigated to show that remittance measurements increase the depth resolution significantly.

Measurements were carried out to reconstruct the absorption coefficient and fluorescent dye concentration contrast of a heterogeneity simulating a lesion within a rectangular cuvette containing a tissue-like scattering and fluorescent fluid, and reconstruction results of time-domain phantom scans in slab geometry are presented. The spatial distribution of the concentration of the fluorescent contrast agent was obtained by solving the forward-model diffusion equation for the propagation of the laser and fluorescence radiation using the Born approximation [139, 170] of the fluorescence diffusion equation. To this end, the density of laser photons within the tissue was reconstructed in a nonlinear fashion using the Rytov approximation.

Results of nonlinear three-dimensional reconstruction of the phantom scans are presented in this section and their spatial resolution is discussed. Reconstruction of the dye concentration was performed by Fourier-transforming time-resolved data to frequency domain and by using the frequency data up to several hundred MHz, provided signal-to-noise ratios were sufficiently high. Using this data, it is shown that additional time-resolved remittance measurements taken at the entrance face of the phantom increase depth resolution compared with reconstructions using transmittance data only.

Due to the large variations in noise for the different frequency components and source-detector combinations, an ART-based reconstruction [164] of DOT data was chosen that uses a noise weighted back projection. By this method, noisy data can be incorporated into the reconstruction scheme without the necessity to increase the regularization term. Hence, rather high cut-off frequencies can be chosen since significant distortions of the reconstructed image are avoided by noisy high-frequency data. A further improvement over existing reconstruction algorithms concerns the use of a normalized image vector during the ART iterations, allowing to improve the separation of absorption and scattering by rescaling to a dimensionless image vector with comparable size of the norm for both images.

The measurements were accomplished with the laboratory setup shown in Fig. 4.1, which is explained in Sec. 4.3.

As phantom simulating a compressed tumor bearing breast, a rectangular cuvette ($25 \times 25 \times 6$ cm^3) filled with a scattering, absorbing, and fluorescent liquid and containing a small scattering, absorbing, and fluorescent object, simulating a lesion was used.

The laser beam was scanned across the incoming face of the cuvette ($z = 0$) from $x = -4$ cm to $x = 4$ cm, $y = -4$ cm to $y = 4$ cm sampling 289 equidistant positions. Several offsets of the detector fiber with respect to the source fiber were selected resulting in a total of 17 source-detector combinations. The phantoms were scanned at a step size of 5 mm. At each source position, time-domain transmittance measurements were carried out within 100 ms using detectors placed at the opposite (exit) face ($z = 6$ cm) of the cuvette with lateral (horizontal) source-detector offsets of $\Delta x = \pm 4$ cm, ± 3 cm, ± 2 cm, ± 1 cm, 0 cm. Offsets in y direction were not included here, $\Delta y = 0$ cm. For remittance measurements detectors were placed on the entrance face at offsets $\Delta y = 0$ cm and $\Delta x = \pm 4$ cm, ± 3 cm, ± 2 cm, and ± 1 cm. Only data collected at detector positions inside the range -4 cm $\leq x \leq 4$ cm were used for image reconstruction.

Breast tissue was simulated by a scattering and absorbing liquid prepared by Philips Research Europe – Eindhoven. Optical properties of this scattering solution were deduced from time-resolved diffuse transmittance measurements. At 730 nm, the diffusion coefficient $D^0 = 1/(3\mu'_{s,0})$ amounted to about $D^0 = 0.0032$ cm, the absorption coefficient $\mu_{a,0}^{chrom}$ to about 0.023 cm^{-1}. A concentration of $c_0 = 10$ nM of the Omocyanine [122] fluorescent dye was added to the scattering fluid to simulate background fluorescence as expected from measurements in tissue.

A lesion-simulating object was made from hollow thin-walled delrin twin cones (Fig. 5.15 left) filled

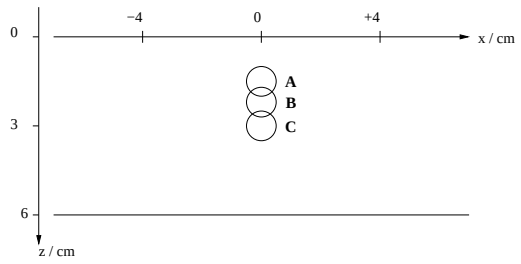

Figure 6.4: Schematic top view of phantom indicating the three selected lesion positions A, B, and C inside the cuvette at $x = y = 0$ and $z = 1.5$ cm, $z = 2.2$ cm, and $z = 3$ cm, respectively. The plane $z = 0$ corresponds to the entrance face of the phantom.

with background scattering fluid and additional Omocyanine fluorescent dye. The fluorescence decay time and quantum efficiency of the Omocyanine dye amount to $\tau \approx 500$ ps and $\eta \approx 0.1$, respectively.

The equatorial diameters of the delrin twin cones amounted to 2 cm, corresponding to an outer lesion volume of 2.1 ml. The delrin twin cones were filled with background scattering fluid with the fluorescent dye concentration increased to 50 nM, i.e. $\mu_{\mathrm{a}}^{\mathrm{sph}} = \mu_{\mathrm{a}}^{\mathrm{chrom}} + 5\mu_{\mathrm{a},0}^{\mathrm{dye}} = 0.031\ \mathrm{cm}^{-1}$. This lesion-simulating heterogeneity was immersed in the scattering fluid and placed at three different positions labeled A, B, and C at $x = y = 0$, $z = 1.5$ cm, 2.2 cm, and 3 cm, respectively (Fig. 6.4). The double cone was suspended from a thin thread and was loaded by an additional weight suspended from its lower tip by means of a thin thread to avoid buoyancy.

Gain of spatial resolution from improved angular sampling (transmittance and reflectance

To investigate to what extent the inclusion of offset measurements taken in transmission and reflection geometry will improve results, reconstructions that use different restricted sets of source-detector combinations are compared. In each case, the pulsed source scanned across the lesion at 5 mm increments. From these measurements, reconstructions are performed using data sets representing three different setups [134], each sketched in Fig. 6.5: (left) projection-shadow geometry corresponding to zero offset data taken in transmission, (middle) slab fan-beam geometry, where detectors measure in transmission ($\Delta y = 0$, $\Delta z = 6$ cm) at offsets $\Delta x = \pm 4$ cm, ± 3 cm, ..., 0 cm, and (right) slab reflection and transmission geometry, where additionally the remission is measured at the entrance face ($z = 0$) within the $y = 0$ plane at offsets $\Delta x = \pm 4$ cm, ± 3 cm, ..., 1 cm. Assuming no prior knowledge of the lesion contrast, $\Delta\mu_{\mathrm{a}}^{\star} = \Delta D^{\star} = 0$ was used for the ART-based reconstructions. Images were obtained by three-dimensional reconstruction from time-domain transmittance and remittance data, selecting three equidistant angular frequencies $\omega_1 = 0$, $\omega_2 = 2\pi \cdot 117$ MHz, and $\omega_3 = 2\pi \cdot 234$ MHz. Nonlinear reconstructions up to iteration $\sigma = 5$ were carried out on the volume of interest $\Omega = 18 \times 12 \times 6\ \mathrm{cm}^3$. The FE grid consisted of approximately 51500 vertices, the Voronoi cell volume amounted to approximately $w(\boldsymbol{x}) = 0.125\ \mathrm{cm}^3$ throughout the volume of interest, but was chosen smaller at source and detector positions, i.e. $w(\boldsymbol{x}_{s_i}) = w(\boldsymbol{x}_{d_i}) = 0.005\ \mathrm{cm}^3$. The regularization parameter was chosen as $\lambda_{\mathrm{reg}}(\mu_{\mathrm{a}}) = \lambda_{\mathrm{reg}}(D) = 0.02$ for reconstructions of the absorption and reduced scattering coefficients, and as $\lambda_{\mathrm{reg}} = 0$ for reconstructions of fluorescent dye concentrations, while in all cases $\Delta D^{\star} = \Delta\mu_{\mathrm{a}}^{\star} = 0$.

The resulting dye concentrations $\delta c(\boldsymbol{x})$ of the three different reconstructions are illustrated in Fig. 6.6 using the belonging source-detector combinations as shown in Fig. 6.5. In all three cases the slice for $y = 0$ is given, and images are presented in min/max scaling. The outer hull of the twin-cone which was positioned at $z = 2.2$ cm is outlined as a circle in these images. As was predicted previously [143], using only zero offset transmittance data does not provide any axial definition of the heterogeneity. Hence, in the resulting image (Fig. 6.6 left) the lesion position can not be reconstructed. Using transmittance

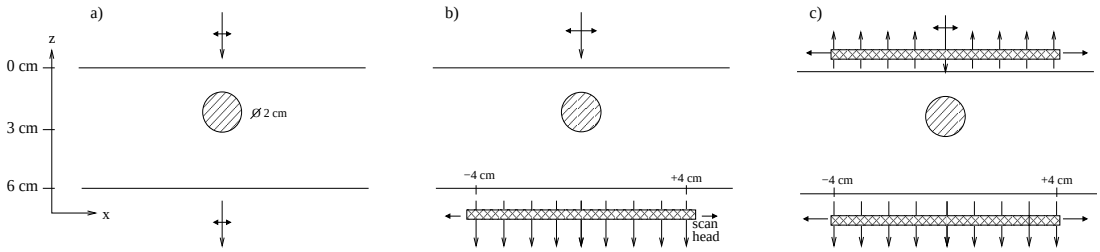

Figure 6.5: Schematic view of different source-detector geometries with a lesion near the entrance face of the slab, i.e. at position $x = y = 0$, $z = 2.2$ cm (position B in Fig. 6.4). The source and the detector fibers are scanned in tandem keeping source-detector offsets fixed. The step size amounted to 5 mm sampling a total of 17 source positions across the front face. (a) Projection-shadow geometry. (b) Slab fan-beam geometry. (c) Slab reflection and transmission geometry.

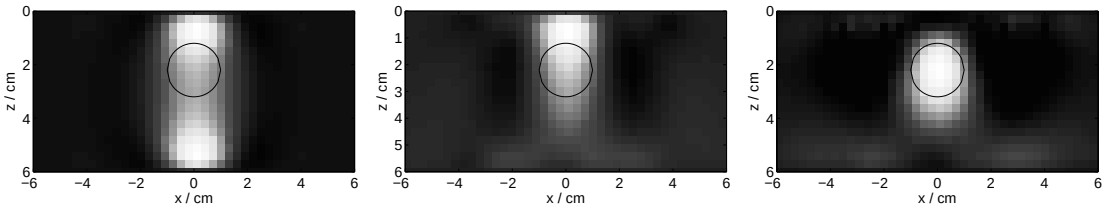

Figure 6.6: Reconstruction of three dimensional dye concentration reconstruction $\delta c(\boldsymbol{x}) = c(\boldsymbol{x}) - c_0$ of fluorescent dye of the delrin twin cone indicated by circle and located at position B ($x = y = 0, z = 2.2$ cm). Dye concentration $\delta c(\boldsymbol{x})$ is given in min/max scaling in the x–z plane through the center of the lesion ($y = 0$). Three images corresponding to the source-detector combinations shown in Fig. 6.5: (left) projection-shadow geometry, (middle) slab fan-beam geometry, and (right) reflection and transmission geometry. Line profiles through the images (middle and right) for $x = 0$ are shown in Fig. 6.7.

data with offsets along the x direction improves the axial definition (Fig. 6.6 middle), although the lesion position is not reconstructed correctly but shifted towards the entrance face. Including additional remittance measurements into the reconstruction enhances axial definition of the lesion and its center is reconstructed at the correct position (see Fig. 6.6 right).

These results are supported by profiles of the absorption coefficient and the fluorescent dye concentration along the horizontal z-axis through the center of the delrin cone ($x = y = 0$) positioned at the three positions A, B, and C (see Fig. 6.4).

Reconstructed absorption coefficients and fluorescent dye concentrations are shown in Fig. 6.7 left and right, respectively. Line profiles along z are given for all three positions A (no symbol), B (stars), and C (triangles). Full lines correspond to reconstructed transmittance and reflectance data, dashed lines were obtained from transmittance data only. As can be seen from Fig. 6.7, inclusion of remittance data besides transmittance data generally narrows line profiles (solid lines) of the absorption coefficient and fluorescent dye concentration compared to profiles (dashed lines) obtained from transmittance data alone, thus improving axial resolution. Furthermore, all line profiles based on transmittance data alone exhibit maxima that are further shifted from the true lesion position towards the entrance face compared to the maxima of the line profiles based on both, remittance and transmittance data. In particular, the maxima of the fluorescent dye concentrations reconstructed from remittance and transmittance data (solid line, solid line with stars) coincide with the true lesion position A and B while for position C the corresponding maximum is shifted only slightly from the true position towards the entrance face. The line profiles (solid lines in Fig. 6.7 right) allow to separate all three lesion positions. In contrast, corresponding

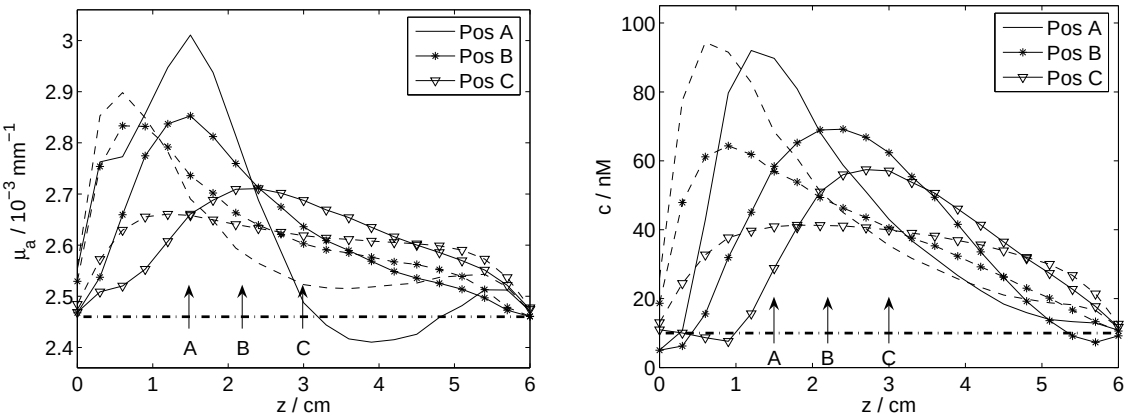

Figure 6.7: Line profiles of three dimensional reconstruction of $\mu_a(x = 0, y = 0, z)$ (left) and of fluorescent dye concentration $c(x = 0, y = 0, z)$ for the three different twin cone positions A (no symbol), B (star), and C (triangle). Full lines correspond to reconstructions using both, remittance ($z = 0$) and transmittance ($z = 6$ cm) data, dashed lines obtained from transmittance data only. The horizontal dash-dot line shows the background value μ_a^0 of the absorption coefficient (left) and the background dye concentration c_0 (left), respectively. The vertical arrows indicate the three positions (A, B, C) of the heterogeneity.

line profiles (solid lines) of the absorption coefficient (Fig. 6.7 left) do not allow to separate positions A and B. The normalized Born approximation used to reconstruct fluorescent dye concentrations involves transmittance and remittance measurements at the excitation and fluorescence wavelength and hence contains more information than measurements at the laser wavelength only.

Generally, line profiles are skewed, exhibiting a rapid drop towards the entrance face (source plane) and a gradual decline towards the exit face (detector plane), although symmetric profiles of the reconstructed absorption coefficients and fluorescent dye concentrations are to be expected. Furthermore, some of the line profiles illustrated in Fig. 6.7 exhibit minima towards the exit face even falling below the reference values μ_a^0 and c_0 respectively, as can be seen most clearly for position A in Fig. 6.7 left. Besides the ill-posedness of the inverse problem, such artefacts probably demonstrate limitations in the data sets used for reconstructions, in particular the limited angular sampling and deficiencies in the forward model used, neglecting for example the spectral dependance of the absorption and diffusion coefficients.

The reconstructed maximal absorption coefficient and the maximal dye concentration are dependent on lesion position, as is the reconstructed axial extension of the object. In each case, the maximum decreases towards the center of the cuvette, while the reconstructed volume increases due to the lower spatial resolution at larger depth of the object. At positions A and B, the absolute value of the reconstructed dye concentrations is too large. Due to uncertainties in the quantum yield η and the Omocyanine dye lifetime τ, such errors are to be expected. Furthermore, while improving the overall image quality, the chosen values of $r(i, \omega_q)$ have some effect on the reconstructed values. It is certainly challenging to achieve the correct absolute dye concentration from phantom experiments, let alone from *in vivo* data.

Conclusions

Several phantom measurements relevant for fluorescence optical mammography were carried out and nonlinearly reconstructed absorption and fluorescence contrast of lesion-simulating heterogeneities using the Rytov approximation (absorption contrast) and the normalized Born approximation (fluorescence contrast) was presented. A rectangular cuvette filled with a fluorescent scattering solution having tissue

like optical properties simulated an average-sized female breast gently compressed between two plates. A small object (2.1 ml) was placed at selected positions inside the phantom. The lesion-simulating object contained the same background scattering solution, yet the concentration of the fluorescent dye was 5 times higher compared to the background medium. Time-domain transmission and remittance measurements were carried out at the excitation and fluorescence wavelength for a large number of source positions sampled across the cuvette's entrance face and at each source position a small number of lateral source-detector offsets. Using the algebraic reconstruction technique, reconstructions of the absorption and fluorescence contrast were performed in Fourier domain for a small number of angular frequencies using data, normalized to the homogeneous (background) part of the phantom. The ART algorithm was extended by a noise-weighted relaxation term to incorporate noisy data into the reconstruction. This way, high frequency components of the measured temporal point spread functions can be used during the reconstruction without distorting the image. Additionally, the image vector was normalized to achieve a comparable regularization effect for the scattering and absorption image. Transmittance measurements taken at selected source-detector offsets improve axial resolution of the reconstructed absorption and fluorescence contrast to a certain degree. By including reflectance data at the excitation and fluorescence wavelength into the reconstruction besides transmittance data, depth resolution is significantly improved. Optimal results will be achieved when transmittance and reflectance measurements are carried out on either side of the compressed breast.

6.2.3 Sub-volume reconstruction

Nonlinear reconstructions of large volumes are computation-intensive. A new method is presented to perform nonlinear reconstructions in diffuse optical tomography including fluorescence mammography on large grids with a larger number of measurement data and more grid nodes than conventional reconstruction schemes. For this purpose, the volume of reconstruction is split into sub-volumes.

To speed up calculations or, in case of large volumes of interest (VOI) Ω, to make calculation feasible at all, the full reconstruction volume is broken down into multiple smaller volumes, on which image reconstruction can be processed independently. For this purpose, the VOI is split into several sub-volumes that altogether contain Ω. For each sub-volume a subset of the experimental or simulated data is used, because not all of the sources and detectors are positioned inside the selected sub-volume.

Throughout this section, the same notation as introduced in Sec. 6.1.2 is used but slightly extended. We denote the set of source-detector combinations i that refer to the entire volume Ω as Ξ. In the following section, we decompose the VOI Ω down to multiple smaller volumes v_j with associated sets ξ_j of source-detector combinations. In order to distinguish the parameters that enter the reconstruction of the entire volume Ω from the analogous quantities that are used in the reconstruction associated with a sub-volume v_j, the notation is augmented by the set of source-detector combinations. For example, the measurement data $\Phi(\boldsymbol{x}_{d_i}, \boldsymbol{x}_{s_i}, \omega_q)$ used in Sec. 6.1.2 is replaced by $\Phi(\boldsymbol{x}_{d_i(\Xi)}, \boldsymbol{x}_{s_i(\Xi)}, \omega_q)$ and $\Phi(\boldsymbol{x}_{d_i(\xi_j)}, \boldsymbol{x}_{s_i(\xi_j)}, \omega_q)$, respectively.

The volumes are chosen in such a way, that for each source-detector combination of the given data subset the integrals over the entire volume Ω of Eq. (6.3) are approximated by integrals over the sub-volume v_j. For this approximation to be valid, the main part of the weighting functions $a_i^\kappa(\boldsymbol{x}, \lambda, \omega_q)$, and $\widehat{a}_i^\kappa(\boldsymbol{x}, \lambda, \omega_q)$ should lie inside the sub-volume. More explicitly, the volume Ω which is probed by the set of source-detector combinations Ξ is split into n_v non-disjunct, convex sub-volumes v_j with

$$\Omega \subseteq \bigcup_{j \in \underline{n_\mathrm{v}}} v_j, \tag{6.32}$$

where $\underline{n_{\mathrm{v}}} = \{1, \ldots, n_{\mathrm{v}}\}$, so that for each sub-volume v_j there exists a non-empty subset of source-detector combinations $\xi_j \subseteq \Xi$ with

$$\boldsymbol{x}_{d_i} \subset v_j \quad \forall i \in \xi_j, \tag{6.33}$$

and

$$\boldsymbol{x}_{s_i} \subset v_j \quad \forall i \in \xi_j. \tag{6.34}$$

Nonlinear reconstruction of arbitrary large regions

The separation into sub-volumes allows one to perform at each iteration step κ a linear reconstruction via ART on each v_j independently and in parallel in the same way as explained in Sec. 6.1.2. Therefore, Green's functions $G_\kappa(\boldsymbol{x}, \boldsymbol{x}_{s_i(\xi_j)}, \omega_q)$ used in reconstructions at iteration step κ defined on the subvolume corresponding to subset ξ_j are obtained by solving the frequency domain diffusion equation for the background medium with absorption and diffusion coefficient calculated iteratively by

$$\begin{aligned} \mu_{\mathrm{a}}^{\kappa}(\boldsymbol{x}, \xi_j) &= \mu_{\mathrm{a}}^{0} + \sum_{0 \le i < \kappa} \delta\mu_{\mathrm{a}}^{i}(\boldsymbol{x}, \xi_j), \\ D^{\kappa}(\boldsymbol{x}, \xi_j) &= D^{0} + \sum_{0 \le i < \kappa} \delta D^{i}(\boldsymbol{x}, \xi_j), \end{aligned} \tag{6.35}$$

where μ_{a}^0 and D^0 are the optical properties of the homogeneous medium used in the reference scan. Considering a spatial and temporal δ-like source, the simulated data is given by $\Phi_\kappa^{\mathrm{sim}}(\boldsymbol{x}_{d_i(\xi_j)}, \boldsymbol{x}_{s_i(\xi_j)}, \omega_q) = G_\kappa(\boldsymbol{x}_{d_i(\xi_j)}, \boldsymbol{x}_{s_i(\xi_j)}, \omega_q)$.

Analogous to the method presented in Sec. 6.1.2, a system of linear equations $\boldsymbol{y} = A\boldsymbol{b}$ can be set up for each sub-volume, with the image vector

$$\boldsymbol{b} = (\delta\mu_{\mathrm{a}}^{\kappa}(\boldsymbol{x}_1, \xi_j), ..., \delta\mu_{\mathrm{a}}^{\kappa}(\boldsymbol{x}_{N(\xi)}, \xi_j), \delta D^{\kappa}(\boldsymbol{x}_1, \xi_j), ..., \delta D^{\kappa}(\boldsymbol{x}_{N(\xi)}, \xi_j))^T, \tag{6.36}$$

and the $2 \cdot k(\xi_j) \cdot p$ component signal vector $\boldsymbol{y}$ corresponding to source-detector combinations of subset ξ_j, and the $(2 \cdot k(\xi_j) \cdot p) \times 2N(\xi_j)$ system matrix A, where $k(\xi_j)$ is the number of source-detector combinations corresponding to ξ_j, p is the number of frequency components used during reconstructions on an FE grid of $N(\xi_j)$ vertices discretizing the sub-volume.

In contrast to the reconstruction carried out in Sec. 6.2.2 , the relaxation parameter r_{rlx} was chosen to be $r_{\mathrm{rlx}} = 0.9$, hence having no dependence on measurement noise and the chosen sub-volume.

At the end of each iteration, additional calculations have to be carried out before a new iteration cycle is started as explained in the following pseudocode and visualized in Fig. 6.8. In principle, arbitrary large VOIs can be reconstructed by this technique, because the volume of the VOI is not correlated to the size of the system matrix A, but only to the number of system matrices, which is given by n_{v}. Increasing the number of sub-volumes allows to decrease the dimension of the system matrices, resulting in multiple reconstruction tasks that can be processed in parallel or sequentially, each requiring less resources to solve for the image vector $\boldsymbol{b}$ compared with a single reconstruction of the entire VOI Ω.

Algorithm 2: nonlinear reconstruction using sub-volumes

Step 1: Collection of experimental time-domain data for the object scan, $\widetilde{\Phi}(\boldsymbol{x}_{d_i(\Xi)}, \boldsymbol{x}_{s_i(\Xi)}, \lambda, t)$, and for the reference scan, $\widetilde{\Phi}_0(\boldsymbol{x}_{d_i(\Xi)}, \boldsymbol{x}_{s_i(\Xi)}, \lambda, t)$, of all source-detector combinations Ξ. Fourier-transformation, and additional preprocessing of measurement data as described in Sec. 6.2.1.

Step 2: The volume Ω is separated into n_{v} sub-volumes v_j (see Eq. (6.32)). For each sub-volume v_j, there exists an associated subset of source-detector combinations, ξ_j. The measurement data, $\Phi(\boldsymbol{x}_{d_i(\Xi)}, \boldsymbol{x}_{s_i(\Xi)}, \lambda, \omega_q)$, and reference data, $\Phi_0(\boldsymbol{x}_{d_i(\Xi)}, \boldsymbol{x}_{s_i(\Xi)}, \lambda, \omega_q)$, are split into n_{v} subsets of measurement data, $\Phi(\boldsymbol{x}_{d_i(\xi_j)}, \boldsymbol{x}_{s_i(\xi_j)}, \lambda, \omega_q)$, and reference data, $\Phi_0(\boldsymbol{x}_{d_i(\xi_j)}, \boldsymbol{x}_{s_i(\xi_j)}, \lambda, \omega_q)$, respectively.

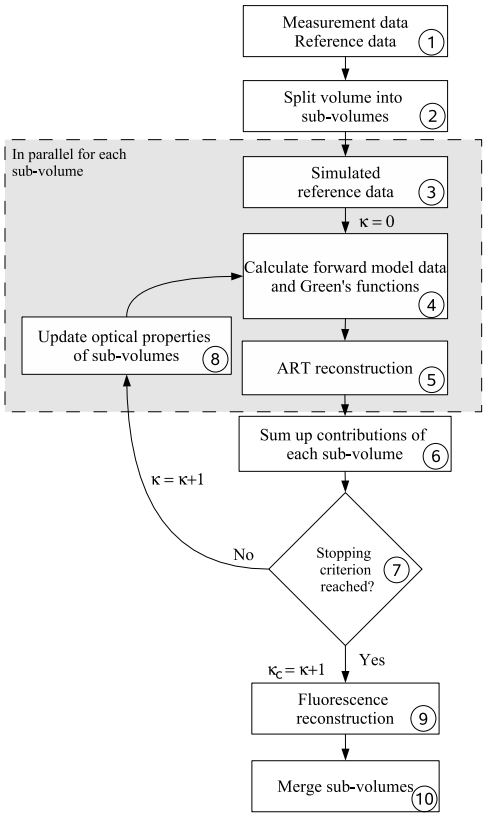

Figure 6.8: Schematic view of nonlinear reconstruction algorithm using sub-volumes. The reconstruction is initialized with a homogeneous distribution at iteration $\kappa = 0$.

Step 3: For each subset of source-detector combinations ξ_j, simulated reference data $\Phi_0^{\mathrm{sim}}(\boldsymbol{x}_{d_i(\xi_j)}, \boldsymbol{x}_{s_i(\xi_j)}, \lambda, \omega_q)$ are calculated for all source-detector combinations of the subset ξ_j and the p angular frequency components ω_q ($q = 1, ..., p$) that are used in the reconstruction. To this end, Eq. (5.11) is solved for a homogeneous medium with the absorption coefficient $\mu_{\mathrm{a}}^0(\lambda)$ and the diffusion coefficient $D^0(\lambda)$ of the reference scan.

Step 4: Calculations of the Green's functions $G_\kappa(\boldsymbol{x}_{d_i(\xi_j)}, \boldsymbol{x}, \lambda, \omega_q)$, $G_\kappa(\boldsymbol{x}, \boldsymbol{x}_{s_i(\xi_j)}, \lambda, \omega_q)$, and $G_\kappa(\boldsymbol{x}_{d_i(\xi_j)}, \boldsymbol{x}_{s_i(\xi_j)}, \lambda, \omega_q)$ are carried out for all detector positions $\boldsymbol{x}_{d_i(\xi_j)}$ and all source positions $\boldsymbol{x}_{s_i(\xi_j)}$ of each subset ξ_j, and p angular frequency components ω_q on an FE grid containing v_j. Simulated data $\Phi_\kappa^{\mathrm{sim}}(\boldsymbol{x}_{d_i(\xi_j)}, \boldsymbol{x}_{s_i(\xi_j)}, \lambda, \omega_q)$ are calculated by solving the inhomogeneous diffusion equation with the reconstructed spatial distribution of absorption coefficients $\mu_{\mathrm{a}}^\kappa(\boldsymbol{x}, \lambda, \xi_j)$ and diffusion coefficients $D^\kappa(\boldsymbol{x}, \lambda, \xi_j)$ for each source-detector combination i and angular frequency ω_q. We initialize the nonlinear iterations with $\kappa = 0$. The calculation of $G_{\kappa=0}(\boldsymbol{x}_{d_i(\xi_j)}, \boldsymbol{x}_{s_i(\xi_j)}, \lambda, \omega_q)$ can be omitted in this case ($\kappa = 0$) since in this case the result is equal to the reference data $\Phi_0^{\mathrm{sim}}(\boldsymbol{x}_{d_i(\xi_j)}, \boldsymbol{x}_{s_i(\xi_j)}, \lambda, \omega_q)$. Calculations for all sub-volumes can be carried out in parallel.

Step 5: The former results (Green's functions $G_\kappa(\boldsymbol{x}, \boldsymbol{x}_{s_i(\xi_j)}, \lambda, \omega_q)$ and $G_\kappa(\boldsymbol{x}_{d_i(\xi_j)}, \boldsymbol{x}, \lambda, \omega_q)$, simulated data $\Phi_0^{\mathrm{sim}}(\boldsymbol{x}_{d_i(\xi_j)}, \boldsymbol{x}_{s_i(\xi_j)}, \lambda, \omega_q)$, $\Phi_\kappa^{\mathrm{sim}}(\boldsymbol{x}_{d_i(\xi_j)}, \boldsymbol{x}_{s_i(\xi_j)}, \lambda, \omega_q)$, and experimental data $\Phi_0(\boldsymbol{x}_{d_i(\xi_j)}, \boldsymbol{x}_{s_i(\xi_j)}, \lambda, \omega_q)$, $\Phi(\boldsymbol{x}_{d_i(\xi_j)}, \boldsymbol{x}_{s_i(\xi_j)}, \lambda, \omega_q)$) obtained for each sub-volume v_j with its associated subset of source-detector combinations ξ_j are used to solve Eq. (6.3) by ART to reconstruct the contributions of the iterative step κ to optical properties, i.e. components $\delta\mu_{\mathrm{a}}^\kappa(\boldsymbol{x}, \lambda, \xi_j)$ and $\delta D^\kappa(\boldsymbol{x}, \lambda, \xi_j)$ of the update vector $\boldsymbol{b}$.

Step 6: The spatial distribution of the absorption coefficient $\mu_{\mathrm{a}}^\kappa(\boldsymbol{x}, \lambda, \Xi)$ in the entire VOI Ω is approximated by the contributions of each sub-volume v_j according to the following equation

$$\mu_{\mathrm{a}}^\kappa(\boldsymbol{x}, \lambda, \Xi) \approx \left[\sum_{j \in \underline{n_{\mathrm{v}}}} \mu_{\mathrm{a}}^\kappa(\boldsymbol{x}, \lambda, \xi_j) a^\kappa(\boldsymbol{x}, \lambda, \xi_j)^2\right] \left[\sum_{j \in \underline{n_{\mathrm{v}}}} a^\kappa(\boldsymbol{x}, \lambda, \xi_j)^2\right]^{-1} \quad \forall \boldsymbol{x} \in \Omega, \tag{6.37}$$

and similarly

$$D^\kappa(\boldsymbol{x}, \lambda, \Xi) \approx \left[\sum_{j \in \underline{n_{\mathrm{v}}}} D^\kappa(\boldsymbol{x}, \lambda, \xi_j) \widehat{a}^\kappa(\boldsymbol{x}, \lambda, \xi_j)^2\right] \left[\sum_{j \in \underline{n_{\mathrm{v}}}} \widehat{a}^\kappa(\boldsymbol{x}, \lambda, \xi_j)^2\right]^{-1} \quad \forall \boldsymbol{x} \in \Omega, \tag{6.38}$$

with the weighting factors $a^\kappa(\boldsymbol{x}, \lambda, \xi_j)$, $\widehat{a}^\kappa(\boldsymbol{x}, \lambda, \xi_j)$ obtained by summing all sensitivity factors over all source-detector combinations and angular frequency components,

$$a^\kappa(\boldsymbol{x}, \lambda, \xi_j) = \sum_{q=1}^{2kp} \sum_{i \in \xi_j} \|a_i^\kappa(\boldsymbol{x}, \lambda, \omega_q, \xi_j)\|, \tag{6.39}$$

$$\widehat{a}^\kappa(\boldsymbol{x}, \lambda, \xi_j) = \sum_{q=1}^{2kp} \sum_{i \in \xi_j} \|\widehat{a}_i^\kappa(\boldsymbol{x}, \lambda, \omega_q, \xi_j)\|. \tag{6.40}$$

Step 7: When the stopping criterion is reached (e.g. the norm of the reconstructed image update vector $\boldsymbol{b}$ is lower than a given limit), we set $\kappa_c = \kappa + 1$ and the fluorescence reconstruction is started in step 9. If the stopping criterion has not been reached, further iterations are needed.

Step 8: The updated absorption coefficients and diffusion coefficients relating to the sub-volume v_j are obtained from Eq. (6.37) by setting $\mu_{\mathrm{a}}^{\kappa}(\boldsymbol{x},\xi_j) = \mu_{\mathrm{a}}^{\kappa}(\boldsymbol{x},\Xi)$ for all $\boldsymbol{x} \in v_j$, and analogously for $D^{\kappa}(\boldsymbol{x},\xi_j) = D^{\kappa}(\boldsymbol{x},\Xi)$, see Eq. (6.38).

Step 9: Using the reconstructed absorption, $\mu_{\mathrm{a}}^{\kappa_c}(\boldsymbol{x},\lambda,\Xi)$, and diffusion coefficient, $D^{\kappa_c}(\boldsymbol{x},\lambda,\Xi)$, the Green's functions $G_{\mathrm{f}}^{\kappa_c}(\boldsymbol{x}_{d_i(\xi_j)},\boldsymbol{x},\lambda,\omega_q)$ and $G^{\kappa_c}(\boldsymbol{x},\boldsymbol{x}_{s_i(\xi_j)},\lambda,\omega_q)$ are calculated for each source and detector position on each subvolume v_j. Fluorescent dye concentrations, $c(\boldsymbol{x},\xi_j)$, are reconstructed by Eq. (6.9) using ART.

Step 10: The reconstructed dye concentration $c(\boldsymbol{x},\Xi)$ in the entire volume Ω is obtained from the reconstructed dye concentrations $c(\boldsymbol{x},\xi_j)$ relating to the sub-volumes v_j according to

$$c(\boldsymbol{x},\Xi) \approx \left[\sum_{j\in\underline{n_{\mathrm{v}}}} c^{\kappa_c}(\boldsymbol{x},\xi_j)a^{\mathrm{f}}(\boldsymbol{x},\lambda,\xi_j)^2\right]\left[\sum_{j\in\underline{n_{\mathrm{v}}}} a^{\mathrm{f}}(\boldsymbol{x},\lambda,\xi_j)^2\right]^{-1} \quad \forall \boldsymbol{x}\in\Omega, \tag{6.41}$$

using the weighting factors

$$a^{\mathrm{f}}(\boldsymbol{x},\lambda,\xi_j) = \sum_{q=1}^{2kp}\sum_{i\in\xi_j} \|a_i^{\mathrm{f}}(\boldsymbol{x},\lambda,\omega_q,\xi_j)\|. \tag{6.42}$$

It can be seen easily that algorithm 2 is equivalent to algorithm 1 for $n_{\mathrm{v}} = 1$ and $\xi_1 = \Xi$.

Comparison of results of standard nonlinear reconstruction technique and of sub-volume method using simulated and experimental data

The convergence of the standard nonlinear technique and of the sub-volume method is investigated by calculating residua between simulated or experimental phantom data (target values) and actual data calculated after each iteration step. Alternatively, reconstruction errors of the absorption and reduced scattering coefficients are determined after each iteration step. Results obtained by the sub-volume method agree with those of the standard technique provided the separation of the entire volume of interest into a small number of sub-volumes does not restrict further the range of angular sampling of the entire data sets, otherwise, reconstruction errors increase.

Standard nonlinear reconstruction of simulated phantom data (no volume decomposition)

In this section convergence of the standard nonlinear reconstruction technique as well as the reconstruction error of the resulting absorption and reduced scattering coefficients are investigated. To this end, a nonlinear reconstruction of absorption and reduced scattering coefficients was performed on a cuboid of volume $\Omega = 8\times 8\times 6$ cm^3, with the origin of the coordinate system defined at the center of the entrance face (source plane) of the cuboid. Simulations using $n_{\mathrm{src}} = 25$ fixed sources at $z = 0$ cm, $x = \pm 2, \pm 1, 0$ cm, $y = \pm 2, \pm 1, 0$ cm with $\sigma_{\mathrm{src}} = 6$ mm (see Eq. (5.62)), and $n_{\mathrm{det}} = 98$ fixed detectors at $z = 6$ cm, 0 cm, $x = \pm 3, \pm 2, \pm 1, 0$ cm, $y = \pm 3, \pm 2, \pm 1, 0$ cm were carried out. The source (A_{src}) and detector (A_{det}) arrangements are symmetrical with respect to the in-plane (x, y) position of the center ($x_{\mathrm{v}} = y_{\mathrm{v}} = 0$, $z_{\mathrm{v}} = 3$ cm) of the volume Ω. For each source position data from 97 detector positions enter the reconstruction, except for the detector which is exactly at the source position.

The (homogeneous) background optical properties of the numerical phantom are $\mu_{\mathrm{a}}^0 = 0.0042$ mm^{-1}, and $D^0 = 1/(3\mu'_{\mathrm{s},0}) = 0.33$ mm. A spherical heterogeneity of 1 cm radius is located at $x = y = 0$, $z = 2$ cm, i.e. shifted from the center position of the phantom towards the source plane. The optical properties

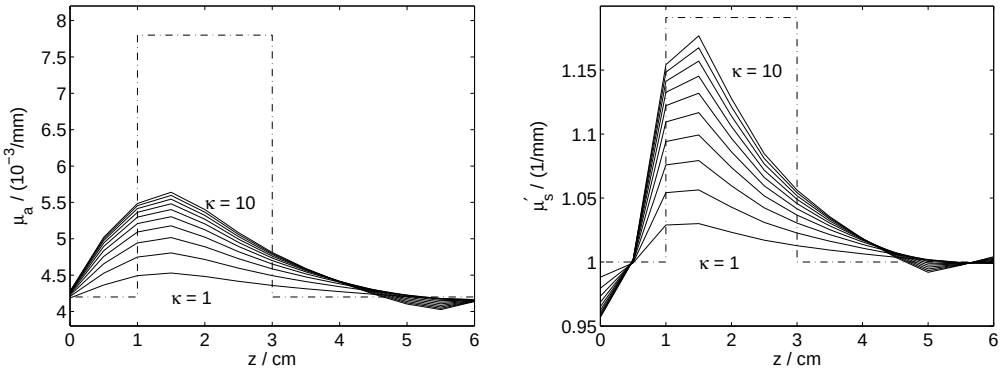

Figure 6.9: Line profiles ($x = y = 0$) of absorption (left) and reduced scattering (right) coefficients nonlinearly reconstructed from noise-free simulated phantom data. The full lines interpolate the results of all ten iteration steps κ of the nonlinear reconstruction with increasing iteration number κ for increasing values at the center of the volume Ω ($z = 3$ cm). The dashed-dotted lines represent the expected profiles of the absorption coefficients $\mu_\mathrm{a}(z)$ (left) and reduced scattering coefficients $\mu_\mathrm{s}'(\mathrm{z})$ (right).

of the spherical heterogeneity are $\mu_\mathrm{a}^\mathrm{sph} = 0.0062$ mm^{-1}, $D^\mathrm{sph} = 0.28$ mm. The reflectivity at the volume surface was chosen to be $K = 0.5$. Since the optical properties are chosen to be independent of the laser wavelength, the wavelength dependence will be neglected in the following of this section. Therefore, we denote the absorption coefficient and the diffusion coefficient of the phantom as $\mu_\mathrm{a}(\boldsymbol{x})$ and $D(\boldsymbol{x})$, respectively.

Ten iterations κ of nonlinear reconstruction were carried out using a coarse FE grid of cubic cells of $(0.25\ \mathrm{cm})^3$ volume together with prior knowledge on the absorption and diffusion contrast of the heterogeneity, i.e. the values $\Delta\mu_\mathrm{a}^\star = 0.004$ mm^{-1} and $\Delta D^\star = 1.67$ mm were used. The ART regularization parameter was chosen as $\lambda_\mathrm{reg}(D) = \lambda_\mathrm{reg}(\mu_\mathrm{a}) = 0.3$ and 7 ART iterations were performed at each reconstruction cycle κ. Only the angular frequency $\omega = 2\pi \cdot 100$ MHz was used during the reconstruction.

The line profiles ($x = y = 0$) of the reconstructed (full lines) absorption coefficient (Fig. 6.9 left) and reduced scattering coefficient (Fig. 6.9 right) were obtained by interpolating the results calculated after each reconstruction cycle, while the dashed-dotted lines indicate the absorption $\mu_\mathrm{a}(\boldsymbol{x})$ and reduced scattering coefficient $D(\boldsymbol{x})$ of the numerical phantom, respectively. As was discussed in Sec. 6.2.2, the maximum of the reconstructed absorption coefficient and reduced scattering coefficient is shifted from the true axial position of the spherical heterogeneity at $z = 2$ cm towards the source plane (entrance face) of the numerical phantom (cuvette). As can bee seen in Fig. 6.9 right, the maximum of the reconstructed scattering coefficient at iteration number $\sigma = 10$ is similar to the value of the spherical heterogeneity, while the maximum of the reconstructed absorption coefficient (Fig. 6.9, right) at the same iteration number is considerably underestimated, due to the chosen regularization parameter.

The relative reconstruction error for absorption ($1 - E^\mathrm{a}(\kappa)$) and for scattering ($1 - E^\mathrm{s}(\kappa)$) is calculated by

$$
\begin{aligned}
E^\mathrm{a}(\kappa) &= \left(\int_\Omega \left(\mu_\mathrm{a}^\kappa(\boldsymbol{x}) - \mu_\mathrm{a}^0 \right)^2 d\Omega \right)^{1/2} \left(\int_\Omega \left(\mu_\mathrm{a}(\boldsymbol{x}) - \mu_\mathrm{a}^0 \right)^2 d\Omega \right)^{-1/2}, \\
E^\mathrm{s}(\kappa) &= \left(\int_\Omega \left(\frac{1}{D^\kappa(\boldsymbol{x})} - \frac{1}{D^0} \right)^2 d\Omega \right)^{1/2} \left(\int_\Omega \left(\frac{1}{D(\boldsymbol{x})} - \frac{1}{D^0} \right)^2 d\Omega \right)^{-1/2}.
\end{aligned}
\tag{6.43}
$$

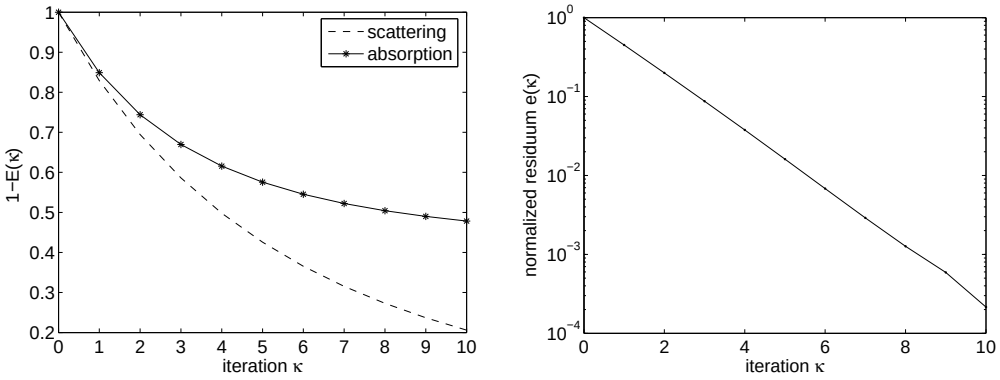

Figure 6.10: (left) Reconstruction error $1 - E(\kappa)$ for absorption and reduced scattering coefficient versus iteration number κ. (right) Normalized residuum $e(\kappa)$ versus iteration number κ.

The result is shown in Fig. 6.10 (left), where the dashed line represents the error of the scattering reconstruction, $1-E^{\mathrm{s}}(\kappa)$, and the full line is the relative error of the absorption reconstruction, $1-E^{\mathrm{a}}(\kappa)$. Convergence of the absorption coefficient is achieved at $\kappa \approx 8$, while the scattering reconstruction error still decreases. It should be noted that the reconstruction converges to a wrong image ($\lim_{\kappa\to\infty} E(\kappa) \neq 1$) in both cases which is to be expected, when the heterogeneity is smaller than the resolution of the measurement system taking the optical properties of the phantom into account. The normalized residuum $e(\kappa)$ is given by the ratio of the norm of the signal vector $\boldsymbol{y}$ at iteration κ to that at $\kappa = 0$,

$$e(\kappa) = \left(\sum_{l=1}^{2kp} \left[y_l(\kappa)\right]^2\right)^{1/2} \Bigg/ \left(\sum_{l=1}^{2kp} \left[y_l(\kappa=0)\right]^2\right)^{1/2}, \tag{6.44}$$

and is shown in Fig. 6.10 (right). For the first ten iterations the residuum decreases approximately exponentially with each iteration step.

Nonlinear reconstruction of simulated phantom data using sub-volumes and optimal angular sampling

In this section we compare the results, in particular reconstruction errors of absorption coefficients and reduced scattering coefficients as well as convergence, of our sub-volume reconstruction technique with those of the standard nonlinear procedure that reconstructs the entire volume of interest at once. The numerical phantom used corresponds to that of the previous paragraph, with the same size, location, and optical properties of the heterogeneity, and the same background optical properties. However, in order to allow for a sufficient number of sub-volume decompositions, the size of the phantom was increased ($\Omega = 16 \times 16 \times 6$ cm^3), and the number of sources and detectors raised to $n_{\mathrm{src}} = 81$ and $n_{\mathrm{det}} = 242$, respectively. The fixed sources ($z = 0$ cm) were placed at $x = \pm4, \pm3, \pm2, \pm1, 0$ cm, $y = \pm4, \pm3, \pm2, \pm1, 0$ cm, the fixed detectors ($z = 6$ cm, 0 cm) at $x = \pm5, \pm4, \pm3, \pm2, \pm1, 0$ cm, $y = \pm5, \pm4, \pm3, \pm2, \pm1, 0$ cm, symmetrically arranged with respect to the center of the phantom. Sources were simulated for $\sigma_{\mathrm{src}} = 6$ mm (see Eq. (5.62)) and noise-free simulated data was calculated for all detector positions. Table 6.2.3 summarizes the sub-volume decompositions. The first three columns list the number of sub-volumes (n_{v}), the number of sources (n_{src}) and detectors (n_{det}) associated with each sub-volume. The next two columns indicate the arrangement of sources (A_{src}) and detectors (A_{det}), with each source/detector separated from its nearest neighbor by 1 cm, and each source and detector arrangement, centered with respect to the

in-plane coordinates (x_v, y_v) of the center of the corresponding sub-volume, listed in the last column. In addition, the sizes of each sub-volume are given in Table 1. When reconstruction was carried out on a selected sub-volume v_j for each source position of the associated source arrangement A_src, data from all detectors of the associated detector arrangement A_det entered the reconstruction apart from the detector located at the source position. All sub-volumes were assumed to have a reflectivity of $K = 0.5$ at their surface.

Reconstruction of optical properties using sub-volume decompositions will lead to additional reconstruction errors compared to the standard single-volume nonlinear reconstruction procedure. With each sub-volume, fictitious boundaries with a reflectivity of $K = 0.5$ are introduced leading to edge effects, i.e. modified photon trajectories. Equation (6.37) and (6.38) used to estimate reconstructed absorption and diffusion coefficients (reduced scattering coefficients) from results obtained by sub-volume reconstructions, are approximations only. Furthermore, the smaller a particular sub-volume v_j is chosen, the smaller is the size of its associate source (A_src) and detector (A_det) arrangements, and hence angular coverage is reduced, leading to increased reconstruction errors. For example, source-detector combinations (i) corresponding to large source-detector offsets $\Delta x, \Delta y, \Delta z$, and hence large projection angles that are contained in the data set of the entire volume Ω ($i \in \Xi$), might not be consistent with smaller sub-volumes v_j ($i \notin \xi_j$) leading to a smaller angular coverage. It follows that the entire data sets used in sub-volume reconstruction is smaller than the data set used to reconstruct the absorption and reduced scattering coefficients by the standard nonlinear technique on the entire volume Ω, i.e. $\bigcup_{j \in n_\mathrm{v}} \xi_j \subset \Xi$.

In order to identify reconstruction errors associated with decompositions into sub-volumes, reconstructions were carried out for four different decompositions of Ω (see Table 6.2.3). In addition, a reconstruction of the entire volume Ω was performed ($n_\mathrm{v} = 1$) for comparison.

The results of the reconstruction are shown in Fig. 6.11 with the reconstruction error of the absorption coefficient $1-E^\mathrm{a}(\kappa)$ on the left, and the reconstruction error of the reduced scattering coefficient $1-E^\mathrm{s}(\kappa)$ on the right, for each of the various decompositions of the entire volume into sub-volumes (see Table 6.2.3). For the absorption coefficient, the error decreases quite rapidly up to $\kappa \approx 5$ followed by a slower decrease. As expected, the error depends quite markedly on the number of sub-volumes used, increasing with the number of sub-volumes, i.e. with decreasing sub-volume size. In the case $n_\mathrm{v} = 4$, the in-plane (x,y) position of the heterogeneity is shifted towards the border of the source (A_src) and detector (A_det) arrangements for all sub-volumes, while in the case $n_\mathrm{v} = 5$ there is an additional sub-volume, where the in-plane (x,y) position of the heterogeneity is at the center of the associated source and detector arrangements. It can be seen from Fig. 6.11 that the error of both sub-volume decompositions is nearly identical for all iterations. It follows that the reconstruction error does not strongly depend on the in-plane position of the heterogeneity, but on the decomposition of source-detector combinations ξ_j included in the reconstruction.

As can be seen from Fig. 6.11 (left) the reconstruction error $1 - E^\mathrm{a}(\kappa = 10)$ is about 0.42 for $n_\mathrm{v} = 4$, while the standard nonlinear technique $n_\mathrm{v} = 1$ yields a value close to $1 - E^\mathrm{a}(\kappa = 10) = 0.37$. The lower reconstruction error in the last case is (at least partially) caused by the better angular coverage compared to the result obtained by the sub-volume method $n_\mathrm{v} = 4$. Likewise, the smaller source ($A_\mathrm{src} = 3 \times 3$) and detector ($A_\mathrm{det} = 7 \times 7$) arrangements considered in the previous paragraph lead to larger reconstruction errors $1 - E^\mathrm{a}(\kappa = 10) \approx 0.5$ by the standard nonlinear reconstruction scheme compared to the larger source ($A_\mathrm{src} = 9 \times 9$) and detector ($A_\mathrm{det} = 11 \times 11$) arrangements that entered the standard reconstruction in the present section. The dependence of the reconstruction error of the reduced scattering coefficient $1 - E^\mathrm{s}(\kappa)$ on iteration number κ is similar to that of the absorption coefficient. The scattering reconstruction error decreases with increasing iteration number κ and drops even below zero at higher iteration numbers and for sub-volume decompositions $n_\mathrm{v} \leq 5$. It follows from Eq. (6.43) that scattering contrast is overestimated in these cases. Similar to absorption, the reconstruction error of the reduced scattering coefficient increases with decreasing size of the sub-volume v_j, and decompositions into $n_\mathrm{v} = 4$ and $n_\mathrm{v} = 5$ sub-volumes (see Table 6.2.3) result in essentially the same scattering reconstruction errors. Furthermore, comparing Fig. 6.10 (dashed line) and Fig. 6.11 right

Table 6.1: Sub-volume decomposition with optimal angular sampling.

n_v	n_src	n_det	A_src	A_det	v_j/cm^3	sub-vol. center pos./cm
1	81	242	9×9	11×11	$16\times 16\times 6$	$x_\mathrm{v}=y_\mathrm{v}=0$
4	49	162	7×7	9×9	$9\times 9\times 6$	$x_\mathrm{v},y_\mathrm{v}=\pm 1$
5	49	162	7×7	9×9	$9\times 9\times 6$	$x_\mathrm{v},y_\mathrm{v}=\pm 1$ and $x_\mathrm{v}=y_\mathrm{v}=0$
9	25	98	5×5	7×7	$8\times 8\times 6$	$x_\mathrm{v},y_\mathrm{v}=\pm 2,0$
49	9	50	3×3	5×5	$7\times 7\times 6$	$x_\mathrm{v},y_\mathrm{v}=\pm 3,\pm 2,\ldots,0$

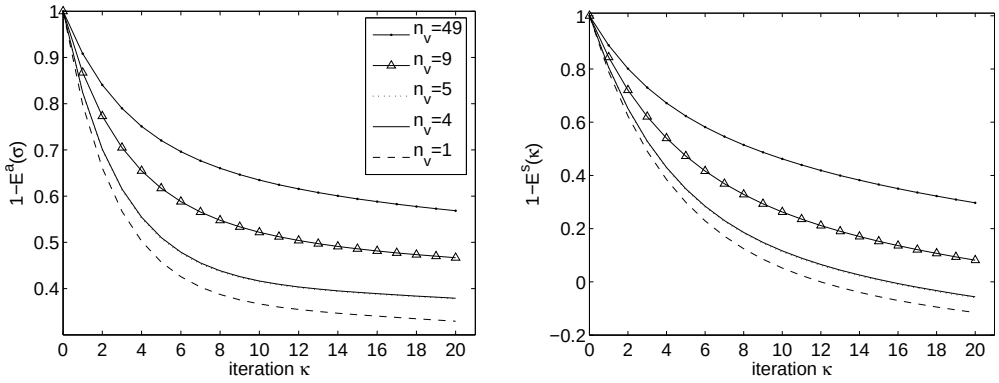

Figure 6.11: Reconstruction error of absorption ($1-E^\mathrm{a}(\kappa)$) coefficient (left) and reduced scattering ($1-E^\mathrm{s}(\kappa)$) coefficient (right), of the nonlinear reconstruction of noise-free simulated phantom data versus iteration number κ from five different sub-volume decompositions (see Table 6.2.3). All source-detector combinations consistent with sub-volume decompositions were included in the reconstruction (optimal angular sampling).

(dashed line), one concludes that the scattering reconstruction error ($1-E^\mathrm{s}(\kappa=10)$) obtained from the standard nonlinear reconstruction procedure $n_\mathrm{v}=1$ decreases with better angular sampling as was the case with the absorption reconstruction error ($1-E^\mathrm{a}(\kappa=10)$).

The normalized residuum of the iterations is shown in Fig. 6.12 and decreases for all sub-volume decompositions approximately exponentially until $\kappa=10$ is reached. From this step on, the residuum of reconstructions using sub-volumes decreases more slowly, while the residuum for the entire volume ($n_\mathrm{v}=1$) continues to decrease approximately exponentially.

Nonlinear reconstruction of simulated phantom data using sub-volumes and restricted angular sampling

In the previous two paragraphs all source detector combinations that are consistent with the source (A_src) and detector (A_det) arrangements of a particular (sub-)volume entered the reconstruction. As mentioned above for the entire volume Ω or sufficiently large sub-volumes v_j, this situation is rather unrealistic, since data from source-detector combinations with large source-detector offsets (Δx, Δy, Δz) and hence large source-detector distances might not provide additional information because of poor signal-to-noise ratios. In this section we consider a more realistic situation by restricting source-detector offsets to e.g. -3 cm $\leq \Delta x \leq$ 3 cm, -3 cm $\leq \Delta y \leq$ 3 cm, and $\Delta z = 0, \pm 6$ cm for all sub-volumes considered. Again,

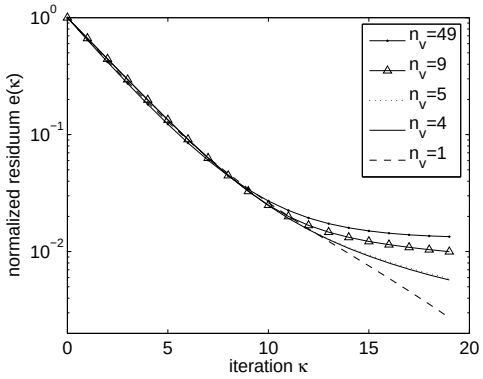

Figure 6.12: Normalized residuum $e(\kappa)$ (see Eq. (6.44)) versus iteration number κ for the five different sub-volume decompositions of the entire volume Ω (see Table 6.2.3).

the same phantom is used as in the previous section with the same size ($\Omega = 16 \times 16 \times 6$ cm^3), the same background optical properties, the same size and optical properties of the spherical heterogeneity, but with the heterogeneity located at the center $x = y = 0$, $z = 3$ cm of the phantom. The entire volume Ω is sub-divided (see Table 6.2) into the same number n_v of sub-volumes, centered at the same positions $x_\mathrm{v}, y_\mathrm{v}$ as in the previous paragraph. However, the size of the sub-volumes v_j and the size of the associated source (A_src) and detector (A_det) arrangements have been enlarged considerably resulting in higher numbers of sources and detectors, with each source/detector separated from its nearest neighbor by 1 cm. Again, the source and detector arrangements associated with a particular sub-volume v_j are centered with respect to the in-plane $(x_\mathrm{v}, y_\mathrm{v})$ coordinates of the center of the sub-volume. All source (A_src) and detector (A_det) arrangements, even those associated with the smallest sub-volumes ($n_\mathrm{v} = 49$, see Table 6.2), are consistent with the (restricted) source-detector offsets $|\Delta x_\mathrm{max}| = 3$ cm, $|\Delta y_\mathrm{max}| = 3$ cm. More precisely, for each sub-volume decomposition of Table 6.2, all source-detector combinations entering reconstruction entirely sample the restricted set of source-detector combinations Ξ of the entire volume Ω, i.e.

$$\Xi = \bigcup_{j \in \underline{n_\mathrm{v}}} \xi_j. \tag{6.45}$$

In the present example, sources are placed on both faces ($z = 0$ and $z = 6$ cm) of the phantom, and for each source position noise-free simulated data were calculated at all detectors in transmission and reflection, apart from the detector that coincides with the particular source. As before, sources were simulated with $\sigma_\mathrm{src} = 6$ mm and reflectivity of sub-volume surfaces was set to $K = 0.5$.

The results of the reconstruction are illustrated in Fig. 6.13 for the five sub-volume decompositions listed in Table 6.2. Reconstruction errors of the absorption ($1 - R^\mathrm{a}(\kappa)$) coefficient (left) and reduced scattering ($1 - R^\mathrm{s}(\kappa)$) coefficient (right) coincide for sub-volume decompositions with $n_\mathrm{v} = 1, 4, 5$ within 1%, whereas decompositions into larger numbers of sub-volumes ($n_\mathrm{v} = 9, 49$) lead to additional reconstruction errors. As can be seen by comparing Fig. 6.13 left and Fig. 6.11 left, the restricted angular sampling generally raises the absorption reconstruction error, this increase being most significant for the standard reconstruction results ($n_\mathrm{v} = 1$), i.e. from 0.37 ($\kappa = 10$) up to 0.54 ($\kappa = 10$). In other words, by excluding large source-detector offsets with $|\Delta x| > 3$ cm, $|\Delta y| > 3$ cm, nearly the same reconstruction errors result from the standard ($n_\mathrm{v} = 1$) and sub-volume reconstructions for $n_\mathrm{v} = 4$ and $n_\mathrm{v} = 5$. In contrast to Fig. 6.11 (left), scattering reconstruction errors no longer turn negative at higher iteration number κ (see Fig. 6.13 right) when using data sets with restricted source-detector offsets (restricted angular sampling).

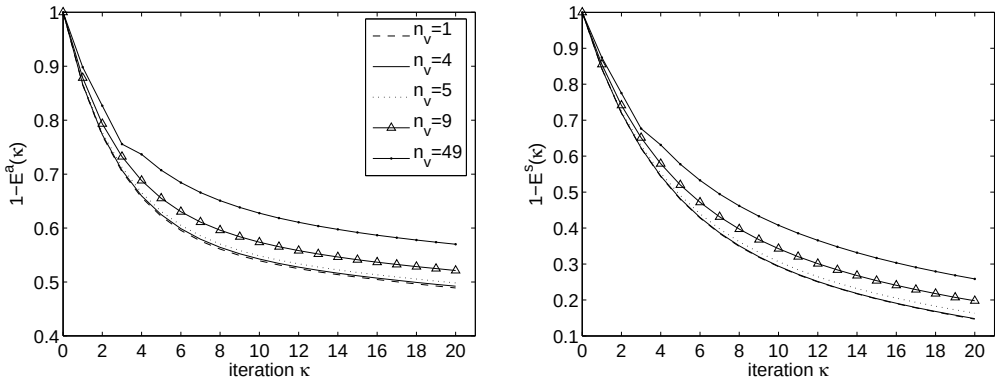

Figure 6.13: Reconstruction error of absorption ($1 - E^{\mathrm{a}}(\kappa)$) coefficient (left) reduced scattering ($1 - E^{\mathrm{s}}(\kappa)$) coefficient (right) of nonlinear reconstruction of noise-free simulated phantom data versus iteration number κ for five different sub-volume decompositions (see Table 6.2). All source-detector combinations consistent with restricted source-detector offsets ($|\Delta x| \leq 3$ cm, $|\Delta y| \leq 3$ cm) were included in the reconstruction (restricted angular sampling).

Table 6.2: Sub-volume decompositions with restricted angular sampling.

n_{v}	n_{src}	n_{det}	A_{src}	A_{det}	v_j/cm^3	sub-vol. center pos./cm
1	162	450	9×9	15×15	$16 \times 16 \times 6$	$x_{\mathrm{v}} = y_{\mathrm{v}} = 0$
4	98	338	7×7	13×13	$16 \times 16 \times 6$	$x_{\mathrm{v}}, y_{\mathrm{v}} = \pm 1$
5	98	338	7×7	13×13	$16 \times 16 \times 6$	$x_{\mathrm{v}}, y_{\mathrm{v}} = \pm 1$ and $x_{\mathrm{v}} = y_{\mathrm{v}} = 0$
9	50	242	5×5	11×11	$14 \times 14 \times 6$	$x_{\mathrm{v}}, y_{\mathrm{v}} = \pm 2, 0$
49	18	162	3×3	9×9	$12 \times 12 \times 6$	$x_{\mathrm{v}}, y_{\mathrm{v}} = \pm 3, \pm 2, \ldots, 0$

The normalized residuum of the various reconstructions is shown in Fig. 6.14. Again, an exponential decrease of the normalized residuum is observed initially, up to iteration number $\kappa = 6$ with a slower decrease at higher iterations. A comparison of Fig. 6.12 and Fig. 6.14 suggests that the slow decrease of the residuum at higher iteration numbers (see Fig. 6.12, $\kappa > 10$) observed for sub-volume decompositions ($n_{\mathrm{v}} > 1$) is caused by further restrictions on angular sampling due to the absence of large source-detector offsets in source (A_{src}) and detector (A_{det}) arrangements associated with the various sub-volume decompositions. The same argument can be put forward to explain the early onset of slow decrease of the residuum at $\kappa > 6$ in Fig. 6.14.

Nonlinear sub-volume reconstruction of experimental phantom data with restricted angular sampling

In this section we use our sub-volume method to reconstruct absorption and reduced scattering coefficients from the same experimental phantom data that were reconstructed by the standard nonlinear technique in Sec. 6.2.2. A rectangular phantom ($25 \times 25 \times 6$ cm^3) simulating a tumor bearing compressed breast and was filled with scattering and absorbing liquid ($D^0 = 0.032$ cm, $\mu_{\mathrm{a}}^0 = 0.025$ cm^{-1}) and contained a twin delrin cone (2.1 ml, in-plane diameter of 2 cm) filled with scattering and absorbing liquid ($D^{\mathrm{sph}} = D^0$,

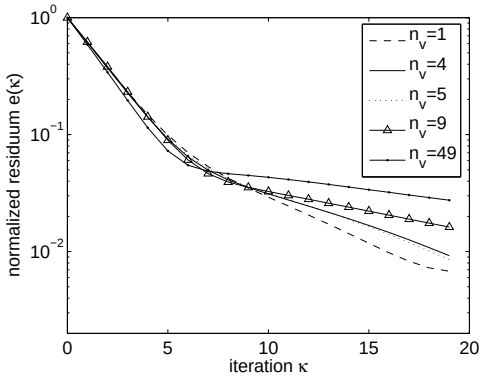

Figure 6.14: Normalized residuum $e(\kappa)$ versus iteration number κ for five different sub-volume decompositions (see Table 6.2). Source-detector combinations consistent with the restricted source-detector offsets $|\Delta x| \leq 3$ cm, $|\Delta y| \leq 3$ cm entered the reconstruction.

$\mu_{\mathrm{a}}^{\mathrm{sph}} = 0.031\ \mathrm{cm}^{-1}$) simulating a lesion. The twin cone was located at $x = y = 0$, $z = 2.2$ cm (position B, see Fig. 6.4). The laser beam (z-direction) was scanned along the horizontal x-direction at increments of 5 mm sampling the entrance face ($z = 0$) of the cuvette in a meander pattern at a total of 298 source positions (-4 cm $\leq x \leq 4$ cm, -4 cm $\leq y \leq 4$ cm). Transmittance and reflectance were recorded at source-detector offsets $\Delta x = \pm 4, \pm 3, ..., 0$ cm ($z = 6$ cm), $\Delta y = 0$, and $\Delta x = \pm 4, \pm 3, ..., \pm 1$ cm ($z = 0$ cm), $\Delta y = 0$, respectively. Table 6.3 lists the number of sources and detectors that enter the reconstruction together with the source (A_{src}) and detector (A_{det}) arrangements, the sizes and centers of the sub-volumes used, with sources/detectors separated from their nearest neighbors by 0.5 cm. The standard nonlinear reconstruction (see Sec. 6.1.2) was carried out using square source and detector arrangements, whereas the $n_{\mathrm{v}} = 21$ sub-volume reconstruction reported on in the present section included data from only one line-scan taken along the x-axis through the in-plane position ($x_{\mathrm{v}} = 0$, y_{v}) of the center of the sub-volume v_j considered, amounting to 17 source positions and 34 detector positions in total. Each cuboid sub-volume $v_j = 18 \times 6 \times 6\ \mathrm{cm}^3$ covered the entire width (18 cm) and depth (6 cm), but only half of the height (6 cm) of the volume of interest $\Omega = 18 \times 12 \times 6\ \mathrm{cm}^3$.

The standard nonlinear and sub-volume reconstructions differed in numerical details. Whereas a 3D Gaussian blurred source was used in the standard nonlinear reconstruction presented in Sec. 6.2.2, the 2D Gaussian blurred and exponentially damped source given in Eq. (5.62) was simulated in the sub-volume reconstructions.

Furthermore, the Voronoi [131] cell volume $w(\boldsymbol{x})$ differed slightly for the standard ($w(\boldsymbol{x}) \approx (1/2)^3\ \mathrm{cm}^3$) and sub-volume reconstructions ($w(\boldsymbol{x}) \approx (1/3)^3\ \mathrm{cm}^3$). ART reconstructions were carried out with standard nonlinear technique and without (sub-volume method) noise-weighted back-projection and somewhat different regularization schemes with only one common regularization parameter $\lambda_{\mathrm{reg}} = 0.02$ (see Sec. 6.2.2) or different regularization parameters ($\lambda_{\mathrm{reg}}(\mu_{\mathrm{a}}) = 0.30$, $\lambda_{\mathrm{reg}}(D) = 0.55$) of absorption and diffusion reconstruction (see Eq. (6.22) and (6.25)) were applied. On the other hand, in each case *a priori* estimates of the lesion contrast were set to $\Delta D^{\star} = \Delta\mu_{\mathrm{a}}^{\star} = 0$ and angular frequencies of $\omega_1 = 0$, $\omega_2 = 2\pi \cdot 117$ MHz and $\omega_3 = 2\pi \cdot 234$ MHz entered the reconstructions.

In Fig. 6.15 (left), we present line profiles ($x = y = 0$) of the absorption coefficients, in Fig. 6.15 (right), profiles of the reduced scattering coefficient reconstructed by the sub-volume method ($n_{\mathrm{v}} = 21$). Dashed lines correspond to the first iteration ($\kappa = 1$), solid lines to subsequent iterations ($\kappa = 2, ..., 7$). Higher iteration cycles increase the maximum of the profiles of the reconstructed absorption and reduced scattering coefficients, while at the same time reducing artefacts of the absorption coefficient close ($z > 5$

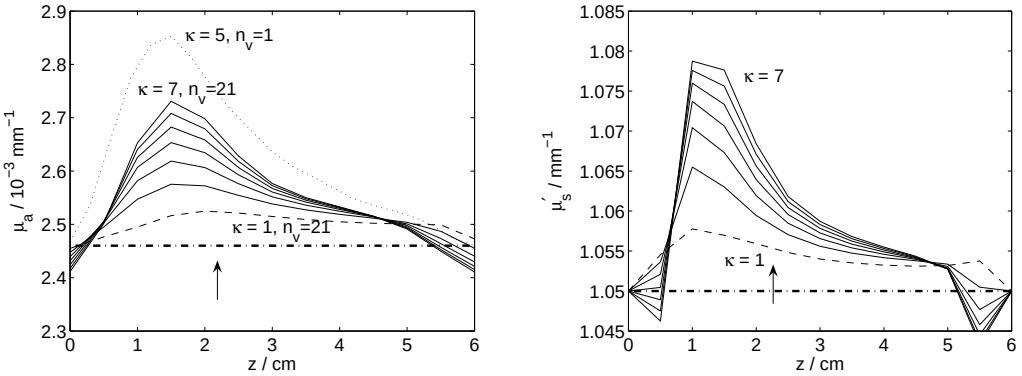

Figure 6.15: Line profiles ($x = y = 0$) of absorption (left) and reduced scattering (right) coefficient for iterations 1 through 7. The dashed lines correspond to the first iteration ($\kappa = 1$), full lines to subsequent ($\kappa = 2, ..., 7$)) iterations. The horizontal dashed-dotted lines correspond to the background absorption coefficient μ_{a}^0 (left) and reduced scattering coefficient $\mu'_{\mathrm{s},0}$ (right). The line profile of the absorption coefficient obtained from the standard ($n_{\mathrm{v}} = 1$) nonlinear ($\sigma = 5$) reconstruction is included (left) for comparison. The position of the twin cone is indicated by the arrows ($z = 2.2$ cm).

Table 6.3: Standard (see Sec. 6.1.2) and sub-volume reconstructions of experimental phantom data with restricted angular sampling ($|\Delta x| \leq 4$ cm, $|\Delta y| = 0$).

n_{v}	n_{src}	n_{det}	A_{src}	A_{det}	v_j/cm^3	sub-vol. center pos./cm
1	289	578	17×17	17×17	$18 \times 12 \times 6$	$x_{\mathrm{v}} = y_{\mathrm{v}} = 0$
21	17	34	17×1	17×1	$18 \times 6 \times 6$	$x_{\mathrm{v}} = 0, y_{\mathrm{v}} = \pm 5, \pm 4.5, ..., 0$

cm) to the exit face of the cuvette. In contrast, profiles of the reconstructed reduced scattering coefficient suffer from severe artefacts close to the entrance as well as the exit face. The maximum of the profiles of the absorption and reduced scattering coefficients are shifted towards the entrance face with respect to the true position of the twin cone, indicated by arrows. In Fig. 6.15 (left, dotted line) we show the results of the standard ($n_{\mathrm{v}} = 1$) nonlinear ($\kappa = 5$) reconstruction (see Fig. 6.7 left, solid line with stars) for the absorption coefficient. Although both results differ quantitatively, the profiles exhibit approximately same shape. It should be noted, however, that different regularization schemes were followed for the standard and sub-volume reconstructions, making a quantitative comparison difficult.

The convergence of the normalized residuum of the sub-volume reconstructions is shown in Fig. 6.16 for iterations $0 \leq \kappa \leq 7$. Compared with reconstructions based on noise-free simulated data (see Fig. 6.10 (right), Fig. 6.12, and Fig. 6.14), in the present case the nonlinear iteration steps do not reduce the residuum exponentially. Instead, the first iteration reduces the residuum by 30%, while the following 5 iteration steps lower the residuum further by only 15% of its initial value. At this point, convergence of the nonlinear sub-volume reconstruction has already been reached.

Conclusions

Non-linear time-resolved three dimensional DOT reconstruction suffers from severe performance problems. Due to the large number of FE grid nodes, and the enormous amount of Green's function data of

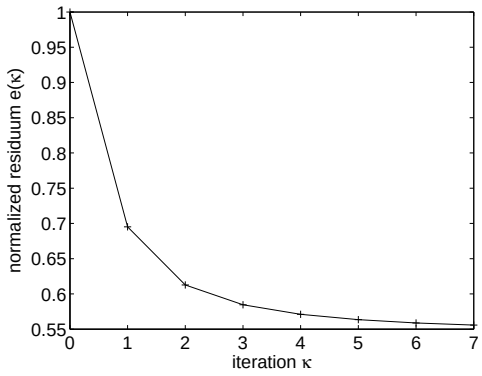

Figure 6.16: Normalized residuum $e(\kappa)$ versus iteration number κ for sub-volume reconstructions of experimental data.

all sources, detectors, angular frequency components, and optical wavelengths, calculations easily reach the limits of todays standard computers. While taking more source-detector combinations into account is beneficial for the reconstruction process and may produce images with improved spatial resolution and higher signal-to-noise ratios, it also causes severe problems in processing the associated amount of data with common computational techniques.

To reduce computational problems associated with large data sets we propose a decomposition of the simulated or experimental data into subsets and reconstructions on sub-volumes associated with each subset. This new method allows to reconstruct volumes of interest of arbitrary size on a fine grid, because the dimension of a sub-volume system matrix is not correlated to the entire volume that is reconstructed. Instead, the large system matrix of the entire volume is split into several smaller system matrices that can be inverted in parallel to gain speed and to lessen memory requirements.

We showed that the error is small when using sub-volume reconstructions compared with a full reconstruction of all source-detector combinations on a single FE grid, provided the source and detector arrangements allow a reconstruction via sub-volumes without omitting source-detector combinations important for e.g. angular sampling, i.e. scans with limited offsets. If this condition is met, examples discussed in the previous paragraphs illustrate that the reconstruction error using multiple grids is comparable with the error of the reconstruction using a single grid. Deviations between both results were smaller than 2%, depending on the number of sub-volumes used. However, when carrying out sub-volume reconstructions that require simulated or experimental data to be omitted thus restricting angular sampling significantly, considerable reconstruction errors are introduced. It follows that the decomposition of the entire volume into sub-volumes must be adapted to the source and detector positions sampled and to the information content including signal-to-noise ratio of the corresponding data.

Our method is limited to reasonable small numbers of sub-volumes. For a larger number of sub-volumes the benefits are offset by calculation overhead (e.g. caused by setting up the system equations), the slower convergence of the non-linear reconstruction, and the higher reconstruction errors.

To prove the feasibility of the proposed method we reconstructed experimental phantom data collected in a slab-like geometry using a cuvette, taking data in transmission and reflection with several offsets in x direction only. The nonlinear reconstruction of these data sets was carried out on 21 sub-volumes, each containing a subset of data belonging to a single line scan. We showed that the nonlinear sub-volume reconstruction converges and the nonlinear steps of higher order result in reduced artifacts and better spatial resolution.

6.2.4 Adaptive reconstruction initialization: handling large mismatches

A method is described to estimate the approximate shape of a patient's breast immersed into the cup filled with scattering liquid. A two compartment model, consisting of the homogeneous breast of estimated shape and the surrounding liquid, improves reconstruction results over a homogeneous one compartment model as was shown reconstructing optical properties of two corresponding phantoms.

Since Eq. (6.3) that is used for the reconstruction uses an perturbative approach which is only valid for small deviations $\delta\mu_\mathrm{a}(\boldsymbol{x},\lambda)$ and $\delta D(\boldsymbol{x},\lambda)$, convergence problems can be expected if the investigated breast is large and has a large mismatch in its optical properties compared with the scattering fluid used for the reference measurement.

To illustrate this effect, phantom scans and the corresponding reference scans were simulated using a 80D cup and optical properties of the (MF4.0) scattering fluid at $\lambda = 690$ nm as background values, i.e. $\mu_\mathrm{a}^0 = 0.0032\ \mathrm{mm}^{-1}$, $D^0 = 0.39$ mm. For the two simulations of object scans, a spherical heterogeneity was placed at the height of the top detector ring, having a radius of $r_\mathrm{sph} = 15$ mm and $r_\mathrm{sph} = 50$ mm, respectively, simulating a patient's breast in the latter case. The absorption coefficient of both spheres was increased moderately to $\mu_\mathrm{a}^\mathrm{sph} = 0.005\ \mathrm{mm}^{-1}$ while the scattering coefficient stayed unchanged. The absorption coefficients of both phantoms are given for the $y = 0$ slice in Fig. 6.17, top row.

The standard (linear) reconstruction of these scenarios is shown in Fig. 6.17, middle row. As can be seen, the small sphere is reconstructed correctly, while the large object shows a strong variation of its absorption coefficient inside the reconstructed sphere, resulting in a high absorption coefficients close to the sphere's surface, but nearly background value at its center.

The reconstruction results can be improved, if a so-called breast shape estimation is introduced, which approximately locates the border of breast from raw data analysis without the need of reconstruction. Details of the algorithm used for the breast shape estimation are given in [160]. The algorithm calculates a scalar field $\beta(\boldsymbol{x})$, where $\beta(\boldsymbol{x}) = 0$ indicates that fluid is present at $\boldsymbol{x}$ and $0 < \beta(\boldsymbol{x}) \leq 1$ indicates that breast tissue can be expected at $\boldsymbol{x}$. Since only a blurred breast rim can be estimated from diffuse optical measurements, values between zero and 1 are allowed for the breast shape function. Therefore, the resulting breast shape depends on the chosen threshold, but as $\beta(\boldsymbol{x})$ has a steep slope at the fluid-tissue interface, the resulting breast shape depends only slightly on this threshold.

Fig. 6.17 (bottom row) shows reconstruction results with prior breast shape estimation, the large sphere is reconstructed having a more homogeneous distribution of the absorption coefficient, and the small object can still be reconstructed. Both spheres show an expansion towards the top of the cup as an artifact, i.e. an increased absorption coefficient above the sphere, which is a result of an optimization of the breast shape estimation algorithm which expects objects (breasts) to have conical geometry instead of being a spherical object.

6.2.5 Fitting of optical properties from spectral cw data

To preserve or improve convergence of reconstructions by initializing them with a homogeneous breast of estimated shape, a fit of averaged optical properties is presented and tested on numerical phantoms and patient data. Averaged absorption and scattering coefficients of the breast are deduced from multi-wavelength cw measurements by applying a spectral model.

Fitting the optical properties of breast tissue is a challenging task, especially if only cw data are available. In such a case, the attenuation k can be fitted quite well, but the separation of the scattering and absorption coefficient is cumbersome, i.e. may depend on the fitting procedure.

The results of the fit can be improved, when a spectral model is included. Using this method on simulated data or on experimental data acquired from the Philips fluorescence mammograph, four parameters of the spectral model are fitted to describe the optical properties of the breast, i.e. the spatially constant

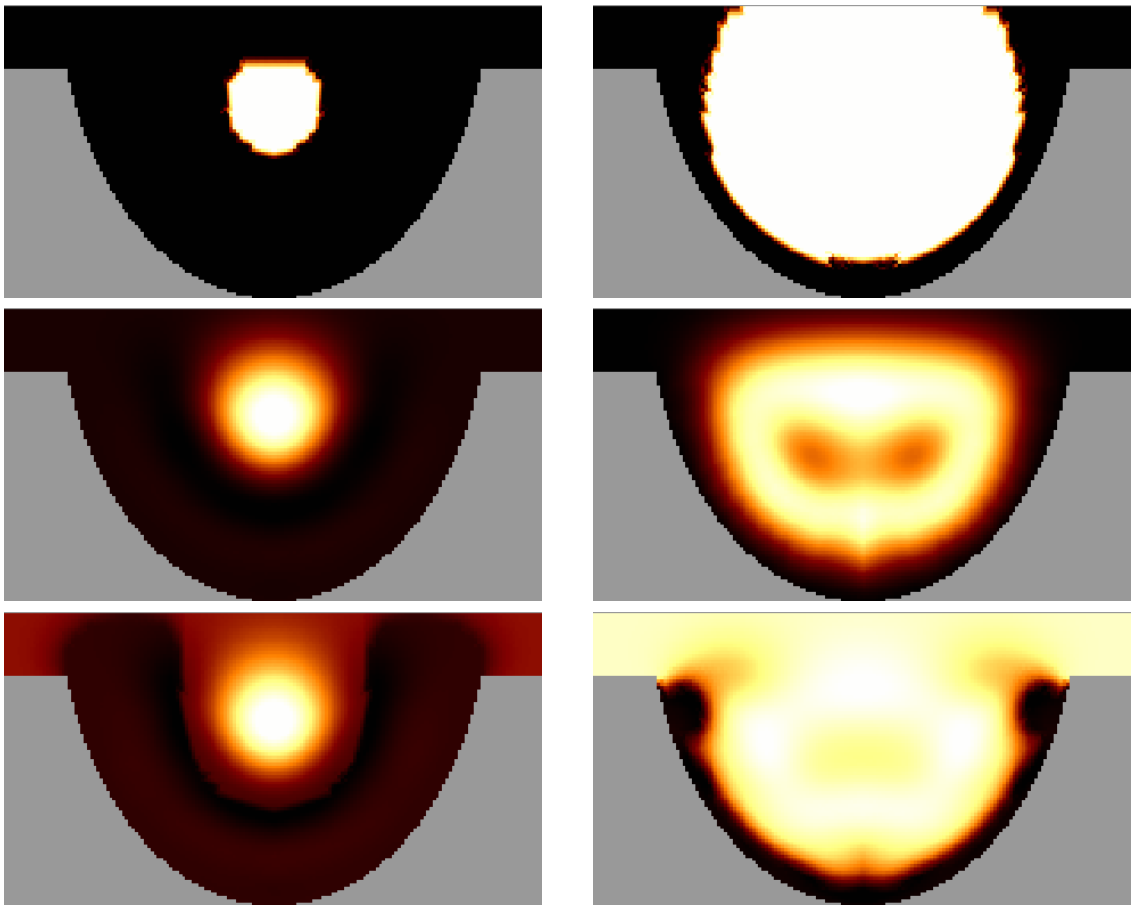

Figure 6.17: Convergence of absorption reconstruction in the presence of a large objects: $\mu_a(\boldsymbol{x}, \lambda)$ of phantom (top row). Reconstruction without breast shape estimation (middle row), reconstruction with breast shape estimation (bottom row). All images are given in min/max scale.

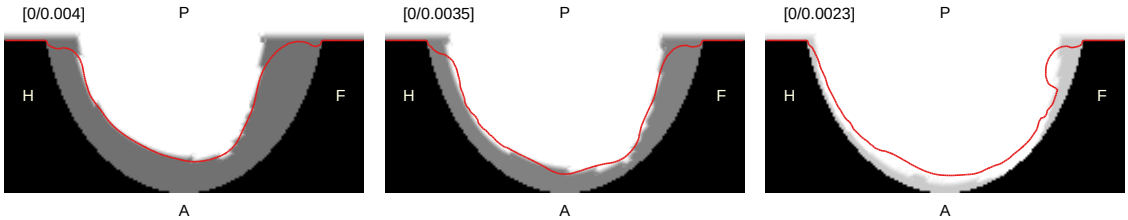

Figure 6.18: Numerical breast phantoms (left to right: dense small, medium attenuation and size, fatty large) and corresponding calculated breast shapes (red lines) for $\beta(\boldsymbol{x}) = 0.5$. The absorption coefficient of the sagittal slices through the center of each phantom is presented in gray scale (from $\mu_a = 0$ to $\mu_a^{\text{breast}}(\lambda = 730 \text{ nm}) = 0.004 \text{ mm}^{-1}$, 0.0035 mm^{-1}, and 0.0023 mm^{-1}, respectively). The orientation of the numerical phantom is indicated by P (posterior), A (anterior), F (feed), H (head).

scattering amplitude (a), the concentration of water ($c_{\mathrm{H_2O}}$), the concentration of oxygenated-hemoglobin (c_{HbO}), and reduced hemoglobin (c_{HbR}). The scattering power was not fitted, for only four wavelengths are available, therefore we set $b = 1$, which is in the range of typical values found in literature [11] to reduce the number of parameters to the number of available wavelengths.

Reconstruction of spatial variations of spectral model parameters has been carried out before [96, 171, 172, 173]. Formalisms presented in those works will be adapted in this section for fitting averaged breast tissue properties without any reconstruction. Furthermore, the breast shape estimated for each patient is included into the fitting procedure as a spatial prior.

For a chosen source-detector combination i, the ratio of the photon density $\Phi(\boldsymbol{x}_{d_i}, \boldsymbol{x}_{s_i}, \lambda)$ for a patient scan and the photon density $\Phi_0(\boldsymbol{x}_{d_i}, \boldsymbol{x}_{s_i}, \lambda)$ for a reference scan measured in cw at wavelength λ can be expressed by the Rytov approximation as given in Eq. (6.1) for $\omega = 0$. The patient breast is approximated as homogeneous tissue having averaged optical properties $\overline{\mu_{\mathrm{a}}^{\mathrm{breast}}}(\lambda) = \overline{\delta\mu_{\mathrm{a}}}(\lambda) + \mu_{\mathrm{a}}^0(\lambda)$ and $\overline{D^0}(\lambda) = \overline{\delta D}(\lambda) + D^{\mathrm{fluid}}(\lambda)$ throughout the complete breast. By using the estimated breast shape $0 \leq \beta(\boldsymbol{x}) \leq 1$ the Rytov approximation can be rewritten as

$$\begin{aligned} \underbrace{-\ln \frac{\Phi(\boldsymbol{x}_{d_i}, \boldsymbol{x}_{s_i}, \lambda)}{\Phi_0(\boldsymbol{x}_{d_i}, \boldsymbol{x}_{s_i}, \lambda)}}_{p_i^\lambda} &= v\overline{\delta\mu_{\mathrm{a}}}(\lambda) \underbrace{\int_\Omega \beta(\boldsymbol{x}) \frac{G_0(\boldsymbol{x}_{d_i}, \boldsymbol{x}, \lambda) G_0(\boldsymbol{x}, \boldsymbol{x}_{s_i}, \lambda)}{G_0(\boldsymbol{x}_{d_i}, \boldsymbol{x}_{s_i}, \lambda)} d\Omega}_{w_{\mathrm{a},i}^\lambda} \\ &\quad + v\overline{\delta D}(\lambda) \underbrace{\int_\Omega \beta(\boldsymbol{x}) \frac{\nabla G_0(\boldsymbol{x}_{d_i}, \boldsymbol{x}, \lambda) \nabla G_0(\boldsymbol{x}, \boldsymbol{x}_{s_i}, \lambda)}{G_0(\boldsymbol{x}_{d_i}, \boldsymbol{x}_{s_i}, \lambda)} d\Omega}_{w_{\mathrm{D},i}^\lambda}, \end{aligned} \tag{6.46}$$

introducing the coefficients p_i^λ, $w_{\mathrm{a},i}^\lambda$, and $w_{\mathrm{D},i}^\lambda$ for each source-detector combination i and wavelength λ.

For each selected source-detector combination, measurements are carried out at n_l different wavelengths. Therefore, for each wavelength an averaged difference in optical properties between breast tissue and fluid can be determined, resulting in a matrix equation

$$\boldsymbol{P}_i = \begin{pmatrix} w_{\mathrm{a},i}^{\lambda_1} & & 0 \\ & \ddots & \\ 0 & & w_{\mathrm{a},i}^{\lambda_{n_l}} \end{pmatrix} \delta\boldsymbol{m}_{\mathrm{a}} + \begin{pmatrix} w_{\mathrm{D},i}^{\lambda_1} & & 0 \\ & \ddots & \\ 0 & & w_{\mathrm{D},i}^{\lambda_{n_l}} \end{pmatrix} \delta\boldsymbol{m}_{\mathrm{D}}, \tag{6.47}$$

with $\boldsymbol{P}_i = \frac{1}{v}(p_i^{\lambda_1}, ..., p_i^{\lambda_{n_l}})^T$ being the n_l component signal vector combining all measured wavelengths, $\delta\boldsymbol{m}_{\mathrm{D}} = (\overline{\delta D}(\lambda_1), ..., \overline{\delta D}(\lambda_{n_l}))^T$, and $\delta\boldsymbol{m}_{\mathrm{a}} = (\overline{\delta\mu_{\mathrm{a}}}(\lambda_1), ..., \overline{\delta\mu_{\mathrm{a}}}(\lambda_{n_l}))^T$ the n_l component vector composed of the differences in optical properties (scattering and absorption coefficient, respectively) at each wavelength.

Equation (6.47) can be rewritten by using Beer's law and the molar absorption coefficient matrix

$$\underline{\epsilon} = \begin{pmatrix} \epsilon_{\mathrm{H_2O}}^{\lambda_1} & \epsilon_{\mathrm{Hb0}}^{\lambda_1} & \epsilon_{\mathrm{HbR}}^{\lambda_1} \\ \vdots & \vdots & \vdots \\ \epsilon_{\mathrm{H_2O}}^{\lambda_{n_l}} & \epsilon_{\mathrm{Hb0}}^{\lambda_{n_l}} & \epsilon_{\mathrm{HbR}}^{\lambda_{n_l}} \end{pmatrix}, \tag{6.48}$$

where ϵ_X^λ is the molar absorption coefficient of substance X at wavelength λ (see Sec. 5.1.3), and

$$h_j = -1/(3a^2)(\lambda_j/\lambda_0)^b \tag{6.49}$$

with $j \in \{1, ..., n_l\}$, where λ_0 is the reference wavelength chosen as 1000 nm, $\delta\boldsymbol{m}_{\mathrm{a}} = \underline{\epsilon}\delta\boldsymbol{c} \ln 10$, and

$\delta \boldsymbol{m}_{\mathrm{D}} = (h_1, ..., h_{n_l})^T \delta a$ as

$$\boldsymbol{P}_i = \begin{pmatrix} w_{\mathrm{a},i}^{\lambda_1} & & 0 \\ & \ddots & \\ 0 & & w_{\mathrm{a},i}^{\lambda_{n_l}} \end{pmatrix} \underline{\epsilon} \delta \boldsymbol{c} \ln 10 + \begin{pmatrix} w_{\mathrm{D},i}^{\lambda_1} & & 0 \\ & \ddots & \\ 0 & & w_{\mathrm{D},i}^{\lambda_{n_l}} \end{pmatrix} \begin{pmatrix} h_1 \\ \vdots \\ h_{n_l} \end{pmatrix} \delta a. \tag{6.50}$$

Here, $\delta \boldsymbol{c} = (\delta c_{\mathrm{H_2 0}}, \delta c_{\mathrm{HbO}}, \delta c_{\mathrm{HbR}})^T$ consists of the averaged chromophore concentrations of the breast. For our fit, we use k source-detector combinations simultaneously by defining the $(k \cdot n_l) \times 4$ matrix

$$W = \begin{pmatrix} w_{\mathrm{a},1}^{\lambda_1} \epsilon_{\mathrm{H_2O}}^{\lambda_1} \ln 10 & w_{\mathrm{a},1}^{\lambda_1} \epsilon_{\mathrm{HbO}}^{\lambda_1} \ln 10 & w_{\mathrm{a},1}^{\lambda_1} \epsilon_{\mathrm{HbR}}^{\lambda_1} \ln 10 & w_{\mathrm{D},1}^{\lambda_1} h_1 \\ \vdots & \vdots & \vdots & \vdots \\ w_{\mathrm{a},1}^{\lambda_{n_l}} \epsilon_{\mathrm{H_2O}}^{\lambda_{n_l}} \ln 10 & w_{\mathrm{a},1}^{\lambda_{n_l}} \epsilon_{\mathrm{HbO}}^{\lambda_{n_l}} \ln 10 & w_{\mathrm{a},1}^{\lambda_{n_l}} \epsilon_{\mathrm{HbR}}^{\lambda_{n_l}} \ln 10 & w_{\mathrm{D},1}^{\lambda_{n_l}} h_{n_l} \\ \vdots & \vdots & \vdots & \vdots \\ w_{\mathrm{a},k}^{\lambda_{n_l}} \epsilon_{\mathrm{H_2O}}^{\lambda_{n_l}} \ln 10 & w_{\mathrm{a},k}^{\lambda_{n_l}} \epsilon_{\mathrm{HbO}}^{\lambda_{n_l}} \ln 10 & w_{\mathrm{a},k}^{\lambda_{n_l}} \epsilon_{\mathrm{HbR}}^{\lambda_{n_l}} \ln 10 & w_{\mathrm{D},k}^{\lambda_{n1}} h_{n_l} \end{pmatrix}, \tag{6.51}$$

and thus can define

$$\boldsymbol{P} := \begin{pmatrix} \boldsymbol{P}_1 \\ \vdots \\ \boldsymbol{P}_k \end{pmatrix} = W \underbrace{\begin{pmatrix} \delta c_{\mathrm{H_2O}} \\ \delta c_{\mathrm{HbO}} \\ \delta c_{\mathrm{HbR}} \\ \delta a \end{pmatrix}}_{\boldsymbol{m}_{\mathrm{sol}}}. \tag{6.52}$$

The minimum of the overdetermined system of equations is searched for by requiring

$$(\boldsymbol{P} - W \boldsymbol{m}_{\mathrm{sol}})^T (\boldsymbol{P} - W \boldsymbol{m}_{\mathrm{sol}}) \stackrel{!}{=} \min. \tag{6.53}$$

We solve Eq. (6.53) by using the pseudo-inverse of W

$$\boldsymbol{m}_{\mathrm{sol}} = \left(W^T W\right)^{-1} W^T \boldsymbol{P}. \tag{6.54}$$

The fit was tested using three numerical phantoms simulating a homogeneous breast immersed in scattering fluid filling a 80D cup. These three numerical phantoms mimic a small dense breast, a medium size breast of average attenuation, and a fatty large breast, respectively. All three simulated breasts have a water fraction of 47% and the same reduced scattering coefficient throughout the complete breast ($a = 0.9$ mm^{-1}, $b = 0.56$). The complete list of constituents can be found in appendix A.6. A sagittal slice through the center of the breast showing the absorption value of all three phantoms can be found in Fig. 6.18. There, the white area indicates the breast having a homogeneous absorption coefficient, the gray area the scattering fluid surrounding the breast, and black the outside of the cup.

The scattering fluid was modeled with the spectral dependence of the MF2.1, with optical properties of the scattering fluid ($a = 0.9$ mm^{-1}, $b = 1.7$) as given in appendix A.5. Data for each breast scan and the reference scan was simulated at four different wavelengths ($\lambda = 690$ nm, 730 nm, 780 nm, and 850 nm). In a next step, the breast shape was estimated from these data, giving results as depicted in Fig. 6.18 as red lines, showing the estimated breast contour for a threshold of $\beta(\boldsymbol{x}) = 0.5$. As can bee seen, the breast shape estimation works quite well, especially for the small breast at lower ring positions, but slightly underestimates the breast shape in this area for the large breast. At the top ring position and above, the breast shape algorithm slightly overestimates the breast size, because the sharp edge of

the numerical phantom at the simulated breast-chest transition can not be estimated correctly from DOT data.

Absorption and scattering coefficients for each numerical breast phantom and each wavelength were fitted by calculating $w^{\lambda}_{\mathrm{a},i}$, $w^{\lambda}_{\mathrm{D},i}$ for all four wavelengths and by using the corresponding estimated breast shapes $\beta(\boldsymbol{x})$. In contrast to in vivo measurements, the scattering power was fixed at the exact value ($b = 0.56$) for the fit. The fitted values of the averaged absorption and reduced scattering coefficients depend on the source-detector combinations that were used during the fit, resulting in errors varying between 2% to 30%. Fitting results are improved if source-detector combinations of positions are used, where the corresponding breast shape estimation gave correct results. Therefore, parameter estimation was more stable (i.e. independent of chosen source-detector combinations) for the smallest breast. If the breast shape is located near to source or detector positions used for the fitting procedure, small variations in the shape can give large variations in $w^{\lambda}_{\mathrm{a},i}$ and $w^{\lambda}_{\mathrm{D},i}$, and hence severely influence the results of the fit. Additionally, modeling the source term in the diffusion approximation as fiber source (see Sec. 5.1.7) results in unphysical values of $w^{\lambda}_{\mathrm{D},i}$ at grid vertices located between the fiber tip and the shifted source position. If the breast touches the cup rim, i.e. $\beta(\boldsymbol{x}) > 0$ at such grid vertices, these values degrade the precision of the scattering coefficient fit. Hence, using only source-detector combinations with fluid at the source and detector positions improves the fit.

To test the fitting procedure on experimental data, averaged absorption and scattering coefficients for each breast of two patients were fitted from 15 scans that have been carried out consecutively. Both patients bore a tumor in one breast (ipsilateral breast). During the examination, nine scans were performed investigating the ipsilateral and six scans investigating the contralateral (healthy) breast, while each scan was carried out at $n_l = 4$ wavelengths ($\lambda = 690$ nm, 730 nm, 780 nm, and 850 nm). For fitting of concentrations of tissue chromophores and scatter amplitude, source-detector combinations mainly from the three top rings were used, corresponding to a total of approximately 9800 source-detector combinations. The scattering power was fixed to $b = 1$.

Results for $\overline{\mu_{\mathrm{a}}^{\mathrm{breast}}}(\lambda)$ and $\overline{\mu_{\mathrm{s}}'^{\,\mathrm{breast}}}(\lambda)$ are presented for $\lambda = 690$ nm in Fig. 6.19 left and right, respectively, where fit results of the ipsilateral breast are shown as plusses (circles) and as crosses (dots) for the contralateral breast of patient A (B). The average value of the ipsilateral breast is plotted as full line and for the contralateral breast as dashed line.

The fitted optical properties show some variations around the average value, mainly resulting from varying positioning of the breast inside the cup between consecutive measurements. This effect can be compensated only partly by the use of the estimated breast shape $\beta(\boldsymbol{x})$. Nontheless, variations are small enough to distinguish the two patients, and even show for patient A that the averaged absorption coefficient of both breasts from the same patient can be quite different.

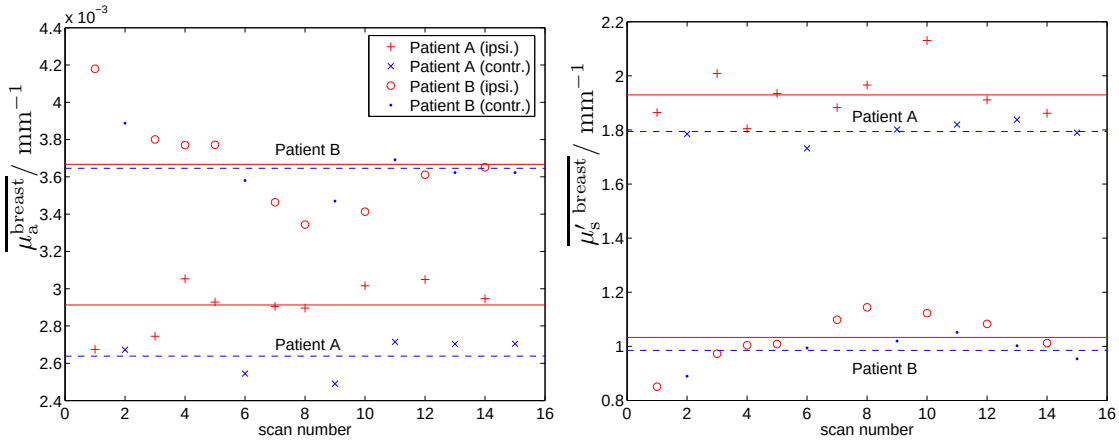

Figure 6.19: Spectral fit using clinical data of two patients with a total of 15 scans performed with each patient on both breasts. Fitted optical properties $\overline{\mu_{\mathrm{a}}^{\mathrm{breast}}}(\lambda)$ and $\overline{\mu_s'^{\,\mathrm{breast}}}(\lambda)$ (left and right plot) for ipsi- and contralateral breast. Full and dashed lines indicate the averaged fitted optical properties, corresponding to the ipsi- and contralateral breast, respectively.

Chapter 7

Reconstruction of patient data

Optical mammograms were generated by nonlinear reconstructions of the absorption coefficient from tomographic data taken by the Philips mammograph on three patients, one carrying a cyst, and two carrying a carcinoma. Fluorescence mammograms were obtained from a fourth patient after administration of an unspecific fluorescent dye (Omocyanine). In each case, the lesion could be detected and optical and fluorescence mammograms were successfully correlated with MR mammograms, whenever available. No variations in scattering were considered, leading to artifacts (negative absorption coefficients or negative concentrations) in selected areas.

A phase I clinical study was carried out at the University Medical Center (UMC) Utrecht by Prof. Dr. Willem P. Th. M. Mali and Stephanie van de Veen involving a small number of patients to evaluate the unspecific fluorescent contrast agent Omocyanine provided by Bayer Schering Pharma. Both, absorption and fluorescence scans were performed prior and after injection of the contrast agent using the cw Philips tomographic fluorescence mammograph.

Within the framework of this thesis, linear and nonlinear reconstructions of patient data were carried out to determine intrinsic contrast based on absorption, whereas fluorescent dye concentrations were reconstructed using linear approaches.

The primary aim of this exploratory study was to determine the optimal dose of the Omocyanine dye and the optimal time at which measurements should be taken after injection of the contrast agent to achieve highest contrast between lesion and background. It was not the aim of the study to differentiate malignant from benign lesions.

Informed consent was approved by the institutional review board, and investigations were in full compliance with the accepted standards for research involving humans. For comparison of optical mammography with other established imaging modalities, in most cases mammograms were recorded additionally using X-ray, US, and MRI, followed by biopsy and histopathology.

Medical results of this study including cases with a cyst (absorption mammograms) and several tumor cases (absorption and fluorescence mammograms) can be found in [65, 174, 175].

For illustration of linear and nonlinear reconstruction of patient data, three selected cases will be discussed in the following.

7.1 Nonlinear absorption reconstruction of patient cw data in cup geometry

Reconstruction algorithms were optimized to reconstruct absorption coefficients since tumors are known to be predominantly absorbing because of the increase in blood volume. Therefore, scattering (diffusion) coefficients were assumed to be constant throughout the breast volume and were not changed during the reconstruction. While this approximation is appropriate for tumors, cysts are known to scatter light considerably less compared to the surrounding tissue, making this approximation less suitable. However, cysts do not present problems clinically and the cyst case only serves to illustrate nonlinear reconstruction of patient data.

Cyst case

Coronal slices of the left breast of a 54 year old patient illustrating linearly and nonlinearly reconstructed absorption coefficients are shown in Fig. 7.1. US and X-ray mammograms showed one large cyst (approximately 2 cm diameter) and many small cysts in this breast (BI-RADS 2). The coronal MR slice[1] through the center of the large cyst is shown in Fig. 7.1 (right), where glandular tissue and fat can be distinguished clearly and the cyst has been indicated. In the optical images the cyst shows up as a black area, whereas glandular and fatty tissue are associated with bright areas (enhanced absorption). The nonlinear reconstruction (middle) leads to fewer artefacts and allows a separation between glandular and fatty tissue that is hardly possibly in the linear reconstruction image (left).

The breast filled the 80D cup insert nearly completely (5% of the volume were filled by the scattering fluid). The linear ($\kappa = 0$) and nonlinear ($\kappa = 4$) reconstruction was started by dividing the cup volume into two parts, one containing the scattering fluid with its known optical parameters, the other one containing the breast. Prior to reconstruction, averaged absorption and diffusion coefficients were obtained by fitting measured and simulated transmitted light intensities assuming the breast to be homogeneous.

The absorption coefficients for $\lambda = 690$ nm displayed in the left image were obtained by assuming $\overline{D^{\text{breast}}} = D^{\text{fluid}}$ during the reconstruction, whereas the absorption coefficients in the middle image were deduced using the fixed values of the diffusion coefficients $\overline{D^{\text{breast}}} = 0.67$ mm and $D^{\text{fluid}} = 0.20$ mm. Both, the right and middle image are given in separate min/max gray scales (from $\mu_{\text{a}} = -0.009$ mm^{-1} (black) to $\mu_{\text{a}} = 0.011$ mm^{-1} (white) and from $\mu_{\text{a}} = -0.013$ mm^{-1} to $\mu_{\text{a}} = 0.030$ mm^{-1}, respectively). Without using the estimated breast shape to deduce averaged optical properties of breast tissue, neither the linear nor the nonlinear reconstruction converged to a meaningful image.

As can be seen from Fig. 7.1, the cyst corresponds to negative absorption coefficients. Negative absorption coefficients are unphysical and represent artefacts due to shortcomings of the model used. Cysts are filled with opaque weakly absorbing fluid, and sometimes additionally with blood. It is commonly accepted that the reduced scattering coefficient of cysts are considerably smaller than that of (breast) tissue. However, as was mentioned above, in this thesis the fluid filled cyst is modelled as absorber rather than as scatterer, causing negative absorption coefficients. This result can be understood in the following way. Since the cyst was assumed to have the same scattering coefficient as the surrounding breast tissue, attenuation of light traversing the cyst due to scattering is grossly overestimated. This effect is compensated for by negative values of the absorption coefficient of the cyst. In addition, it is not clear whether the condition $\mu_{\text{a}} \ll \mu_{\text{s}}'$ necessary to approximate photon transport by the diffusion equation holds true within the volume of the cyst. Despite the unphysical absorption coefficients deduced for cysts and the questionable model, cysts often can be detected easily in this way.

Generally, artefacts occur in linear reconstruction images at positions where the breast touches the cup surface. Furthermore, in case of a large mismatch between the scattering coefficients of the breast tissue

[1] T1 3D SENSE scan protocol (TE/TR 3.0/6.2 ms, acquired voxel size $0.74 \times 0.74 \times 1.8$ mm^3)

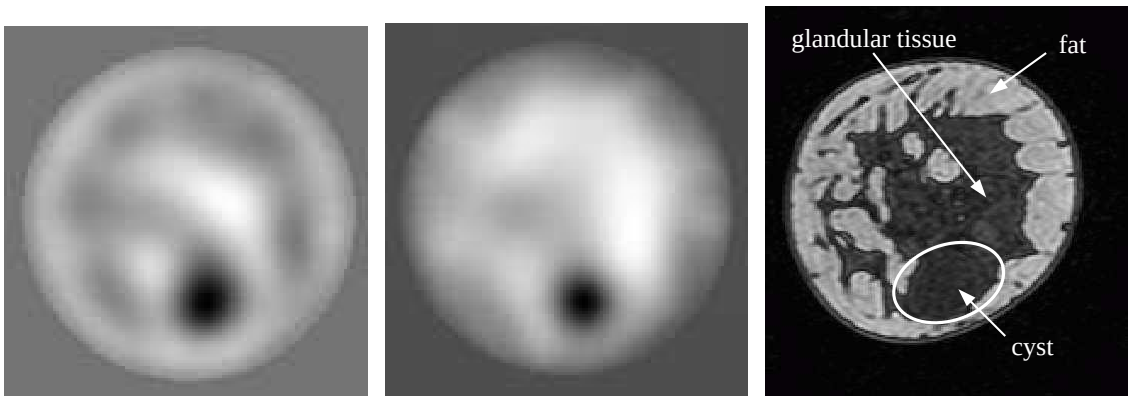

Figure 7.1: Linear (left) and nonlinear (middle) reconstruction of a cyst case. (right) Coronal MR image through cyst center. The nonlinear reconstruction with corrected scattering coefficient enhances the spatial resolution and hence allows a separation of cyst, glandular, and fatty tissue as can be seen in the MR image.

and the scattering fluid, artefacts appear at the tissue-fluid interface. These artefacts can be reduced by nonlinear reconstructions and by using realistic (average) optical properties of breast tissue.

Tumor case A

Fig. 7.2 illustrates the convergence of the nonlinear reconstruction using measured data from a patient's breast bearing a tumor (assessed as BI-RADS 4 after X-ray and US investigation). The patient's breast filled the 80D cup insert only partly, i.e. approximately 40% of the cup volume was filled with the scattering fluid. US mammograms show a 11 mm × 16 mm lesion surrounded by fatty tissue in the left breast of a 67 year old patient. Histopathology unveiled the lesion as a malignancy (plasmacytoma).

In Fig. 7.2 we plot the frequency of occurrence of values $R_i^{\kappa=0}$ derived from raw data and of R_i^{κ} ($\kappa = 1, ..., 3$) representing weighted raw data for $\lambda = 690$ nm, where

$$R_i^{\kappa} = -\ln\left(\frac{\Phi(\boldsymbol{x}_{d_i}, \boldsymbol{x}_{s_i}, \lambda)}{\Phi_0(\boldsymbol{x}_{d_i}, \boldsymbol{x}_{s_i}, \lambda)} \frac{\Phi_0^{\mathrm{sim}}(\boldsymbol{x}_{d_i}, \boldsymbol{x}_{s_i}, \lambda)}{\Phi_{\kappa}^{\mathrm{sim}}(\boldsymbol{x}_{d_i}, \boldsymbol{x}_{s_i}, \lambda)}\right). \tag{7.1}$$

$R_i^{\kappa=0}$ corresponds to the LHS of the Rytov approximation (see Sec. 6.1.2) and the weights in $R_i^{\kappa\geq 1}$ are obtained by nonlinear reconstruction. Fig. 7.2 contains results of all source-detector combinations.

The large peak in Fig. 7.2a at values $R_i^{\kappa=0}$ close to zero corresponds to source-detector combinations for which the light travels through scattering fluid only and was only slightly influenced by the presence of the breast. In contrast, the broad distribution of values $R_i^{\kappa=0}$ centered around 1.5 corresponds to source-detector combinations joined by photon trajectories sampling the breast. The larger values of $R_i^{\kappa=0}$ can be explained by the stronger attenuation of diffusely transmitted light by breast tissue compared to the scattering fluid.

When using as model the cup filled with scattering fluid and with the breast of realistic shape together with average fitted absorption and diffusion coefficients of the breast tissue, the width of the distribution $R_i^{\kappa=1}$ is considerably reduced. However, as a result of improperly fitted optical properties that were determined at a single wavelength without using a spectral model for the given example, the distribution $R_i^{\kappa=1}$ is not centered around $R_i^{\kappa=1} = 0$. Simulated photon densities $\Phi_{\kappa}^{\mathrm{sim}}(\boldsymbol{x}_{d_i}, \boldsymbol{x}_{s_i}, \lambda)$ derived from inhomogeneous distributions of absorption coefficients in breast tissue obtained by nonlinear iteration steps properly weight the raw data, i.e. making the RHS term of Eq. (7.1) close to zero. Fig. 7.2b to Fig. 7.2d illustrate the corresponding narrowing of the R_i^{κ} distribution and its shift towards zero.

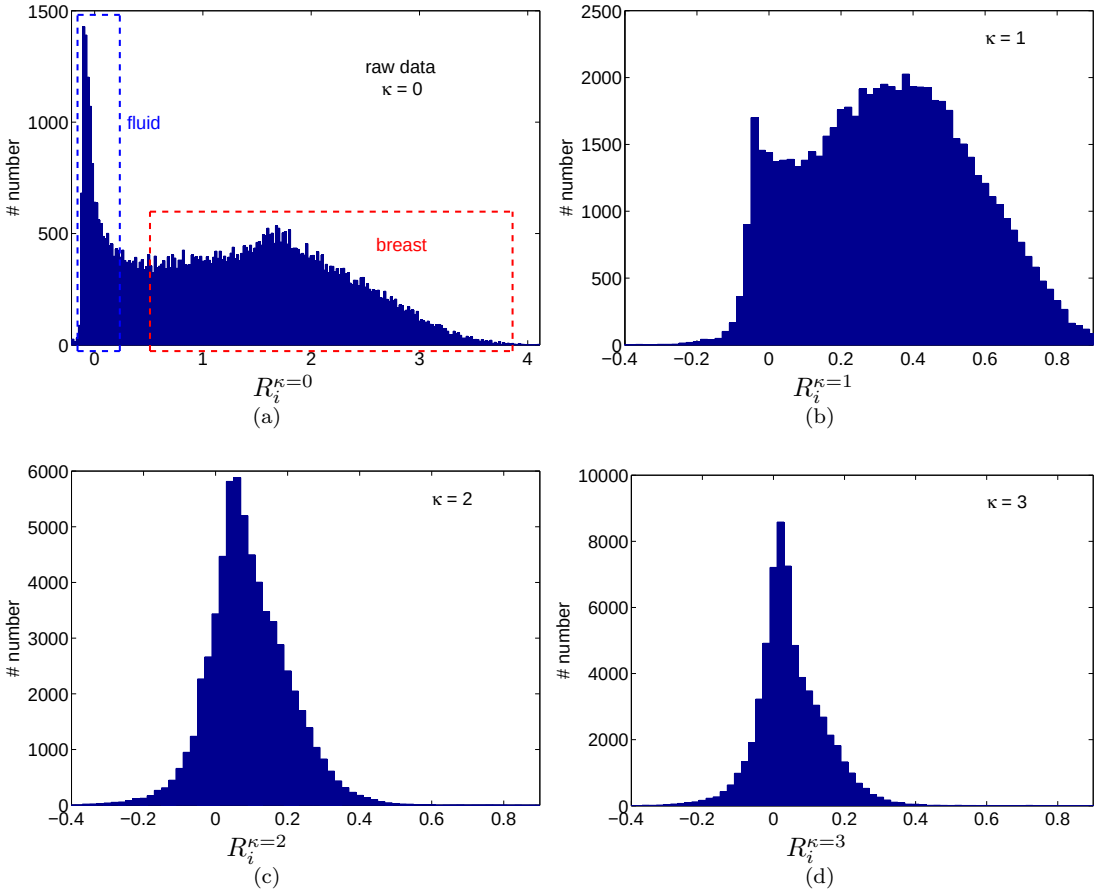

Figure 7.2: Histogram of raw data ($R_i^{\kappa=0}(\lambda = 690$ nm)) and weighted raw data ($R_i^{\kappa}(\lambda = 690$ nm) for various iteration steps ($\kappa = 1, ..., 3$) of nonlinear reconstruction of measured data of a tumour patient.

Additional nonlinear steps improve the distribution only marginally and convergence has been reached.

Tumor case B

As a third example of a nonlinear absorption reconstruction we present measurements of a 47 year old patient, who according to histology bore a ductal invasive carcinoma with a diameter of approximately 2 cm in her right breast. The tumor showed a high contrast in Gd-enhanced MRI (assessed as BI-RADS 5), as can be seen in Fig. 7.3. The tumor, indicated by a yellow arrow, is located in the upper outer quadrant of the right (ipsilateral) breast at the boundary of the glandular tissue. No suspicious lesions were found in the left (contralateral) breast. The optical properties of the patient's breasts were fitted as $\overline{\mu_a^{\text{breast}}} = 0.0039\ \text{mm}^{-1}$ and $\overline{D^{\text{breast}}} = 0.28$ mm with the breasts filling the 80D cup insert only partly (30% of the cup filled with scattering fluid). Absorption reconstruction results for iteration $\kappa = 3$ are presented in Fig. 7.4 showing coronal slices (same scan protocol as given in Sec. 3.2) in the top row (left and middle) and axial slices in the bottom row (left and middle) for the ipsilateral and contralateral breast, respectively. Fig. 7.4 uses the same orientation of slices as the MR images in Fig. 7.3. Absorption coefficients are given in gray scale values using the same min/max scaling for all reconstruction images. All slices shown intersect the reconstructed tumor position. The maximum

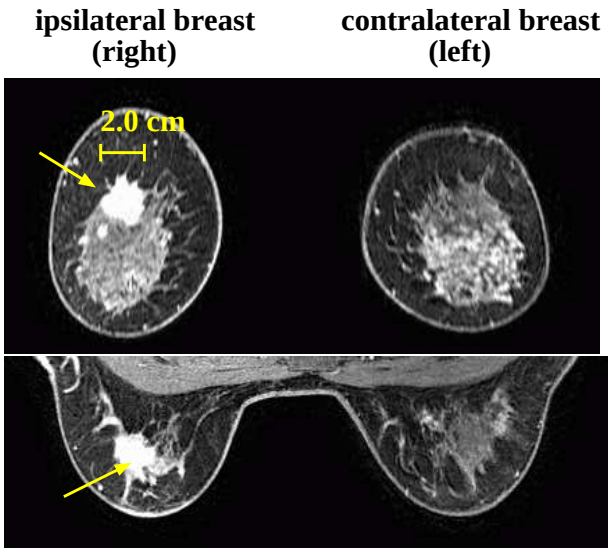

Figure 7.3: Coronal (top) and axial (bottom) Gd-enhanced MR images through tumor center. The tumor (ductal invasive carcinoma) is located in the right (ipsilateral) breast (indicated by yellow arrow) and has an estimated diameter of 2 cm. No suspicious lesion was found in the left (contralateral) breast.

absorption coefficient (white) of the reconstructed volume is found at the reconstructed tumor position (indicated by a yellow arrow) with a value of $\mu_a = 0.017$ mm^{-1} being higher than the initial homogeneous absorption coefficient ($\mu_a = 0.0039$ mm^{-1}) by a factor of four. This result is consistent with published ratios of absorption coefficients of tumors and average (homogeneous) absorption coefficients of breast tissue [11]. The mammilla, not present in the given slices, shows a comparable high absorption coefficient ($\mu_a = 0.016$ mm^{-1}) as the tumor. Between tumor and mammilla, negative absorption values are observed, and such values are also present in Fig. 7.4 indicated by black areas. These negative absorption values are unphysical and, as mentioned above, indicate shortcomings of the model used. However, in the present case the lowest absorption coefficient ($\mu_a = -0.0021$ mm^{-1}) is considerably less negative than that found for the cyst. The negative absorption values may be explained in the same way as for the cyst case. Variations in scattering within breast tissue are not taken into account by our breast model and areas with a lower diffusion coefficient compared to the average value $\overline{D^{\text{breast}}}$ will result in lower or even negative absorption coefficients.

One might be tempted to restrict reconstructed absorption coefficients to positive values only, but keeping the constraint $\overline{D^{\text{breast}}} = \text{const}$. In this case the deficiency of the model, i.e. scattering assumed to be spatially constant, is not corrected for and instead of small volumes with negative absorption coefficients, large volumes with positive absorption coefficients close to zero appear after reconstruction.

The images representing reconstructed absorption coefficients of the contralateral breast (middle column) clearly show the interface between breast and scattering fluid as well as the glandular tissue at the center of the breast (middle top image). Apart from the mammilla, in the entire volume of the contralateral breast no large reconstructed absorption values were found that would indicate the presence of a lesion.

The two images of the right column show schematically the orientation of the slices and the location of the tumor deduced from palpation.

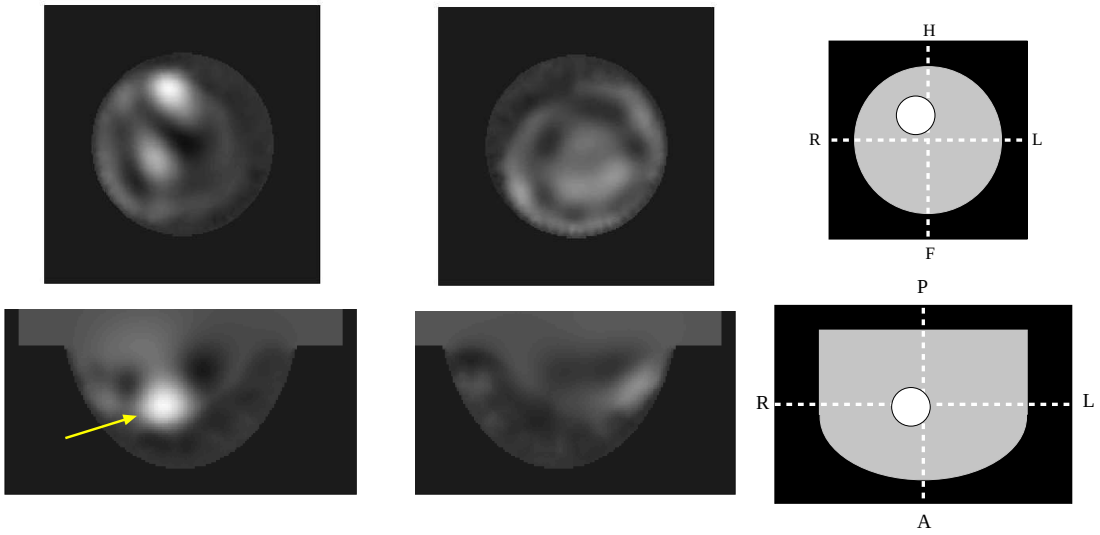

Figure 7.4: Images displaying reconstructed ($\kappa = 3$) absorption coefficients of the right and left breast of the same patient as in Fig. 7.3. The arrangement of the panels corresponds to the images shown in this figure, i.e. the diseased right breast appears in the column on the LHS, the healthy breast in the middle column and the column on the RHS shows schematically the orientation of the breast and tumor position expected from palpation. The top and bottom panels display coronal and axial slices respectively through the reconstructed tumor center (indicated by yellow arrow). Identical min/max scaling (from $\mu_a = -0.0021$ mm^{-1} (black) to $\mu_a = 0.017$ mm^{-1} (white)) is used for all four DOT images and contra- and ipsilateral breasts are presented using the same slices. (right column) Orientation of images and tumor position: head (H), feet (F), right (R), left (L), anterior (A), posterior (P).

7.2 Optical mammograms based on reconstructed dye concentrations

We present one selected example of fluorescence mammograms obtained with the fluorescent dye Omocyanine. Details of the entire clinical study on fluorescence mammography are published in [175].

X-ray and MR mammograms of a 74 year old patient revealed a tumor in her right breast (BI-RADS 5), and histopathology diagnosed it to be an invasive ductal carcinoma. Fig. 7.5 (top) shows the Gd-enhanced MR image (same scan protocol as given in Sec. 3.2) of both breasts in a top to bottom view. The slightly tilted axial slice contained the clearly visible tumor in the right breast and the mammilla of the left breast.

After injection of the Omocyanine dye and positioning of the breast in the 80D cup insert (30% of the volume was filled with scattering fluid), fluorescence scans were performed. The fluorescence mammograms of the right and left breast show reconstructed dye concentrations (bottom panels of Fig. 7.5). The axial slice illustrated by the lower left panel intersects the tumor, while the slice of the panel on the RHS intersects the mammilla. The arrangement of both panels corresponds to the upper MR image. Reconstructed dye concentrations are normalized to the dye concentration in the mammilla of each breast and relative concentrations are given as gray scale values corresponding to separate min/max scaling.

Maximum dye concentration is reconstructed at the expected tumor position but the mammilla and the skin show an increased dye contrast in both breasts, too. Additional fluorescent dye accumulates in the remaining glandular tissue.

There are conspicuous ring shaped black areas in both fluorescence mammograms corresponding to negative normalized reconstructed dye concentrations or negative normalized reconstructed dye absorption coefficients. As was discussed for the previous cases, variations of the diffusion coefficient within the breast volume that are not taken into account by our breast model are compensated by variations in the absorption coefficient, leading even to negative (dye) absorption coefficients. It is, therefore, not surprising that negative relative dye concentrations appear in the reconstructed mammograms.

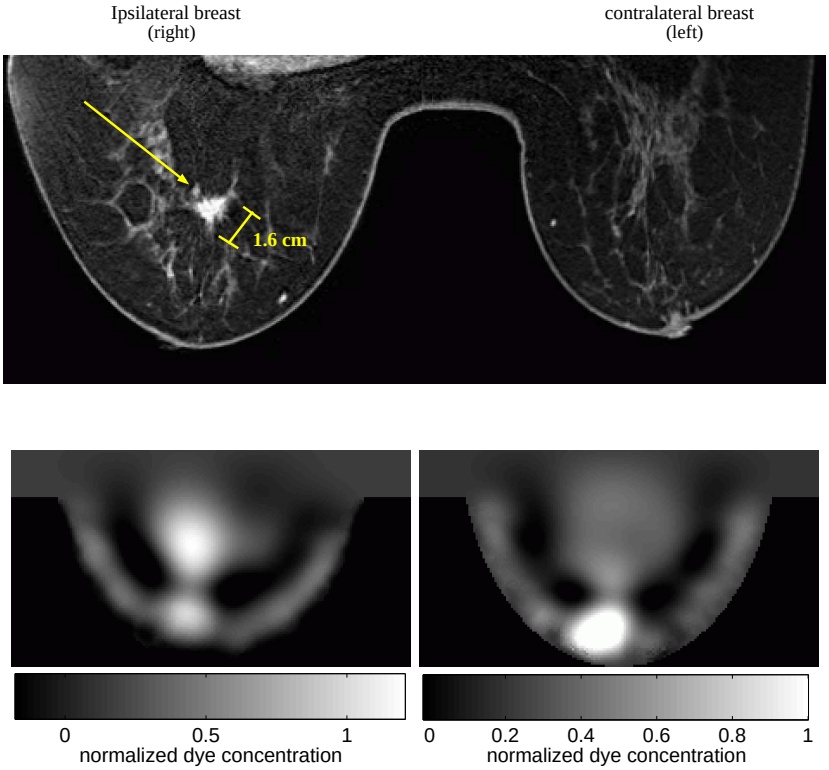

Figure 7.5: (top) MR slice (nearly axial but slightly tilted) through tumor position in right (ipsilateral) patient breast and through mammilla of left (contralateral) breast. Both breasts of the 74 year old patient mainly consist of fatty tissue and only a to small amount of glandular tissue. (bottom left, right) Fluorescence dye contrast reconstructions of ipsi- and contralateral breast. Slices through tumor and mammilla are shown with maximum dye concentration in the tumor and around the nipple for ipsi- and contralateral breast, respectively.

Chapter 8

Summary, outlook and conclusions

8.1 Summary

It was the aim of the present thesis to develop and validate statistical and numerical methods as well as software tools necessary to quantitatively assess various instrumental concepts, measurement schemes and methods of data analysis for optical and fluorescence mammography, including analysis of clinical data.

To this end, a software suite was developed based on the finite element method (FEM) to simulate propagation of NIR (laser) light and fluorescence radiation through inhomogeneous turbid media based on the diffusion approximation of the radiative transfer equation and to carry out linear and nonlinear reconstructions of the absorption and scattering properties of the medium from simulated or experimental data taken in frequency domain or time-domain. Simulations of photon densities of diffusely transmitted or remitted laser radiation and fluorescence radiation from an exogenous fluorescent contrast agent are supported by the software package for arbitrary object (breast) geometries and arrangements of sources and detectors.

In this thesis, a statistical method was developed to quantitatively assess detection limits for a lesion achieved by the two instrumental concepts implemented in optical mammographs that are presently used in clinical trials of laser and fluorescence mammography. Tomographic instrumentation require the patient to lie in prone position with one of her breasts immersed in a cup-shaped measurement chamber filled with scattering liquid (tomographic geometry) and equipped with a large number of light sources and photon detectors at its surface. Transmittance of laser and fluorescence radiation is measured for a large number of source-detector combinations amounting to essentially complete angular sampling. Scanning mammographs, on the other hand, slightly compress the breast between two parallel glass plates (slab geometry) and scan the source across one compression plate, taking transmittance measurements at a large number of source positions yet at only a limited number of source-detector offsets (limited angular sampling). The statistical analysis of noisy simulated photon densities of diffusely transmitted laser and fluorescence radiation is based on a chi-square test (test of null hypothesis) and allows to quantitatively determine the minimal size (radius) of a single (spherical) heterogeneity for it to be detectable at assumed absorption and fluorescence contrast with respect to the (homogeneous) background medium. For this purpose, numerical breast models were developed with estimated breast shapes consistent with the particular measurement geometry and covering a realistic range of tissue absorption and scattering properties, i.e. of light attenuation. From measurements carried out with existing tomographic instrumentation, a realistic noise model was derived to determine absolute and relative noise contributions to simulated photon densities of transmitted laser and fluorescence radiation. From the statistical analysis, the minimal detectable size of a (spherical) lesion was determined at each position inside the breast,

depending on breast (cup) size (tomographic geometry) and thickness of the compressed breast (slab geometry) as well as on background tissue optical properties. In addition, it was studied how lesion detectability depends on breast compression (slab geometry), on absolute and relative noise of simulated photon densities, on lesion size and on fluorescence contrast of the lesion. Because of the generally smaller source-detector distances associated with the compressed breast geometry, and hence higher transmitted laser and fluorescence intensities, lesion detection sensitivities are generally higher for scanning compared to tomographic mammographs and are less affected by the absolute noise floor. A minimal fluorescence contrast of 2.5 : 1 of the lesion above a homogeneous background was estimated for it to be detectable in fluorescence mammograms. Although such investigations could also be carried out by reconstructing absorption coefficients and the concentration of the exogenous fluorescent dye to generate optical mammograms, the excessive computational efforts required would prevent such systematic studies.

Interpretation of time-domain projection optical mammograms (slab geometry) is feasible even without the need for reconstruction of tissue optical properties. For this purpose, a time-window analysis of temporal point spread functions of transmitted laser pulses is used as standard technique to generate projection mammograms displaying predominantly absorption and scattering properties of breast tissue. By using a numerical phantom for a tumor bearing compressed breast (slab geometry) and by simulating noisy temporal point spread functions, an improved method of data analysis of time-domain transmission mammograms was developed in this thesis that allows to reduce cross talk between absorption and scattering images compared with the standard time-window analysis.

Whereas the results summarized in the preceding paragraphs were obtained from simulated data, other findings of the present thesis are based on linear and nonlinear reconstructions of tissue absorption coefficients, reduced scattering coefficients, and the concentration of an exogenous fluorescent dye. Several improvements were made on the reconstruction algorithms, e.g. introduction of a noise-weighted back projection for the algebraic reconstruction technique (ART) used to calculate the image vector, and separate regularization parameters for absorption and scattering reconstruction. Furthermore, in order to handle the amount of time-domain data that were collected by scanning mammographs (slab geometry) and to accelerate reconstructions, the standard nonlinear reconstruction technique was extended by introducing a sub-volume method. To this end, the entire (cuboid) volume of interest, where reconstructions are to be carried out, is split up into several (overlapping) cuboid sub-volumes. Likewise, the entire data set entering the reconstruction, and hence set of source-detector combinations associated with the entire volume, is divided into sub-sets of source-detector combinations adapted to each sub-volume. Subsequently, reconstructions of optical properties on the various sub-volumes are carried out in parallel, resulting in a considerable acceleration compared to the standard one-volume reconstruction method. Convergence of the standard method and of nonlinear sub-volume reconstructions was studied using simulated and experimental phantom data. Furthermore, errors and limitations introduced by the decomposition of the volume of interest into sub-volumes were investigated. Such errors can be tolerated as long as the number of sub-volumes is small and the entire data set entering the standard reconstruction is also used by the sub-volume method. In other words, the sizes of the sub-volumes must be consistent with all source-detector offsets, i.e. the data of which enter the standard nonlinear method so that no additional reduction takes place of the (limited) angular sampling range of the initial data set. The feasibility of sub-volume reconstructions using experimental phantom data was shown.

The compressed breast geometry allows to record transmittance of laser and fluorescence radiation over only a restricted range of projection angles, leading to an axial resolution in reconstructed images of tissue optical properties that is even worse compared to the poor spatial resolution of tomographic mammographs. It was shown in this thesis that axial resolution of time-domain scanning mammographs (slab geometry) can be improved by using diffuse reflectance besides transmittance data. To this end, reconstructions were carried out and spatial localization was compared using simulated and experimental data including and excluding time-domain diffuse reflectance measurements. To account for the different noise levels of experimental data taken at various source-detector offsets and of data corresponding to different angular frequency components used in the reconstruction, the noise-weighted back-projection

was applied, and quantitative reconstructions of fluorescent dye concentrations were carried out.

Linear and nonlinear absorption reconstructions as well as (linear) fluorescence reconstructions were carried out using clinical data of four patients involved in a clinical trial on tomographic fluorescence mammography. In all cases, the lesion could be detected in absorption (reconstructed absorption coefficients, first three cases) or fluorescence (reconstructed dye concentration, forth patient) mammograms and successfully correlated with MR mammograms, whenever available. An improved initialization model was introduced for linear and nonlinear reconstructions of the clinical data, by dividing the reconstructed cup volume into two compartments, one consisting of the matching scattering liquid surrounding the immersed breast, the other compartment representing a homogeneous breast with an estimated shape and absorption and scattering optical properties that were fitted in a preprocessing step to the *in vivo* data taken at several optical wavelengths. Reconstructed absorption coefficients and reconstructed concentrations of the exogenous fluorescent dye used exhibited artifacts compensating for changes in scattering properties of breast tissue including lesions whereas all lesions were assumed to be pure absorbers and no variations in the reduced scattering coefficient of the tissue were taken into account.

8.2 Outlook: topics for further investigation

This paragraph points out several areas, where improvements are possible beyond the results of this thesis. Investigations of detection sensitivities presented in this thesis were carried out for an ideal but highly unrealistic situation, where a single heterogeneity is located in an otherwise homogeneous numerical breast phantom, thus predicting fundamental detection limits of the instrumental setup. The assessment of detection sensitivity would be more relevant by using more realistic, i.e. inhomogeneous numerical breast phantoms that better mimic patient measurements [176, 177, 178]. Furthermore, the statistical method could be employed or a set of reconstructions could be carried out to quantitatively assess and compare the spatial resolution achieved by different source-detector arrangements, employing numerical phantoms with two neighboring heterogeneities. Rather than determining a minimal detection radius for a single lesion, the smallest distance required to resolve both lesions could be determined as a measure of spatial resolution.

Presently, despite parallelization, nonlinear reconstructions of absorption coefficients and fluorescent dye concentrations from continuous wave clinical data require up to several hours of computer time. However, with hardware improvements (e.g. calculations executed on graphics cards with high memory bandwidth [179]), accelerations are conceivable that will allow near real time reconstructions without impeding clinical workflow.

8.3 Conclusions

Due to superior angular sampling, tomographic optical mammography based on ring or cup shaped source-detector arrangements yields better spatial resolution along source-detector lines of sight compared to scanning mammography employing a compressed breast geometry. However, statistical analyses on simulated data showed that the compressed breast geometry provides superior detection sensitivity because of shorter average photon trajectories, and greatly reduces requirements on dynamic range of detection and acceptable noise floor. Furthermore, reconstructions of simulated and experimental phantom data showed that axial definition of lesions in slab geometry is improved by recording transmittance and reflectance data, preferably from either side of the compressed breast. Nonetheless, due to light scattering, optical mammography generally suffers from poor spatial resolution compared to X-ray mammography, MRI, and US mammography.

Reconstructions of clinical data carried out in this thesis revealed that fitted absorption and scattering coefficients averaged over the entire breast are needed for each patient to improve image quality rather

than assuming typical optical properties of breast tissue. Therefore, continuous wave measurements alone are not ideal to achieve this goal. Rather, a fluorescence mammograph should include a limited number of additional time-domain or frequency domain channels to measure these optical properties reliably besides a large number of continuous wave channels used for angular sampling.

Future clinical trials on fluorescence mammography should be carried out using such hybrid instrumentation together with nonlinear reconstruction of absorption and fluorescence contrast. Clinically, differential diagnosis, i.e. the distinction of benign and malignant tumors, although not being investigated in this thesis, is equally important as is the detection of lesions. Distinction of benign and malignant lesions cannot be achieved based on intrinsic (absorption and scattering) contrast alone, but may be possible by using a fluorescent contrast agent.

The results of this thesis suggest that scanning fluorescence mammography is feasible and may have clinical applications in detection and differentiation of breast tumors, provided suitable fluorescent contrast agents become available. However, despite many conceivable technical improvements, the clinical study on tomographic fluorescence mammography showed that clinical usefulness, application and impact of fluorescence mammography will largely depend on the fluorescent contrast agent used rather than on technical details, even if taking financial constraints on commercial instrumentation into account.

Appendix A

Appendix

A.1 Philips tomographic fluorescence mammograph

In the 1990's, Philips Research built a tomographic optical mammography system [15] that was able to perform absorption measurements of breast tissue at three wavelengths and was used in a clinical trial in Leiden 1999 – 2000. The system consists of a patient couch in which a cup-shaped measurement chamber is mounted. During examination, the patient lies in a prone position having one breast hanging freely (uncompressed) in the measurement cup. To ensure good optical contact between cup and breast, the remaining volume of the cup is filled with a scattering fluid having optical properties similar to breast tissue.

In 2005 Philips Medical Systems decided to build a clinical prototype of an improved optical mammograph, which bases on the prior system but was designed to additionally detect fluorescence light to enable imaging of fluorescent contrast agents. Furthermore, the number of source wavelengths was increased to four and the size of the measurement cup was adaptable to the size of the breast by the concept of exchangeable cup inserts. The fluorescence tomographic mammograph was used in 2006 – 2007 in two clinical trials, one for investigating intrinsic properties of breast tissue and one for characterizing the fluorescent dye Omocyanine (phase I clinical trial) that was provided by Bayer Schering Pharma.

A photo of the Philips tomographic fluorescence mammograph is shown in Fig. A.1. Cup inserts of three sizes (75B, 80D, 80F) can be attached to the base plate (shown in Fig. A.2). Light guides are mounted into the wall of the cup insert to illuminate the breast and allow detection of the transmitted laser light and emitted fluorescence light at attached photodiode detectors. The base contains 510 fiber ends that fit to the same number of fibers inside each cup insert. 255 fiber positions are connected to four steady-state lasers ($\lambda = 690$ nm, 730 nm, 780 nm, and 850 nm) via a fiber switch to illuminate the breast sequentially from various positions. Each of the remaining 255 fibers is connected via light guides to a photodiode detector, to allow detection at all 255 detector positions synchronously. To perform measurements of fluorescence photon densities, band filters are moved mechanically into the front of the photodiodes to suppress transmitted laser light. Before a measurement is performed, the scattering liquid (see Sec. A.5) is pumped into the cup insert via a valve placed at the bottom of the base plate and the cup inserts.

The 80D cup insert is rotationally symmetric with respect to the vertical y axis, its axial cross section an ellipse with a semi-major axis of 97 mm and a semi-minor axis of 67.5 mm (see Fig. 5.14). The prolate ellipsoid is cut perpendicularly to its major axis at a position ($y = 0$), 25 mm below its center. The first ring of optical fibers is located 10° below the $y = 0$ plane, with the remaining 11 fiber rings each separated by 6° from their neighbors. Starting from the fiber ring at the top, there are 30, 29, 28, 27, 26, 24, 22, 19, 17, 14, 11, and 8 equidistant source and detector fibers mounted into the cup wall resulting in a

total of 255 source fibers and 255 detection fibers. The source fibers are illuminated sequentially using cw diode laser radiation, and the signals of all detectors are recorded simultaneously. The setup of the cup-tomographic system is described in more detail in [180].

Figure A.1: Photo of Philips tomographic fluorescence mammograph. The patient is lying in prone position with one breast immersed in the fluid filled detection chamber which is mounted at the top center of the couch. The mammograph can be controlled via two identical displays attached at both front sides.

A.2 Boundary conditions

The air-tissue boundary $\partial\Omega$ is modeled by an index-mismatched Robin-type condition, i.e. by Eq. (5.15), where the flux leaving the boundary is proportional to the fluence rate at the boundary. The proportionality factor $A(\lambda)$ accounts for internal reflection of light back into the tissue, where the value of $A(\lambda)$ depends on the relative refractive index mismatch n_{rel} at the boundary. The approximate solution of $A(\lambda)$ is given in Eq. (5.16) and was derived in [114] using the reflectivity $K(\lambda)$ that can be approximated by [181]

$$K(\lambda) = -1.4399 n_{\mathrm{rel}}(\lambda)^{-2} + 0.7099 n_{\mathrm{rel}}(\lambda)^{-1} + 0.6681 + 0.0636 n_{\mathrm{rel}}(\lambda). \tag{A.1}$$

For a tissue-air boundary, and at a wavelength λ in the NIR spectral range, a typical value of $n_{\mathrm{rel}} = 1.33$ results in $A = 2.82$.

Figure A.2: Photo of base plate (without cup insert) with mounted (510) fiber tips. 255 fibers are connected to four steady-state lasers via a fiber switch, the remaining 255 fibers are connected to 255 photo diodes. The vent at the bottom of the base plate (and cup insert) allows pumping of scattering fluid into the detection chamber.

A different approach giving slightly different results for A and being derived from Fresnel's law has been proposed in [182] as

$$A(\lambda) = \frac{\frac{2}{1-R_0} - 1 + |\cos\theta_c|^3}{1 - |\cos\theta_c|^2}, \tag{A.2}$$

where the critical angle θ_c is given by

$$\theta_c = \arcsin\left(1/n_{rel}\right), \tag{A.3}$$

and

$$R_0 = \frac{(n_{rel}-1)^2}{(n_{rel}+1)^2}. \tag{A.4}$$

For a matched boundary, i.e. $n_{rel} = 1$, Eq. (5.16) and Eq. (A.2) yield $A = 1$.

Although the Dirac boundary condition (DBC), i.e.

$$\Phi(\boldsymbol{x}, \boldsymbol{x}_s, \lambda, \omega) = 0 \,\forall\, \boldsymbol{x} \in \partial\Omega, \tag{A.5}$$

describes the physical situation less accurately than the RBC, it leads to a simpler mathematical model. Hence, one approximates the RBC by extrapolated boundary conditions in analytical calculations, i.e. using a DBC fullfilled on a border $\partial\Omega'$ shifted outwards along the surface normals $\boldsymbol{n}$ of $\partial\Omega$ [115].

A.3 FEM implementation

Numerical forward model calculations and reconstructions were carried out by two separate computer programs, whose typical simulation times and details on the implementation of the algorithms, e.g. stopping criteria and grid triangulation, are given.

A.3.1 Forward model simulations

Numerical forward model calculations are performed by an in-house software using the `deal.II` library [183] for grid generation (triangulation) and inversion of system matrices. This software calculates and stores Green's functions for given source positions and can simulate data for all defined source-detector combinations. The numerical solution of the frequency domain diffusion equation by this software has been implemented throughout this thesis.

For calculations in slab geometry, the grid was triangulated by cuboids having an edge length between 1 mm to 2 mm. For cup geometry, the grid was generated by using ANSYS [184] and the basic elements of the grid were chosen to be hexahedrals, allowing an improved sampling of the curved surface compared with cuboids. Grids are refined at source and detector positions, which depend on the optical properties of the medium simulated. The number of vertices of the refined grids corresponding to the different cup sizes varies between approximately 100.000 to 280.000. For a refined slab, the number of vertices varies strongly depending on the slab thickness and the number of source and detector positions simulated, and can exceed 400.000 vertices for simulations of large volumes and many sources and detectors (scanning source and CCD detector). Therefore, all vertex numbers were resorted by the Cuthill-McKee renumbering algorithm [185] subsequently to the setup of the grid, to reduce the bandwith needed for the sparse system matrix.

The finite element method associates a shape function $\varphi_i(\boldsymbol{x})$ with each vertex i of the grid. During all forward model calculations, these shape function were chosen as being linear functions, i.e. being 1 s m^{-3} at vertex i, decreasing linearly to 0 towards adjacent neighbor vertices, and being 0 at all other vertices. Such choice results in a sparse system matrix being only nonzero if column and row numbers correspond to adjacent vertices or the same vertex.

The quadrature formula given in Eq. (5.42) approximates the integration needed for solving the diffusion equation via Galerkin's method by a finite sum. The 2-point-Gauss quadrature formula was chosen throughout this thesis, which is exact for polynomials of degree 3 [186].

With those settings, the solution of the cw diffusion equation at laser wavelength (fluorescence wavelength) via FEM corresponds to an inversions of a symmetric and positive definite system matrix that is carried out by a conjugate gradient solver having a stopping criterion of a maximum of 10000 (5000) steps or the Euclidian norm of the residual of the corresponding nodal solution vectors being smaller than approximately $0.3 \cdot 10^{-23}$ s/m^3. To speed up convergence of the inversion, the symmetric successive overrelaxation method (SSOR) has been chosen as a preconditioner with a relaxation factor of 1.2 [128]. To carry out frequency domain calculations, the complex valued elements of the system matrix have been split into real and imaginary part, resulting in an asymmetric sparse matrix, that was inverted by a biconjugate gradient method (BI-CGSTAB) with a Jacobian preconditioner having an relaxation factor of 1.2 for laser wavelength simulations and 1.4 for fluorescence wavelength simulations. The stopping criterion chosen for the laser (fluorescence) wavelength simulations was a maximum of 50000 (10000) steps or the weighted Euclidian norm of the photon density being smaller than approximately $1.7 \cdot 10^{-23}$ s/m^3 ($0.3 \cdot 10^{-23}$ s/m^3). All stopping criteria were selected by hand.

To improve the speed of numerical simulations, parallelization of calculations was implemented. A similar approach but limited to simultaneous calculation of different source positions has been proposed before [187]. The in-house software was extended to perform numerical calculations corresponding to different sources, frequency components, and wavelengths as separate processes. For this purpose, the simulation software was extended to support forward model simulations on many computers in parallel, so that simulations were carried out in parallel on 20-30 computers simultaneously (depending on the availability of resources) using a heterogeneous cluster. PCs available for calculations ranged from single core P4 (32 bit), dual core K8 (64 bit), to quad core P5 (64 bit) machines. However, splitting simulations into too many processes can be unfavorable, as the speed gain does not increase linearly due to additional calculation overhead, e.g. creation of the FE grid and renumbering of vertices.

Calculation time strongly depends on the situation that is simulated (i.e. solving the cw or frequency

domain diffusion equation, using a coarse or fine grid, simulating a small or large number of sources) an can range from minutes to several hours. Performed on a single computer, calculation time can exceed several days in worst cases.

A.3.2 Reconstruction

Nonlinear reconstructions are carried out by a suite of in-house software on the same grid that was used for the corresponding forward model calculations. This approach is not optimal regarding calculation time, because the grid is finer than the expected resolution of DOT. Nevertheless, using the same grid for forward model simulations and reconstructions avoids transformation of Green's functions between different grids. State-of-the-art methods like the implementation of adaptive meshes [188, 189] that can reduce the number of voxels between iterations have not been implemented in the reconstruction software.

To suppress artefacts during the reconstruction, Green's functions have been smeared out at their corresponding source positions by using a Gaussian blurred or an exponentially attenuated source term instead of a delta peak. Therefore, a source width of $\sigma_{\mathrm{src}} = 6$ mm has been used in all calculations throughout this thesis for both types of source term, motivated by multicore fibers that have been used in experiments carried out in slab geometry. The scanning source used during these experiments radiated light out of a fiber bundle of 2 mm diameter consisting of 100 μm fibers having a numerical aperture of $NA = 0.22$. Depending on the distance between fiber tip and tissue, and the medium used in between (air or glass plates for compression), the laser source illuminates a spot on the tissue of several millimeter in diameter. Therefore, the chosen value of $\sigma_{\mathrm{src}} = 6$ mm is in a realistic range.

Preprocessing of experimental data before reconstruction (see Sec. 6.2.1), i.e. discrete Fourier transformation of time-domain data, subtracting background fluorescence, and calculating instrumental factors for source-detector combinations, is carried out using several MATLAB [190] scripts that have been programmed during this thesis.

Depending on the geometry (e.g. slab thickness, cup size, number of grid vertices) and from the type of input data (cw or frequency domain data) that is used, reconstructions can take from several minutes (e.g. linear reconstruction in 75B cup geometry using cw data) to several days (e.g. nonlinear reconstruction in slab geometry using frequency domain data). Nonlinear reconstruction using experimental cw data and linear and nonlinear reconstruction using frequency domain data has been implemented within this thesis. Additionally, a parallelization of nonlinear reconstruction was integrated into the software for acceleration of calculations. For this purpose, calculations of inhomogeneous Green's functions corresponding to the various sources and detectors of the simulated geometry can be carried out in parallel on the cluster mentioned above. In slab geometry, the volume of interest can be separated into sub-volumes and reconstructions on each sub-volume can be calculated independently on a separate core. Using this method, nonlinear reconstructions in slab geometry were carried out on up to 20-30 computers, reducing calculation time to hours instead of days, or even making reconstruction possible at all because of reduced memory requirements for each sub-volume reconstruction compared with a reconstruction of the corresponding complete volume of interest due to the reduced size of the system matrix.

A.3.3 Discrete Fourier transformation of TPSFs

This paragraph illustrates how temporal point spread functions are transformed into frequency domain prior to reconstructions and how time-domain solutions of the diffusion equation are obtained from frequency domain solutions by inverse discrete Fourier transformation.

Temporal point spread functions measured via TCSPC are discrete functions, usually having about 600 sampling points and a sampling interval of $\Delta t \approx 16$ ps. Hence, the discrete TPSF is given by $\widetilde{\Phi}(\boldsymbol{x}_{\mathrm{d}}, \boldsymbol{x}_{\mathrm{s}}, \lambda, t_k)$ with $t_k = t_0 + k\Delta t$, where t_0 is the start time of detection and k is the sampling point number. In case of an even number N of time steps $k = 0, ..., N-1$, we define the discrete Fourier

transformation of the TPSF by

$$\Phi(\boldsymbol{x}_\mathrm{d}, \boldsymbol{x}_\mathrm{s}, \lambda, \omega_q) = \sum_{k=0}^{N-1} \widetilde{\Phi}(\boldsymbol{x}_\mathrm{d}, \boldsymbol{x}_\mathrm{s}, \lambda, t_k) \exp\left(-2\pi i k q/N\right) \Delta t, \tag{A.6}$$

for $q = -N/2, ..., N/2$. Therefore, calculations provide $N+1$ (complex) values of the TPSF in frequency domain, corresponding to frequencies limited by the Nyquist frequency, i.e. $\omega_\mathrm{min} = -\pi/\Delta t$ to $\omega_\mathrm{max} = \pi/\Delta t$. Due to the periodicity of Eq. (A.6) given by

$$\Phi(\boldsymbol{x}_\mathrm{d}, \boldsymbol{x}_\mathrm{s}, \lambda, \omega_{-q}) = \Phi(\boldsymbol{x}_\mathrm{d}, \boldsymbol{x}_\mathrm{s}, \lambda, \omega_{N-q}), \tag{A.7}$$

only N values are independent after the discrete Fourier transformation. Usually, the values in frequency domain are resorted, i.e. angular frequency components $0 \leq \omega \leq \omega_\mathrm{max}$ correspond to the index $q = 0, ..., N/2$, while angular frequency component $\omega_\mathrm{min} < \omega < 0$ correspond to the index $q = N/2+1, ..., N-1$, now giving a total of N components. Using this numeration, the inverse discrete Fourier transformation is given by

$$\widetilde{\Phi}(\boldsymbol{x}_\mathrm{d}, \boldsymbol{x}_\mathrm{s}, \lambda, t_k) = \frac{1}{N\Delta t} \sum_{q=0}^{N-1} \Phi(\boldsymbol{x}_\mathrm{d}, \boldsymbol{x}_\mathrm{s}, \lambda, \omega_q) \exp\left(2\pi i k q/N\right), \tag{A.8}$$

for $k = 0, ..., N-1$.

To circumvent numerical instabilities during calculations of TPSFs (see Sec. 5.1.6), the diffusion equation is solved in frequency domain instead of time-domain. Hence, Eq. (5.11) is solved for several frequency components ω_q, followed by an inverse Fourier transformation of the corresponding photon densities $\Phi(\boldsymbol{x}_\mathrm{d}, \boldsymbol{x}_\mathrm{s}, \lambda, \omega_q)$, yielding a TPSF in time-domain.

To achieve a simulation of a TPSF corresponding to a measurement interval $t_\mathrm{m} \approx 8$ ns and sampling interval $\Delta t \approx 16$ ps (i.e. having $N = t_\mathrm{m}/\Delta t \approx 500$ time steps), the maximal angular (Nyquist) frequency component that has to be chosen is given by $\omega_\mathrm{max} = \pi/\Delta t \approx 200$ GHz. Due to the symmetry of the diffusion equation, the complex conjugated photon densities corresponding to negative angular frequencies fullfill the relation

$$\Phi(\boldsymbol{x}, -\omega_q) = \Phi(\boldsymbol{x}, \omega_q)^*. \tag{A.9}$$

Therefore, only $1 + N/2$ non-negative frequency components have to be computed ranging from $\omega_q = 0$ to $\omega_q = \omega_\mathrm{max}$, reducing computation time approximately by a factor of two.

As a side-note, the constraint given in Eq. (5.56) does not vanish simply by performing calculations in frequency domain. Instead, it enforces high frequency components to be calculated on fine grids. Nonetheless, compared with time-domain calculation, the frequency domain relation has two major benefits:

1) Each frequency component can be calculated independently, i.e. numerical errors of one calculation do not disturb results corresponding to other frequency components, unlike the iterative calculations in time-domain, where the numerical errors emerging in an iterative solution $\widetilde{\boldsymbol{\Phi}}_\mathrm{nodal}(\boldsymbol{x}_\mathrm{s}, \lambda, t = k\Delta t)$ reappear in the next iteration step via the source term $F_- \widetilde{\boldsymbol{\Phi}}_\mathrm{nodal}(\boldsymbol{x}_\mathrm{s}, \lambda, t = k\Delta t)$, as can be seen in Eq. (5.55).

2) The diffusion equation in frequency domain can be solved in parallel for each frequency component. By carrying out the computations of selected frequency components on several computers (CPU cores) simultaneously, a tremendous speed gain in forward model calculations is achievable.

3) Since the maximum frequency component that can be transmitted through a compressed breast is $\omega \approx 6$ GHz, high frequency components can be neglected, reducing the computation time.

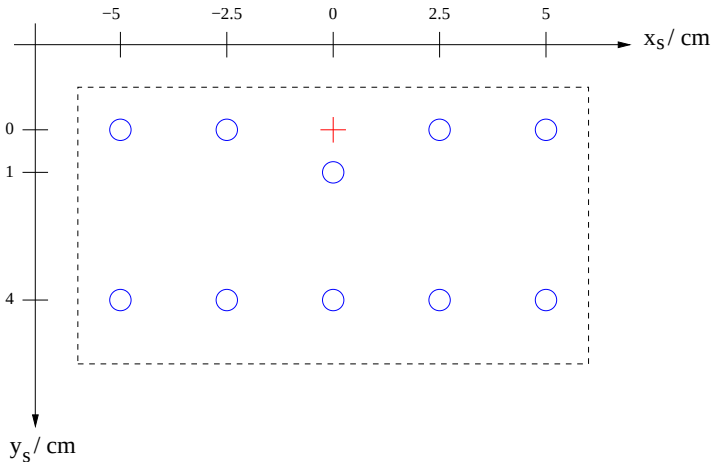

Figure A.3: Scan head for transmission and reflectance measurement with positions of source and detectors in the scanning ($x_s y_s$) coordinate system. The red plus sign indicates the source position, the blue circles indicate the cw detector positions.

A.4 Sensitivity simulation parameters

Details on the performance analysis of instrumentation in optical mammography (see Sec. 5.2.2) are given in this section. Lesion positions that have been investigated in slab geometry during this analysis, the source and detector positions that were used to simulate data, and the geometries of the numerical (compressed) breast phantoms are described.

A.4.1 Lesion positions sampled in slab geometry

Several positions $(x_\mathrm{l}, y_\mathrm{l}, z_\mathrm{l})$ of the lesion within the yz plane ($x_\mathrm{l} = 0$) where selected to probe lesion detectability throughout this slice of the (compressed) breast phantom (see Fig. 5.20). In slab geometry, the y_l and z_l coordinates were varied at increments of 1 cm within the limits -2 cm $\leq y_\mathrm{l} \leq 6$ cm, $0 \leq z_\mathrm{l} \leq 2$ cm ($d = 6$ cm, $d = 7$ cm) and $0 \leq z_\mathrm{l} \leq 3$ cm ($d = 9$ cm). Results for coordinates $z_\mathrm{l} < 0$ where obtained from those at $z_\mathrm{l} > 0$ exploiting symmetry.

A.4.2 Scan geometry

In slab geometry, the source at $\boldsymbol{x}_\mathrm{s} = (x_\mathrm{s}, y_\mathrm{s}, z_\mathrm{s})$ is scanned at the top and bottom faces of the phantom with -4 cm $\leq x_\mathrm{s} \leq 4$ cm, $0 \leq y_\mathrm{s} \leq 9$ cm, and $z_\mathrm{s} = \pm d/2$. Each scan head contains one source and ten photodiode detectors positioned at various source-detector offsets ($\Delta y = 0$ cm, 4 cm with $\Delta x = \pm 5$ cm, ± 2.5 cm, and $\Delta y = 1$ cm, 4 cm with $\Delta x = 0$) as illustrated in Fig. A.3.

A.4.3 Phantom geometry

Spheres, cylinders, and cuboids were used as basic geometric elements to construct the numerical breast phantoms. Complex objects can be generated from these elements by joining selected parts that were properly cut.

The construction scheme of the numerical breast phantom in slab geometry used in Sec. 5.2.2 is given in Fig. A.4, where a projection onto the $z = 0$ plane is shown. Cuboids, cylinders, and spheres are

Table A.1: Postions P with coordinates (x, y), lines L and radii R of the phantom geometry as illustrated in Fig. A.4

thickness d	6 cm	7 cm	9 cm
P1 / mm	(-40, -44)	(-46.7, -52.5)	(-60, -69.5)
P2 / mm	(-40, 46)	(-46.7, 52.5)	(-60, 65.5)
P3 / mm	(0, 10)	(0, 0)	(0, -20)
P4 / mm	(-70, -44)	(-81.7, -52.5)	(-105, -69.5)
P5 / mm	(-70, 46)	(-81.7, 52.5)	(-105, 65.5)
P6 / mm	(0, -44)	(0, -52.5)	(0, -69.5)
L1 / mm	90	105	135
R1 / mm	98.5	114.9	147.7
R2 / mm	60.2	70.3	90.3

depicted by full lines, dashed lines, and dotted lines, respectively. Radius vectors are shown for the spheres starting at their centers. All three phantoms, corresponding to the three slab thicknesses, consist of four elements:

1) The breast bulk is built up by the cuboid (P1, P1', P2', P2) of thickness d and depth L1, centered at position P3, i.e. $(x, y) = (0, 1\text{ cm})$, $(0, 0)$, and $(0, -2\text{ cm})$ for the three breast thicknesses $d = 6\text{ cm}, 7\text{ cm}$, and 9 cm, respectively.

2) Each of the two elements representing the left and right segments of the breast is built from the half cylinders (P4, P1, P2, P5) and (P4', P5', P2', P1') of radius $d/2$. A large sphere of radius R1 centered at position P6 intersects with the half cylinders to create rounded surfaces.

3) The tip of the breast is simulated by adding a spherical calotte to the front face of the cuboid. The spherical calotte corresponds to a sphere of radius R2 centered at P3. The circular base plane of the calotte has a diameter of P2P2' but is truncated along the z direction to d.

The numerical breast phantoms constructed in this way do not have an entirely smooth surface, however remaining vertices and edges are far enough from assumed lesion positions to neglect their influence. Although the breast wall with optical properties considerably different from breast tissue does not enter into our simulations, the approximate position of the breast wall is indicated in Fig. A.4 for clarity. The coordinates of points (P), lines (L), and sphere radii (R) of the 3 phantoms are given in Tab. A.1. Primed points P' are obtained from points P by symmetry.

The forward model calculations are performed on a finite element grid (for more details see [145]). Most cells of the FE grid have a volume of $(0.25\text{ cm})^3$, but the cells at source and detector positions are refined additionally and have a volume of $(0.125\text{ cm})^3$. For the phantom with thickness $d = 6$ cm a total of approximately 250000 grid nodes is used, and the entire grid encloses a volume of $25 \times 18 \times 6\text{ cm}^3$. The grid was chosen large enough to span a volume that includes all source positions, lesion positions and detector positions. The resulting grid dimensions for the three different phantoms are listed in Table A.2.

A total of 2442 source positions and 7738 detector positions for each phantom scan are sampled using measurements in transmission and reflection geometry taken on both compression plates. For each source position 20 detectors collect data, which results in a total of 48840 simulated data for an absorption and fluorescence scan.

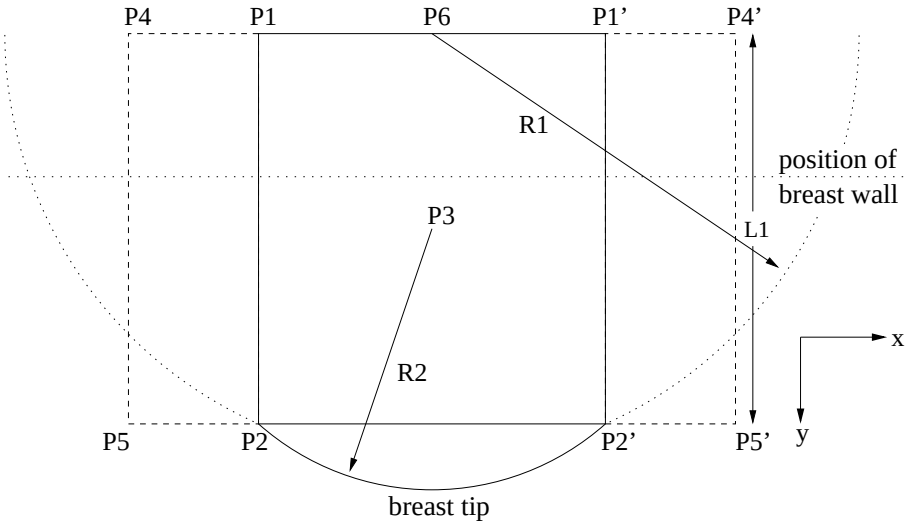

Figure A.4: Breast phantoms generated from cuboids (solid line), half cylinders (dashed line), and spherical calottes (solid line). Projections of these elements on the $z = 0$ plane are shown. In addition a large sphere (radius R1) is indicated intersecting and limiting the half cylinders. Positions P, lines L and radii R are given in Table A.1. Although the breast wall is not included in the simulations its approximate location is indicated to facilitate 3D perception.

Table A.2: Minimal and maximal grid node coordinates (x_g, y_g, z_g) of the three different grids used for phantom simulations.

Grid size	$d = 6$ cm	$d = 7$ cm	$d = 9$ cm
$\max(x_g)$ / cm	12.5	12.5	12.5
$\min(x_g)$ / cm	-12.5	-12.5	-12.5
$\max(y_g)$ / cm	14	14	16
$\min(y_g)$ / cm	-4	-4	-6
$\max(z_g)$ / cm	3	3.5	4
$\min(z_g)$ / cm	-3	-3.5	-4
number of nodes	248871	278461	405229

Table A.3: Approximated optical properties of scattering liquid MF2.1 at the four laser wavelengths used in the Philips tomographic fluorescence mammograph.

	$\lambda = 690$ nm	$\lambda = 730$ nm	$\lambda = 780$ nm	$\lambda = 850$ nm
k/m	95	115	110	115
μ_s'/mm^{-1}	1.7	1.5	1.3	1.2
μ_a/mm^{-1}	0.0018	0.0029	0.0031	0.0037

The solution of one forward model simulation for a single phantom scan with a lesion at one position needs approximately 9h to 12h on a standard PC, mainly depending on the thickness of the slab. Simulations are carried out at the excitation and fluorescence wavelength for the breast phantom containing a single lesion and for all five lesion radii. In addition, one simulation is performed for each breast phantom without a lesion, and a single simulation for the reference measurement, where the slab is completely filled with scattering fluid. For lesion diameters smaller than 1 cm, the grid is additionally refined and the same holds true for simulations involving the homogeneous breast phantom used for comparison. In this way, a total of 816 simulations were carried out, comprising 326 simulations for the $d = 9$ cm phantom and 245 simulations for each of the two smaller phantoms.

A.5 Optical properties of scattering liquid MF2.1

The scattering liquid called Matching Fluid 2.1 (MF2.1) that has been used in several phantom and patient scans was provided by Philips Research Europe – Eindhoven. Its optical properties at the four laser wavelengths $\lambda = 690$ nm, 730 nm, 780 nm, and 850 nm have been determined by measurements and are given in Table A.3. The reduced scattering coefficient $\mu_s'(\lambda)$ can be modeled by a Mie model (see Sec. 5.1.3) having a scattering amplitude of $a = 0.9$ mm^{-1} (normalized to $\lambda_0 = 1000$ nm), and a scattering power of $b = 1.7$.

A.6 Numerical breast phantoms used for spectral fits

To test the spectral fit derived in Sec. 6.2.5, three numerical breast phantoms were simulated, modeling three different breasts (strong attenuation (dense) and small size, medium attenuation and medium size, small attenuation (fatty) and large size), with each filling the 80D cup only partly while scattering liquid (MF2.1) fills the remaining gap. All three numerical breast phantoms used the same Mie scattering model with scattering amplitude $a = 1.17$ mm^{-1} (normalized to $\lambda_0 = 1000$ nm) and scattering power $b = 0.56$. The spectral model of the intrinsic absorption coefficient $\mu_a^{\text{chrom}}(\lambda)$ of the three breasts was given by the three major constituents, i.e. water (H_2O), deoxyhemoglobin (HbR), and oxyhemoglobin (HbO), and their corresponding concentrations, given in Table A.4. In all three numerical breast phantoms, a concentration of 10 nM of the Omocyanine dye was simulated.

The corresponding total absorption coefficient μ_a (chromophore absorption μ_a^{chrom} plus the additional absorption caused by the fluorescent dye μ_a^{dye}) is given in Table A.5 for the four simulated laser wavelengths, i.e. $\lambda = 690$ nm, 730 nm, 780 nm, and 850 nm.

Table A.4: Constituents of three numerical 80D breast phantoms, scattering amplitude a (normalized by $\lambda_0 = 1000$ nm), and scattering power b shown in Fig. 6.18.

	c_{H_2O}/μM	c_{HbR}/μM	c_{HbO}/μM	dye conc. c/nM	a/ mm^{-1}	b
dense small	47%	6	13	10	1.17	0.56
medium	47%	5	12	10	1.17	0.56
fatty large	47%	3	8	10	1.17	0.56

Table A.5: Absorption and scattering coefficient of three 80D breast phantoms used for breast shape estimation and spectral fit.

	$\lambda = 690$ nm	$\lambda = 730$ nm	$\lambda = 780$ nm	$\lambda = 850$ nm
μ_a/mm^{-1} (dense small)	0.0040	0.0038	0.0049	0.0061
μ_a/mm^{-1} (medium)	0.0035	0.0035	0.0045	0.0058
μ_a/mm^{-1} (fatty large)	0.0023	0.0029	0.0033	0.0045
μ_s'/mm^{-1}	1.435	1.391	1.340	1.277

A.7 BI-RADS assessment categories

The Breast Imaging Reporting and Data System (BI-RADS) assessment categories are formulated by the American-College of Radiology (ACR) [191]. This subjective classification stages benign and malignant findings in mammograms into six categories.

- Category 0 – Assessment incomplete, additional image evaluation needed.
- Category 1 – Negative finding.
- Category 2 – Benign finding.
- Category 3 – Probably benign finding. Short interval follow-up suggested.
- Category 4 – Finding of suspicious abnormality. Biopsy should be considered.
- Category 5 – Highly suggestive of malignancy. Appropriate follow-up action should be taken.

Appendix B

Publications and output

B.1 Papers

- Investigation of Detection Limits for Diffuse Optical Tomography Systems: I. Theory and Experiment, R. Ziegler, B. Brendel, A. Schipper, R. Habers, M. v. Beek, H. Rinneberg, and T. Nielsen, 2008, *Physics in Medicine and Biology*, submitted (related to Sec. 5.2.2)

- Investigation of detection limits for diffuse optical tomography systems: II. Comparison of slab and cup geometry, R. Ziegler, B. Brendel, H. Rinneberg, and T. Nielsen, 2008, *Physics in Medicine an Biology*, submitted (related to Sec. 5.2.2)

- Nonlinear reconstruction of absorption and fluorescence contrast from measured diffuse transmittance and reflectance of a compressed-breast-simulating phantom, R. Ziegler, T. Nielsen, T. Köhler, D. Grosenick, O. Steinkellner, A. Hagen, R. Macdonald, and H. Rinneberg, 2008, *Applied Optics*, in preparation (related to Sec. 6.1.3, 6.2.1, and 6.2.2)

- DOT reconstruction of arbitrary large regions using a sub-volume method, R. Ziegler, T. Nielsen, O. Steinkellner, A. Hagen, D. Grosenick, R. Macdonald, and H. Rinneberg, 2008, *Applied Optics*, in preparation (related to Sec. 6.2.3)

- Linear image reconstruction for a diffuse optical mammography system in a non-compressed geometry using scattering fluid, T. Nielsen, B. Brendel, R. Ziegler, F. Uhlemann, C. Bontus and T. Köhler, 2008, *Applied Optics*, submitted

- Algebraic Reconstruction Techniques for Spectral Reconstruction in Diffuse Optical Tomography, B. Brendel, R. Ziegler, and T. Nielsen, 2008, *Applied Optics*, submitted

B.2 Awards

- Philips research lab Hamburg innovation award 2006, "Reconstruction Techniques for Optical Tomography"

B.3 Patents

- EP06126442.0 "Imaging of Turbid Medium", R. Ziegler, T. Nielsen

- EP07118848.6 "Cup-Shape Diffuse Optical Tomography System", T. Köhler, T. Nielsen, B. Brendel, A. Ziegler, R. Ziegler
- EP08153363.0 "Method for reconstructing a fluorescence image of the interior of a turbid medium and device for imaging of a turbid medium", R. Ziegler, A. Ziegler, T. Nielsen

B.4 Referee

- for Communications in Numerical Engineering

B.5 Conferences

- Spatial Resolution for Time-Resolved Optical Tomography in Slab Geometry R. Ziegler, T. Köhler, T. Nielsen, O. Steinkellner, D. Grosenick, H. Rinneberg, NSS/MIC 2006, poster M11-196
- Optical Fluorescence Mammography, M. van der Voort, L. Bakker, M. van der Mark, M. van Beek, T. Nielsen, T. Köhler, R. Ziegler, K. Licha, M. Pessel, Gordon Research Conference 2006 - Meeting on Lasers in Medicine & Biology, talk
- Optical Fluorescence Mammography: A Phantom Feasibility Study, M. van Beek, M. van der Voort, L. Bakker, M. van der Mark, T. Nielsen, T. Köhler, R. Ziegler, K. Licha, M. Pessel, Fifth Annual Meeting of The Society for Molecular Imaging 2006, talk
- Diffuse optical imaging of the female breast, M. van der Mark, G. t'Hooft, L. Bakker, M. van der Voort, M. van Beek, T. Nielsen, T. Köhler, R. Ziegler, K. Licha, M. Pessel, EOS 2006
- Optical Fluorescence Imaging of Breast Cancer, L. Bakker, M. van der Mark, M. van Beek, M. van der Voort, G. t'Hooft, T. Nielsen, T. Köhler, R. Ziegler, K. Licha, M. Pessel, OSA 2006, poster
- Optical Fluorescence Imaging of Breast Cancer, M. van Beek, L. Bakker, M. van der Mark, M. van der Voort, T. Nielsen, T. Köhler, R. Ziegler, K. Licha, M. Pessel, A. Feuerabend, J.P. Meeuwse, D. van Pijkeren, S. Deckers, SMI conference 2006, talk
- Towards Fluorescence Mediated Laser Scanning Mammography: Phantom Experiments and Contrast Mechanism, O. Steinkellner, D. Grosenick, R. Ziegler, T. Nielsen, R. Macdonald, H. Rinneberg, OSA 2006, poster
- Optical Fluorescence Imaging of Breast Cancer, L. Bakker, M. van der Mark, M. van Beek, M. van der Voort, T. Nielsen, T. Köhler, R. Ziegler, K. Licha, M. Pessel, BioNanoMeter conference 2006, talk
- Image reconstruction and evaluation of system performance of optical fluorescence tomography, T. Nielsen, B. Brendel, T. Köhler, R. Ziegler, A. Ziegler, L. Bakker, M. van Beek, M. B. van der Mark, M. van der Voort, R. Harbers, K. Licha, M. Pessel, J. P. Meeuwse, A. Feuerabend, D. van Pijkeren, S. Deckers, Bios 2007, 6431-07, invited talk
- Optical Fluorescence Mammography: A Phantom Feasibility Study, M. van Beek, M. van der Voort, L. Bakker, M. van der Mark, T. Nielsen, R. Ziegler, K. Licha, M. Pessel, Society of Molecular Imaging Conference 2007, poster
- Reconstruction of absorption and fluorescence contrast for scanning time-domain fluorescence mammography, R. Ziegler, T. Nielsen, T. Köhler, D. Grosenick, O. Steinkellner, A. Hagen, R Macdonald, H. Rinneberg, Bios 2007, 6434-17, talk

- Phantom study on combined cw and time-domain fluorescence mammography, D. Grosenick, O. Steinkellner, A. Hagen, R. Ziegler, T. Nielsen, R. Macdonald, H. Rinneberg, Bios 2007, 6434-18, talk
- Development of a time-domain fluorescence mammograph, A. Hagen, O. Steinkellner, D. Grosenick, R. Ziegler, T. Nielsen, K. Lauritsen, R. Macdonald, H. Rinneberg, Bios 2007, 6434-35, talk
- Development of a multi-channel time-domain fluorescence mammograph, A. Hagen, O. Steinkellner, D. Grosenick, M. Möller, R. Ziegler, T. Nielsen, K. Lauritsen, R. Macdonald, H. Rinneberg, ECBO 2007, 6629-39, talk
- Phantom study on contrast and detection limits of scanning time-domain fluorescence mammography, O. Steinkellner, D. Grosenick, A. Hagen, R. Macdonald, H. Rinneberg, R. Ziegler, T. Nielsen, ECBO 2007, 6629-04, talk
- Phantom development for optical fluorescence mammography M. van Beek, L. Bakker, B. Brendel, H. Compen, R. Harbers, T. Köhler, K. Licha, M. B. van der Mark, R. Nachabe, T. Nielsen, M. Pessel, M. van der Voort, R. Ziegler, Bios 2008, 6870-10, talk
- Accelerated DOT reconstruction using multiple sub-volumes, R. Ziegler, T. Nielsen, D. Grosenick, O. Steinkellner, A. Hagen, R. Macdonald, H. Rinneberg, Bios 2008, 6850-09, talk
- Nonlinear Reconstruction of Continuous Wave Diffuse Optical Tomography Using Fitted Diffusion Coefficients, R. Ziegler, B. Brendel, A. Ziegler, T. Nielsen, H. Rinneberg, OSA Biomed 2008, poster
- Recording of Artifact-Free Reflection Data with a Laser and a Fluorescence Scanning Mammograph for improved axial resolution, O. Steinkellner, A. Hagen, C. Stadelhoff, D. Grosenick, R. Macdonald, H. Rinneberg, R. Ziegler, T. Nielsen, OSA Biomed 2008, poster
- Linear image reconstruction for a diffuse optical mammography system in a non-compressend geometry using scattering fluid, T. Nielsen, B. Brendel, R. Ziegler, T. Köhler, OSA Biomed 2008, poster
- Optical Imaging of Breast Cancer from an Industrial Perspective, Martin B. van der Mark, Leon Bakker, Michiel van Beek, Claas Bontus, Bernhard Brendel, Rik Harbers, Thomas Köhler, Anais Leproux, Tim Nielsen, Marjolein van der Voort, Falk Uhleman, Andrea Wiethoff, Ronny Ziegler, Andy Ziegler, Kai Licha, Lueder Fels, Martin Pessel, Stephanie van de Ven, Sjoerd Elias, Willem Mali, Peter Luijten, OSA Biomed 2008, invited talk
- Optical imaging of breast cancer by spectral and fluorescence diffuse optical tomography, Martin van der Mark, Anais Leproux, Tim Nielsen, Marjolein van der Voort, Leon Bakker, Michiel van Beek, Claas Bontus, Bernhard Brendel, Rik Harbers, Thomas Köhler, Falk Uhleman, Andrea Wiethoff, Ronny Ziegler, Andy Ziegler, Lueder Fels, Martin Pessel, Stephanie van de Ven, Sjoerd Elias, Willem Mali, Peter Luijten, Frontiers in Optics 2008, invited talk

Appendix C

Derivations

C.1 Homogeneous medium with spherical heterogeneity

Diffuse photon density waves (DPDW) give analytical solutions for homogeneous and partially homogeneous turbid media for simple geometries [25], provided the heterogeneity is a sphere. In the following, we present the derivation of fluorescence DPDW for the homogeneous infinite medium and of attenuation DPDW for the infinite medium with a spherical heterogeneity embedded. We follow [26, 27], but adapted formulas to the Fourier transformation and source term normalization as was chosen in Sec. 5.1.1.

C.1.1 Homogeneous infinite medium: fluorescence DPDW

For a laser pulse represented by temporal and spatial delta functions at $\boldsymbol{x}_\mathrm{s}$ the Fourier amplitude of the source term is given by

$$q_0(\boldsymbol{x}, \boldsymbol{x}_\mathrm{s}, \lambda, \omega) = \delta(\boldsymbol{x} - \boldsymbol{x}_\mathrm{s})/v\,, \tag{C.1}$$

for all angular modulation frequencies (see Sec. 5.1.2), yielding for the laser photon density per unit angular frequency interval $\Phi_0^\mathrm{inf}(\boldsymbol{x}, \boldsymbol{x}_\mathrm{s}, \lambda, \omega)$ the expression given in Eq. (5.24). It should be noted that the absorption coefficient entering the complex wave number $k(\lambda, \omega)$ contains the background chromophore contribution and the contribution of the fluorescent dye, i.e. $\mu_\mathrm{a}^0(\lambda) = \mu_\mathrm{a,0}^\mathrm{chrom}(\lambda) + \mu_\mathrm{a,0}^\mathrm{dye}(\lambda)$.

The excited fluorophores, distributed over the entire medium are the source term of the fluorescence DPDW,

$$q_0^\mathrm{f}(\boldsymbol{x}, \boldsymbol{x}_\mathrm{s}, \lambda, \omega) = \frac{\eta \mu_\mathrm{a}^\mathrm{dye}(\lambda)}{1 + i\omega\tau} \Phi_0^\mathrm{inf}(\boldsymbol{x}, \boldsymbol{x}_\mathrm{s}, \lambda, \omega). \tag{C.2}$$

Integrating over all fluorescence DPDWs of the distributed fluorescence sources $q_0^\mathrm{f}(\boldsymbol{x}_1, \boldsymbol{x}_\mathrm{s}, \lambda, \omega)$ results in the detected fluorescence DPDW

$$\Phi_{0,\mathrm{f}}^\mathrm{inf}(\boldsymbol{x}, \boldsymbol{x}_\mathrm{s}, \lambda, \omega) = \int_\Omega d\boldsymbol{x}_1 q_0^\mathrm{f}(\boldsymbol{x}_1, \boldsymbol{x}_\mathrm{s}, \lambda, \omega) \frac{1}{D^0(\lambda_\mathrm{f})} \frac{\exp\left(-ik(\lambda_\mathrm{f}, \omega)\left|\boldsymbol{x} - \boldsymbol{x}_1\right|\right)}{4\pi\left|\boldsymbol{x} - \boldsymbol{x}_1\right|}. \tag{C.3}$$

The diffusion coefficient and the complex wave number at the fluorescence wavelength λ_f are denoted by $D^0(\lambda_\mathrm{f})$ and $k(\lambda_\mathrm{f}, \omega)$, respectively. The integral in equation (C.3) can be solved analytically for an infinite homogeneous medium as shown in [26] and results in

$$\begin{aligned}\Phi_{0,\mathrm{f}}^\mathrm{inf}(\boldsymbol{x}, \boldsymbol{x}_\mathrm{s}, \lambda, \omega) = & \frac{\eta \mu_\mathrm{a}^\mathrm{dye}(\lambda)}{v D^0(\lambda) D^0(\lambda_\mathrm{f})} \frac{1}{1 + i\omega\tau} \frac{1}{k^2(\lambda, \omega) - k^2(\lambda_\mathrm{f}, \omega)} \\ & \left[\frac{\exp\left(-ik(\lambda, \omega)\left|\boldsymbol{x} - \boldsymbol{x}_\mathrm{s}\right|\right)}{4\pi\left|\boldsymbol{x} - \boldsymbol{x}_\mathrm{s}\right|} - \frac{\exp\left(-ik(\lambda_\mathrm{f}, \omega)\left|\boldsymbol{x} - \boldsymbol{x}_\mathrm{s}\right|\right)}{4\pi\left|\boldsymbol{x} - \boldsymbol{x}_\mathrm{s}\right|}\right],\end{aligned} \tag{C.4}$$

which is a superposition of two spherical waves with different wave numbers, $k(\lambda,\omega)$ at the laser wavelength, and $k(\lambda_\mathrm{f},\omega)$ at the fluorescence wavelength. In the limit $\lambda_\mathrm{f}\to\lambda$ equation (C.4) simplifies to

$$\lim_{\lambda_\mathrm{f}\to\lambda}\Phi^{\mathrm{inf}}_{0,\mathrm{f}}(\boldsymbol{x},\boldsymbol{x}_\mathrm{s},\lambda,\omega)=\frac{\eta\mu_\mathrm{a}^{\mathrm{dye}}(\lambda)}{4\pi v\left(D^0(\lambda)\right)^2}\frac{1}{1+i\omega\tau}\frac{1}{2k(\lambda,\omega)}\exp\left(-ik(\lambda,\omega)\left|\boldsymbol{x}-\boldsymbol{x}_\mathrm{s}\right|-\frac{i\pi}{2}\right). \tag{C.5}$$

Eq. (C.5) is no longer a diffusive spherical wave. This can be explained by the absorption of laser photons after the free absorption length $1/\mu_\mathrm{a}^{\mathrm{dye}}$ and isotropic re-emission of photons rather than elastic forward scattering.

C.1.2 Homogeneous infinite medium with spherical heterogeneity

Attenuation DPDW

For the infinite homogeneous medium with an additional spherical object and a point source of laser photons at $\boldsymbol{x}_\mathrm{s}$ outside the sphere, the solution of the diffusion equation (Eq. (5.11)) is provided by the diffraction of the attenuation DPDW $\Phi_0^{\mathrm{inf}}(\boldsymbol{x},\boldsymbol{x}_\mathrm{s},\lambda,\omega)$. In the following, the subscript 1 always denotes quantities outside the sphere, subscript 2 quantities inside the sphere. The origin of the coordinate system coincides with the center of the sphere, and for simplicity, the refraction indices outside and inside the sphere are assumed to be equal, i.e. $n_1=n_2$.

Shown in Fig. C.1a is the attenuation DPDW at the laser wavelength, which consists of the homogeneous component Φ_{10}^{inf} and the scattered component $\Phi_{1\mathrm{sc}}$ expanded into partial waves and built up by spherical Hankel functions of the first kind $h_l^{(1)}$ and spherical harmonics $Y_{lm}(\Omega)$:

$$\begin{aligned}\Phi_1(\boldsymbol{x},\boldsymbol{x}_\mathrm{s},\lambda,\omega) &= \Phi_{10}^{\mathrm{inf}}(\boldsymbol{x},\boldsymbol{x}_\mathrm{s},\lambda,\omega)+\Phi_{1\mathrm{sc}}(\boldsymbol{x},\boldsymbol{x}_\mathrm{s},\lambda,\omega) &\text{(C.6)}\\ &= \Phi_{10}^{\mathrm{inf}}(\boldsymbol{x},\boldsymbol{x}_\mathrm{s},\lambda,\omega)+\sum_{l,m}A_{lm}(\boldsymbol{x}_\mathrm{s},\lambda,\omega,r_{\mathrm{sph}})h_l^{(1)}(k_1(\lambda,\omega)\left|\boldsymbol{x}\right|)Y_{lm}(\Omega), &\text{(C.7)}\end{aligned}$$

with the homogeneous medium solution

$$\Phi_{10}^{\mathrm{inf}}(\boldsymbol{x},\boldsymbol{x}_\mathrm{s},\lambda,\omega)=\frac{1}{vD_1(\lambda)}\frac{\exp\left(-ik_1(\lambda,\omega)\left|\boldsymbol{x}-\boldsymbol{x}_\mathrm{s}\right|\right)}{4\pi\left|\boldsymbol{x}-\boldsymbol{x}_\mathrm{s}\right|}, \tag{C.8}$$

and coefficients A_{lm}, which can be calculated from the boundary conditions at the surface of the sphere B [25, 27]. $A_{lm}(\boldsymbol{x}_\mathrm{s},\lambda,\omega,r_{\mathrm{sph}})$ is shorthand for

$$A_{lm}(\boldsymbol{x}_\mathrm{s},\lambda,\omega,r_{\mathrm{sph}})=A_{lm}(\boldsymbol{x}_\mathrm{s},k_1(\lambda,\omega),k_2(\lambda,\omega),D_1(\lambda),D_2(\lambda),r_{\mathrm{sph}}). \tag{C.9}$$

The attenuation DPDW inside the sphere is given by

$$\Phi_2(\boldsymbol{x}_2,\boldsymbol{x}_\mathrm{s},\lambda,\omega)=\sum_{l,m}B_{lm}(\boldsymbol{x}_\mathrm{s},\lambda,\omega,r_{\mathrm{sph}})j_l(k_2(\lambda,\omega)\left|\boldsymbol{x}_2\right|)Y_{lm}(\Omega_2), \tag{C.10}$$

where $j_l(k_2(\lambda,\omega)\left|\boldsymbol{x}_2\right|)$ are spherical Bessel functions and $B_{lm}(\boldsymbol{x}_\mathrm{s},\lambda,\omega,r_{\mathrm{sph}})$ stands for $B_{lm}(\boldsymbol{x}_\mathrm{s},\lambda,\omega,r_{\mathrm{sph}})=B_{lm}(\boldsymbol{x}_\mathrm{s},k_1(\lambda,\omega),k_2(\lambda,\omega),D_1(\lambda),D_2(\lambda),r_{\mathrm{sph}})$. These coefficients are given in [26, 27].

Fluorescence DPDW

The fluorescence DPDW

$$\Phi_{1,\mathrm{f}}(\boldsymbol{x},\boldsymbol{x}_\mathrm{s},\lambda,\omega)=\Phi'_{1,\mathrm{f}}(\boldsymbol{x},\boldsymbol{x}_\mathrm{s},\lambda,\omega)+\Phi''_{1,\mathrm{f}}(\boldsymbol{x},\boldsymbol{x}_\mathrm{s},\lambda,\omega) \tag{C.11}$$

is separated in two contributions, one ($\Phi''_{1,\mathrm{f}}(\boldsymbol{x},\boldsymbol{x}_\mathrm{s},\lambda,\omega)$) originating from excited fluorophores inside the sphere, another one ($\Phi'_{1,\mathrm{f}}(\boldsymbol{x},\boldsymbol{x}_\mathrm{s},\lambda,\omega)$) generated by excited fluorophores outside the sphere. The

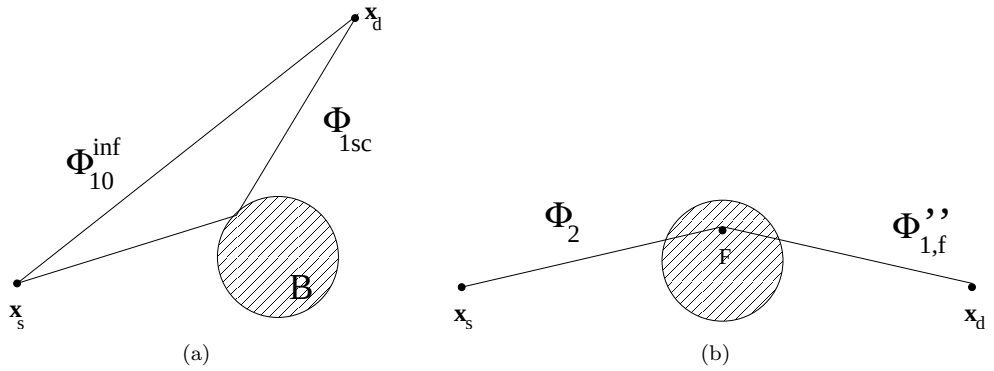

Figure C.1: (a) Attenuation DPDW with a component Φ_{10}^{inf} running straight from source position $\boldsymbol{x}_{\mathrm{s}}$ to detector position $\boldsymbol{x}_{\mathrm{d}}$ and a component $\Phi_{1\mathrm{sc}}$ scattered by the sphere B. (b) Detected fluorescence DPDW $\Phi''_{1,\mathrm{f}}$ emitted from fluorophores inside the sphere ("lesion fluorescence") and excited by the attenuation DPDW Φ_2 inside the sphere.

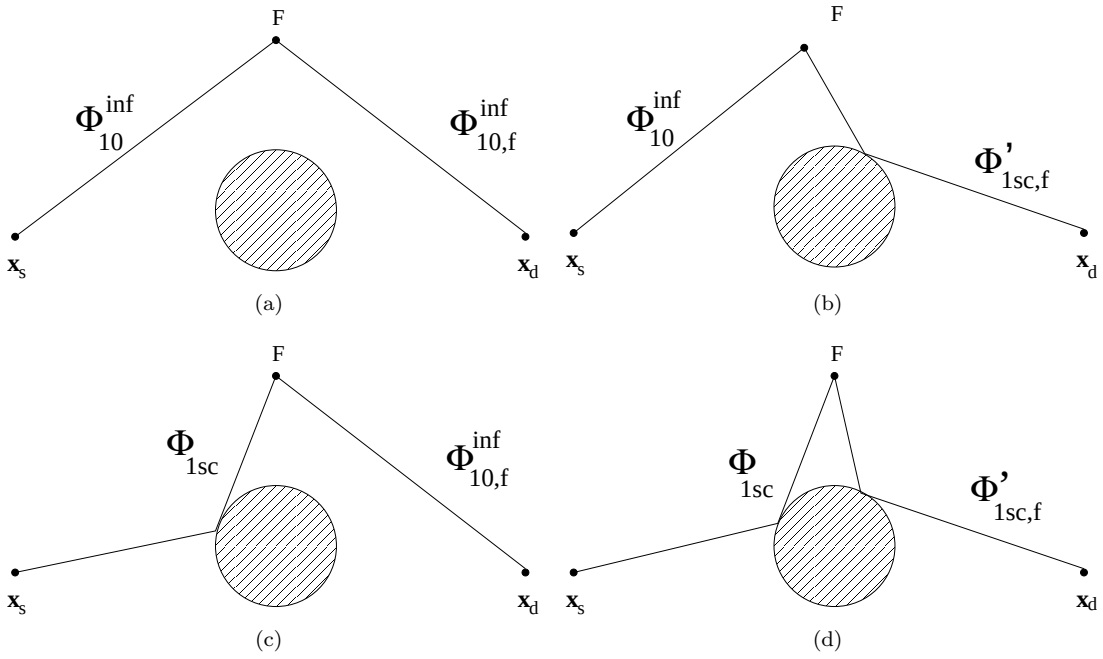

Figure C.2: Various contributions to fluorescence DPDW from fluorophores outside the sphere ("background fluorescence"). (a) Fluorescence DPDW at detector position $\boldsymbol{x}_{\mathrm{d}}$ without scattering excited by unscattered attenuation DPDW, (b) scattered fluorescence DPDW excited by unscattered attenuation DPDW, (c) unscattered fluorescence DPDW excited by scattered attenuation DPDW, (d) scattered fluorescence DPDW excited by scattered attenuation DPDW.

attenuation DPDW $\Phi_2(\boldsymbol{x}_2, \boldsymbol{x}_\mathrm{s}, \lambda, \omega)$ penetrating the sphere excites fluorophores inside the sphere, e.g. at position $\boldsymbol{x}_2$, generating fluorescence sources

$$q_2^\mathrm{f}(\boldsymbol{x}_2, \boldsymbol{x}_\mathrm{s}, \lambda, \omega) = \frac{\eta \mu_\mathrm{a}^\mathrm{dye}(\boldsymbol{x}_2, \lambda)}{1 + i\omega\tau} \Phi_2(\boldsymbol{x}_2, \boldsymbol{x}_\mathrm{s}, \lambda, \omega) \tag{C.12}$$

that in turn generate the fluorescence DPDW $\Phi''_{1,\mathrm{f}}(\boldsymbol{x}, \boldsymbol{x}_\mathrm{s}, \lambda, \omega)$. Generally, a δ-like source of photons of wavelength λ' at position $\boldsymbol{x}_2$ inside the sphere generates a DPDW in the outside medium that can be expressed as

$$\Phi(\boldsymbol{x}, \boldsymbol{x}_2, \lambda', \omega) = \sum_{l,m} C_{lm}(\boldsymbol{x}_2, \lambda', \omega, r_\mathrm{sph}) h_l^{(1)}(k_1(\lambda', \omega)\,|\boldsymbol{x}|) Y_{lm}(\Omega), \tag{C.13}$$

where the coefficients stand for $C_{lm}(\boldsymbol{x}_2, \lambda_\mathrm{f}, \omega, r_\mathrm{sph}) = C_{lm}(\boldsymbol{x}_2, k_1(\lambda_\mathrm{f}, \omega), k_2(\lambda_\mathrm{f}, \omega), D_1(\lambda_\mathrm{f}), D_2(\lambda_\mathrm{f}), r_\mathrm{sph})$ and are given in [26, 27]. Therefore, the fluorescence DPDW from fluorophores inside the sphere ("lesion fluorescence") is given by

$$\Phi''_{1,\mathrm{f}}(\boldsymbol{x}, \boldsymbol{x}_\mathrm{s}, \lambda, \omega) = \int_B d\boldsymbol{x}_2 v q_2^\mathrm{f}(\boldsymbol{x}_2, \boldsymbol{x}_\mathrm{s}, \lambda, \omega) \sum_{l,m} C_{lm}(\boldsymbol{x}_2, \lambda_\mathrm{f}, \omega, r_\mathrm{sph}) h_l^{(1)}(k_1(\lambda_\mathrm{f}, \omega)\,|\boldsymbol{x}|) Y_{lm}(\Omega). \tag{C.14}$$

The integral can be evaluated analytically and the result is given in [26, 27]. Besides fluorophores inside the sphere, those outside the sphere contribute to the fluorescence DPDW. The attenuation DPDW excites fluorophores at position $\boldsymbol{x}_1$ outside the sphere generating a source of fluorescence photons

$$q_1^\mathrm{f}(\boldsymbol{x}_1, \boldsymbol{x}_\mathrm{s}, \lambda, \omega) = \frac{\eta \mu_\mathrm{a}^\mathrm{dye}(\boldsymbol{x}_1, \lambda)}{1 + i\omega\tau} \Phi_1(\boldsymbol{x}_1, \boldsymbol{x}_\mathrm{s}, \lambda, \omega). \tag{C.15}$$

According to Eq. (C.6, C.7) the photon density $\Phi_1(\boldsymbol{x}_1, \boldsymbol{x}_\mathrm{s}, \lambda, \omega)$ consists of a direct part and of a scattered part, as illustrated in Fig. C.1a and Fig. C.2a,c. Furthermore, a δ-like source $(1/v)\delta(\boldsymbol{x} - \boldsymbol{x}_\mathrm{s})$ of fluorescence photons at location $\boldsymbol{x}_1$ generates a fluorescence DPDW that can be written analogously to Eq. (C.7), consisting of the direct part

$$\Phi_{10,\mathrm{f}}^\mathrm{inf}(\boldsymbol{x}, \boldsymbol{x}_1, \lambda_\mathrm{f}, \omega) = \frac{1}{v D_1(\lambda_\mathrm{f})} \frac{\exp\left(-ik_1(\lambda_\mathrm{f}, \omega)|\boldsymbol{x} - \boldsymbol{x}_1|\right)}{4\pi|\boldsymbol{x} - \boldsymbol{x}_1|}, \tag{C.16}$$

and a scattered part

$$\Phi'_{1\mathrm{sc},\mathrm{f}}(\boldsymbol{x}, \boldsymbol{x}_1, \lambda_\mathrm{f}, \omega) = \sum_{l,m} A_{lm}(\boldsymbol{x}_1, \lambda_\mathrm{f}, \omega, r_\mathrm{sph}) h_l^{(1)}(k_1(\lambda_\mathrm{f}, \omega)\,|\boldsymbol{x}|) Y_{lm}(\Omega), \tag{C.17}$$

where the coefficients $A_{lm}(\boldsymbol{x}_1, \lambda_\mathrm{f}, \omega, r_\mathrm{sph}) = A_{lm}(\boldsymbol{x}_1, k_1(\lambda_\mathrm{f}, \omega), k_2(\lambda_\mathrm{f}, \omega), D_1(\lambda_\mathrm{f}), D_2(\lambda_\mathrm{f}), r_\mathrm{sph})$ are given in [26, 27]. The scattered part $\Phi'_{1\mathrm{sc},\mathrm{f}}(\boldsymbol{x}, \boldsymbol{x}_1, \lambda_f, \omega)$ is illustrated in Fig. C.2b+d. Therefore, the entire fluorescence DPDW from fluorophores outside the sphere ("background fluorescence") is obtained as

$$\begin{aligned} \Phi'_{1,\mathrm{f}}(\boldsymbol{x}, \boldsymbol{x}_\mathrm{s}, \lambda, \omega) = &\int_{\Omega\setminus B} d\boldsymbol{x}_1 v q_1^\mathrm{f}(\boldsymbol{x}_1, \boldsymbol{x}_\mathrm{s}, \lambda, \omega) \Phi_{10,\mathrm{f}}^\mathrm{inf}(\boldsymbol{x}, \boldsymbol{x}_1, \lambda_\mathrm{f}, \omega) \\ &+ \int_{\Omega\setminus B} d\boldsymbol{x}_1 v q_1^\mathrm{f}(\boldsymbol{x}_1, \boldsymbol{x}_\mathrm{s}, \lambda, \omega) \Phi'_{1\mathrm{sc},\mathrm{f}}(\boldsymbol{x}, \boldsymbol{x}_1, \lambda_\mathrm{f}, \omega). \end{aligned} \tag{C.18}$$

The first integral corresponds to the unscattered, the second to the scattered fluorescence DPDW. Both integrals can be evaluated analytically and the result is given in [26, 27]. The entire fluorescence DPDW

is given by

$$\begin{aligned}\Phi_{1,\mathrm{f}}(\boldsymbol{x},\boldsymbol{x}_\mathrm{s},\lambda,\omega) = &\int_B d\boldsymbol{x}_2 v q_2^\mathrm{f}(\boldsymbol{x}_2,\boldsymbol{x}_\mathrm{s},\lambda,\omega)\sum_{l,m} C_{lm}(\boldsymbol{x}_2,\lambda_\mathrm{f},\omega,r_\mathrm{sph})h_l^{(1)}(k_1(\lambda_\mathrm{f},\omega)\,|\boldsymbol{x}|)Y_{lm}(\Omega)\\ &+\int_{\Omega\setminus B} d\boldsymbol{x}_1 q_1^\mathrm{f}(\boldsymbol{x}_1,\boldsymbol{x}_\mathrm{s},\lambda,\omega)\frac{1}{D_1(\lambda_\mathrm{f})}\frac{\exp\left(-ik_1(\lambda_\mathrm{f},\omega)|\boldsymbol{x}-\boldsymbol{x}_1|\right)}{4\pi|\boldsymbol{x}-\boldsymbol{x}_1|}\\ &+\int_{\Omega\setminus B} d\boldsymbol{x}_1 q_1^\mathrm{f}(\boldsymbol{x}_1,\boldsymbol{x}_\mathrm{s},\lambda,\omega)\sum_{l,m} A_{lm}(\boldsymbol{x}_1,\lambda_\mathrm{f},\omega,r_\mathrm{sph})h_l^{(1)}(k_1(\lambda_\mathrm{f},\omega)\,|\boldsymbol{x}|)Y_{lm}(\Omega),\end{aligned} \tag{C.19}$$

where the first integral corresponds to the "lesion fluorescence" and the remaining two integrals to the "background fluorescence".

A solution such as (C.19) for infinite homogeneous slab with a spherical heterogeneity can be reformulated from the infinite medium solution similarly to the derivation given in Sec. 5.1.4 by using extrapolated boundaries and mirrored sources and sinks. But this solution is only valid approximately, for it does not incorporate the diffraction of diffracted DPDW on mirrored spheres.

Due to the analytical representation of the solution, the DPDW at fluorescence and absorption wavelength can be computed quite fast on a modern PC compared with numerical FEM implementations.

C.2 The Rytov approximation

C.2.1 The Rytov approximation using homogeneous Green's functions

If $D^0(\lambda)$ and $\mu_\mathrm{a}^0(\lambda)$ are the optical properties of an unperturbed (homogeneous) medium, and $D(\boldsymbol{x},\lambda)$, $\mu_\mathrm{a}(\boldsymbol{x},\lambda)$ are the optical properties of a perturbed medium with an additional inhomogeneity, the definition of the diffusion equation in frequency domain is given by

$$\nabla\cdot D(\boldsymbol{x},\lambda)\nabla\Phi(\boldsymbol{x},\boldsymbol{x}_\mathrm{s},\lambda,\omega) - \mu_\mathrm{a}(\boldsymbol{x},\lambda)\Phi(\boldsymbol{x},\boldsymbol{x}_\mathrm{s},\lambda,\omega) - \frac{i\omega}{v}\Phi(\boldsymbol{x},\boldsymbol{x}_\mathrm{s},\lambda,\omega) = -q_0(\boldsymbol{x},\boldsymbol{x}_\mathrm{s},\lambda,\omega). \tag{C.20}$$

The perturbation of the absorption and scattering coefficient can be written as

$$\delta\mu_\mathrm{a}(\boldsymbol{x},\lambda) = \mu_\mathrm{a}(\boldsymbol{x},\lambda) - \mu_\mathrm{a}^0(\lambda), \tag{C.21}$$

$$\delta D(\boldsymbol{x},\lambda) = D(\boldsymbol{x},\lambda) - D^0(\lambda), \tag{C.22}$$

resulting in

$$\begin{aligned}&\nabla\cdot\left(D^0(\lambda)+\delta D(\boldsymbol{x},\lambda)\right)\nabla\Phi(\boldsymbol{x},\boldsymbol{x}_\mathrm{s},\lambda,\omega)\\ &-\left(\mu_\mathrm{a}^0(\lambda)+\delta\mu_\mathrm{a}(\boldsymbol{x},\lambda)\right)\Phi(\boldsymbol{x},\boldsymbol{x}_\mathrm{s},\lambda,\omega) - \frac{i\omega}{v}\Phi(\boldsymbol{x},\boldsymbol{x}_\mathrm{s},\lambda,\omega) = -q_0(\boldsymbol{x},\boldsymbol{x}_\mathrm{s},\lambda,\omega).\end{aligned} \tag{C.23}$$

We rewrite this equation, having the LHS correspond to the homogeneous diffusion equation, and interpret the RHS as a source term consisting of the physical source term and additional terms due to the perturbation of the optical properties

$$\begin{aligned}&\nabla\cdot D^0(\lambda)\nabla\Phi(\boldsymbol{x},\boldsymbol{x}_\mathrm{s},\lambda,\omega) - \mu_\mathrm{a}^0(\lambda)\Phi(\boldsymbol{x},\boldsymbol{x}_\mathrm{s},\lambda,\omega) - \frac{i\omega}{v}\Phi(\boldsymbol{x},\boldsymbol{x}_\mathrm{s},\lambda,\omega) =\\ &-q_0(\boldsymbol{x},\boldsymbol{x}_\mathrm{s},\lambda,\omega) - \nabla\cdot\delta D(\boldsymbol{x},\lambda)\nabla\Phi(\boldsymbol{x},\boldsymbol{x}_\mathrm{s},\lambda,\omega) + \delta\mu_\mathrm{a}(\boldsymbol{x},\lambda)\Phi(\boldsymbol{x},\boldsymbol{x}_\mathrm{s},\lambda,\omega).\end{aligned} \tag{C.24}$$

Every solution of Eq. (5.11) for an arbitrary source term $-q_0(\boldsymbol{x},\boldsymbol{x}_\mathrm{s},\lambda,\omega)$ and a homogeneous medium can be constructed from the fundamental solution $G_0(\boldsymbol{x},\boldsymbol{x}',\lambda,\omega)$, which is a solution of Eq. (5.11) replacing the source term by $-\delta(\boldsymbol{x}-\boldsymbol{x}')/v$, i.e.

$$\Phi_0(\boldsymbol{x},\boldsymbol{x}_\mathrm{s},\lambda,\omega) = v\int_\Omega G_0(\boldsymbol{x},\boldsymbol{x}',\lambda,\omega)q_0(\boldsymbol{x}',\boldsymbol{x}_\mathrm{s},\lambda,\omega)d\boldsymbol{x}'. \tag{C.25}$$

The complete RHS of Eq. (C.24) then acts as a source in Eq. (C.25) and we get the solution of the diffusion equation as

$$\begin{aligned}\delta\Phi(\boldsymbol{x},\boldsymbol{x}_\mathrm{s},\lambda,\omega) &= \Phi(\boldsymbol{x},\boldsymbol{x}_\mathrm{s},\lambda,\omega) - \Phi_0(\boldsymbol{x},\boldsymbol{x}_\mathrm{s},\lambda,\omega) = \\ &- v\int_\Omega G_0(\boldsymbol{x},\boldsymbol{x}',\lambda,\omega)\delta\mu_\mathrm{a}(\boldsymbol{x}',\lambda)\Phi(\boldsymbol{x}',\boldsymbol{x}_\mathrm{s},\lambda,\omega)d\boldsymbol{x}' \\ &+ v\int_\Omega G_0(\boldsymbol{x},\boldsymbol{x}',\lambda,\omega)\nabla\cdot\delta D(\boldsymbol{x}',\lambda)\nabla\Phi(\boldsymbol{x}',\boldsymbol{x}_\mathrm{s},\lambda,\omega)d\boldsymbol{x}',\end{aligned} \tag{C.26}$$

where the term containing $\delta D(\boldsymbol{x}',\lambda)$ simplifies by partial integration to

$$\begin{aligned}&\int_\Omega G_0(\boldsymbol{x},\boldsymbol{x}',\lambda,\omega)\nabla\cdot(\delta D(\boldsymbol{x}',\lambda)\nabla\Phi(\boldsymbol{x}',\boldsymbol{x}_\mathrm{s},\lambda,\omega))\,d\boldsymbol{x}' \\ &= \int_\Omega G_0(\boldsymbol{x},\boldsymbol{x}',\lambda,\omega)\nabla\Phi(\boldsymbol{x}',\boldsymbol{x}_\mathrm{s},\lambda,\omega)\cdot\nabla\delta D(\boldsymbol{x}',\lambda)d\boldsymbol{x}' + \int_\Omega G_0(\boldsymbol{x},\boldsymbol{x}',\lambda,\omega)\delta D(\boldsymbol{x}',\lambda)\triangle\Phi(\boldsymbol{x}',\boldsymbol{x}_\mathrm{s},\lambda,\omega)d\boldsymbol{x}' \\ &= \int_\Omega G_0(\boldsymbol{x},\boldsymbol{x}',\lambda,\omega)\nabla\Phi(\boldsymbol{x},\boldsymbol{x}_\mathrm{s},\lambda,\omega)\cdot\nabla\delta D(\boldsymbol{x}',\lambda)d\boldsymbol{x}' - \int_\Omega\nabla(G_0(\boldsymbol{x},\boldsymbol{x}',\lambda,\omega)\delta D(\boldsymbol{x}',\lambda))\cdot\nabla\Phi(\boldsymbol{x}',\boldsymbol{x}_\mathrm{s},\lambda,\omega)d\boldsymbol{x}' \\ &+ \int_{\partial\Omega} G_0(\boldsymbol{x},\boldsymbol{x}',\omega)\delta D(\boldsymbol{x}',\lambda)\partial_n\Phi(\boldsymbol{x}',\boldsymbol{x}_\mathrm{s},\lambda,\omega)d\omega \\ &= -\int_\Omega\delta D(\boldsymbol{x}',\lambda)\nabla G_0(\boldsymbol{x},\boldsymbol{x}',\lambda,\omega)\cdot\nabla\Phi(\boldsymbol{x}',\boldsymbol{x}_\mathrm{s},\lambda,\omega),\end{aligned} \tag{C.27}$$

where we used $\nabla\cdot a\nabla b = \nabla a\cdot\nabla b + a\triangle b$ in line one, Green's formula I in line two and $\nabla U_1U_2 = U_1\nabla U_2 + U_2\nabla U_1$ in line three. The surface term vanishes, because we have no variation in optical properties at the surface, i.e. $\delta D(\boldsymbol{x},\lambda) = 0$ for $\boldsymbol{x}\in\partial\Omega$.

The photon density $\Phi_0(\boldsymbol{x}_\mathrm{d},\boldsymbol{x}_\mathrm{s},\lambda,\omega)$ at the detector position $\boldsymbol{x}_\mathrm{d}$ following injection of a spatial δ-like pulse at position $\boldsymbol{x}_\mathrm{s}$ into the homogeneous medium is given by $\Phi_0(\boldsymbol{x}_\mathrm{d},\boldsymbol{x}_\mathrm{s},\lambda,\omega) = G_0(\boldsymbol{x}_\mathrm{d},\boldsymbol{x}_\mathrm{s},\lambda,\omega)$. In the linear approximation we use $\Phi(\boldsymbol{x}_\mathrm{d},\boldsymbol{x}_\mathrm{s},\lambda,\omega)\approx G_0(\boldsymbol{x}_\mathrm{d},\boldsymbol{x}_\mathrm{s},\lambda,\omega)$ on the RHS of Eq. (C.26). Using Eq. (C.27), the well known (normalized) Born approximation is obtained from Eq. (C.26) yielding

$$\begin{aligned}\frac{\delta\Phi(\boldsymbol{x}_\mathrm{d},\boldsymbol{x}_\mathrm{s},\lambda,\omega)}{\Phi_0(\boldsymbol{x}_\mathrm{d},\boldsymbol{x}_\mathrm{s},\lambda,\omega)} &= -\,v\int_\Omega\delta\mu_\mathrm{a}(\boldsymbol{x}',\lambda)\frac{G_0(\boldsymbol{x}_\mathrm{d},\boldsymbol{x}',\lambda,\omega)G_0(\boldsymbol{x}',\boldsymbol{x}_\mathrm{s},\lambda,\omega)}{G_0(\boldsymbol{x}_\mathrm{d},\boldsymbol{x}_\mathrm{s},\lambda,\omega)}d\boldsymbol{x}' \\ &- v\int_\Omega\delta D(\boldsymbol{x}',\lambda)\frac{\nabla G_0(\boldsymbol{x}_\mathrm{d},\boldsymbol{x}',\lambda,\omega)\cdot\nabla G_0(\boldsymbol{x}',\boldsymbol{x}_\mathrm{s},\lambda,\omega)}{G_0(\boldsymbol{x}_\mathrm{d},\boldsymbol{x}_\mathrm{s},\lambda,\omega)}d\boldsymbol{x}'.\end{aligned} \tag{C.28}$$

In contrast to the Born approximation, the Rytov approximation assumes that the perturbations $\delta\mu_\mathrm{a}(\boldsymbol{x},\lambda)$ and $\delta D(\boldsymbol{x},\lambda)$ cause changes in a complex (Rytov) phase $\varphi_\mathrm{Rytov}(\boldsymbol{x},\boldsymbol{x}_\mathrm{s},\lambda,\omega)$, rather than in the amplitude $\Phi_0(\boldsymbol{x},\boldsymbol{x}_\mathrm{s},\lambda,\omega)$, setting

$$\Phi(\boldsymbol{x},\boldsymbol{x}_\mathrm{s},\lambda,\omega) = \Phi_0(\boldsymbol{x},\boldsymbol{x}_\mathrm{s},\lambda,\omega)\exp\left(\varphi_\mathrm{Rytov}(\boldsymbol{x},\boldsymbol{x}_\mathrm{s},\lambda,\omega)\right), \tag{C.29}$$

or in first order

$$\varphi_\mathrm{Rytov}(\boldsymbol{x},\boldsymbol{x}_\mathrm{s},\lambda,\omega) = \frac{\delta\Phi(\boldsymbol{x},\boldsymbol{x}_\mathrm{s},\lambda,\omega)}{\Phi_0(\boldsymbol{x},\boldsymbol{x}_\mathrm{s},\lambda,\omega)}, \tag{C.30}$$

yielding the Rytov approximation

$$\begin{aligned}\ln\left(\frac{\Phi(\boldsymbol{x}_\mathrm{d},\boldsymbol{x}_\mathrm{s},\lambda,\omega)}{\Phi_0(\boldsymbol{x}_\mathrm{d},\boldsymbol{x}_\mathrm{s},\lambda,\omega)}\right) &= -\,v\int_\Omega\delta\mu_\mathrm{a}(\boldsymbol{x}',\lambda)\frac{G_0(\boldsymbol{x}_\mathrm{d},\boldsymbol{x}',\lambda,\omega)G_0(\boldsymbol{x}',\boldsymbol{x}_\mathrm{s},\lambda,\omega)}{G_0(\boldsymbol{x}_\mathrm{d},\boldsymbol{x}_\mathrm{s},\lambda,\omega)}d\boldsymbol{x}' \\ &- v\int_\Omega\delta D(\boldsymbol{x}',\lambda)\frac{\nabla G_0(\boldsymbol{x}_\mathrm{d},\boldsymbol{x}',\lambda,\omega)\cdot\nabla G_0(\boldsymbol{x}',\boldsymbol{x}_\mathrm{s},\lambda,\omega)}{G_0(\boldsymbol{x}_\mathrm{d},\boldsymbol{x}_\mathrm{s},\lambda,\omega)}d\boldsymbol{x}'.\end{aligned} \tag{C.31}$$

The first integral in Eq. (C.31) related to absorption changes generalizes the well known result of the attenuation of X-rays, traveling on the straight line s from the source at position $\boldsymbol{x}_\mathrm{s}$ to the detector at position $\boldsymbol{x}_\mathrm{d}$ through a homogeneous medium with absorption coefficient μ^0_Xray, and through a (inhomogeneous) medium with absorption coefficient $\mu_\mathrm{Xray}(\boldsymbol{x}) = \mu^0_\mathrm{Xray} + \delta\mu_\mathrm{Xray}(\boldsymbol{x})$. It follows readily from Eq. (3.3) that

$$\ln\left(\frac{I^\mathrm{Xray}(\boldsymbol{x}_\mathrm{d},\boldsymbol{x}_\mathrm{s},\mu_\mathrm{Xray}(\boldsymbol{x}))}{I^\mathrm{Xray}(\boldsymbol{x}_\mathrm{d},\boldsymbol{x}_\mathrm{s},\mu^0_\mathrm{Xray})}\right) = -\int_s \delta\mu_\mathrm{Xray}(\boldsymbol{x})ds, \tag{C.32}$$

where the integral has to be taken over the line s.

The normalized Born approximation given in Eq. (C.28) can be rewritten to calculate the contribution to the fluorescent photon density at the detector position, when a laser photon is absorbed at position $\boldsymbol{x}'$ and a fluorescence photon is emitted. In this case the transmitted laser photon density $\Phi(\boldsymbol{x}_\mathrm{d},\boldsymbol{x}_\mathrm{s},\lambda,\omega)$ at the detector position serves as reference. We denote the fundamental solution of the (inhomogeneous) diffusion equation at the laser wavelength (see Eq. (5.11)) as $G(\boldsymbol{x},\boldsymbol{x}',\lambda,\omega)$, obtained by replacing its RHS by $-\delta(\boldsymbol{x}-\boldsymbol{x}')/v$. Likewise, $G(\boldsymbol{x},\boldsymbol{x}',\lambda_\mathrm{f},\omega)$ stands for the fundamental solution of the inhomogeneous diffusion equation at the fluorescence wavelength, calculated from Eq. (5.13) with the term on the RHS replaced by $-\delta(\boldsymbol{x}-\boldsymbol{x}')/v$. The first order normalized Born approximation for the fluorescence photon density $\Phi_\mathrm{f}(\boldsymbol{x}_\mathrm{d},\boldsymbol{x}_\mathrm{s},\lambda,\omega)$ at the detector is then obtained from Eq. (C.28) replacing $\delta\Phi(\boldsymbol{x}_\mathrm{d},\boldsymbol{x}_\mathrm{s},\lambda,\omega)$ by $\Phi_\mathrm{f}(\boldsymbol{x}_\mathrm{d},\boldsymbol{x}_\mathrm{s},\lambda,\omega)$, i.e. neglecting tissue autofluorescence, and substituting in the denominator the reference $\Phi_0(\boldsymbol{x}_\mathrm{d},\boldsymbol{x}_\mathrm{s},\lambda,\omega)$ by the attenuation measurement at the laser wavelength $\Phi(\boldsymbol{x}_\mathrm{d},\boldsymbol{x}_\mathrm{s},\lambda,\omega)$. On the RHS, the second term is set to zero, and in the first term we replace $-\mu_\mathrm{a}(\boldsymbol{x},\lambda)$ by $+\eta\mu_\mathrm{a}^\mathrm{dye}(\boldsymbol{x},\lambda)/(1+i\omega\tau)$, and the Green's functions $G_0(\boldsymbol{x}_\mathrm{d},\boldsymbol{x}',\lambda,\omega)$, $G_0\mathrm{f}(\boldsymbol{x}',\boldsymbol{x}_\mathrm{s},\lambda,\omega)$, $G_0(\boldsymbol{x}_\mathrm{d},\boldsymbol{x}_\mathrm{s},\lambda,\omega)$ by $G(\boldsymbol{x}_\mathrm{d},\boldsymbol{x}',\lambda_\mathrm{f},\omega)$, $G(\boldsymbol{x}',\boldsymbol{x}_\mathrm{s},\lambda_\mathrm{f},\omega)$ and $G(\boldsymbol{x}_\mathrm{d},\boldsymbol{x}_\mathrm{s},\lambda_\mathrm{f},\omega)$, respectively, yielding

$$\frac{\delta\Phi_\mathrm{f}(\boldsymbol{x}_\mathrm{d},\boldsymbol{x}_\mathrm{s},\lambda,\omega)}{\Phi(\boldsymbol{x}_\mathrm{d},\boldsymbol{x}_\mathrm{s},\lambda,\omega)} = +\frac{\eta v}{1+i\omega\tau}\int_\Omega \mu_\mathrm{a}^\mathrm{dye}(\boldsymbol{x}',\lambda)\frac{G(\boldsymbol{x}_\mathrm{d},\boldsymbol{x}',\lambda,\omega)G(\boldsymbol{x}',\boldsymbol{x}_\mathrm{s},\lambda,\omega)}{G(\boldsymbol{x}_\mathrm{d},\boldsymbol{x}_\mathrm{s},\lambda,\omega)}d\boldsymbol{x}'. \tag{C.33}$$

However, the exact Green's functions are not known initially and are replaced by the homogeneous Green's functions, yielding

$$\frac{\delta\Phi_\mathrm{f}(\boldsymbol{x}_\mathrm{d},\boldsymbol{x}_\mathrm{s},\lambda,\omega)}{\Phi(\boldsymbol{x}_\mathrm{d},\boldsymbol{x}_\mathrm{s},\lambda,\omega)} = +\frac{\eta v}{1+i\omega\tau}\int_\Omega \mu_\mathrm{a}^\mathrm{dye}(\boldsymbol{x}',\lambda)\frac{G_0(\boldsymbol{x}_\mathrm{d},\boldsymbol{x}',\lambda,\omega)G_0(\boldsymbol{x}',\boldsymbol{x}_\mathrm{s},\lambda,\omega)}{G_0(\boldsymbol{x}_\mathrm{d},\boldsymbol{x}_\mathrm{s},\lambda,\omega)}d\boldsymbol{x}'. \tag{C.34}$$

Eq. (C.34) corresponds to the result given in Eq. (6.2). Alternatively, the Green's functions at the laser wavelength $G(\boldsymbol{x}',\boldsymbol{x}_\mathrm{s},\lambda,\omega)$, $G(\boldsymbol{x}_\mathrm{d},\boldsymbol{x}',\lambda,\omega)$ can be calculated iteratively by nonlinear reconstruction and, $G(\boldsymbol{x}_\mathrm{d},\boldsymbol{x}',\lambda_\mathrm{f},\omega)$ is approximated by $G(\boldsymbol{x}_\mathrm{d},\boldsymbol{x}',\lambda_\mathrm{f},\omega) \approx G(\boldsymbol{x}_\mathrm{d},\boldsymbol{x}',\lambda,\omega)$, thus calculating fluorescence photon densities by first order Born approximation, using Green's functions at the laser wavelength obtained by iterative nonlinear reconstructions.

C.2.2 The iterative Rytov approximation

In a nonlinear reconstruction the optical properties are approximated iteratively in several iteration steps κ beginning at $\kappa = 0$

$$\begin{aligned}
\mu_\mathrm{a}^0(\boldsymbol{x},\lambda) &= \mu_\mathrm{a}^0(\lambda),\\
\mu_\mathrm{a}^1(\boldsymbol{x},\lambda) &= \mu_\mathrm{a}^0(\boldsymbol{x},\lambda) + \delta\mu_\mathrm{a}^0(\boldsymbol{x},\lambda),\\
&\vdots\\
\mu_\mathrm{a}^{\kappa+1}(\boldsymbol{x},\lambda) &= \mu_\mathrm{a}^\kappa(\boldsymbol{x},\lambda) + \delta\mu_\mathrm{a}^\kappa(\boldsymbol{x},\lambda).
\end{aligned} \tag{C.35}$$

Analogous relations apply to the diffusion coefficient $D^\kappa(\boldsymbol{x},\lambda)$. The optical properties $D^\kappa(\boldsymbol{x},\lambda)$ and $\mu_\mathrm{a}^\kappa(\boldsymbol{x},\lambda)$ are reconstructed at iteration $\kappa-1$. These optical properties solve the diffusion equation

$$\nabla\cdot D^\kappa(\boldsymbol{x},\lambda)\nabla\Phi_\kappa^\mathrm{sim}(\boldsymbol{x},\boldsymbol{x}_\mathrm{s},\lambda,\omega) - \mu_\mathrm{a}^\kappa(\boldsymbol{x},\lambda)\Phi_\kappa^\mathrm{sim}(\boldsymbol{x},\boldsymbol{x}_\mathrm{s},\lambda,\omega) - \frac{i\omega}{v}\Phi_\kappa^\mathrm{sim}(\boldsymbol{x},\boldsymbol{x}_\mathrm{s},\lambda,\omega) = -q_0(\boldsymbol{x},\boldsymbol{x}_\mathrm{s},\lambda,\omega). \tag{C.36}$$

The fundamental solution of the diffusion equation with optical properties reconstructed in iteration step κ is given by $G_\kappa(\boldsymbol{x}, \boldsymbol{x}_\mathrm{s}, \lambda, \omega)$, and the solution for an arbitrary source term $-q_0(\boldsymbol{x}, \boldsymbol{x}_\mathrm{s}, \lambda, \omega)$ can be reconstructed by

$$\Phi_\kappa^\mathrm{sim}(\boldsymbol{x}, \boldsymbol{x}_\mathrm{s}, \lambda, \omega) = v \int_\Omega G_\kappa(\boldsymbol{x}, \boldsymbol{x}', \lambda, \omega) q_0(\boldsymbol{x}', \boldsymbol{x}_\mathrm{s}, \lambda, \omega) d\boldsymbol{x}'. \tag{C.37}$$

If we want to improve the solution $(\mu_\mathrm{a}^\kappa(\boldsymbol{x}, \lambda), D^\kappa(\boldsymbol{x}, \lambda))$ in the next iteration, we have to solve the equation

$$\begin{aligned} &\nabla \cdot D^\kappa(\boldsymbol{x}, \lambda) \nabla \Phi_{\kappa+1}^\mathrm{sim}(\boldsymbol{x}, \boldsymbol{x}_\mathrm{s}, \lambda, \omega) - \mu_\mathrm{a}^\kappa(\boldsymbol{x}, \lambda) \Phi_{\kappa+1}^\mathrm{sim}(\boldsymbol{x}, \boldsymbol{x}_\mathrm{s}, \lambda, \omega) - \frac{i\omega}{v} \Phi_{\kappa+1}^\mathrm{sim}(\boldsymbol{x}, \boldsymbol{x}_\mathrm{s}, \lambda, \omega) = \\ &- q_0(\boldsymbol{x}, \boldsymbol{x}_\mathrm{s}, \lambda, \omega) - \nabla \cdot \delta D^\kappa(\boldsymbol{x}, \lambda) \nabla \Phi_{\kappa+1}^\mathrm{sim}(\boldsymbol{x}, \boldsymbol{x}_\mathrm{s}, \lambda, \omega) + \delta \mu_\mathrm{a}^\kappa(\boldsymbol{x}, \lambda) \Phi_{\kappa+1}^\mathrm{sim}(\boldsymbol{x}, \boldsymbol{x}_\mathrm{s}, \lambda, \omega). \end{aligned} \tag{C.38}$$

Since we do not know the Green's function $G_{\kappa+1}(\boldsymbol{x}, \boldsymbol{x}_\mathrm{s}, \lambda, \omega)$ at this iteration step, we use the following approximation,

$$\Phi_{\kappa+1}^\mathrm{sim}(\boldsymbol{x}, \boldsymbol{x}_\mathrm{s}, \lambda, \omega) \approx \Phi_\kappa^\mathrm{sim}(\boldsymbol{x}, \boldsymbol{x}_\mathrm{s}, \lambda, \omega). \tag{C.39}$$

Since a spatial δ-like pulse is injected at $\boldsymbol{x}_\mathrm{s}$, we have

$$\Phi_\kappa^\mathrm{sim}(\boldsymbol{x}, \boldsymbol{x}_\mathrm{s}, \lambda, \omega) = G_\kappa(\boldsymbol{x}, \boldsymbol{x}_\mathrm{s}, \lambda, \omega). \tag{C.40}$$

Analogously to Eq. (C.31) the Rytov approximation is obtained by

$$\begin{aligned} \ln\left(\frac{\Phi_{\kappa+1}^\mathrm{sim}(\boldsymbol{x}_\mathrm{d}, \boldsymbol{x}_\mathrm{s}, \lambda, \omega)}{\Phi_\kappa^\mathrm{sim}(\boldsymbol{x}_\mathrm{d}, \boldsymbol{x}_\mathrm{s}, \lambda, \omega)}\right) = &- v \int_\Omega \delta \mu_\mathrm{a}^\kappa(\boldsymbol{x}', \lambda) \frac{G_\kappa(\boldsymbol{x}_\mathrm{d}, \boldsymbol{x}', \lambda, \omega) G_\kappa(\boldsymbol{x}', \boldsymbol{x}_\mathrm{s}, \lambda, \omega)}{G_\kappa(\boldsymbol{x}_\mathrm{d}, \boldsymbol{x}_\mathrm{s}, \lambda, \omega)} d\boldsymbol{x}' \\ &- v \int_\Omega \delta D^\kappa(\boldsymbol{x}', \lambda) \frac{\nabla G_\kappa(\boldsymbol{x}_\mathrm{d}, \boldsymbol{x}', \lambda, \omega) \cdot \nabla G_\kappa(\boldsymbol{x}', \boldsymbol{x}_\mathrm{s}, \lambda, \omega)}{G_\kappa(\boldsymbol{x}_\mathrm{d}, \boldsymbol{x}_\mathrm{s}, \lambda, \omega)} d\boldsymbol{x}'. \end{aligned} \tag{C.41}$$

Experimental data $\Phi(\boldsymbol{x}_\mathrm{d}, \boldsymbol{x}_\mathrm{s}, \lambda, \omega)$ contain instrumental factors that are eliminated by scaling with the ration $\Phi_0^\mathrm{sim}(\boldsymbol{x}_\mathrm{d}, \boldsymbol{x}_\mathrm{s}, \lambda, \omega)/\Phi_0(\boldsymbol{x}_\mathrm{d}, \boldsymbol{x}_\mathrm{s}, \lambda, \omega)$, where $\Phi_0(\boldsymbol{x}_\mathrm{d}, \boldsymbol{x}_\mathrm{s}, \lambda, \omega)$ corresponds to the experimental data obtained from the reference experiment on the homogeneous medium. We then set

$$\Phi_{\kappa+1}^\mathrm{sim}(\boldsymbol{x}_\mathrm{d}, \boldsymbol{x}_\mathrm{s}, \lambda, \omega) \approx \frac{\Phi(\boldsymbol{x}_\mathrm{d}, \boldsymbol{x}_\mathrm{s}, \lambda, \omega) \Phi_0^\mathrm{sim}(\boldsymbol{x}_\mathrm{d}, \boldsymbol{x}_\mathrm{s}, \lambda, \omega)}{\Phi_0(\boldsymbol{x}_\mathrm{d}, \boldsymbol{x}_\mathrm{s}, \lambda, \omega)}. \tag{C.42}$$

This approximation should improve with every iteration. Using Eq. (C.42) and Eq. (C.41) finally results in the nonlinear reconstruction relation as presented in Eq. (6.3).

C.2.3 Amplitude and phase of the attenuation coefficient

The attenuation coefficient

$$k(\lambda, \omega) = k_\mathrm{re}(\lambda, \omega) - i k_\mathrm{im}(\lambda, \omega) \tag{C.43}$$

in a homogeneous medium is given by

$$k^2(\lambda, \omega) = -\frac{\mu_\mathrm{a}^0(\lambda) + \frac{i\omega}{v}}{D^0(\lambda)}. \tag{C.44}$$

The sign of the imaginary part has been chosen to make the DPDW of the homogeneous medium

$$\Phi_0^\mathrm{inf}(\boldsymbol{x}, \boldsymbol{x}_\mathrm{s}, \lambda, \omega) = \frac{1}{4\pi v D^0(\lambda)} \frac{\exp\left(-ik(\lambda, \omega)\left|\boldsymbol{x} - \boldsymbol{x}_\mathrm{s}\right|\right)}{\left|\boldsymbol{x} - \boldsymbol{x}_\mathrm{s}\right|}. \tag{C.45}$$

a damped spherical wave as expected. Using Eq. (C.43) and Eq. (C.44) one can show that

$$k_\mathrm{re}(\lambda, \omega) k_\mathrm{im}(\lambda, \omega) = \frac{\omega}{2 v D^0(\lambda)}, \tag{C.46}$$

and

$$k_{\mathrm{im}}^4(\lambda,\omega) - \frac{\mu_{\mathrm{a}}^0(\lambda)}{D^0(\lambda)} k_{\mathrm{im}}^2(\lambda,\omega) - \frac{\omega^2}{4v^2\left(D^0(\lambda)\right)^2} = 0. \tag{C.47}$$

It follows that

$$k_{\mathrm{im}}^2(\lambda,\omega) = \frac{\mu_{\mathrm{a}}^0(\lambda)}{2D^0(\lambda)} \left(1 \pm \sqrt{1 + \left(\frac{\omega}{v\mu_{\mathrm{a}}^0(\lambda)}\right)^2}\right). \tag{C.48}$$

As k_{im} has to be real, only the solution

$$k_{\mathrm{im}}(\lambda,\omega) = \sqrt{\frac{\mu_{\mathrm{a}}^0(\lambda)}{2D^0(\lambda)}} \sqrt{1 + \sqrt{1 + \left(\frac{\omega}{v\mu_{\mathrm{a}}^0(\lambda)}\right)^2}} \tag{C.49}$$

is valid. Analogous calculations for the real part of the attenuation show that

$$k_{\mathrm{re}}(\lambda,\omega) = \sqrt{\frac{\mu_{\mathrm{a}}^0(\lambda)}{2D^0(\lambda)}} \sqrt{\sqrt{1 + \left(\frac{\omega}{v\mu_{\mathrm{a}}^0(\lambda)}\right)^2} - 1}. \tag{C.50}$$

For the cw situation ($\omega = 0$) we get $k_{\mathrm{re}}(\lambda, \omega = 0) = 0$ and

$$k_{\mathrm{im}}(\lambda,\omega=0) = \sqrt{\frac{\mu_{\mathrm{a}}^0(\lambda)}{D^0(\lambda)}} = \sqrt{3\mu_{\mathrm{a}}^0(\lambda)\mu_{\mathrm{s},0}'(\lambda)}. \tag{C.51}$$

The diffuse photon density wave $\Phi_0^{\mathrm{inf}}(\boldsymbol{x}, \boldsymbol{x}_{\mathrm{s}}, \lambda, \omega)$, i.e. the solution of the diffusion equation (5.11) for an infinite homogeneous medium with a source located at $\boldsymbol{x}_{\mathrm{s}}$ is given in Eq. (5.24). This solution simplifies for $\omega = 0$ by using Eq. (C.51) to

$$\Phi_0^{\mathrm{inf}}(\boldsymbol{x}, \boldsymbol{x}_{\mathrm{s}}, \lambda, \omega = 0) = \frac{1}{4\pi v D^0(\lambda)} \frac{\exp\left(-\sqrt{\frac{\mu_{\mathrm{a}}^0(\lambda)}{D^0(\lambda)}}|\boldsymbol{x} - \boldsymbol{x}_{\mathrm{s}}|\right)}{|\boldsymbol{x} - \boldsymbol{x}_{\mathrm{s}}|}. \tag{C.52}$$

The amplitude of $k(\lambda, \omega)$ is calculated by

$$\begin{aligned} |k(\lambda,\omega)| &= \sqrt{k_{\mathrm{re}}^2(\lambda,\omega) + k_{\mathrm{im}}^2(\lambda,\omega)} \\ &= \left(\frac{\left(\mu_{\mathrm{a}}^0(\lambda)\right)^2 + \omega^2/v^2}{\left(D^0(\lambda)\right)^2}\right)^{1/4}, \end{aligned} \tag{C.53}$$

and its phase φ by

$$\begin{aligned} \tan\varphi &= -\frac{k_{\mathrm{im}}}{k_{\mathrm{re}}} \\ &= -\frac{v\mu_{\mathrm{a}}^0(\lambda)}{\omega} \left(\sqrt{1 + \left(\frac{\omega}{v\mu_{\mathrm{a}}^0(\lambda)}\right)^2} + 1\right). \end{aligned} \tag{C.54}$$

For $\omega = 0$, the phase is

$$\varphi = -\frac{\pi}{2}, \tag{C.55}$$

which is expected from Eq. (C.43).

C.3 Derivation of diffusion equation from radiative transfer equation

This section follows closely the derivations presented in [192]. By inserting the (dipole) expansion for the source term $\widetilde{\boldsymbol{S}}(\boldsymbol{x}, \boldsymbol{x}_\mathrm{s}, \lambda, \boldsymbol{n}, t)$ and for the radiance $\widetilde{\boldsymbol{I}}(\boldsymbol{x}, \boldsymbol{x}_\mathrm{s}, \lambda, \boldsymbol{n}, t)$ given in Eq. (5.5) and Eq. (5.6), respectively, into the RTE (Eq. (5.1)) and by using the expression in Eq. (5.7) and Eq. (5.8) for the photon density $\widetilde{\Phi}(\boldsymbol{x}, \boldsymbol{x}_\mathrm{s}, \lambda, t)$ and for the (net) photon current density $\widetilde{\boldsymbol{J}}(\boldsymbol{x}, \boldsymbol{x}_\mathrm{s}, \lambda, t)$, respectively, one obtains

$$\begin{aligned}\frac{\partial}{\partial t}\widetilde{\Phi}(\boldsymbol{x}, \boldsymbol{x}_\mathrm{s}, \lambda, t) + \frac{3}{v}\frac{\partial}{\partial t}\widetilde{\boldsymbol{J}}(\boldsymbol{x}, \boldsymbol{x}_\mathrm{s}, \lambda, t)\cdot\boldsymbol{n} = &- v\left(\boldsymbol{n}\cdot\nabla + \mu_\mathrm{a}(\boldsymbol{x}, \lambda)\right)\widetilde{\Phi}(\boldsymbol{x}, \boldsymbol{x}_\mathrm{s}, \lambda, t)\\ &- 3\left(\boldsymbol{n}\cdot\nabla + \mu_\mathrm{a}(\boldsymbol{x}, \lambda) + \mu_\mathrm{s}'(\boldsymbol{x}, \lambda)\right)\widetilde{\boldsymbol{J}}(\boldsymbol{x}, \boldsymbol{x}_\mathrm{s}, \lambda, t)\cdot\boldsymbol{n}\\ &+ v\widetilde{q}_0(\boldsymbol{x}, \boldsymbol{x}_\mathrm{s}, \lambda, t) + 3\widetilde{\boldsymbol{S}}_1(\boldsymbol{x}, \boldsymbol{x}_\mathrm{s}, \lambda, t)\cdot\boldsymbol{n}.\end{aligned} \tag{C.56}$$

Integrating Eq. (C.56) over all directions $\boldsymbol{n}$ yields

$$\frac{\partial}{\partial t}\widetilde{\Phi}(\boldsymbol{x}, \boldsymbol{x}_\mathrm{s}, \lambda, t) = -v\mu_\mathrm{a}(\boldsymbol{x}, \lambda)\widetilde{\Phi}(\boldsymbol{x}, \boldsymbol{x}_\mathrm{s}, \lambda, t) - \nabla\cdot\widetilde{\boldsymbol{J}}(\boldsymbol{x}, \boldsymbol{x}_\mathrm{s}, \lambda, t) + v\widetilde{q}_0(\boldsymbol{x}, \boldsymbol{x}_\mathrm{s}, \lambda, t). \tag{C.57}$$

Similarly, by multiplying Eq. (C.56) by $\boldsymbol{n}$ and subsequently integrating over all directions $\boldsymbol{n}$, one obtains

$$\frac{1}{v^2}\frac{\partial}{\partial t}\widetilde{\boldsymbol{J}}(\boldsymbol{x}, \boldsymbol{x}_\mathrm{s}, \lambda, t) = -\frac{1}{3}\nabla\widetilde{\Phi}(\boldsymbol{x}, \boldsymbol{x}_\mathrm{s}, \lambda, t) - \frac{\mu_\mathrm{a}(\boldsymbol{x}, \lambda) + \mu_\mathrm{s}'(\boldsymbol{x}, \lambda)}{v}\widetilde{\boldsymbol{J}}(\boldsymbol{x}, \boldsymbol{x}_\mathrm{s}, \lambda, t) + \frac{1}{v}\widetilde{\boldsymbol{S}_1}(\boldsymbol{x}, \boldsymbol{x}_\mathrm{s}, \lambda, t). \tag{C.58}$$

The following expressions were used to derive the latter two equations

$$\begin{aligned}&\int_{4\pi}(\boldsymbol{a}\cdot\boldsymbol{n})\,d\boldsymbol{n} = 0,\\ &\int_{4\pi}(\boldsymbol{a}\cdot\boldsymbol{n})(\boldsymbol{b}\cdot\boldsymbol{n})\,d\boldsymbol{n} = \frac{4\pi}{3}\boldsymbol{a}\cdot\boldsymbol{b},\\ &\int_{4\pi}(\boldsymbol{a}\cdot\boldsymbol{n})\,\boldsymbol{n}d\boldsymbol{n} = \frac{4\pi}{3}\boldsymbol{a},\\ &\int_{4\pi}(\boldsymbol{a}\cdot\boldsymbol{n})(\boldsymbol{b}\cdot\boldsymbol{n})\,\boldsymbol{n}d\boldsymbol{n} = 0,\end{aligned} \tag{C.59}$$

where $\boldsymbol{a} = \boldsymbol{a}(\boldsymbol{x})$ and $\boldsymbol{b} = \boldsymbol{b}(\boldsymbol{x})$ are vectors, such as $\widetilde{\boldsymbol{J}}(\boldsymbol{x}, \boldsymbol{x}_\mathrm{s}, \lambda, t)$ that may depend on position $\boldsymbol{x}$, but not explicitly on direction $\boldsymbol{n}$, and $d\boldsymbol{n}$ is shorthand for the surface element $(\sin\vartheta)d\vartheta d\varphi$ of the unit sphere.

On the conditions

$$\begin{aligned}&\mu_\mathrm{a}(\boldsymbol{x}, \lambda) \ll \mu_\mathrm{s}'(\boldsymbol{x}, \lambda),\\ &\widetilde{\boldsymbol{S}}_1(\boldsymbol{x}, \boldsymbol{x}_\mathrm{s}, \lambda, t) = 0,\\ &\frac{1}{v\mu_\mathrm{s}'(\boldsymbol{x}, \lambda)}\left|\frac{\partial}{\partial t}\widetilde{\boldsymbol{J}}(\boldsymbol{x}, \boldsymbol{x}_\mathrm{s}, \lambda, t)\right| \ll \left|\widetilde{\boldsymbol{J}}(\boldsymbol{x}, \boldsymbol{x}_\mathrm{s}, \lambda, t)\right|,\end{aligned} \tag{C.60}$$

i.e. that the free absorption length l_a is much longer than the free transport scattering length l_s', that the source can be assumed to be isotropic and that the change which the net photon current density experiences during the time a photon needs to travel one free transport scattering length l_s' is much smaller than the net photon current density itself, Eq. (C.58) can be written as

$$\widetilde{\boldsymbol{J}}(\boldsymbol{x}, \boldsymbol{x}_\mathrm{s}, \lambda, t) = -vD(\boldsymbol{x}, \lambda)\nabla\widetilde{\Phi}(\boldsymbol{x}, \boldsymbol{x}_\mathrm{s}, \lambda, t), \tag{C.61}$$

where $D(\boldsymbol{x}, \lambda) = 1/(3\mu_\mathrm{s}'(\boldsymbol{x}, \lambda))$. Equation (C.61) corresponds to the Fick law. Inserting Eq. (C.61) into Eq. (C.57) yields the time-domain diffusion equation

$$\nabla\cdot D(\boldsymbol{x}, \lambda)\nabla\widetilde{\Phi}(\boldsymbol{x}, \boldsymbol{x}_\mathrm{s}, \lambda, t) - \mu_\mathrm{a}(\boldsymbol{x}, \lambda)\widetilde{\Phi}(\boldsymbol{x}, \boldsymbol{x}_\mathrm{s}, \lambda, t) - \frac{1}{v}\frac{\partial}{\partial t}\widetilde{\Phi}(\boldsymbol{x}, \boldsymbol{x}_\mathrm{s}, \lambda, t) = -\widetilde{q}_0(\boldsymbol{x}, \boldsymbol{x}_\mathrm{s}, \lambda, t). \tag{C.62}$$

C.4 Integration by parts

It can be shown by using the Gauss's theorem on the product $v(\boldsymbol{x})\boldsymbol{a}(\boldsymbol{x})$ of the scalar field $v(\boldsymbol{x})$ and the vector field $\boldsymbol{a}(\boldsymbol{x})$ that

$$\int_{\Omega} d\Omega \, \nabla v(\boldsymbol{x}) \cdot \boldsymbol{a}(\boldsymbol{x}) = \int_{\partial\Omega} d\omega \, v(\boldsymbol{x})\boldsymbol{a}(\boldsymbol{x}) \cdot \boldsymbol{n} - \int_{\Omega} d\Omega v(\boldsymbol{x}) \left(\nabla \cdot \boldsymbol{a}(\boldsymbol{x})\right) . \tag{C.63}$$

Acknowledgments

While working in two projects in parallel, i.e. in the Tomographic Imaging group of Philips Research Hamburg and the BMBF funded "FLUOROMAMM" project in close collaboration with the PTB Berlin, I became acquainted with many colleagues over the past three years. I would like to direct my acknowledgments to all of them individually for their contributions to my work, their support for my thesis, and their help during my studies.

First of all, I want to thank my two supervisors Prof. Dr. Herbert Rinneberg and Dr. Tim Nielsen for their support of my work, for many fruitful discussions we held, and for providing direction where to focus my research. I especially want to credit Dr. Tim Nielsen for always taking time for conversations, even on busy days, for inspiring new approaches on tenacious problems, for squashing software bugs, and for sometimes exerting helpful influence inside the large company. Furthermore, I want to acknowledge Prof. Dr. Herbert Rinneberg for our close collaboration, although having a large distance between our two workplaces. His support was excellent, and his engagement was very impressive all the time. Especially, writing together on our publications helped me tremendously improving my academic abilities.

Furthermore, I want to thank Prof. Dr. William D. Brewer for making me a member of his research group and for giving me the opportunity to present my work at the FU Berlin.

But there are more persons I want to highlight, particularly Dr. Bernhard Brendel, who became a valued colleague over the last two years, and whose efforts in the interpretation and evaluation of clinical data were quite important for the whole project. He helped us all by finding technical challenges (or even the scan number) simply by looking at raw data. Our conversations regarding the depths of ART regularization and spectral fitting helped me a lot during my thesis. Additional gratitude goes to Dr. Thomas Köhler, Dr. Falk Uhlemann, and Dr. Claas Bontus, who supported the project and my work during the last years.

From my further colleagues located at the PTB in Berlin, I want to thank Prof. Dr. Rainer Macdonald, Dr. Dirk Grosenick, Dr. Axel Hagen, and Dr. Oliver Steinkellner for their great support, which was not limited to the FLUOROMAMM project only. They performed time-domain measurements that valorized my thesis, which otherwise would be limited to theoretical predictions. I personally wish them a big success with their ongoing clinical trial.

In addition, several colleagues from Eindhoven supported my work with measurements, preparation of phantoms, discussions, and, above all, with the development of the Philips tomographic fluorescence mammograph. Therefore, kudos to Dr. Leon Bakker, Dr. Michiel van Beek, Dr. Marjolein van de Voort, Rami Nachabe, Dr. Rik Harbers, Fons Schipper, and Louis Stroucken for their great work, and special thanks to Dr. Martin B. van der Mark for the inspiring, and open-minded discussions we shared, for his cheerful soul and his keen sense of good restaurants. Thanks to all of you for letting me feel welcomed in Eindhoven on each visit. Further gratitude goes to Prof. Dr. Willem P. Th. M. Mali, to Stephanie van de Ven, and to Andrea Wiethoff for the clinical study performed at the UMC Utrecht, because my thesis benefited a lot from their work.

I want to thank Dr. Dye Jensen as my group leader of Philips Research Hamburg, who made all this work possible, revised diligently, and approved publications and trips quickly, even if he was pressed for time. Furthermore, he permitted me to present my work at conferences and on several other occasions, for

which I am very grateful. For similar reasons, thanks go to Dr. Dirk van Pijkeren, Dr. Gertjan Keesman, and Dr. Sjaak Deckers from Philips Healthcare, making the whole project possible.

Also, the colleagues from PicoQuant, from the Charité Berlin, and the project executing organization VDI for the "FLUOROMAMM" collaboration have to be mentioned for their support. Acknowledgments go to Bayer Schering Pharma for providing the Omocyanine dye and supporting the clinical study in Utrecht.

Additionally, I want to thank all the people who are often overlooked as long as everything runs smoothly, like the colleagues from our IT department, especially Thomas Blidung and Otmar Tschendel, who always provided fast support if the cluster ran into trouble due to being overloaded by my reconstructions, or Gabriele Ziem for creating conference posters, Anja Koue, and Astrid Jacob for organizing my travels.

Of course, all these great years would not have been possible without the other nice colleagues, Ph.D., and diploma students that I can not mention here individually, due to their sheer number.

Last but not least, special thanks go to my family and my friends whose support, although non-academic, was at least equally important during the last years. Very special thanks go to my brother Dr. Andy Ziegler, who, as a part-time member of the project, supported me during my thesis and beyond.

Bibliography

[1] P. Boyle and J. Ferlay. Cancer incidence and mortality in europe, 2004. *Annals of Oncology*, 16:481 – 488, 2005.

[2] I. Weinberg, S. Majewski, A. Weisenberger, A. Markowitz, L. Aloj, L. Majewski, D. Danforth, J. Mulshine, K. Cowan, C. Chow, E. Jones, V. Chang, W. Berg, and J. Frank. Preliminary results for positron emission mammography - real-time functional breast imaging in a conventional mammography gantry. *European Journal of Nuclear Medicine*, 23:804 – 806, 1996.

[3] R. Freifelder and J. S. Karp. Dedicated pet scanners for breast imaging. *Physics in Medicine and Biology*, 42:2463 – 2480, 1998.

[4] G. Pipermo, E. H. Frei, and M. Moshitzky. Breast cancer screening by impedance measurements. *Front. Med. Biol. Eng.*, 2:111 – 117, 1990.

[5] G. Martin, R. Martin, M. J. Brieva, and L. Santamaria. Electrical impedance scanning in breast cancer imaging: correlation with mammographic and histologic diagnosis. *European Radiology*, 12:1471 – 1478, 2002.

[6] J. Lorenzen, R. Sinkus, M. Lorenzen, M. Dargatz, C. Leussler, P. Roschmann, and G. Adam. MR elastography of the breast: preliminary clinical results. *RöFo Fortschritte auf dem Gebiet der Röntgenstrahlen und der bildgebenden Verfahren*, 174:830 – 834, 2002.

[7] M. Cutler. Transillumination as an aid in the diagnosis of breast lesions. *Surgery, Gynecology and Obstetrics*, 48:721 – 727, 1929.

[8] R. K. Jain. Barriers to drug delivery in solid tumors. *Scientific American*, 271:42 – 49, 1994.

[9] A. E. Cerussi, N. Shah, D. Hsiang, M. Compton, and B. Tromberg. In vivo absorption, scattering and physiologic properties of 58 malignant breast tumors determined by broadband diffuse optical spectroscopy. *Journal of Biomedical Optics*, 11:044005 01 – 16, 2006.

[10] P. Vaupel, S. Briest, and M. Hoeckel. Hypoxia in breast cancer: pathogenesis, characterization and biological/therapeutic implications. *Wiener Medizinische Wochenschrift*, 50:2451 – 2468, 2004.

[11] D. Grosenick, H. Wabnitz, K. T. Moesta, J. Mucke, P. M. Schlag, and H. Rinneberg. Time-domain scanning optical mammography: II. optical properties and tissue parameters of 87 carcinomas. *Physics in Medicine and Biology*, 50:2451 – 2468, 2005.

[12] L Spinelli, A. Torricelli, A. Pifferi, P. Taroni, G. Danesini, and R. Cubeddu. Characterization of female breast lesions from multi-wavelength time-resolved optical mammography. *Physics in Medicine and Biology*, 50:2489 – 2502, 2005.

[13] D. Grosenick, K. T. Moesta, M. Möller, J. Mucke, H. Wabnitz, B. Gebauer, C. Stroszczynski, B. Wassermann, P. M. Schlag, and H. Rinneberg. Time-domain scanning optical mammography: I. recording and assessment of mammograms of 154 patients. *Physics in Medicine and Biology*, 50:2429 – 2449, 2005.

[14] L. Göetz, S. H. Heywang-Köbrunner, O. Schütz, and H. Siebold. Optical mammography on preoperative patients (optische mammographie an präoperativen patientinnen). *Aktuelle Radiologie*, 8:31 – 33, 1998.

[15] S. B. Colak, M. B. van der Mark, G. W. 't Hooft, J. H. Hoogenraad, E. S. van der Linden, and F. A. Kuijpers. Clinical optical tomography and NIR spectroscopy for breast cancer detection. *IEEE Journal of Selected Topics in Quantum Electronics*, 5(4):1143 – 1158, 1999.

[16] D. Grosenick, H. Wabnitz, H. Rinneberg, K. T. Moesta, and P. Schlag. Development of a time-domain optical mammograph and first in vivo applications. *Applied Optics*, 38:2927 – 2943, 1999.

[17] A. Pifferi, P. Taroni, A. Torricelli, F. Messina, R. Cubeddu, and G. Danesini. Four-wavelength time-resolved optical mammography in the 680-980-nm range. *Optics Letters*, 28:1138 – 1140, 2003.

[18] T. D. Yates, J. C. Hebden, A. P. Gibson, N. Everdell, S. R. Arridge, and M. Douck. Optical tomography of the breast using a multi-channel time-resolved imager. *Physics in Medicine and Biology*, 50:2503 – 2517, 2005.

[19] M. A. Franceschini, K. T. Moesta, S. Fantini, G. Gaida, E. Gratton, H. Jess, W. W. Mantulin, M. Seeber, P. M. Schlag, and M. Kaschke. Frequency-domain techniques enhance optical mammography: initial clinical results. *Proceedings of the National Academy of Sciences*, 94:6468 – 6473, 1997.

[20] J. P. Culver, T. Durduran, D. Furuya, C. Cheung, J. H. Greenberg, and A. G. Yodh. Diffuse optical tomography of cerebral blood flow, oxygenation, and metabolism in rat during focal ischemia. *Journal of Cerebral Blood Flow and Metabolism*, 23:911 – 924, 2003.

[21] H. Dehghani, B. W. Pogue, S. P. Poplack, and K. D. Paulsen. Multiwavelength three-dimensional near-infrared tomography of the breast: initial simulation, phantom, and clinical results. *Applied Optics*, 42:135 – 145, 2003.

[22] P. Taronim, A. Toricelli, L. Spinelli, A. Pifferi, F. Arpaia, G. Danesini, and R. Cubeddu. Time-resolved optical mammography between 637 and 985 nm: clinical study on the detection and identification of breast lesions. *Physics in Medicine and Biology*, 50:2469 – 2488, 2005.

[23] T. D. Yates, J. C. Hebden, A. P. Gibson, L. Enfield, N. L. Everdell, S. R. Arridge, and D. T. Delpy. Time-resolved optical mammography using a liquid coupled interface. *Journal of Biomedical Optics*, 10(5):054011–1 – 054011–11, 2005.

[24] M. S. Patterson, Britton Chance, and B. C. Wilson. Time resolved reflectance and transmittance for the non-invasive measurement of tissue optical properties. *Applied Optics*, 28(12):2331 – 2335, 1989.

[25] D. A. Boas, M. A. O'Leary, B. Chance, and A. G. Yodh. Scattering of diffuse photon density waves by spherical inhomogeneities within turbid media: Analytic solution and applications. *Proceedings of the National Academy of Sciences*, 91:4887 – 4891, 1994.

[26] X. D. Li, M. A. O'Leary, D. A. Boas, B. Chance, and A. G. Yodh. Fluorescent diffuse photon densitiy waves in homogeneous and heterogeneous turbid media: analytic solutions and applications. *Applied Optics*, 35(19):3746–3758, 1996.

[27] D. Nolte. *Erkennung und Abbildung pathologischer Gewebeveränderungen mittels laserinduzierter Fluoreszenz in-vivo: physikalische Grundlagen, apparative Entwicklungen und medizinische Anwendungen.* PhD thesis, Freie Universität Berlin, 1998.

[28] S. R. Arridge, Schweiger, M. Hiraoka, and D. T. Delpy. A finite element approach for modeling photon transport in tissue. *Medical Physics*, 20:299–309, 1993.

[29] M. Schweiger, S. R. Arridge, and D. T. Delpy. Application of the finite-element method for the forward and inverse models in optical tomography. *Journal of Mathematival Imaging and Vision*, 3:263 – 283, 1993.

[30] Simon R. Arridge. Optical tomography in medical imaging. *Inverse Problems*, 15(2):R41 – R93, 1999.

[31] A. E. Cerussi, D. Hsiang, N. Shah, R. Mehta, A. Durkin, J. Butler, and B. Tromberg. Predicting response to breast cancer neoadjuvant chemotherapy using diffuse optical spectroscopy. *Proceedings of the National Academy of Sciences*, 104:4014 – 4019, 2007.

[32] M. W. Ah-See and A. R. Pradhain. *"Dynamic Magnetic Resonance Imaging" in: "Dynamic Contrast-Enhanced Magnetic Resonance Imaging in Oncology".* Springer Series in Medical Radiology, Sub-Series Diagnostic Imaging, 2005.

[33] G. J. M. Parker and D. Buckley. *"Tracer Kinetic Modelling for T_1-Weighted DCE-MRI" in: Dynamic Contrast-Enhanced Magnetic Resonance Imaging in Oncology.* Springer Series in Medical Radiology, Sub-Series Diagnostic Imaging, 2005.

[34] A. Corlu, R. Choe, T. Durduran, M. A. Rosen, M. Schweiger, S. R. Arridge, M. D. Schnall, and A. G. Yodh. Three-dimensional in vivo fluorescence diffuse optical tomography of breast cancer in humans. *Optics Express*, 15(11):6697 – 6716, 2007.

[35] N Loman, O. Johannson, U. Kristoffersson, H. Olsson, and A. Borg. Family history of breast and ovarian cancers and brca1 and brca2 mutations in a population-based series of early-onset breast cancer. *Journal of National Cancer Institute*, 93(16):1215 – 1223, 2001.

[36] D. Ford, D. F. Easton, M. Stratton, M. Stratton, S. Narod, D. Goldgar, P. Devilee, D. T. Bishop, B. Weber, G. Lenoir, J. Chang-Claude, H. Sobol, M.D. Teare, J. Struewing, A. Arason, S. Scherneck, J. Peto, T. R. Rebbeck, P. Tonin, S. Neuhausen, R. Barkardottir, J. Eyfjord, H. Lynch, B. A. J. Ponder, S.A. Gayther, J. M. Birch, A. Lindblom, D. Stoppa-Lyonnet, Y. Bignon, A. Borg, U. Hamann, N. Haites, R. J. Scott, C.M. Maugard, H. Vasen, S. Seitz, L. A. Cannon-Albright, A. Schofield, M. Zelada-Hedma, and Breast Cancer Linkage Consortium. Genetic heterogeneity and penetrance analysis of the brca1 and brca2 genes in breast cancer families. *American Journal of Human Genetics*, 62(3):676 – 689, 1998.

[37] L. J. Esserman. New apporaches to the imaging, diagnosis and biopsy of breast lesions. *Cancer Journal*, 8, 2002.

[38] I. S. Fentiman. Fixed and modifiable risk factors for breast cancer. *International Journal of Clinical Practice*, 55(8):527 – 530, 2001.

[39] H. L. Olsson, C. Ingvar, and A. Bladstrom. Hormone replacement therapy containing pregestins and given continuously increases breast carcinoma risk in sweden. *Cancer*, 97(6):1387 – 1392, 2003.

[40] I. T. Gram, E. Funkhouser, L. Nordgard, L. Tabar, and G. Ursing. Oral contraceptive use and mammographic patterns. *European Journal of Cancer Prevention*, 11(3):265 – 270, 2002.

[41] M. Kumle, E. Weiderpass, T. Braaten, I. Persson, H. O. Adami, and E. Lund. Use of oral contraceptives and breast cancer risk: The norwegian-swedish women's lifestyle and health cohort study. *Cancer Epidemiology Biomarkers and Preventions*, 11(11):1375 – 1381, 2002.

[42] D. K Mirick, S. Davis, and D. B. Thomas. Antitransperant use and the risk of breast cancer. *Journal of National Cancer Institute*, 94(20):1578 – 1580, 2002.

[43] J. Couzin. Cancer risk: Review rules out abortion-cancer link. *Science*, 299(5612):1498, 2003.

[44] L. C. Hartmann, D. J. Schaid, J. E. Woods, T. P. Crotty, J. L. Myers, P. G. Arnold, P. M. Petty, T. A. Sellers, J. L. Johnson, S. K. McDonnell, M. H. Frost, C. S. Grant, V. V. Michels, and R. B. Jenkins. Efficacy of bilateral prophylactic mastectomy in women with a family history of breast cancer. *The New England Journal of Medicine*, 340(2):77 – 84, 1999.

[45] R. Smith, D. Saslow, K. Sawyer, and W. Burke. American cancer society guidelines for breast cancer screening: Update 2003. *CA: A Cancer Journal for Clinicians*, 53(3):141 – 169, 2003.

[46] G. N. Hortobagyi. Treatment of breast cancer. *The New England Journal of Medicine*, 339(14):974 – 984, 1998.

[47] American Cancer Society. *Breast Cancer Facts & Figures 2003 – 2004.* Atlanta: American Cancer Society, Inc., 2003.

[48] American Cancer Society. *Breast Cancer Facts & Figures 2005.* Atlanta: American Cancer Society, Inc., 2003.

[49] National Academy of Sciencens, National Academy of Engineering, Institute of Medicine, and National Research Council. *Mammography and Beyond.* National Academy Press, http://www.nap.edu, 2001.

[50] P. C. Gotzsche and O. Olsen. Is screening for breast cancer with mammography justifiable? *The Lancet*, 355(9198):129 – 134, 2000.

[51] L. L. Humphrey, M. Helfand, B. K. Chan, and S. H. Woolf. Breast cancer screening: a summary of the evidence for the U. S. preventive services task force. *Annals of International Medicine*, 137(5 part 1):347 – 360, 2002.

[52] L. Tabar, M. F. Yen, B. Vitak, H. H. Chen, R. A. Smith, and S. W. Duffy. Mammography service screening and mortality in breast cancer patients: 20-year follow-up before and after introduction of screening. *The Lancet*, 361(9367):1405 – 1410, 2003.

[53] S. W. Duffy, L. Tabar, and H. H. Chen. The impact of organized mammography service screening on breast carcinoma mortality in seven swedish coutries. *Cancer*, 95(3):458 – 469, 2002.

[54] L. Tabar, B. Vitak, H. H. Chen, M. F. Yen, S. W. Duffy, and R. A. Smith. Beyond randomized controlled trials: organized mammographic screening substantially reduces breast carcinoma mortality. *Cancer*, 91(9):1724 – 1731, 2001.

[55] O. Olsen and P .C. Gøtzsche. Systematic review of screening for breast cancer with mammography. Technical report, The Nordic Cochrane Centre, 2001.

[56] P. C. Gøetzsche and O. Olsen. Is screening for breast cancer with mammography justifiable? *The Lancet*, 355(9198):129 – 134, 2000.

[57] K. Kerkilowske and J. Barclay. Outcomes of modern screeing mamography. *Journal of National Cancer Institute Monographs*, 22:105 – 111, 1997.

[58] National Cancer Policy Board. *Mammography and Beyond: Developing Technologies for the Early Detection of Breast Cancer*. NATIONAL ACADEMY PRESS, Washington, DC, 2001.

[59] S. A. Feig and R. E. Hendrick. Radiation risk from screening mammography of women aged 40-49 years. *Journal of National Cancer Institute Monographs*, 22:119–124, 1997.

[60] T. M. Kolb, J. Lichy, and J. H. Newhouse. Performance of screening mammography, physical examination and ultrasound and evaluation of factors that influence them. *Radiology*, 225:165 – 175, 2002.

[61] F. Bloch. Nuclear induction. *Physical Review*, 70:460 – 474, 1946.

[62] E. L. Hahn. Spin echoes. *PhysRev*, 80(4):580 – 594, 1950.

[63] M. Kriege, C. T. M. Brekelmans, C. Boetes, P. E. Besnard, H. M. Zonderland, I. M. Obdeijn, R. A. Manoliu, T. Kok, H. Peterse H, M. M. A. Tilanus-Linthorst, S. H. Muller, S. Meijer S, J. C. Oosterwijk, L. V. A. M. Beex, R. A. E. M. Tollenaar, H. J. de Koning, E. J. T. Rutgers, and J. G. M. Klijn. Efficacy of mri and mammography for breast-cancer screening in women with a familial or genetic predisposition. *The New England Journal of Medicine*, 351(5):427 – 437, 2004.

[64] P. J. Kneeshaw, L. W. Turnbull, and P. J. Drew. Current applictions and future direction of mr mammography. *British Journal of Cancer*, 88:4 – 10, 2003.

[65] Stephanie M.W.Y. van de Ven, Sjoerd G. Elias, Andrea J. Wiethoff, Marjolein van der Voort, Anais Leproux, Tim Nielsen, Bernhard Brendel, Leon P. Bakker, Martin B. van der Mark, Willem P.Th.M. Mali, and Peter Luijten. Spectroscopic diffuse optical tomography of the breast: initial validation study in a cyst model. *Molecular Imaging and Biology*, page accepted, 2008.

[66] Detlef Kamke and Wilhem Walcher. *Physik für Mediziner*. Vieweg + Teubner Verlag, 1994.

[67] F. F. Jobsis. Noninvasive, infrared monitoring of cerebral and myocardial oxygen sufficiency and circulatory parameters. *Science*, 198:1264 – 1267, 1977.

[68] S. P. Gopinath, C. S. Robertson, C. F. Contant, R. K. Narayan, R. G. Grossman, and B. Chance. Early detection of delayed traumatic intracranial hematomas using near-infrared spectroscopy. *Journal of Neurology*, 83:438 – 444, 1995.

[69] S. R. Hintz, W. F. Cheong, J. P. van Houten, D. K. Stevenson, and D. A. Benaron. Bedside imaging of intracranial hemorrhage in the neonate using light: comparison with ultrasound, computed tomography, and magnetic resonance imaging. *Pediatric Research*, 45:60 – 65, 1999.

[70] C. Hock, K. Villringer, F. Muller-Spahn, R. Wenzel, H. Heekeren, S. Schuh-Hofer, M. Hoffmann, S. Minsohima, M. Schwaiger, U. Dirnagl, and A. Villringer. Decrease in parietal cerebral hemoglobin oxygenation during performance of a verbal fluency task in patients with alzheimer's disease monitored by means of near-infrared spectroscopy (NIRS) – correlation with simultaneous CBF-PET measurements. *BrainRes*, 755:293 – 303, 1997.

[71] T. Durduran, G. Yu, M. G. Burnett, J. A. Detre, J. H. Greenberg, J. Wang, C. Zhou, and A. G. Yodh. Diffuse optical measurement of blood flow, blood oxygenation and metabolism in a human brain during sensoimotor cortex activation. *Optics Letters*, 29:1766 – 1768, 2004.

[72] R. Wenzel, H. Obrig, J. Ruben, K. Villringer, A. Thiel, J. Bernardinger, U. Dirnagl, and A. Villringer. Cerebral blood oxygenation changes induced by visual stimulation in humans. *Journal of Biomedical Optics*, 4:399 – 404, 1996.

[73] C. Hock, K. Villringer, F. Muller-Spahn, M. Hoffmann, S. Schuh-Hofer, H. Heekeren, R. Wenzel, and A. Villringer. Near infrared spectroscopy in the diagnosis of alzheimer's disease. *Annals of the New Yorker Acadadmy of Sciences*, 777:22 – 29, 1996.

[74] U. Netz, J. Beuthan, H. J. Capius, H. C. Koch, A. D. Klose, and A. H. Hielscher. Imaging of rheumatoid arthritis in finger joints by sagittal optical tomography. *Medical Laser Application*, 16:306 – 310, 2001.

[75] C. Musgrove, C. F. Bunting, H. Deghani, B. W. Pogue, and D. Piao. Computational aspects of endoscopic (trans-rectal) near-infrared optical tomography initial investiagtions. In *Progress in Biomedical Optics and Imaging – Optical Tomography and Spectroscopy of Tissue VII*, volume 8, pages 6434091 – 64340910, 2007.

[76] R. Choe, A. Corlu, K. Lee, T. Durduran, S. D. Konecky, M. Grosicka-Koptyra, S. Arridge, B. J. Czerniecki, D. L. Fraker, A. DeMichele, B. Chance, M. A. Rosen, and A. G. Yodh. Diffuse optical tomography of breast cancer during neoadjuvant chemotherapy: A case study with comparison to MRI. *Medical Physics*, 32(4):1128 – 1139, 2005.

[77] Q. Zhu, M. Huangm, N.G. Chen, K. Zarfos, B. Jagjivan, M. Kane, P. Hegde, and S. H. Kurtzman. Ultrasound-guided optical tomographic imaging of malignant and benign breast lesions. *Neoplasia*, 5:379–388, 2003.

[78] N. G. Chen, P. Guo, S. Yan, D. Piao, and Q. Zhu. Simultaneous near infrared diffuse light and ultrasound imaging. *Applied Optics*, 40:6367–6280, 2001.

[79] V. Ntziachristos, A. G. Yodh, M. D. Schnall, and B. Chance. Mri-guided diffuse optical spectroscopy of malignant and benign breast lesions. *Neoplasia*, 4(4):347 – 354, 2002.

[80] A. Li, E. Miller, M. E. Kilmer, T. J. Brukilacchio, T. Chaves, J. Stott, Q. Zhang, T. Wu, M. Charlton, R. H. Moore, D. B. Kopans, and D. A. Boas. Tomographic optical breast imaging guided by three-dimensional mammography. *Applied Optics*, 42(25):5183–5190, 2003.

[81] Ben Brooksby, Subhadra Srinivasan, Shudong Jiang, Hamid Deghani, Brian W. Pogue, Keith D. Paulsen, John Weaver, Christine Kogel, and Steven P. Poplack. Spectral priors improve near-infrared diffuse tomography more than spatial priors. *Optics Letters*, 30:1968–1970, 2005.

[82] B. Brooksby, B. W. Pogue, S. Jiang, H. Deghani, S. Srinivasan, C. Kogel, T. D. Tosteson, J. Weaver, S. P. Poplack, and K. D. Paulsen. Imaging breast adipose and fibroglandular tissue molecular signatures by using hybrid mri-guided near-infrared spectral tomography. *Proceedings of the National Academy of Sciences*, 103(13):8828 – 8833, 2006.

[83] D. S. Kepshire, M. Hutchins, A. Provencher, N. Mincu, F. Leblond, B. W. Pogue, and M. Khayat. Design and performance analysis of a small-animal fluorescence tomography system coupled to microct. In *Progress in Biomedical Optics and Imaging – Optical Tomography and Spectroscopy of Tissue VIII*, page in preparation, 2008.

[84] S. P. Poplack, T. D. Tosteson, W. A. Wells, B. W. Pogue, P. M Meaney, A. Hartov, C. A. Kogel, S. K. Soho, J. J. Gibson, and K. D. Paulsen. Electromagnetic breast imaging: Results of a pilot study in women with abnormal mammograms. *Radiology*, 243(2):350 – 359, 2007.

[85] H. Rinneberg, D. Grosenick, K. T. Moesta, H. Wabnitz, J. Mucke, G. Wübbeler, R. Macdonald, and P. Schlag. Detection and characterization of breast tumors by time-domain scanning optical mammography. *Opto-Electronics Review*, 2(16):147 – 162, 2008.

[86] D. J. Hawrysz and E. M. Sevick-Muraca. Developments toward diagnostic breast cancer imaging unsing near-infrared optical measurements and fluorescent contras agents. *Neoplasia*, 2(5):388 – 417, 2000.

[87] Vasilis Ntziachristos, A. G. Yodh, Mitchell D. Schnall, and Britton Chance. Concurrent MRI and diffuse optical tomography of breast after indocyanine green enhancement. *Proceedings of the National Academy of Sciences*, 97(6):2767 – 2772, 2000.

[88] X. Intes, J. Ripoll, Y. Chen, S. Nioka, A. G. Yodh, and B. Chance. In vivo continuous-wave optical breast imaging enhanced with indocyanine green. *Medical Physics*, 30(6):1039 – 1047, 2003.

[89] K. Licha, B. Riefke, V. Ntziachristos, A. Becker, B. Chance, and W. Semmler. Hydrophylic cyanine dyes as contrast agents for near-infrared tumor imaging: synthesis, photophysical properties and spectroscopic in-vivo characterization. *Photochemistry and Photobiology*, 72:392 – 398, 2000.

[90] P. L. Porter, A. Y. El-Bastawissi, M. T. Mandelson, M. G. Lin, N. Khalid, E. A. Watney, L. Cousens, D. White, S. Taplin, and E. White. Breast tumor characteristics as predictors of mammographic detection: Comparison of interval- and screen-detected cancers. *Journal of National Cancer Institute*, 91(23):2020 – 2028, 1999.

[91] B. Chance, M. Cope, E. Gratton, N. Rmanujam, and B. Tromberg. Phase measurement of light absorption and scatter in human tissue. *Review of Scientific Instruments*, 69(10):3457–3481, 1998.

[92] A. B. Milstein, J. J. Stott, S. Oh, D .A. Boas, R. P. Millane, C. A. Bouman, and K. J. Webb. Fluorescence optical diffusion tomography using multiple-frequency data. *Journal of the Optical Society of America A*, 21(6):1035 – 1049, 2004.

[93] X. Intes, S. Djeziri, Z. Ichalalene, N. Mincu, and Y. Wang. Time-domain optical mammography softscan: intial results. *Academic Radiology*, 12(8):934 – 947, 2005.

[94] A. Hagen, O. Steinkellner, D. Grosenick, M. Möller, R. Ziegler, T. Nielsen, K. Lauritsen, R. Macdonald, and H. Rinneberg. Development of a multi-channel time-domain fluorescence mammograph. In *Progress in Biomedical Optics and Imaging – Optical Tomography and Spectroscopy of Tissue VII*, volume 8, pages 64340Z1 – 64340Z9, 2007.

[95] S. Srinivasan, B. W. Pogue, H. Dehghani, F. Leblond, and X. Intes. Data subset algorithm for computationally efficient reconstruction of 3-d spectral imaging in diffuse optical tomography. *Applied Optics*, 44:1858 – 1869, 2005.

[96] A. Corlu, T. Durduran, R. Choe, M. Schweiger, E. M. C. Hillman, S. R. Arridge, and A. G. Yodh. Uniqueness and wavelength optimization in continuous-wave multispectral diffuse optical tomography. *Optics Letters*, 28(23):2339 – 2341, 2003.

[97] B. Brendel and T. Nielsen. Wavelength optimization in multispectral diffuse optical tomography considering uncertainties in absorption spectra. In *European Conference on Biomedical Optics*, pages 6629–09. OSA, 2007.

[98] Natasha Shah, Albert Cerussi, Charlotta Eker, Jenny Espinoza, John Butler, Joshua Fishkin, Rene Hornung, and Bruce Tromberg. Noninvasive functional optical spectroscopy of human breast tissue. *Proceedings of the National Academy of Sciences*, 98:4420 – 4425, 2001.

[99] S. R. Arridge, J. C. Hebden, M. Schweiger, F. E. W. Schmidt, M. R. Fry, E. M. C. Hillman, H. Dehghani, and D. T. Delpy. A method for three-dimensional time-resolved optical tomography. *International Journal of Imaging Systems and Technology*, 11:2 – 11, 2000.

[100] J. C. Hebden, H. Veenstra, H. Dehghani, E. M. C. Hilman, M. Schweiger, S. R. Arridge, and D. T. Delpy. Three-dimensional time-resolved optical tomography of a conical breast phantom. *Applied Optics*, 40(19):3278 – 3287, 2001.

[101] O. Steinkellner, A. Hagen, C. Stadelhoff, D. Grosenick, R. Macdonald, H. Rinneberg, R. Ziegler, and T. Nielsen. Recording of artifact-free reflection data with a laser and fluorescence scanning mammograph for improved axial resolution. *Proceedings of the OSA Biomedical Optics Meeting*, submitted, 2008.

[102] D. T. Delpy, M. Cope, P. van der Zee, S. Arridge, S. Wray, and J. Wyatt. Estimation of optical pathlength through tissue from direct time of flight measurement. *Physics in Medicine and Biology*, 33(12):1433 – 1442, 1988.

[103] S. Chandrasekhar. *Radiative Transfer*. Dover Publications, 1960.

[104] F. Martelli, M. Bassani, L. Alianelli, L. Zangheri, and G. Zaccanti. Accuracy of the diffusion equation to describe photon migration through an infinite medium: numerical and experimental investigation. *Physics in Medicine and Biology*, 45:1359 – 1373, 2000.

[105] Lihong V. Wang and Steven L. Jacques. Source of error in calculation of optical diffuse reflectance from turbid media using diffusion theory. *Computer Methods and Programs in Biomedicine*, 61:163 – 170, 2000.

[106] H. Dehghani, D. T. Delpy, and S. R. Arridge. Photon migration in non-scattering tissue and the effects on image reconstruction. *Physics in Medicine and Biology*, 44:2897 – 2906, 1999.

[107] J. Riley, H. Deghani, M. Schweiger, S. R. Arridge, J. Ripoll, and M. Nieto-Vesperinas. 3D optical tomography in the presence of void regions. *Optics Express*, 7(13):462 – 467, 2000.

[108] A. D. Kim and M. Moscoso. Radiative transport theory for optical molecular imaging. *Applied Optics*, 21:1 – 20, 2005.

[109] J. C. J. Paasschens. Diffusion theory for medical imaging purposes: derivation, solutions, and approximations. Technical Report NatLab report 7028, Philips Research, 1998.

[110] L. Henyey and J. Greenstein. Diffuse radiation in the galaxy. *Astrophysical Journal*, 93:70 – 83, 1941.

[111] W. F. Cheong, S. A. Prahl, and A. J. Welch. A review of the optical properties of biological tissues. *IEEE Journal of Selected Topics in Quantum Electronics*, 26:2166 – 2185, 1990.

[112] R. Pierrat, J.-J. Greffet, and R. Carminati. Photon diffusion coefficient in scattering and absorbing media. *Journal of the Optical Society of America A*, 23(5):1106 – 1110, 2006.

[113] W. Bangerth, R. Hartmann, and G. Kanschat. deal.II differential equations analysis library, technical reference. Technical report, http://www.dealii.org, 2004.

[114] R. A. J. Groenhuis, H. A. Ferwerda, and J. J. Ten Bosch. Scattering and absorption of turbid materials determined from reflection measurements. *Applied Optics*, 22:2456 – 2462, 1983.

[115] M. Schweiger, S. R. Arridge, M. Hiraoka, and D.T. Delpy. The finite element method for the propagation of light in scattering media: Boundary and source conditions. *Medical Physics*, 22:1779 – 1792, 1995.

[116] R. L. P. van Veen, H. J. C. M. Sterenborg, A. Pifferi, A. Torricelli, and R. Cubeddu. Determination of VIS-NIR absorption coefficients of mammalian fat, with time- and spatially resolved diffuse reflectance and transmission spectroscopy. In *Proceedings of Biomedical Topical Meetings*, volume SF-5, Washington, DC, 2004. Optical Society of America.

[117] D. J. Segelstein. *The complex refractive index of water*. PhD thesis, University of Missouri-Kansas City, 1981.

[118] Scott Prahl. Tabulated molar extinction coefficient for hemoglobin in water. compiled by scott prahl (prahl@ece.ogi.edu) using data from w. b. gratzer, med. res. council labs, holly hill, london and n. kollias, wellman laboratories, harvard medical school, boston, http://omlc.ogi.edu/spectra/hemoglobin/summary.html, Oregon Medical Laser Center, Dec 19 1999.

[119] J. R. Mourant, M. Canpolat, C. Brocker, O. Esponda-Ramos, T. M. Johnson, A. Matanock, K. Stetter, and J. P. Freyer. Light scattering from cells: The contribution of the nucleus and the effects of proliferative status. *Journal of Biomedical Optics*, 5:131 – 137, 2000.

[120] X. Wang, B. W. Pogue, S. Jiang, X. Song, K. D. Paulsen, C. Kogel, S. P. Poplack, and W. A. Wells. Approximation of mie scattering parameters in near-infrared tomography of normal breast tissue in vivo. *Journal of Biomedical Optics*, 10:0517041–0517048, 2005.

[121] A. E. Cerussi, D. Jakubowski, N. Shah, F. Bevilacqua, R. Lanning, A. J. Berger, D. Hsian, J. Butler, R. F. Holcombe, and B. J. Tromberg. Spectroscopy enhances the information content of optical mammography. *Journal of Biomedical Optics*, 7(1):60 – 71, 2002.

[122] C. Perlitz, K. Licha, F.-D. Scholle, B. Ebert, M. Bahner, P. Hauff, K. T. Moesta, and M. Schirner. Comparison of two tricarbocyanine-based dyes for fluorescence optical imaging. *Journal of Fluorescence*, 15:443 – 454, 2005.

[123] K. Licha, B. Riefke, and W. Semmler. Synthesis and characterization of cyanine dyes as contrast agents for near-infrared imaging. *Proceedings of the Optical and Imaging Techniques for Biomonitoring II*, 2927:192–198, 1996.

[124] M. L. J. Landsman, G. Kwant, G. A. Mook, and W. G. Zijlstra. Light- absorbing properties, stability, and spectral stabilization of indocyanine green. *Journal of Applied Physiology*, 40:575 – 583, 1976.

[125] M. L. J. Landsman. Tabulated molar extinction coefficient for icg in plasma. 1976.

[126] Dirk Grosenick, Heidrun Wabnitz, K. Thomas Moesta, Jörg Mucke, Michael Mller, Christian Stroszczynski, Jana Stößel, Bernhard Wassermann, Peter M. Schlag, and Herbert Rinneberg. Concentration and oxygen saturation of haemoglobin of 50 breast tumours determined by time-domain optical mammography. *Physics in Medicine and Biology*, 49:1165 – 1181, 2004.

[127] K. Eriksson, D. Estep, P. Hansbo, and C. Johnson. *Computational Differential Equations*. Cambridge University Press, 1996.

[128] R. Barrett, M. Berry, T.F. Chan, J. Demmel, J. Donato, J. Dongarra, V. Eijkhout, R. Pozo, C. Romine, and H. Van der Vorst. *Templates for the Solution of Linear Systems: Building Blocks for Iterative Methods*. SIAM, 1994.

[129] J. Crank and P. Nicolson. A practical method for numerical evaluation of solutions of partial differential equations of the heat conduction type. *Proceedings of the Cambridge Philosophical Society*, 43:50 – 64, 1947.

[130] R.. Courant, K. Friedrichs, and H. Lewy. über die partiellen Differentialgleichungen der mathematischen Physik. *Mathematische Annalen*, 100(1):32–74, 1928.

[131] Georgy Voronoi. Nouvelles applications des paramètres continus à la théorie des formes quadratiques. *Journal für die Reine und Angewandte Mathematik*, 133:97 – 178, 1907.

[132] S. Carraresi, T. S. M. Shatir, F. Martelli, and G. Zaccanti. Accuracy of a perturbation model to predict the effect of scattering and absorbing inhomogeneities on photon migration. *Applied Optics*, 40(25):4622 – 4632, 2001.

[133] B. Wassermann, A. Kummrow, K. T. Moesta, D. Grosenick, J. Mucke, H. Wabnitz, M. Möller, R. Macdonald, P. M. Schlag, and H. Rinneberg. In-vivo tissue optical properties derived by linear perturbation theory for edge-corrected time-domain mammograms. *Optics Express*, 13(21):8571 – 8583, 2005.

[134] B. W. Pogue, T. O. McBride, S. Jiang, U. L. Osterberg, and K. D. Paulsen. Comparison of imaging geometries for diffuse optical tomography of tissue. *Optics Express*, 4(8):270 – 286, 1999.

[135] S. C. Davis, B. W. Pogue, H. Dehghani, and K. D. Paulsen. Contrast-detail analysis of diffuse optical fluorescence tomography reconstruction. *Journal of Biomedical Optics*, 10(5):1 – 3, 2005.

[136] J. P. Culver, V. Ntziachristos, and A. G. Yodh. Optimization of optode arrangements for diffuse optical tomography: a singular-value analysis. *Optics Letters*, 26:701 – 703, 2001.

[137] H. Xu, H. Dehghani, B. W. Pogue, R. Springett, K. D. Paulsen, and J. F. Dunn. Near-infrared imaging in the small animal brain: optimization of fiber positions. *Journal of Biomedical Optics*, 8(1):102–110, 2003.

[138] Karl Pearson. On the criterion that a given system of deviations from the probable in the case of correlated system of variables is such that it can be reasonably supposed to have arisen from random sampling. *Philosophical Mag.*, 50:157 – 175, 1900.

[139] V. Ntziachristos and R. Weissleder. Experimental three-dimensional fluorescence reconstruction of diffuse media by use of a normalized born approximation. *Optics Letters*, 26:893 – 895, 2001.

[140] A. Soubret, J. Ripoll, and Vasilis Ntziachristos. Accuracy of fluorescent tomography in the presence of heterogeneities: study of the normalized born ratio. *IEEE Transactions on Medical Imaging*, 24:1377 – 1386, 2005.

[141] P. E. Greenwood and M. S. Nikulin. *A Guide to Chi-squared Testing*. Wiley-Interscience, 1996.

[142] A. Ishimaru. *Wave Propagation and Scattering in Random Media*. Academic Press, New York, U.S.A., 1978.

[143] V. A. Markel and J. C. Schotland. Scanning paraxial optical tomography. *Optics Letters*, 27:1123 – 1125, 2002.

[144] R. Ziegler, T. Nielsen, Th. Koehler, D. Grosenick, O. Steinkellner, A. Hagen, R. Macdonald, and H. Rinneberg. Reconstruction of absorption and fluorescence contrast for scanning time-domain fluorescence mammography. In *Progress in Biomedical Optics and Imaging – Optical Tomography and Spectroscopy of Tissue VII*, volume 8, pages 64340H1 – 64340H11, 2007.

[145] R. Ziegler, B. Brendel, A. Schipper, R. Habers, M. v. Beek, H. Rinneberg, and T. Nielsen. Investigation of detection limits for diffuse optical tomography systems: I. theory and experiment. *Physics in Medicine and Biology*, page submitted, 2008.

[146] A. Pifferi, J. Swartling, E. Chikoidze, A. Torricelli, P. Taroni, and A. Bassi. Spectroscopic time-resolved diffuse reflectance and transmittance measurements of the female breast at different inter-fiber distances. *Journal of Biomedical Optics*, 9(6):1143 – 1151, Nov 2004.

[147] R. Grable, N. A. Gkanatsios, and S. L. Ponder. Optical mammography. *Applied Radiology*, Feb 2000:18 – 20, 2000.

[148] D. Floery, T. H. Helbich, C. C. Riedl, S. Jaromi, M. Weber, S. Leodolter, and M. H. Fuchsjaeger. Characterization of benign and malignant breast lesions with computed tomography laser mammography (CTLM): Initial experience. *IEEE Transactions on Medical Imaging*, 40(6):328 – 335, 2005.

[149] O. Dorn. Shape reconstruction in scattering media with voids using a transport model and level sets. *Canadian Applied Math Quaterly*, 10(2):239 – 275, 2002.

[150] M. Schweiger, S. R. Arridge, O. Dorn, A. Zacharopoulos, and V. Kolehmainen. Reconstructing absorption and diffusion shape profiles in optical tomography by a level set technique. *Optics Letters*, 31(4):471 – 473, 2006.

[151] A. D. Zacharopoulos, S. R. Arridge, O. Dorn, V. Kolehmainen, and J. Sikora. Three-dimensional reconstruction of shape and piecewise constant region values for optical tomography using spherical harmonic parametrization and a boundary element method. *Inverse Problems*, 22:1509 – 1532, 2006.

[152] A. D. Klose and A. H. Hielscher. Optical tomography using the time-independent equation of radiative transfer. part 2: Inverse model. *Journal of Quantitative Spectroscopy and Radiative Transfer*, 72(5):715 – 732, 2002.

[153] Simon R. Arridge, , and M. Schweiger. Photon-measurement density functions. part 2: Finite-element-method calculations. *Applied Optics*, 34:8026–8037, 1995.

[154] Shechao Feng, Fan-An Zeng, and Britton Chance. Photon migration in the presence of a single defect: a perturbation analysis. *Applied Optics*, 34(19):3826 – 3837, 1995.

[155] W. R. B. Lionheart. EIT reconstruction algorithms: pitfalls, challanges and recent developments. *Physiological Measurements*, 25:125 – 142, 2004.

[156] S. R. Arridge and M. Schweiger. A gradient-based optimisation scheme for optical tomography. *Optics Express*, 2(6):213 – 226, 1998.

[157] B. Brendel, R.Ziegler, and T. Nielsen. Algebraic reconstruction techniques for spectral reconstruction in diffuse optical tomography. *Applied Optics*, page submitted, 2008.

[158] S. R. Arridge and W. R. B. Lionheart. Nonuniqueness in diffusion-based optical tomography. *Optics Letters*, 23:882 – 884, 1998.

[159] A. N. Tikhonoc an V. A. Arsenin. *Solution of Ill-posed Problems.* Winston & Sons, Washington, 1977.

[160] T. Nielsen, B. Brendel, R. Ziegler, F. Uhlemann, C. Bontus, and T. Koehler. Linear image reconstruction for a diffuse optical mammography system in a non-compressed geometry using scattering fluid. *Applied Optics*, submitted, 2008.

[161] S. R. Arridge and J. C. Hebden. Optical imaging in medicine: II. modelling and reconstruction. *Physics in Medicine and Biology*, 42:841 – 853, 1997.

[162] Regine Choe. *Diffuse optical tomography and spectroscopy of breast cancer and fetal brain.* PhD thesis, University of Pennsylvania, 2005.

[163] R. Ziegler, T. Nielsen, T. Köhler, D. Grosenick, O. Steinkellner, A. Hagen, R. Macdonald, and H. Rinneberg. Nonlinear reconstruction of absorption and fluorescence contrast from measured diffuse transmittance and reflectance of a compressed-breast-simulating phantom. *Applied Optics*, page in preparation, 2008.

[164] Y. Censor. Row-action methods for huge and sparse systems and their applications. *SIAM Review*, 4:444 – 466, 1981.

[165] Th. Köhler, R. Proksa, and T. Nielsen. SNR-weighted ART applied to transmission tomography. In *Nuclear Science Symposium Conference Record*, pages 2739 – 2742. IEEE, 2003.

[166] B. Brooksby, H. Deghani, B. W. Pogue, and K. D. Paulsen. Near infrared (NIR) tomography breast image reconstruction with a priori structural information from MRI: algorithm development for reconstructing heterogeneities. *IEEE Journal of Selected Topics in Quantum Electronics*, 9:199 – 209, 2003.

[167] M. Schweiger and S. R. Arridge. Application of temporal filters to time resolved data in optical tomography. *Physics in Medicine and Biology*, 44:1699 – 1717, 1999.

[168] D. A. Boas, T. Gaudette, and S. R. Arridge. Simultaneous imaging and optode calibration with diffuse optical tomography. *Optics Express*, 8(9):263 – 270, 2001.

[169] A. Soubret and Vasilis Ntziachristos. Fluorescence molecular tomography in the presence of background fluorescence. *Physics in Medicine and Biology*, 51:3983 – 4001, 2006.

[170] E. Scherleitner and B. G. Zagar. Optical tomography imaging based on higher order born approximation of diffuse photon densitiy waves. *IEEE Transactions on Instrumentation and Measurement*, 54(4):1607 – 1611, 2005.

[171] Alper Corlu, Regine Choe, Turgut Durduran, Kijoon Lee, Martin Schweiger, Simon R. Arridge, Elizabeth M. C. Hillman, and Arjun G. Yodh. Diffuse optical tomography with spectral constraints and wavelength optimization. *Applied Optics*, 44(11):2082–2093, 2005.

[172] A. Li, Q. Zhang, J. P. Culver, E. L. Miller, and D. A. Boas. Reconstructing chromosphere concentration images directly by continuous-wave diffuse optical tomography. *Optics Letters*, 29(3):256 – 258, 2004.

[173] S. Srinivasan, B. W. Pogue, S. Jiang, H. Dehghani, and K. D. Paulsen. Spectrally constrained chromophore and scattering near-infrared tomography provides quantitative and robust reconstruction. *Optics Express*, 14(12):5394 – 5410, 2006.

[174] Stephanie M.W.Y. van de Ven, Sjoerd G. Elias, Andrea J. Wiethoff, Marjolein van der Voort, Anais Leproux, Tim Nielsen, Bernhard Brendel, Leon P. Bakker, Martin B. van der Mark, Willem P.Th.M. Mali, and Peter Luijten. non-dye paper. *Investigative Radiology*, page submitted, 2008.

[175] Stephanie M.W.Y. van de Ven, Andrea J. Wiethoff, Tim Nielsen, Bernhard Brendel, Claas Bontus, Rami Nachabe, Marjolein van der Voort, Michiel van Beek, Leon P. Bakker, Peter Luijten, Lueder Fels, and Willem P.Th.M. Mali. Dye-study paper. *Journal of Clinical Oncology*, submitted, 2008.

[176] Predag R. Bakic, Michael Albert, Dragana Brazkovic, and Andrew D. A. Maidment. Mammogram synthesis using a 3D simulation. I. breast tissue model and image acquisition simulation. *Medical Physics*, 29(9):2131 – 2139, 2002.

[177] K. Bliznakova, Z. Bliznakov, V. Bravou, Z. Kolitsi, and N. Pallikarakis. A three-dimensional breast software phantom for mammography simulation. *Physics in Medicine and Biology*, 48:3699 – 2719, 2003.

[178] Christos Zyganatidis, Kristina Bliznakova, and Nicolas Pallikarakis. A novel simulation algorithm for soft tissue compression. *Medical & Biological Engineering & Computing*, 45:661 – 669, 2007.

[179] Wouter Wiggers. Architecture for volume reconstruction in diffuse optical tomography. Master's thesis, University of Twente, 2007.

[180] T. Nielsen, B. Brendel, Th. Köhler, R. Ziegler, A. Ziegler, L. Backer, M. v. Beek, M. v. d. Mark, M. v. d. Voort, R. Habers, K. Licha, M. Pessel, F. Schippers, J. P. Meeuwse, A. Feuerabend, D. v. Pijkeren, and S. Deckers. Image reconstruction and evaluation of system performance for optical fluorescence tomography. In *Progress in Biomedical Optics and Imaging – Multimodal Imaging*, volume 8, 2007.

[181] W. G. Egan and T. W. Hilgeman. *Optical Properties of Inhomogeneous Materials*. Academic, New York, 1979.

[182] M. Keijzer, W. M. Star, and P. R. M. Storchi. Optical diffusion in layered media. *Applied Optics*, 27(9):1820 – 1824, 1988.

[183] Wolfgang Bangerth, Ralf Hartmann, and Guido Kanschat. deal.II — a general-purpose object-oriented finite element library. *ACM Trans. Math. Softw.*, 33(4):1–27, 2007.

[184] Inc. ANSYS. Ansys homepage http://www.ansys.com/, 2007.

[185] E. Cuthill and J. McKee. Reducing the bandwidth of sparse symmetric matrices. In *Proceedings of the 1969 24th national conference*, pages 157 – 172, New York, NY, USA, 1969. ACM Press.

[186] A. H. Stroud and D. Secrest. *Gaussian Quadrature Formulas*. Englewood Cliffs, NJ: Prentice-Hall, 1966.

[187] Andreas H. Hielscher and Sebastian Bartel. Parallel programming of gradient-based iterative image reconstruction schemes for optical tomography. *Computer Methods and Programs in Biomedicine*, 73:101 – 113, 2004.

[188] A. Joshi, W. Bangerth, and E. M. Sevick-Muraca. Adaptive finite element based tomography for fluorescence optical imaging in tissue. *Optics Express*, 12(22):5402 – 5417, 2004.

[189] Wolfgang Bangerth, Amit Joshi, and Eva M. Sevick-Muraca. Inverse biomedical imaging using separately adapted meshes for parameters and forward model variables. *Proceedings of the IEEE International Symposium on Biomedical Imaging, Arlington, VA, 2007*, pages 1368–1371, 2007.

[190] Joseph Hoffmann. *Matlab und Simulink: Beispielorientierte Einführung in die Simulation dynamischer Systeme*. Addison-Wesley, 1998.

[191] American College of Radiology. *BI-RADS - Mammography, Fourth Edition*. Reston, VA: American College of Radiology, 2003.

[192] H. Danlewski. *Physikalische Grundlagen der zeitaufgelösten optischen Mammographie einschliesslich Anwendungen*. PhD thesis, Free University of Berlin, 1998.

Zusammenfassung, Ausblick und Schlussfolgerungen

Zusammenfassung

Ziel der vorliegenden Doktorarbeit war die Entwicklung und Validierung statistischer und numerischer Methoden, sowie die Entwicklung von benötigten Computerprogrammen zur quantitativen Bewertung verschiedener Messkonzepte, Messsysteme und Methoden der Datenanlyse der optischen und Fluoreszenzmammographie, einschließlich der Analyse von klinischen Daten.

Zu diesem Zweck wurde ein Softwarepaket entwickelt, das auf Basis der Finite-Elemente-Methode (FEM) die Ausbreitung von Nahinfrarotlicht (Laserlicht) und Fluoreszenzlicht durch inhomogenes diffus streuendes Gewebe mittels der Diffusionsnäherung der Strahlungstransportgleichung simuliert, und lineare sowie nichtlineare Rekonstruktionen der Absorptions- und Streueigenschaften des Mediums unter Verwendung von simulierten oder experimentellen Daten ausführt, die im Frequenz- oder Zeitraum gewonnen wurden. Für beliebige Objektgeometrien (Brust) und Anordnungen von Quellen und Detektoren werden Simulationen der Photonendichte von diffusiv transmittiertem oder remittiertem Laserlicht und Fluoreszenzlicht eines exogenen Fluoreszenzkontrastmittels vom Softwarepaket unterstützt.

In dieser Doktorarbeit wurde eine statistische Methode entwickelt, um Nachweisgrenzen von Läsionen für zwei verschiedene, momentan in klinischen Studien zur Laser- und Fluoreszenzmammographie eingesetzte instrumentelle Konzepte der optischen Mammographie zu bestimmen. Bei tomographischen Mammographen liegt die Patientin auf dem Bauch, während eine der beiden Brüste in eine Streuflüssigkeit eintaucht, die sich in einer schalenförmigen Messkammer (tomographische Geometrie) befindet, welche an ihrer Oberfläche mit einer Vielzahl von Lichtquellen und Detektoren ausgestattet ist. Die Transmittanz des Laser- und Fluoreszenzlichts wird für eine große Anzahl von Quell-Detektor-Kombinationen gemessen und erlaubt somit eine nahezu komplette Winkelabdeckung der Brust. Raster-Mammographen hingegen komprimieren die Brust leicht zwischen zwei parallelen Glassplatten (planparallele Geometrie) und rastern die Quelle über eine der Kompressionsplatten. Dabei wird die Transmittanz an einer großen Zahl von Quellpositionen (Rasterpositionen), jedoch nur für eine kleine Anzahl von seitlichen Versätzen zwischen Quelle und Detektor gemessen (eingeschränkte Winkelabdeckung). Die statistische Analyse von verrauschten simulierten Photonendichten diffusiv transmittierten Laser- und Fluoreszenzlichts basiert auf einem Chi-Quadrat-Test (Test der Nullhypothese) und erlaubt es, die minimale Größe (Radius) einer einzelnen (sphärischen) Heterogenität quantitativ zu bestimmen, damit sie bei einem im Vergleich zum (homogenen) Hintergrundmedium angenommen Absorptions- und Fluoreszenzkontrast noch detektierbar ist. Für diese Simulationen wurden numerische Brustmodelle mit einer zur Messgeometrie angepassten Brustform entwickelt, welche einen realistischen Bereich der Gewebeabsorption und -streuung, d.h. der Lichtschwächung, abdecken. Aus Messungen an einem existierenden optischem Mammographen wurde ein realistisches Rauschmodell bestimmt, um den Anteil von absolutem und relativem Rauschen zur simulierten Photonendichte der transmittierten Laser- und Fluoreszenzstrahlung zu bestimmen. Aus der statistischen Analyse simulierter Daten wurde die minimale noch detektierbare Größe einer (sphärischen)

Läsion an verschiendenen Positionen innerhalb der Brust berechnet, und deren Abhängigkeit von der Brustgröße (tomographische Geometrie), der Dicke der komprimierten Brust (planparallele Geometrie), sowie den optischen Eigenschaften des Hintergrundgewebes (normales Brustgewebe) simuliert. Zusätzlich wurde untersucht, wie die Detektierbarkeit einer Läsion von der Brustkompression (planparallele Geometrie), vom absoluten und relativen Rauschen der simulierten Photonendichten, der Läsionsgröße und vom Fluoreszenzkontrast der Läsion abhängt. Aufgrund der im allgemeinen kleineren Quell-Detektor-Abstände der planparallelen Geometrie und der daraus folgenden größeren transmittierten Laser- und Fluoreszenzintensitäten, ist die Empfindlichkeit bezüglich einer Detektierbarkeit einer Läsion höher für Raster-Mammographen als bei tomographischen Mammographen und wird weniger durch das absolute Rauschen beeinflusst. Ein minimaler in Fluoreszenzmammogrammen noch detektierbarer Fluoreszenzkontrast der Läsion gegenüber dem homogenen Hintergrund wurde zu $2.5:1$ abgeschätzt. Zwar könnten derartige Untersuchungen auch durch Rekonstruktionen der Absorptionskoeffizienten und der Konzentration des exogenen Fluoreszenzfarbstoffs ohne statistische Analyse erreicht werden, jedoch verhindert der hierfür enorme Rechenaufwand derartige Studien.

In planparalleler Geometrie ist eine Interpretation von Projektionen optischer Mammogramme auch ohne vorhergehende Rekonstruktion der optischen Eigenschaften des Gewebes möglich. Bei zeitaufgelösten Messungen werden dazu standardmäßig Zeitfenster der Impusantwortfunktion der transmittierten Laserpulse analysiert, um Projektionsmammogramme zu erhalten, welche hauptsächlich die Absorptions- und Streueigenschaften des Brustgewebes aufzeigen. Mittels eines numerischen Phantoms für eine komprimierte Brust mit Läsion (planparallele Geometrie) und Simulationen von verrauschten Zeitverteilungskurven, wurde die Datenanalyse von Transmissionsmammogrammen im Zeitraum verbessert, indem das Übersprechen zwischen Absorptions- und Streubildern im Vergleich zur Standardmethode reduziert werden konnte.

Während die bisherigen Resultate mittels simulierter Daten erreicht wurden, basieren weitere Ergebnisse dieser Doktorarbeit auf linearen und nichtlinearen Rekonstruktionen von Absorptionskoeffizienten und reduzierten Streukoeffizienten von Gewebe und der Konzentration eines exogenen Fluoreszenzfarbstoffs. Dazu wurden verschiedene Verbesserungen an Rekonstruktionsalgorithmen entwickelt, wie z.B. eine rauschgewichtete Rückprojektion der zur Berechnung des Bildvektors eingesetzten algebraischen Rekonstruktionstechnik (ART) sowie separate Regularisierungsparameter für Absorptions- und Streurekonstruktionen eingeführt. Weiterhin wurde die standardmäßige nichtlineare Rekonstruktion um eine Partialvolumen-Methode erweitert, um die bei Raster-Mammographie (planparallele Geometrie) anfallende Datenmenge bearbeiten zu können, und um die Rekonstruktionen zu beschleunigen. Bei dieser Rekonstruktionsmethode wird das gesamte Rekonstruktionsvolumen (Quader) in mehrere (überlappende) Partialvolumina aufgeteilt. Zusätzlich werden auch die gesamten Messdaten einer Standardrekonstruktion in zu den jeweiligen Partialvolumina zugehörige Untermengen von Quell-Detektor-Kombinationen aufgeteilt. Danach wird die Rekonstruktion der optischen Eigenschaften auf den verschiedenen Partialvolumina auf Rechner-Cluster parallel ausgeführt, wodurch eine deutliche Beschleunigung der Rekonstruktion im Vergleich zur Standardmethode erreicht wird. Mittels simulierter und experimenteller Phantom-Daten eines Brust-Phantoms wurde die Konvergenz der Standardmethode und der Methode der nichtlinearen Partialvolumina-Rekonstruktion untersucht. Zusätzlich wurden die durch die Zerlegung des Rekonstruktionsvolumens in Untervolumen entstehenden Fehler und Einschränkungen analysiert. Derartige Fehler sind tolerierbar so lange die Anzahl an Partialvolumina klein ist, und der gesamte Datensatz, der in der Standardrekonstruktion verwendet wird, auch von der Partialvolumina-Methode genutzt werden kann. Mit anderen Worten, die Größen der Partialvolumina müssen konsistent mit allen seitlichen Quell-Detektor Versätzen sein, so dass der Winkelbereich der Daten, die von der Partialvolumina-Methode verwendet werden im Vergleich zur (bereits beschränkten) Winkelabdeckung des anfänglichen Datensatzes nicht weiter eingeschränkt wird. Der Einsatz der Partialvolumina-Rekonstruktionsmethode wurde unter Verwendung von experimentellen Daten erfolgreich geprüft.

In planparalleler Geometrie ist eine Messung der Transmittanz von Laser- und Fluoreszenzlicht nur über einen eingeschränkten Bereich von Projektionswinkeln möglich, was zu einer weiteren Reduzierung

der axialen Auflösung der rekonstruierten Bilder von optischen Eigenschaften im Vergleich mit der Ortsauflösung von tomographischen Mammographen führt. In dieser Arbeit wurde gezeigt, dass die axiale Auflösung von zeitaufgelösten Raster-Mammographen (planparallele Geometrie) durch Hinzunahme der Messung der diffusen Remission zusätzlich zur Transmission verbessert werden kann. Dazu wurden Rekonstruktionen von simulierten und experimentellen Daten mit und ohne zeitaufgelöster diffuser Remittanzmessung ausgeführt, und die dabei erhaltene Ortsauflösung verglichen. Um das unterschiedlich starke Rauschen der experimentellen Daten bei verschiedenen seitlichen Quell-Detektor Versätzen und verschiedenen Modulations-Frequenzen zu berücksichtigen, wurde eine rauschgewichtete Rückprojektion angewendet, um quantitative Fluoreszenzfarbstoffkonzentration zu rekonstruieren.

Mit den bei einer klinischen Studie vom tomographischen Fluoreszenzmammographen gesammelten Daten von vier Patientinnen wurden sowohl lineare und nichtlineare Absorptionsrekonstruktionen als auch (lineare) Fluoreszenzfarbstoffrekonstruktionen ausgeführt. In allen Fällen konnte die Läsion in den Absorptions- (erste drei Patientinnen) und im Fluoreszenzmammogramm (vierte Patientin) entdeckt werden, und auch eine Korrelation mit den zugehörigen MR-Mammogrammen war erfolgreich, sofern diese vorhanden. Ein verbessertes Initialisierungsmodell für eine lineare und nichtlineare Rekonstruktion der klinischen Daten wurde eingeführt. Hierbei wurde das zu rekonstruierende Volumen der schalenförmigen Messkammer in zwei Bereiche aufgeteilt, wobei einer dem Volumen der Streuflüssigkeit entspricht, welche die eingetauchte Brust umgibt, und der andere eine homogene Brust mit einer abgeschätzten Form und gefitteten Absorptions- und Streu-Eigenschaften repräsentiert, welche in einem Vorverarbeitungsschritt unter Einbeziehung der bei verschiedenen Wellenlängen gemessenen in vivo Daten abgeschätzt wurden. Rekonstruierte Absorptionskoeffizienten und rekonstruierte Konzentrationen des benutzten Fluoreszenzfarbstoffs zeigten Artefakte, die Änderungen in den Streu-Eigenschaften des Brustgewebes ausgleichen, da alle Läsionen als reine Absorber angenommen wurden und keine Änderungen des reduzierten Streukoeffizienten im Brustgewebe berücksichtigt wurden.

Ausblick: Themen für weitere Untersuchungen

Dieser Abschnitt zeigt Möglichkeiten für weitere Untersuchungen auf, die über die in dieser Doktorarbeit vorgestellten Resultate hinaus gehen. Die hier präsentierten Untersuchungen zu Nachweisgrenzen sind für eine idealisierte und damit unrealistische Situation ausgeführt worden, bei der sich eine einzelne Heterogenität in einem ansonsten homogenen numerischen Brust-Phantom befand. Hiermit konnten instrumentelle Nachweisgrenzen der untersuchten Mammographen analysiert werden. Für die Bestimmung von klinischen Nachweisgrenzen wäre es relevanter, realistischere Phantome zu benutzen, d.h. inhomogene numerische Brust-Phantome, die Messungen an Patientinnen besser nachbilden [176, 177, 178]. Weiterhin könnte die aufgezeigte statistische Methode oder auch Rekonstruktionen dazu benutzt werden, um mittels der Trennung zweier nebeneinander liegender Heterogenitäten die Ortsauflösung verschiedener Quell-Detektor Aufbauten quantitativ zu bestimmen. Anstatt den minimalen Detektionsradius einer einzelnen Läsion zu berechnen, würde der kleinste benötigte Abstand zum Trennen zweier Heterogenitäten als Maß der Ortsauflösung dienen.

Trotz einer Parallelisierung der Rechnungen benötigen nichtlineare Rekonstruktionen von Absorptionskoeffizienten und der Fluoreszenzfarbstoffkonzentration ausgehend von klinischen Daten, die mit kontinuierlichem Laserlicht gemessen wurden, bis zu mehreren Stunden an Rechenzeit. Durch Hardware-Verbesserungen (z.B. durch Auslagern der Rechnungen auf Grafikkarten die Prozessoren mit hohem Datendurchsatz enthalten [179]) könnten deutliche Beschleunigungen erreicht werden. Dies würde nahzu Echtzeit-Berechnungen erlauben, und dem Arbeitsablauf in der Klink entgegenkommen.

Schlussfolgerungen

Aufgrund der besseren Winkelabtastung von tomographischen Mammographen mit ring- oder schalenförmiger Anordnung werden bessere Ortsauflösungen in Quell-Detektor Richtung erreicht, als für Raster-Mammographen mit komprimierter Brust. Trotzdem zeigte die statistische Analyse simulierter Daten, dass die planparallele Geometrie aufgrund der kürzeren Trajektorien der Photonen, dem kleineren absoluten Rauschen und dem deutlich kleineren benötigten Dynamikbereich der Detektoren eine niedrigere Detektionsgrenze besitzt. Zusätzlich zeigten Rekonstruktionen von simulierten und experimentellen Phantom-Daten, dass die axiale Auflösung von Läsionen in planparalleler Geometrie durch Messung der Transmittanz und der zeitaufgelösten Reflektanz, am besten auf beiden Seiten der komprimierten Brust, verbessert werden kann. Aufgrund der starken Streuung leidet die diffuse optische Tomographie unter der schlechten Ortsauflösung verglichen mit Röntgenmammographie, Kernspintomographie und Ultraschall-Mammographie. Die innerhalb dieser Arbeit ausgeführten Rekonstruktionen klinischer Daten zeigen, dass für jede einzelne Patientin die über die gesamte Brust gemittelten und gefitteten Absorptions- und Streukoeffizienten benötigt werden, um die Bildqualität im Vergleich zu einem Ansatz unter Benutzung typischer optischer Eigenschaften von Brustgewebe zu verbessern. Experimentelle Daten, die mit kontinuierlichem Laserlicht aufgenommen wurden, erlauben alleine dies jedoch nicht. Stattdessen sollte ein Fluoreszenzmammograph einige Kanäle für Messungen im Frequenz- oder Zeit-Raum besitzen, um mit diesen die optischen Eigenschaften zuverlässig zu bestimmen, während durch eine größere Anzahl von zusätzlichen Kanälen mit kontinuierlichem Laserlicht eine gute Winkelabdeckung erreicht werden sollte. Zukünftige klinische Versuche zur Fluoreszenzmammographie sollten mit einem derartigen Hybridsystem zusammen mit einer nichtlinearen Rekonstruktion des Absorptions- und Fluoreszenzkontrastes ausgeführt werden.

Obwohl in dieser Arbeit nicht behandelt, ist aus klinischer Sicht eine Untersuchung der differentiellen Diagnose, d.h. der Unterscheidbarkeit von malignen und benignen Tumoren, genauso wichtig, wie die Detektionsfähigkeit von Läsionen an sich. Unterscheidung von benignen und malignen Läsionen kann aber nicht alleine durch intrinsische Eigenschaften (Absorption und Streuung) erreicht werden, dies könnte aber durch Benutzung eines Fluoreszenzfarbstoffs möglich sein. Resultate dieser Arbeit legen es nahe, dass eine Raster-Fluoreszenz-Mammographie technisch möglich ist und Detektion und Unterscheidung von Brust-Tumoren ein Anwendungsszenario sein könnte, wenn ein klinisch geeigneter Farbstoff erhältlich wird. Trotz vieler möglicher technischer Verbesserungen zeigte die klinische Studie des Fluoreszenzmammographen, dass ein klinischer Nutzen, ein Anwendungsszenario und ein Erfolg der Fluoreszenzmammographie stark vom benutzten Fluoreszenzkontrastmittel und weniger von den technischen Details abhängen, selbst unter dem Gesichtspunkt der finanziellen Beschränkungen eines kommerziellen Gerätes.

Curriculum Vitae

Der Lebenslauf ist in der Online-Version
aus Gründen des Datenschutzes nicht enthalten